Initial break-up process of Gondwana, off South Africa and in the Cosmonauts Sea off East Antarctica

HANYU TOMOKO

Doctor of Philosophy

Department of Polar Science
School of Multidisciplinary Sciences
SOKENDAI (The Graduate University for Advanced Studies)

Initial break-up process of Gondwana, off South Africa and in the Cosmonauts Sea off East Antarctica

Tomoko Hanyu

Doctor of Philosophy

Department of Polar Science
School of Multidisciplinary Sciences
SOKENDAI (The Graduate University for Advanced Studies)

2017

Contents

Glossary

Abbreviations

2D	two dimensional
AFFZ	Agulhas-Falkland fracture zone
AFR	Africa
AG	Ariel Graben
ANT	Antarctica
AP	Agulhas Plateau
AR	Astrid Ridge
AUS	Australia
BB	Bay of Bengal
CEB	central Enderby Basin
CIR	Central Indian Ridge
CNS	Cretaceous Normal Superchron
COB	Continent-ocean boundary
COTZ	continent-ocean transition zone
CR	Conrad Rise
DSDP	Deep Sea Drilling Project
EB	Enderby Basin
EE	Explora Escarpment
FP	Falkland Plateau
FZ	Fracture zone
GPS	Global Positioning System
GR	Gunnerus Ridge
IGRF	International Geomagnetic Reference Field
IND	India
ISDV	Intensities of the spatial differential vectors
JARE	Japanese Antarctica Research Expedition
JQZ	Jurassic Quiet Zone
KP	Kerguelen Plateau
LIP	Large igneous province
LZS	Lazarev Sea

M-series	geological timescale during late Jurassic to early Cretaceous
Ma	Million years ago
MAD	Madagascar
MAR	Mid Atlantic Ridge
MB	Mozambique Basin
MBS	Magnetic boundary strikes
MEB	Maurice Ewing Bank
MOZCP	Mozambique Coastal Plains
MOZR	Mozambique Ridge
MR	Maud Rise
Myr	Million years
N-MOZR	north part of the Mozambique Ridge
N-SNV	north part of the northern Natal Valley
NEGR	Northeast Georgia Rise
NNV	Northern Natal Valley
RLS	Riiser-Larsen Sea
S-MOZR	south part of the Mozambique Ridge
S-SNV	south part of the southern Natal Valley
SA	South America
SB	Somali Basin
SD	Standard deviation
SDR	Seaward dipping reflector
SEIR	Southeast Indian Ridge
SL	Sri Lanka
SNV	Southern Natal Valley
STCM	Shipboard three-component magnetometer
SWIR	Southwest Indian Ridge
UTC	Coorinated Universal Time
VGG	Vertical Gravity Gradient
XR	Extinct ridge

Beginning age of the magnetic isochron based on after Gradstein (2008)

C34	84.00 Ma	
M0 (M0r)	124.61 Ma	
M1n	125.00 Ma	
M1r	127.24 Ma	
M3n	127.61 Ma	M2 in Rabinowitz and LaBreque Synthetic model
M3r	128.11 Ma	M3 in Rabinowitz and LaBreque Synthetic model
M5n	129.76 Ma	M4 in Rabinowitz and LaBreque Synthetic model
M5r	130.80 Ma	M5 in Rabinowitz and LaBreque Synthetic model
M6	131.19 Ma	
M7	131.56 Ma	
M8	132.20 Ma	
M9	132.83 Ma	
M10	133.50 Ma	
M10r	133.87 Ma	
M10N	134.30 Ma	
M11	135.69 Ma	
M12	137.60 Ma	
M25	154.08 Ma	

Abstract

The initial break-up of Gondwana was one of the most significant geological events to have affected the southern hemisphere in the past 200 Myr. The evolution of seafloor spreading in the Indian Ocean is key to understanding the break-up process of Gondwana. Reconstruction models of Gondwana have been proposed based on geophysical data; however, the detailed initial break-up process of Gondwana is poorly understood because of the sparse geophysical data, especially around the continental margins of the Indian Ocean. To reveal the initial break-up process of Gondwana, systematic vector geomagnetic surveys were conducted in the Natal Valley and Mozambique Ridge, off South Africa, and the Cosmonauts Sea, off East Antarctica.

The Natal Valley and Mozambique Ridge were formed as a result of opening between Africa, South America and Antarctica during the initial stage of Gondwana break-up, and there was an unsolved problem as to whether the underlying crust is continental and/or oceanic in this region. I summarize the nature of the crust using the results of dense vector geomagnetic anomaly data, as well as satellite gravity data. Based on both inversion and forward analytical results, I identified areas of stretched continental crust, with basaltic magma intrusion in parts, as the northern Natal Valley, the north part of the Mozambique Ridge, and the north part of the southern Natal Valley. Oceanic crust was identified in the south part of the southern Natal Valley and the south part of the Mozambique Ridge. Magnetic isochrons M0–M10 (125.0–133.5 Ma) were identified in the south part of the southern Natal Valley. Clear magnetic lineations were observed in the south part of the Mozambique Ridge, where parts of these areas were distorted by hotspot volcanism. Seafloor spreading between Africa and South America in the study area occurred at chron M10 (133.5 Ma). The formation of the Natal Valley and Mozambique Ridge finished at chron M0 (124.6 Ma); therefore, I inferred that the seafloor spreading between Africa and Antarctica likely started at chron M0. The location of the continent–ocean boundary in the Natal Valley and Mozambique Ridge is newly proposed along with a four-stage model of tectonic evolution of the study area since about 183 Ma.

The Cosmonauts Sea in the western Enderby Basin, off East Antarctica, was formed as a result of opening between Antarctica and Sri Lanka/India/Madagascar. The seafloor spreading history of this region is still poorly understood because of sparse marine

geophysical data. A systematic vector geomagnetic survey of SE–NW oriented four track lines was carried out in the Cosmonauts Sea using the icebreaker *Shirase* during the 54th Japanese Antarctic Research Expedition (JARE). Data acquired during other JARE marine geophysical surveys were also used. The isochrons M10N–M3n (134.3 Ma–127.6 Ma) with an almost WNW–ESE spreading direction in the south of the Cosmonauts Sea were newly identified with several smaller segments. Moreover, the thinned continental crust, which was implied by the previous study, was inferred from multiple analytical results from vector geomagnetic anomalies, as well as satellite gravity data. One possibility for the Kainan-Maru Seamount, a northern portion of the Gunnerus Ridge, is that it was divided from the Gunnerus Ridge, and was a replacement from the continental shelf, based on to the WNW–ESE continental extension and seafloor spreading. The seafloor spreading occurred at about chron M10N (134.3 Ma). The transition of seafloor spreading around the 65°S likely occurred during chron M3n–M0r (127.6–124.6 Ma). Then, the NNE–SSW oriented seafloor spreading started since chron M0 (124.6 Ma) in the north of the Cosmonauts Sea.

Seafloor spreading was initiated in chron M10 (133.5 Ma), and the change in spreading regime occurred in chron M0 (124.6 Ma) in both the Natal Valley and Mozambique Ridge, off South Africa, and in the Cosmonauts Sea, off East Antarctica. During the initial break-up of Gondwana, continental extension occurred before seafloor spreading around each continental margin. The intense basaltic magmatic activity, which was likely related to the large igneous province (LIP) or hotspot, was suggested to have occurred prior to seafloor spreading at some parts of the continental margins between Africa and South America. In contrast, there is no evidence of intense magmatic activity before the seafloor spreading at the continental margins between Antarctica, Sri Lanka/India, and Australia. I organized the Gondwana break-up system by compiling the spreading rate, spreading direction, initiation age of seafloor spreading, and the relationships of spreading ridges with LIPs or hotspot located at each continental margin based on my study and previous studies. My conclusion was that intense volcanic activities such as LIPs and hotspots were not indispensable for the initial fragmentation of Gondwana. The configuration of the subduction zones surrounding Gondwana likely forced seafloor spreading during chron M10 and M0. My new findings constrain the initial break-up process of Gondwana in the Indian Ocean, especially around chron M10 and M0.

Chapter 1. General Introduction

1.1 Gondwana Break-up

The theory of continental drift was first developed by Alfred Lothar Wegener in 1912. He proposed that the Earth's continents had once formed a single supercontinent named "Pangea", which slowly drifted and broke apart into the present continental positions. His hypothesis had higher scientific accuracy than the previous theories (e.g., Land-bridge; Expanding Earth) based on geodesy, geology, paleontology, paleoclimatology, and geophysics. However, he could not explain the physical driving force of the drift and separation velocity of 2,500 mm/yr in his examination. Many geologists and biologists of that time did not accept his hypothesis for many years. Arthur Holmes (1931) suggested that the sub-continental circulations of the mantle caused by radioactive heat moved the crust at the surface, and that continental drift was probably caused by mantle convection. Evidence for continental drift such as "mid-ocean ridges" and "magnetic lineation" were obtained through marine observations from core sampling, sub-bottom profiling, and magnetic surveys in the 1950s–1960s. Based on seismic, magnetic, and petrologic studies, the theory of "seafloor spreading" was proposed (Dietz, 1961). Studies of rock samples and seismic velocities revealed that the composition and structure of the oceanic crust was basically different from that of the continental crust, and that the uniform thickness of the oceanic crust was formed at the mid-ocean ridge by mantle convection systems (Hess, 1962). Moreover, large amplitudes of magnetic anomalies across the mid-ocean ridges were observed. Vine and Matthew (1963) suggested that the magnetic lineation, distributed asymmetrically centered on the mid-ocean ridge, represents the record of geomagnetic reversal patterns. Additionally, the study of rock magnetism revealed that the oceanic floor became older farther away from the ridge axis (Morley and Larochelle, 1964). Magnetic lineation is the zebra-stripe pattern of the crustal magnetization anomaly, and is considered to be an expression of the reversal pattern of the Earth's magnetic field. The Earth's magnetic field reversal, which repeats at random cycles every few million years, was identified based on studies of rock magnetism and K–Ar radiometric dating methods. On the mid-ocean ridge, at the eruption point of hot mantle material,

upwelling volcanic material is cooled by the seawater to below the “Curie temperature”. The Curie temperature is the temperature at which magnetic materials obtain heat from residual magnetization; for example, the Curie temperature of magnetite, which is a major magnetic mineral in the earth’s crust, is 858 K. Mantle materials exist in temperature conditions higher than the Curie point, and the magnetization direction of these magnetic materials is disturbed by heat. The magnetic materials acquire a remanent magnetization parallel to the direction of the Earth’s magnetization when volcanic material with ferromagnetic minerals is exposed over the ridge. The volcanic product obtains a paleo-geomagnetic field at that time as heat residual magnetization, and becomes solid oceanic crust. The theory of seafloor spreading demonstrates that the mid-ocean ridge is where new oceanic crust is produced, and that oceanic crust moves away from the central axis of the mid-ocean ridge accompanied with mantle convection. Wegener’s hypothesis of continental drift attracted renewed attention, and “Plate Tectonics”, including the theory of continental drift and seafloor spreading, was developed in late 1960s (e.g., Le Pichon, 1968; Morgan, 1968; Wilson, 1968a,b). Actual observation of continental drift was enabled after the development of survey technology using a radio star and satellite in the late 1980s. In the present day, a movement speed of up to several centimeters per year for many continents has been revealed on a global scale.

The investigation of oceanic crust is necessary to reveal the history of seafloor spreading according to continental drift. Oceanic crust accounts for about 70% of the surface of the earth, and is dominated by an average 3,000–6,000 m depth of flat oceanic floor, although there are a variety of bathymetric features such as ridges, trenches, and seamounts. Oceanic crust produced at the mid-ocean ridge moves and sinks down to the subduction zone after about 200 million years in the generation cycle of the oceanic crust. Most oceanic crust is not deformed by large-scale modifications, such as orogeny of the continental crust. Volcanic activity at the oceanic crust is focused in sparse areas of the spreading axis region. The oceanic crust preserves geophysical information, such as geomagnetism, acquired on the ridge before it sinks into the subduction zone.

Marine geomagnetic observations can clarify the magnetic lineations that demonstrate the history of seafloor spreading, such as the spreading direction and the formation age. Geomagnetic surveys using satellites have also been conducted in recent

years. However, these observation signals do not have enough resolution to determine seafloor history because of the high satellite altitude (4 km above mean sea level). Therefore, necessary evidence for magnetic lineation can only be acquired using ships, underwater vehicles, and near-surface airborne surveys.

Areas where the magnetic lineation is not obtained are typically another constraint on the spreading direction using topographic structures such as fracture zones, which are deduced from acoustic bathymetry, seismic, and gravity surveys. A fracture zone extends far away from a corresponding transform fault produced by the discontinuity of the oceanic crust on the mid-ocean ridge with seafloor spreading. For example, the Cretaceous Normal Superchron is known as a very long period with only normal magnetization polarity for 40 million years, from 124.6 million years ago (Ma) to 84 Ma (Gradstein, 2008). There is only a change in amplitude; therefore, the magnetic lineation for seafloor history could not be detected in this period. Spreading direction from 124.6–84 Ma is only constrained by fracture zones in general. In addition, the clear magnetic lineation from which the formation age could be determined is also disturbed by volcanic activities, such as hotspots and large igneous provinces. However, age determination of the rock samples dredged or drilled from the seafloor constrains the formation age of volcanic plateaus and seamounts. The formation age and spreading direction of the seafloor are finally obtained based on a number of marine geophysical and geological observations, and constrain the break-up history of the supercontinent.

The Supercontinent “Pangea” existed on the earth from the Permian Period to the Triassic Period (e.g., Dietz, 1970; Van der Voo et al., 1976; Torsvik and Voo, 2002; Shephard et al., 2013). In the early Jurassic at about 200 Ma, Pangea was divided into two supercontinents, “Laurasia” and “Gondwana”. Gondwana was constructed from the plates of Africa, South America, the Indian subcontinent, Madagascar, Antarctica, Australia, and the Arabian Peninsula, and separated from Laurasia in the mid–Jurassic, about 180 Ma. Gondwana underwent further separation into West Gondwana and East Gondwana. In the Cretaceous, West Gondwana split into Africa and South America in association with the seafloor spreading of the Atlantic Ocean, while East Gondwana was divided into the Indian subcontinent, Madagascar, Antarctica, and Australia, accompanied by seafloor spreading of the Indian Ocean. Based on the observed seafloor ages and spreading directions, many Gondwana reconstruction models were proposed (e.g., Royer and Coffin, 1992; Storey, 1995; Seton et al., 2012). The most of the present

Antarctic margin and African east–west margins are surrounded by mid-ocean ridge. Because there is almost no subduction around these areas, the history of the break-up of Gondwana should be recorded well enough.

The Indian Ocean and Atlantic Ocean were formed as a result of the break-up of Gondwana. The initial break-up process of Gondwana is under discussion based on geological and geophysical data for the Indian and Atlantic Oceans (e.g., Eagles, 2007; Eagles and König, 2008). Magnetic lineation indicating formation before about 154 Ma has not been observed in the Indian and Atlantic Oceans. Continental extension during the initial break-up process of Gondwana was implied by the wide-spread seaward dipping reflectors with thickened crust. Observed magnetic lineations around Africa, South America, the Indian subcontinent, Madagascar, Antarctica, and Australia indicate that seafloor spreading in Gondwana first started at about 154 Ma (M25; e.g., Jokat et al., 2003), separating the supercontinent into West and East Gondwana, and secondly at about 137–133.5 Ma (M12–M10; e.g., Martin et al., 1982; Rabinowitz and RaBrecque, 1979), separating into each modern continent. The seafloor spreading directions and/or spreading rates in the Indian and Atlantic Oceans likely changed at around 124.6 Ma (e.g., Gibbons et al., 2012), based on geomagnetic and gravity data. The detailed initial break-up processes are still debated, with speculation about issues such as the nature of the crust, the timing of seafloor spreading, and the spreading direction at the continental margins. In addition, several hypotheses have been proposed, with different opinions about the formation process of nearby continental margins, especially in the Indian Ocean, such as whether it was caused by seafloor spreading or continental extension/fragmentation, and about what rotation the continent underwent (e.g., Eagles and König, 2008). However, a common opinion about the detailed initial break-up process of Gondwana has not yet been provided, because of limited geophysical data such as geomagnetic and seismic data around the continental margins.

The break-up of Gondwana was one of the most significant geological events in the southern hemisphere in the past 200 Myr, and greatly influenced the paleo-environment and paleoclimatic changes, as well as biological evolution. Revealing the break-up process of the supercontinent provides fundamental information about solid-earth dynamics such as mantle convection. Gondwana is the only supercontinent in the southern hemisphere that could reveal the break-up process based on marine geophysical data such as geomagnetic anomalies because of the generation cycle of

oceanic crust. Within a reasonable time-scale, it is uncertain whether the initiation of the break-up of Gondwana was caused by a mantle plume or subduction. The initial break-up process of Gondwana began with the break-up of West and East Gondwana. Thus, the understanding of the tectonics of advantageous seafloor areas, such as the Antarctic and African margins along the present boundary between West and East Gondwana, is key to investigating the initial break-up process of Gondwana. The opening of the Atlantic Ocean has been well studied since the 1960s, whereas the spreading history in the Indian Ocean is still debated. Recent studies provide consideration of new evolutionary processes in the Lazarew Sea, off East Antarctica (e.g., Hinz et al., 2004). The Lazarew Sea was located at the east edge of West Gondwana, and the evolutionary process of the Lazarew Sea and conjugate areas is considered to have a strong relationship with the initiation of the break-up of Gondwana. However, revealing the formation and evolution processes of the conjugate areas, such as off South Africa, is necessary for understanding the initial break-up of Gondwana; the fragmentation history of East Gondwana is still enigmatic (e.g., Seton et al., 2012). Understanding the formation and spreading process of areas such as the Cosmonauts Sea offshore of Syowa Station, located at the western edge of East Gondwana, is also required.

The location of the continent–ocean boundary (COB) is one of a number of features that can be used for constructing the Gondwana reconstruction model, although there are many uncertainties about the definition of the COB (Eagles et al., 2015). The location of the COB is estimated based on seismic, magnetic, and gravity studies. The COB is assigned to the boundary between the continental and oceanic crust, in general. The crustal magnetic susceptibility and density contrast between the continental and oceanic crust make an ‘edge effect’ anomaly of geomagnetism and gravity, respectively. Because of the continental extension of pre-spreading and/or the products of pre-spreading volcanism to the extended continental crust, it is difficult to determine the precise location of the COB. The finite-width continent–ocean transition zone (COTZ) is often used instead of a linear COB, because of the existence of the extended continental crust (with or without intense volcanism). The COTZ is observed as the seaward-dipping reflector (SDR), and is accompanied by normal faults, based on seismic reflection studies. Moreover, intermediate seismic velocity and crustal thickness between the continental and oceanic crust has been observed on the COTZ based on

seismic refraction studies. The magnetic anomaly in the COTZ shows similarities to those of the basalt layer of oceanic crust. The edge effect of the gravity anomaly is related to the continental and oceanic crust boundary, the distribution of sediment, underplated thermal composition, and underplated rock composition. Only the magnetic and gravity anomalies are therefore unlikely to show the precise location and scale of the COB and COTZ. Insufficient seismic data around the continental margins, especially in the Antarctic and Indian Oceans, make it difficult to identify the COB and COTZ.

The sparse observation lines caused by the difficulty of access interfere with the identification of continuity of magnetic isochrons and the actual spreading direction, especially at the Antarctic margin. Additionally, ambiguous magnetic signals (e.g., Seton et al., 2014) also prevented identification of magnetic anomaly lineation because of the thick sediment and/or long interval of the Cretaceous Normal Superchron at the continental margins. These factors make it difficult to understand the detailed initial break-up process of Gondwana.

Shipboard vector geomagnetic anomaly analysis is an effective tool for investigating both magnetic lineation and structural boundaries (e.g., Seama et al., 1993). Magnetic boundary strikes are only calculated from vector geomagnetic anomalies. The biaxial spatial differential derives a unique boundary of magnetization contrast. Therefore, a few observation lines of geomagnetic vectors make it possible to observe the clear magnetic lineation. Additionally, low magnetization contrast caused by the topographic effect can be selected out based on the intensity of spatial differential vectors (ISDV). Seama et al. (1993) demonstrated the magnetic boundaries of magnetization polarity change, morphological structures, and magnetization contrast using vector geomagnetic anomalies. Magnetic lineations with distinct spreading direction and segment boundaries in the southernmost central Indian Ocean were presented by Sato et al. (2009) base on a systematic vector geomagnetic survey. The structure boundaries were estimated by magnetic boundary strikes, as well as satellite-derived free-air gravity anomalies. The ISDV is a useful way to select the magnetic boundary strikes indicating whether the magnetic polarity changes or if there is another origin such as the COB or segmentation boundary. To reveal the initial break-up process of Gondwana in detail, vector geomagnetic observation to investigate the magnetic lineation and structural boundary around the continental margins is needed.

1.2 Goal of this study

The missing piece for understanding the initial break-up process of Gondwana exists in the Natal Valley and Mozambique Ridge, off South Africa, and the Cosmonauts Sea, off east Antarctica. The COB, COTZ, and the oldest oceanic crust are expected to exist in these areas. The other area linked to the initial break-up process of West Gondwana, between Africa and South America, the Atlantic Ocean, has been well studied during the last half century. In contrast, the Indian Ocean is the result of the fragmentation of many continents. Seafloor spreading of the Indian Ocean comprises the main stage of the break-up process of Gondwana. Because the fragmentation history of Gondwana in the Indian Ocean is still under debate, geophysical observations are especially required in these areas.

In this study, the Natal Valley and the Mozambique Ridge off South Africa, which is the present eastern margin of West Gondwana, and the Cosmonauts Sea off East Antarctica, which is the present western margin of East Gondwana, were selected as the study areas. I aim to reveal the initial break-up process of Gondwana in detail based on vector geomagnetic anomaly analysis, as well as satellite-derived free-air gravity anomalies. The obtained geomagnetic anomaly data are compared with the results of previous studies, and reveal what the geomagnetic anomalies and structural boundaries indicate.

These study areas have several problems: (1) low-amplitude magnetic anomalies make it difficult to identify the record of magnetic polarity change because of the thick sediment and/or old oceanic crust around the continental margin, (2) unsolved problems, such as the location of the continent–ocean boundary (COB), are still under discussion, and (3) multiple hypotheses for the initial break-up process of Gondwana have been proposed. In this study, the COB is defined: (1) on the oldest magnetic isochron, or (2) on the edge of the oceanic crust based on the magnetic and gravity data where magnetic isochrons could not be observed. I reveal the formation and evolution processes, including the location of the COB off of South Africa and Antarctica, in the Indian Ocean, based on systematic vector geomagnetic surveys conducted in the Natal Valley and Mozambique Ridge, off South Africa, and in the Cosmonauts Sea, off Antarctica (Fig. 1-1).

For Chapter 2, I conducted a dense vector geomagnetic survey in the Natal Valley and Mozambique Ridge, off South Africa. In the Natal Valley and Mozambique Ridge at the east African margin, there are several problems still to be discussed. (1) Does continental or oceanic crust exist beneath the northern Natal Valley? (2) How do the magnetic lineations continue further east in the southern Natal Valley where the western side was well identified in previous studies? (3) What is the crustal nature between the northern Natal Valley and southern Natal Valley? (4) Finally, why was rock of continental origin obtained from the Mozambique Ridge? Detailed evolution and formation processes in this area are still under debate. I used multiple analytical results of vector geomagnetic data as well as satellite-derived free-air gravity anomalies to solve each problem. Thus, I have clarified the processes of continental extension and seafloor spreading in the Natal Valley and Mozambique Ridge during about 180–120 Ma.

For Chapter 3, systematic vector geomagnetic data were acquired from the Cosmonauts Sea in the west Enderby Basin, off East Antarctica. For the Cosmonauts Sea, as the East Antarctica margin, four theories have been proposed regarding the initial break-up process of Gondwana: (1) N–S-oriented seafloor spreading started about M11, (2) N–S-oriented seafloor spreading started about M9, (3) seafloor spreading perpendicular to the coastline occurred during the Cretaceous Normal Superchron, and (4) there was a wide-spreading continent–ocean transition zone. The seafloor spreading history in this area has not yet been revealed because of limited geomagnetic data. Therefore, I have carried out an analysis of systematic geomagnetic data as well as satellite-derived free-air gravity data to reveal the seafloor spreading history in this area. I present the process of continental extension and seafloor spreading in the Cosmonauts Sea from break-up to 120 Ma.

Finally, in Chapter 4, I discuss the direction and spreading rate of seafloor spreading of each study area with conjugate areas during the initial break-up of Gondwana. Based on comparison of my findings for the Natal Valley, Mozambique Ridge, and Cosmonaut Sea with those of previous studies on the western margin of Australia, south of Sri Lanka, the Bay of Bengal, the corresponding margin of eastern South America, and the west margin of Africa, I propose a new model of the initial break-up process of Gondwana, especially around 130–120 Ma.

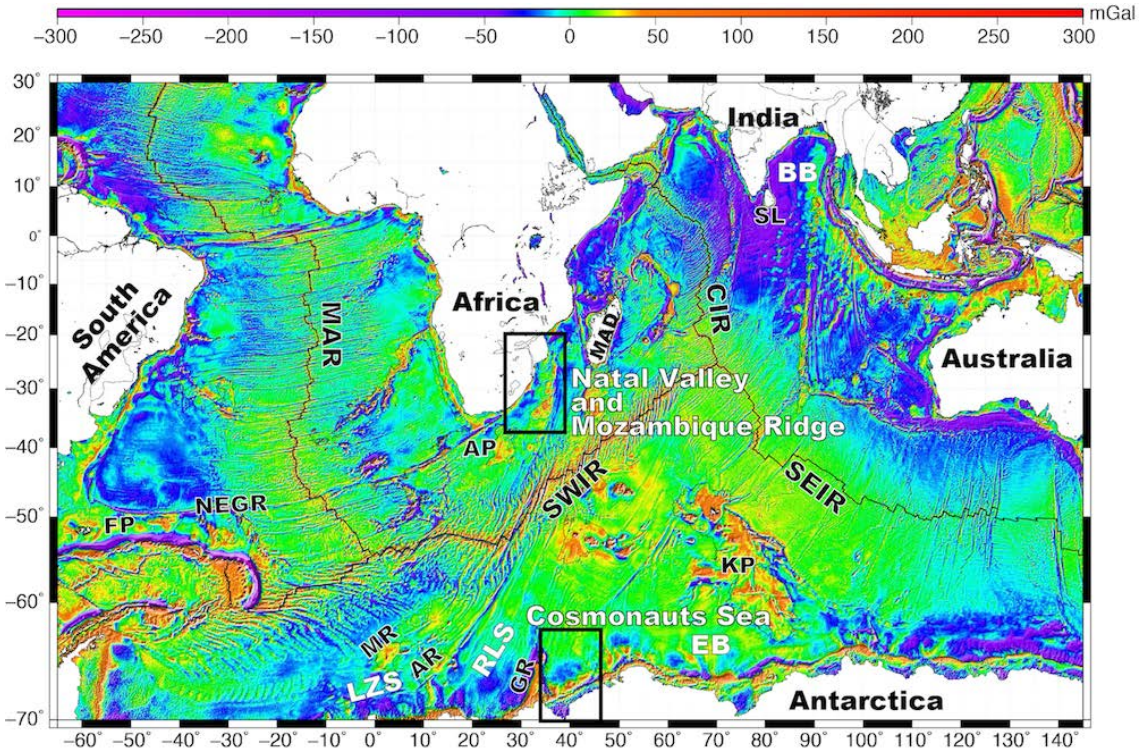

Fig. 1-1

Overview of the study area and conjugate area superimposed on the free air gravity anomaly map (Sandwell, 2014). MAD, Madagascar; SL, Sri Lanka; MAR, Mid-Atlantic Ridge; SWIR, Southwest Indian Ridge; SEIR, Southeast Indian Ridge; CIR, Central Indian Ridge; FP, Falkland Plateau; NEGR, North East Georgia Rise; AP, Agulhas Plateau; MR, Maud Rise; AR, Astrid Ridge; GR, Gunnerus Ridge; KP, Kerguelen Plateau; LZS, Lazarev Sea; RLS, Riiser-Larsen Sea; EB, Enderby Basin; BB, Bay of Bengal.

Chapter 2. Crustal formation and evolution processes of the Natal Valley and Mozambique Ridge, off South Africa

2.1 Introduction

2.1.1 Geological setting

The break-up of Gondwana was one of the most significant geological events to have affected the southern hemisphere in the past 200 Ma. A number of recent reconstruction models of Gondwana have been reported based on geophysical data (e.g., Cox, 1992; König and Jokat, 2010; Lawver et al., 1998; Eagles and König, 2008; Leinweber and Jokat, 2012; Reeves and Wit, 2000; Reeves et al., 2016). Geophysical research around the continental margins that formed Gondwana is key to understanding the fragmentation processes during the initial stage of the break-up. The Natal Valley and Mozambique Ridge off South Africa (Figs. 2-1a and 2-1b) are considered to have formed as a result of separation between South America–Africa–Madagascar and the Antarctic continents during the initial break-up (e.g., Tikku et al., 2002). The Natal Valley is separated into two areas along the Ariel Graben (AG; Fig. 2-1b): the southern Natal Valley (SNV), and the northern Natal Valley (NNV). Magnetic isochrons M0–M10 (124.6–133.5 Ma) associated with seafloor spreading in the SNV were interpreted (e.g., Goodlad et al., 1982). The Mozambique Ridge (MOZR), located to the east of the Natal Valley, is an aseismic ridge. Precambrian rocks were obtained by dredging from the MOZR (e.g., Mougenot et al., 1991). The Explora Escarpment (Hinz et al., 2004) in the Lazarev Sea off Antarctica and the Falkland Plateau off South America (Fig. 2-1a) are considered a conjugate pair with the Natal Valley and Mozambique Ridge (e.g., König and Jokat, 2010). The details of the geological setting are described in the following sections.

Vector geomagnetic anomalies are a useful tool for detecting the history of seafloor spreading. In this study, I present the first dense vector geomagnetic anomaly data for the Natal Valley and Mozambique Ridge, and use multiple analytical results, alongside satellite gravity data, to evaluate the nature of the crust and processes related to the initial break-up of Gondwana.

2.1.2 Southern Natal Valley (SNV)

The SNV is located within 30–35°S and 31–33°E off South Africa (Fig. 2-1b). The direction of seafloor spreading in the SNV is constrained by the Agulhas-Falkland fracture zone (AFFZ). A NW–SE-directed Mesozoic-spreading anomaly sequence of M0–M10 was identified by Goodlad et al. (1982) and Martin et al. (1982) in the northwest of the SNV. M11 and M12 anomalies were inferred in the northern part of the SNV following M10 (Goodlad et al., 1982; Martin et al., 1982); however, they do not correlate with their modeled profile. Because the opening of the South Atlantic initiated at M10N (e.g., Rabinowitz and LaBrecque, 1979), Goodlad et al. (1982) and Martin et al. (1982) inferred that seafloor spreading in the SNV likely began at M10N. They suggested that the observed M11 and M12 were formed by intense volcanic activity at the rifted continental margin in relation to the initiation of seafloor spreading in the SNV.

In the southeast of the SNV, the seafloor spreading process is unclear because of poor coverage of geophysical data on fracture zone offsets and other spreading systems (Du Plessis, 1977; Leinweber and Jokat, 2011; Martin et al., 1982; Reznikov et al., 2005). Based on seismic reflection data, Reznikov et al. (2005) suggested a fracture zone in the SNV, and identified M0–M4 sequences in the east of the SNV using the total geomagnetic anomaly profile, which correlates with the M0–M10 sequence proposed by Goodlad et al. (1982). Alternatively, Leinweber and Jokat (2011) noted a NNE–SSW-oriented extinct ridge in the east of the SNV based on marine geomagnetic data, showing that the symmetric geomagnetic anomaly sequences coincide with the center of the moderate gravity high. However, the timing of seafloor spreading has not been determined because of a lack of geomagnetic data. The orientation of the suggested extinct ridge is parallel to the fracture zone and perpendicular to the magnetic lineations identified by Reznikov et al. (2005).

2.1.3 Northern Natal Valley (NNV)

The NNV is located between the Mozambique Coastal Plain (MOZCP) and the Ariel Graben (AG; Fig. 2-1b). The presence of continental crust beneath the NNV was determined from gravimetric analysis and seismic data (Darracott, 1974; Ludwig et al., 1968; Scrutton, 1976). Ludwig et al. (1968) proposed that a seismic velocity of 5.22–

6.88 km/s at a depth of 7.5 km below sea level indicated oceanic crust. Darracott (1974) and Scrutton (1976) proposed, based on an isostatic model, that a thinned continental crust was present underneath the oceanic crust, indicating a continent–ocean transition zone. Tikku et al. (2002) identified an extinct spreading center, along with magnetic isochrons M4 and M10N with W–E orientation, and suggested that opening of the NNV occurred at the same time as that of the SNV, and that a continental fragment may remain between the SNV and NNV.

2.1.4 Mozambique Ridge (MOZR)

The MOZR, located to the east of the Natal Valley, is an aseismic ridge. Dredge samples obtained from the MOZR, including 'kinzigite', which contained metamorphosed components such as high-grade gneiss, correlating with the Precambrian orogeny (DR1; Fig. 2-1b); metamorphic rock, including a garnet-bearing metapelite that correlates with the Natal Belt in South Africa (DBA; Fig. 2-1b); and fragments of Archean basement, which are reported to be similar in composition to the Rhodesian craton (DR3; Fig. 2-1b), have all been interpreted as indicative of continental crust (Ben-Avraham et al., 1995; Mougenot et al., 1991). In contrast, Erlank and Reid (1974) reported that drilled core samples collected at Deep Sea Drilling Project (DSDP) site 249 included fresh volcanic glass. However, Ben-Avraham et al. (1995) reported a seismic velocity of 5.8–6.3 km/s approximately 6 km beneath the MOZR, based on seismic refraction data, and inferred that the MOZR is on continental crust. They interpreted the fresh volcanic glass samples as evidence of recent volcanic activity. Conversely, König and Jokat (2010) and Leinweber and Jokat (2011) interpreted the MOZR as oceanic crust thickened by basaltic intrusion of the Karoo volcanism and the subsequent large igneous province, based on ocean-bottom seismometry and multichannel seismic reflection data from Gohl et al. (2011). They also interpreted the dredged continental rocks as smaller embedded continental fragments and/or ice-rafted debris. However, Gohl et al. (2011)'s seismic data were limited to the S-MOZR.

2.1.5 Continent–Ocean Boundary (COB)

Two models of the COB have been proposed for the Natal Valley and Mozambique Ridge. The first model places the COB at the AG based on geomagnetic, gravity, and seismic studies (e.g., Darracott, 1974; Martin et al., 1982; Scrutton, 1973), and assumes

that the NNV and MOZR are continental or transitional crust. If this is the case, kinematic reconstruction models show a large overlap onto the Explora Escarpment and Dronning Maud Land in Antarctica (e.g., König and Jokat, 2010). This interpretation cannot explain the proposed volume of continental crust beneath the NNV and MOZR. To resolve this overlap problem, it is necessary to understand the crustal nature of the Natal Valley, Mozambique Ridge, and the Explora Escarpment, and detailed geophysical data, such as marine geomagnetic anomalies, are required. The second model places the COB at the Lebombo and Mateke-Sabi monoclines in South Africa (Fig. 2-1b) (e.g., Cox, 1992; Eagles and König 2008; Leinweber and Jokat, 2012). Cox (1992) suggested that the Lebombo and Mateke-Sabi monoclines and the Explora Escarpment represent continental margins, and that they were continuous structures during Karoo and Ferra igneous activity. Eagles and König (2008) removed the entire area east and south of the Lebombo and Mateke-Sabi monoclines from their reconstruction, and interpreted that the MOZR and Astrid Ridge (Fig. 2-1a) formed parts of Karoo-aged volcanic margin conjugate to the Lebombo and Mateke-Sabi monoclines. Because there is no magnetic signature indicating the COB to the south of the Lebombo and Mateke-Sabi monoclines, Leinweber and Jokat (2012) proposed a new Gondwana reconstruction model, which follows the second model of COB based on Cox (1992). However, this model is based only on total geomagnetic anomalies, in which magnetic lineations in the NNV and MOZR may not be distinct, and are inappropriate for the interpretation of structural boundaries. It remains unclear, therefore, whether the Natal Valley and Mozambique Ridge are on oceanic or continental crust, and the origin of continental fragments in the MOZR is still enigmatic. Consequently, the details of crustal formation and evolution in the study area remain poorly understood.

2.2 Data and data processing

2.2.1 Vector geomagnetic survey and analysis

Sea-surface vector geomagnetic data were acquired in the Natal Valley and Mozambique Ridge using a shipboard three-component magnetometer (STCM; Isezaki, 1986) during the AISTEK III expedition of the R/V *Pelagia* (April 9–June 1, 2009). The total length of the survey line was 16,455 km, with line spacing of approximately 18 km in the N–S direction and 36 km in the E–W direction for the NNV, and 36 km in the N–S and NNE–SSW directions for the SNV and MOZR (Fig. 2-1c–f). Total geomagnetic data were also acquired using a ship-towed Overhauser magnetometer during the same cruise.

The STCM consists of the three orthogonal axes of fluxgate sensors (SFG2005; Tierra Tecnica, Ltd.) and a gyro compass. The fluxgate sensor part was set on the top deck. The antenna of the Global Positioning System (GPS) was also set on the top deck to measure the Coordinated Universal Time (UTC) and the ship's location. A ring laser gyro (JIMS-200R; Japan Aviation Electronics Industry, Limited) was used to measure the ship's attitude, such as angles of the heading, roll, and pitch. The controller, ring laser gyro, and a laptop computer were set in the ship's laboratory to collect vector geomagnetic data, UTC, and the ship's location and attitude.

The vector geomagnetic field was used for the calculation according to the method of Isezaki (1986). The vector geomagnetic fields measured using the STCM are obtained as follows,

$$\mathbf{H_{ob}} = \tilde{A}\tilde{R}\tilde{P}\tilde{Y}\mathbf{F}_{rf} + \mathbf{H_p} \qquad (1)$$

where $\mathbf{F}_{rf}$ is the geomagnetic field, $\mathbf{H_{ob}}$ is the observed magnetic field, and $\mathbf{H_p}$ is the ship's permanent magnetic field. $\tilde{A}$ is a 3×3 constant matrix that depends on the distribution of the magnetic susceptibility of the ship, the location of the STCM sensors, and the shape of the ship. $\tilde{R}$, $\tilde{P}$, and $\tilde{Y}$ are matrices of rotation based on the roll, pitch, and heading of the ship. In this study, $\tilde{A}^{-1} = \tilde{B}$ was applied for equation (1) as follows:

$$\tilde{B}\mathbf{H_{ob}} + \mathbf{H_{pb}} = \tilde{R}\tilde{P}\tilde{Y}\mathbf{F}_{rf}. \qquad (2)$$

To determine $\tilde{B}$ and $\mathbf{H_{pb}}$, 360-degree rotation data of the ship were measured at a place where $\mathbf{F}_{rf}$ was estimated using the International Geomagnetic Reference Field (IGRF). The data obtained during the 360-degree clockwise rotation were biased because the roll came close to one side. To correct for this bias, 360-degree counterclockwise rotation data were also acquired at the same point. Because the ship track resembles a figure eight, this measurement is known as a 'figure eight turn'. The 'figure eight turn' was conducted at six different locations during the AISTEK-III expedition (Table 2-1), and $\tilde{B}$ and $\mathbf{H_{pb}}$ were estimated using the least-squares method (Table 2-2). The vector geomagnetic anomalies were obtained from the acquired vector geomagnetic field by subtracting the 10th International Geomagnetic Reference Field (IGRF2005; Macmillan and Maus, 2005). Crossover error correction was also performed by removing the linear trend for each component of the calculated vector geomagnetic anomalies for level adjustment.

2.2.2 Analysis of magnetic boundary strikes

The intensities of the spatial differential vectors (ISDV) were calculated from the observed vector geomagnetic anomalies based on Seama et al. (1993).

A horizontally infinite plate at depth h_1 with thickness $h_2 - h_1$ is assumed on a three-dimensional Cartesian coordinate system, with origin 0 and axis lines x, y, and z. The magnetization of the plate has constant values of J and $-J$ with a boundary parallel to the axis line x at y = 0, as follows:

$$\mathbf{J} = \begin{cases} J(\widehat{J_x},\ \widehat{J_y},\ \widehat{J_z}) & y < 0 \\ -J(\widehat{J_x},\ \widehat{J_y},\ \widehat{J_z}) & y > 0 \end{cases}.$$

The magnetic field $\mathbf{F} = (Fx,\ Fy,\ Fz)$, which is produced by these magnetic structures, is given by the following equations:

$$F_x = 0 \qquad (3)$$
$$F_y = J\times\left(-\widehat{J_y}\times A + \widehat{J_z}\times B\right)$$

$$F_z = J\times\left(\widehat{J_z}\times A + \widehat{J_y}\times B\right)$$

where,

$$A = -4\times\left[\tan^{-1}\left(\frac{y}{h_1}\right) - \tan^{-1}\left(\frac{y}{h_2}\right)\right]$$

$$B = -2\times\log\frac{y^2+h_2^2}{y^2+h_1^2}.$$

The ISDV is calculated as follows:

$$\left|\frac{\partial \mathbf{F}}{\partial y}\right| = \sqrt{\left(\frac{\partial F_x}{\partial y}\right)^2 + \left(\frac{\partial F_y}{\partial y}\right)^2 + \left(\frac{\partial F_z}{\partial y}\right)^2}$$

$$= 4\times J\times\sqrt{\widehat{J_y^2} + \widehat{J_z^2}}\times\frac{h_2 - h_1}{\sqrt{(y^2+h_1^2)(y^2+h_2^2)}}. \qquad (4)$$

The ISDV reaches a peak when y = 0, at the position of the magnetic boundary. This equation shows that the peak value of the ISDV depends on the depth of the magnetization body and the magnetization contrast.

The ISDV was calculated from the acquired vector geomagnetic anomaly $\mathbf{F} = (F_n,\ F_e,\ F_d)$ as follows:

$$\text{ISDV} = \left|\frac{\partial \mathbf{F}}{\partial p}\right| = \sqrt{\left(\frac{\partial F_n}{\partial p}\right)^2 + \left(\frac{\partial F_e}{\partial p}\right)^2 + \left(\frac{\partial F_d}{\partial p}\right)^2}$$

where p is the distance in the ship's direction. The ISDV is a local maximum value at the magnetic boundary. Note that if there is an angle q between the ship's direction and the magnetic boundary, the ISDV is decreased as follows:

$$\left|\frac{\partial \mathbf{F}}{\partial p}\right| = \left|\frac{\partial \mathbf{F}}{\partial y}\right| \times \sin q.$$

The magnetic boundary, which is parallel to the ship's direction, could not be detected using the ISDV.

Equation (3) means that the component of the magnetic field parallel to the boundary is zero. If the boundary vector is defined as **X,** then the inner product of the orthogonal vectors **X** and **F** is:

$$\mathbf{F} \cdot \mathbf{X} = 0. \qquad (5)$$

The actual geomagnetic anomaly field data contain biases because of measurement errors and/or errors in the reference field. Assuming that the bias $\mathbf{F_b}$ is constant near the magnetic boundary, equation (5) can be rewritten as:

$$(\mathbf{F} - \mathbf{F_b}) \cdot \mathbf{X} = 0.$$

Here, using the constant $C = -\mathbf{F_b} \cdot \mathbf{X}$:

$$F_n \times \widehat{X_n} + F_e \times \widehat{X_e} + F_d \times \widehat{X_d} = 0. \qquad (6)$$

The boundary vector **X** is calculated using equation (6) and applying more than four data points for magnetic anomaly **F**, using the least-squares method. Note that all biases appear only in C and have no effect on $\widehat{X_n}$, $\widehat{X_e}$, and $\widehat{X_d}$, even if the geomagnetic anomaly field has biases. Therefore, the boundary vector **X** is correctly determined using only the relative change of the geomagnetic field vectors.

There are several ways to distinguish whether the magnetic structure is three-dimensional or two-dimensional using vector geomagnetic data. The first way is using the standard deviation of the calculated strike. The boundary vector is constant over a two-dimensional magnetic structure, but not over a three-dimensional magnetic structure. Therefore, the magnetic field caused by a three-dimensional structure should have a large standard deviation. The second way is using the inclination of the boundary vector (Isezaki, 1986). Three-dimensional magnetic structures can be identified based on the phase shift between the horizontal and the downward components of vector geomagnetic anomalies. The boundary vector in the normal mid-ocean (distant from the

trenches) should be nearly horizontal, and the boundary inclination should be approximately zero. The boundary vector is calculated in three dimensions using equation (6); therefore, the boundary inclination is also obtained. If the boundary inclination is large, the magnetic structure is three-dimensional.

The positions and directions of magnetic boundary strikes given by the calculated vector geomagnetic anomalies were estimated based on a threshold ISDV level of 20 nT/km (Fig. 2-2a). In this figure, the black bar and the white bar indicate the 'magnetic boundary strike'. The cross point of the black and white bars indicates the position of the magnetic boundary. The black bar is along the magnetic boundary, indicating the direction of the magnetic boundary. The length of the black bar is proportional to the cosine of the boundary inclination. The length of the white bar is proportional to the standard deviation of the strike.

In this study, ISDV in the NNV, SNV, and MOZR were classed into three types (Table 2-3) based on the results of simple 2D magnetic structure models (Fig. 2-3), where two horizontally infinite plates, at depth h_{11} with thickness $h_{12} - h_{11}$ and at depth h_{21} with thickness $h_{22} - h_{21}$, were considered, and the magnetization values of the plates are constant values J_1 and J_2, with a boundary parallel to the axis line x at y = 0, as follows:

$$\mathbf{J} = \begin{cases} J_1(\widehat{J_x},\ \widehat{J_y},\ \widehat{J_z}) & y < 0 \\ J_2(\widehat{J_x},\ \widehat{J_y},\ \widehat{J_z}) & y > 0. \end{cases}$$

The magnetic field $\mathbf{F} = (Fx,\ Fy,\ Fz)$ produced by these magnetic structures is given by:

$$F_x = 0$$

$$F_y = \begin{cases} J_1 \times (-\widehat{J_y} \times A + \widehat{J_z} \times B) & y < 0 \\ J_2 \times (-\widehat{J_y} \times A + \widehat{J_z} \times B) & y > 0 \end{cases}$$

$$F_z = \begin{cases} J_1 \times (\widehat{J_z} \times A + \widehat{J_y} \times B) & y < 0 \\ J_2 \times (\widehat{J_z} \times A + \widehat{J_y} \times B) & y > 0. \end{cases}$$

To construct the models, equation (4) was rewritten as:

$$\left|\frac{\partial \mathbf{F}}{\partial y}\right| = \begin{cases} 4\times\left(J_1\times\sqrt{\widehat{J_y^2}+\widehat{J_z^2}}\times\dfrac{h_{12}-h_{11}}{\sqrt{(y^2+h_{11}^2)(y^2+h_{12}^2)}}\right) & y<0 \\ 4\times\left(J_2\times\sqrt{\widehat{J_y^2}+\widehat{J_z^2}}\times\dfrac{h_{22}-h_{21}}{\sqrt{(y^2+h_{21}^2)(y^2+h_{22}^2)}}\right) & y>0. \end{cases}$$

Several models were applied to select the threshold levels of the ISDV peaks (Fig. 2-3). The thickness of the magnetization layer ($h_{12} - h_{11}$ and $h_{22} - h_{21}$) was assumed as 1 km, which is appropriate for oceanic crust. Models with inclinations of 90° and 0° were applied to check that the ISDV intensity was not affected by the inclination variability of magnetized bodies (Fig. 2-3a). The mean top depths of the magnetization layers (h_{11}) in the NNV, SNV, and MOZR were estimated as 4, 6, and 3.5 km, respectively, based on ETOPO1 topographic data (Amante and Eakins, 2009) and sediment thicknesses from the global sediment thickness model (Laske and Masters, 1997). In general, the magnetization intensity of oceanic crust is > ± 5 A/m(e.g., McKenzie and Sclater, 1971); therefore, I assumed ± 5 A/m ($h_{11} = h_{12}$, $J_1 = 5$ A/m and $J_2 = -5$ A/m) of magnetized bodies for the magnetic polarity boundary model (Figs. 2-3b1, c1, and d1). Taking into account any effects of magnetization intensity (e.g., decreasing geomagnetic anomaly amplitude from Jurassic to Cretaceous; Cande et al., 1978), magnetizations exceeding ± 3 A/m ($h_{11} = h_{12}$, $J_1 = 3$ A/m and $J_2 = -3$ A/m) were considered for magnetic polarity boundary modeling in the study area (Figs. 2-3b2, c2, and d2). I assumed that lower magnetizations ($h_{11} = h_{12}$, $J_1 = 5$ A/m and $J_2 = 0$ A/m) were not indicative of seafloor spreading (Figs. 2-3b3, c3, and d3). Topographic effects with same polarity magnetized bodies were assumed for topographic contrast boundary modeling ($h_{11} - h_{21} = 0.5$ km, $J_1 = J_2 = 5$ A/m) (Figs. 2-3b4, c4, and d4). Thresholds of the ISDV peaks were determined using the mean top depth in each region (Figs. 2-3b–d). Finally, magnetic structure features from the ISDV were categorized into three types (Table 2-3): 1) high magnetization contrast boundary (e.g., magnetic polarity boundary); 2) low magnetization contrast boundary; and 3) topographic effects (i.e., consideration of the topographic gap of the magnetized block, assuming the same polarity and layer thickness). Magnetic boundary strikes of types 1) and 2) of were selected for further examination (Fig. 2-2b).

2.2.3 Estimation of intensity of crustal magnetization and two-dimensional magnetic

structure model

Total geomagnetic anomalies obtained from the AISTEK II cruise, and the published data of König and Jokat (2010) and the National Geophysical Data Center (NGDC; https://www.ngdc.noaa.gov) were merged with the vector geomagnetic anomalies for the offshore area, and crossover error corrections were applied. Total geomagnetic anomalies from the Earth Magnetic Anomaly Grid (EMAG2; Mause et al, 2009) were used to evaluate the geomagnetic anomaly features of the onshore area. The resolution of the compiled total intensity geomagnetic anomaly map is 2 arc-minutes onshore and 1 arc-minute offshore.

The distribution of crustal magnetization was estimated from the compiled total geomagnetic anomalies using the inversion method of Parker and Huestis (1974). The two-dimensional Fourier transform of the function $f(p)$ is generally defined by:

$$\mathcal{F}[f(\vec{r})] = \int_X dSf(\vec{r})e^{i\vec{k}\cdot\vec{r}} \qquad (7)$$

where,

$\mathbf{r} = (\vec{r}, z) = (\vec{r}, \hat{\mathbf{z}} \cdot \mathbf{r})$
$\vec{k} \cdot \mathbf{r} = \vec{k} \cdot \vec{r}.$

In this equation, $\vec{k}$ is the wave vector of the transform function, and $\mathbf{r}$ is the projection onto the x-y plane at observation position p, written as $\mathbf{r} = (x, \ y, \ z)$ in the three-dimensional Cartesian coordinate system with the unit vector $\hat{\mathbf{z}}$, which is directed vertically upward.

For magnetic model calculation, it is commonly assumed that the restriction in the direction of magnetization is constant, but the intensity may vary, as follows:

$\mathbf{M}(\vec{r}) = \widehat{\mathbf{M}}_0 M(\vec{r}).$

The perturbations in the observed field caused by the magnetized material are always very small. The total field $|\mathbf{B}|$ is observed based on the geomagnetic measurement

taken at sea; thus, the geomagnetic anomaly $\Delta|\mathbf{B}|$ can be approximated by:

$$\Delta|\mathbf{B}| = \widehat{\mathbf{B}}_0 \cdot \Delta\mathbf{B}$$

where $\widehat{\mathbf{B}}_0$ is the unit vector in the direction of the unperturbed field and $\Delta\mathbf{B}$ is the perturbing field. A constant thickness of the magnetized layer h_0 is also assumed, so equation (7) for A displaced from $\Delta|\mathbf{B}|$ can be rewritten and solved as follows:

$$\mathcal{F}[\Delta|\mathbf{B}|] = F[\mathrm{A}] = \tfrac{1}{2}\mu_0 e^{-|k|z_0}\left(1 - \mathrm{e}^{-|k|h_0}\right)\mathrm{V(k)} \cdot \textstyle\sum_{n!}^{\infty} \frac{|k|^2}{n!}\mathcal{F}[\mathrm{M(x)h(x)}^n] \qquad (8)$$

where,

$$\mathcal{F}[\mathrm{A}] = \int_{-\infty}^{\infty} dx\, \mathrm{e}^{-\mathrm{ikx}}\mathrm{A(x)}$$

$$\mathrm{V(k)} = \widehat{\mathbf{B}}_0 \cdot (\hat{\mathbf{z}} + \frac{\mathrm{i}\hat{\mathbf{x}}\mathrm{k}}{|k|})\widehat{\mathbf{M}}_0 \cdot (\hat{\mathbf{z}} + \frac{\mathrm{i}\hat{\mathbf{x}}\mathrm{k}}{|k|}).$$

In this equation, the summation begins at n = 0, and A(x) is the geomagnetic anomaly measured on a level line everywhere above the topography at a height z_0 from the x-y plane. Based on the inversion method and the consideration of an inhomogeneous Fredholm integral equation, equation (8) can be rearranged into the inversion procedure using the $n = 0$ term of the summation on the left side of equation (8):

$$\mathcal{F}[M(k)] = f(k) - \frac{1}{2\pi}\int_{-\infty}^{\infty} dk_0\, \mathcal{F}[M(k_0)]G(k - k_0, k) \qquad (9)$$

with

$$f(k) = \frac{\mathcal{F}[A]e^{|k|z_0}}{\frac{\mu_0}{2}[1 - e^{-|k|h_0}]V(k)}$$

$$G(k, k_1) = \mathcal{F}[e^{|k_1|h(x)} - 1].$$

Equation (9) can be solved according to an iterative process with the assumption of a uniform magnetization layer thickness. There is a linear relationship between the observed geomagnetic anomalies and the magnetic source; thus, the linear operator $\mathcal{L}$ is used:

$$A = \mathcal{L}[M]. \qquad (10)$$

Suppose that magnetization exists, which is not identically zero but satisfies:

$$\mathcal{L}[a] = 0.$$

The $\mathcal{L}$ is called an annihilator. If an annihilator exists, the solution of an inverse problem to equation (10) cannot be unique. The magnetization $a(x)$ that is associated with an anomaly of zero, because of the $1 - \mathrm{e}^{-|k|h_0}$ of equation (8), vanishes at $k = 0$, can be solved using the Dirac delta function:

$$\delta(k) = \sum_{n=0}^{\infty} \frac{|k|^n}{n!} \mathcal{F}[a(x)h^n(x)].$$

If $h(x)$ is assumed as constant, then $a(x)$ is also constant. The annihilator $a(x)$ will be reduced from the solution of the intensity of the magnetization.

In this study, the thickness of the magnetization layer was assumed as 1 km, and its surface geometry was assumed using ETOPO1 topographic data for the onshore area. For the offshore area, the sedimentation layer was considered as a non-magnetized layer using ETOPO1 topography data and sediment thickness from the global sediment thickness model, and the surface geometry of the magnetization layer was assumed as the base of the sediment layer. The direction of crustal magnetization was assumed to be parallel to the present-day geocentric axial dipole field, because it is considered that the African plate has been almost fixed since the break-up of Gondwana (e.g., Schettino and Scotese, 2005). The inclination of magnetization was set as −69°. An annihilator was estimated and added using a clear normal-reversed lineation sequence in the Mozambique Basin (Leinweber and Jokat, 2012).

Two-dimensional magnetic structure models were constructed to fit the observed

profiles of line 34 (Figs. 2-1e and 2-5b). A two-dimensional magnetic structure model of the M-sequence was constructed based on the forward modeling method of Talwani (1964). When the observation position $\mathbf{r} = r\vec{\mathbf{r}}$ is directed from the dipole, the magnetic field $\mathbf{B}$ of a single dipole is given by:

$$\mathbf{B} = \frac{\mu_0}{4\pi}\frac{m}{r^3}[3(\hat{\mathbf{m}} \cdot \hat{\mathbf{r}})\hat{\mathbf{r}} - \hat{\mathbf{m}}] \qquad r \neq 0 \qquad (11)$$

where μ_0 is the magnetic permeability of free space, and $\mathbf{m} = m\hat{\mathbf{m}}$ is the dipole moment. If there are several magnetic bodies, assuming that each body appears at a distance as a dipole, equation (11) can be used to derive the field of each dipole. The dipole moment *m* of each body is given by the product of its magnetization and volume. Finally, the effects of all dipoles are summed. In this study, magnetized body inclinations are set to −69° as the geocentric axial dipole field. The magnetization of the bodies is set to 2.5 A/m for a normal magnetized block and −2.5 A/m for a reversed magnetized block, considering the decreased magnetization intensity of the oceanic crust that formed during the Jurassic Period (e.g., Tivey et al., 2006). Magnetized block boundaries were also defined using observed magnetic boundary strikes from the vector geomagnetic data of observation line 34 (Figs. 2-6). The model profile is calculated with consideration of only the two-dimensional structure.

2.2.4 Estimation of the crustal thickness

Crustal thickness was estimated using satellite gravity anomalies. At first, Bouguer anomalies were calculated from free-air gravity anomalies following the method presented by Parker (1972). The Bouguer anomalies can be calculated by subtracting the effects of the sea-water, sediment, and crust layer from the free-air gravity anomalies:

$$\Delta g_{bouguer} = \Delta g_{free-air} - (\Delta g_{crust} + \Delta g_{sediment} + \Delta g_{sea-water}).$$

To calculate the effect of each layer, the Fourier transform and inverse Fourier transforms can been used. Equation (7) could be applied to the gravitational field. Here, the mass between the upper boundary $\mathrm{z}_1(\mathrm{x},\mathrm{y})$, lower boundary $\mathrm{z}_2(\mathrm{x},\mathrm{y})$ of the gravity

layer, and the density $\rho(\mathrm{x},\mathrm{y})$ between the upper boundary and lower boundary are assumed, so the Fourier transform of the vertical attraction at observation surface $z = z_0$ is described as:

$$\mathcal{F}[\Delta g] = -2\pi G e^{-|\vec{k}|z_0} \sum_{1}^{\infty} \frac{|\vec{k}|^{n-1}}{n!} \mathcal{F}[\rho(z_1^n - z_2^n)] \qquad (12)$$

where G is Newton's gravitational constant. Equation (12) is used to estimate the effect of each layer with the assumption of the density and thickness of each layer.

The density contrast interfaces of seawater, sediments, and the crust were considered in the calculation of Bouguer anomalies for the offshore area. Offshore Bouguer anomalies were deduced from a 1-arc-minute grid of satellite-derived gravity anomalies (Sandwell and Smith, 2009) combined with ETOPO1 topography data and the global sediment thickness model. The two data sets, ETOPO1 bathymetry data and satellite gravity anomaly data, are not independent; therefore, I estimate the difference between the ETOPO1 data and sounding data. ETOPO1 was built from numerous global and regional data sets derived from satellite measurements and ocean soundings (Amante and Eakins, 2009). Multibeam sounding data were obtained during the AISTEK II and AISTEK III cruises (Fig. 2-4a). I also estimate the offset between ETOPO1 and multibeam sounding data (Fig. 2-4b). Large discrepancies are only shown at the edges of rugged features within ± 500 m (Fig. 2-4b, c). Therefore, I concluded that my analysis of crustal thickness using both ETOPO1 bathymetry and satellite-derived gravity anomaly data could be used for understanding large-scale structures.

The results of Bouguer anomaly computation in this study are focused on estimating crustal thickness for large-scale structures. The comparison of the ETOPO1 bathymetry with acoustic bathymetry data shows good consistency; therefore, my rough estimation of crustal thickness is valuable for this study area. Bouguer anomalies for the onshore area were also calculated using a 2.5-arc-minute grid of the Earth Gravitational Model (EGM2008; Pavlis et al., 2012) combined with ETOPO1 topography data. The density of the crust was assumed to be 2,750 kg/m^3. The densities of ocean water and sediment were also assumed to be 1,030 and 2,200 kg/m^3, respectively, for the offshore area. The density contrast between continental crust and oceanic crust was not considered. No

thermal effect was considered. Secondly, crustal thickness distributions were estimated from the Bouguer anomalies based on the method of Kuo and Forsyth (1988), and equation (11) was solved by assuming that the Bouguer anomalies were only attributable to variations in crustal thickness. The Bouguer anomalies continued downward to the hypothetical average Moho depth of 14 km, assuming a mean oceanic crust thickness of 8 km and a mean water depth of 6 km in the study area, and these data were converted to variations in the Moho depth, assuming that the density contrast of the crust and mantle is 550 kg/m^3. A cosine-tapered low-pass filter with a length of 50–100 km was applied to reduce short wavelength variations. Finally, offshore and onshore crustal thickness data were obtained using ETOPO1 topographic data and estimated Moho depth data, and combined along the coastline.

2.3 Results

2.3.1 Geomagnetic anomalies

The corrected northward (Fig. 2-1c) components of the geomagnetic anomalies show mostly inverse correlations with the corrected eastward (Fig. 2-1d) components of the geomagnetic anomalies. The corrected downward component of geomagnetic anomalies (Fig. 2-1e) shows a good inverse correlation with the calculated total geomagnetic anomalies (Figs. 2-1f). The calculated total geomagnetic anomalies (Fig. 2-1f) coincide well with those measured by the ship-towed Overhauser magnetometer during AISTEK III (Fig. 2-1g). The total and each component of the geomagnetic anomalies show a clear boundary with a positive and negative pattern along the Ariel Graben (AG: Fig. 2-1f). This SW–NE-oriented high-amplitude geomagnetic anomaly pattern that accompanies the AG is divided into two regions: the NNV, and the SNV and MOZR.

First, in the NNV, the geomagnetic anomalies were almost within a 600 nT amplitude except in a wedge-shaped region around 28.5°S, 33°E–30°S, 35°E. The geomagnetic anomalies demonstrated a large amplitude of more than 600 nT in this wedge-shaped region. Predominantly SW–NE and SE–NW trends of the geomagnetic anomaly pattern are shown. The geomagnetic anomalies indicate a short wavelength wiggle pattern (< 50 km) that is biased toward positive and a predominantly SW–NE direction.

Secondly, in the SNV and MOZR, variable wavelength geomagnetic anomalies (20–100 km) are observed, and each area can be sub-divided further.

The SNV is divided into two regions by a WSW–ENE boundary at 32.5ºS (SB in Fig. 2-1f): (1) to the north of SB (N-SNV), the geomagnetic anomalies were almost within 300 nT except around 30°S, 32.5°E–31°S, 33°E. The geomagnetic anomalies exhibited a high amplitude of more than 300 nT around 33°S, 32°E–35°S, 33.5°E, and negative long-wavelength (> 50 km) geomagnetic anomalies dominate; (2) to the south of SB (S-SNV), large-amplitude (more than 600 nT) and long-wavelength (approximately 100 km) geomagnetic anomalies with a NW–SE direction dominate, and there are three offsets annotated as m1, m2, and m3 with NE–SW orientation between wiggles (Fig. 2-1f).

The MOZR is divided into two regions around the NW–SE-oriented boundary at 31–32°S (MB in Fig. 2-1f): (1) north of the MB (N-MOZR), a within 600 nT amplitude of

the geomagnetic anomalies was observed. A short wavelength wiggle pattern (< 50 km) that biases toward the positive, similar to those of the NNV, was dominant; (2) south of the MB (S-MOZR), geomagnetic anomalies more than 600 nT in amplitude were demonstrated. Long-wavelength (> 50 km) magnetic anomalies similar to those of the S-SNV were observed. Note that the total and downward component of a geomagnetic anomaly with very high amplitude, more than 900 nT in total (−900 nT in the downward direction), was observed around 30–30.5°S, 36°E.

2.3.2 Magnetic boundary strikes

Magnetic boundary strikes, which indicate high magnetization contrasts (type 1), low magnetization contrasts (type 2), and topographic variation (type 3) (e.g., Seama et al., 1993), were selected using ISDV peak thresholds for each region (Table 2-3 and Fig. 2-2b). The SW–NE-dominated magnetic boundary strikes show the Ariel Graben (Figs. 2-2b and 2-5a).

In the NNV, the spacing of observed magnetic boundary strikes of type (1) and type (2) was approximately 50–100 km, with dominant directions of NE–SW and NW–SE. These strikes were also demonstrated in the results of the geomagnetic anomalies map (Fig. 2-5a). Most of the magnetic boundary strikes indicate two-dimensionality, although the high standard deviations are studded around the high contrast on the magnetic anomaly map. In the SNV, the characteristics of magnetic boundary strikes differ between the south and the north, consistent with the geomagnetic anomaly distribution (Figs. 2-1f and 2-5a). In the N-SNV, no magnetic boundary strikes of type 1 were observed. The observed magnetic boundary strikes of type 2 imply the topographic effect. In the S-SNV, magnetic boundary strikes have short intervals and are dominantly oriented NW–SE. There are offsets between the magnetic boundary strikes on each observation line. The MOZR also has different magnetic boundary strike characteristics in the south and north. In the N-MOZR, the spacing and orientation of magnetic boundary strikes is mostly the same as that in the NNV, with dominant directions of NE–SW, E–W, and NW–SE. A few NNW–SSE- and NNE–SSW-oriented magnetic boundary strikes are also observed in the N-MOZR. In contrast, in the S-MOZR, the magnetic boundary strikes, which indicate magnetic polarity boundaries, have short intervals (approximately 20 km) and primarily NW–SE directions, as also observed in the S-SNV. Two-dimensional magnetic boundary strikes were widely observed in the

S-MOZR.

The E–W-oriented extinct ridge and seafloor spreading anomalies in the NNV proposed by Tikku et al. (2002) are not interpretable in the observed magnetic boundary strikes or geomagnetic anomaly profiles (Figs. 2-1f and 2-5a). In contrast, the obtained magnetic boundary strikes and geomagnetic anomaly profiles are concordant with the magnetic lineations in the SNV proposed by Goodlad et al. (1982). The NNE–SSW-oriented extinct ridge and seafloor spreading anomalies in the S-SNV proposed by Leinweber and Jokat (2011) were also not detected in my results. There are a few boundaries annotated as b1, b2, and b3 with NE–SW orientation, between wiggles (Fig. 2-2b). Two-dimensional magnetic boundary strikes are mainly used for the discussion (Fig. 2-2c).

2.3.3 Intensity of crustal magnetization

The intensity of magnetization was calculated using total geomagnetic anomalies (Fig. 2-5b). In the onshore area, a low magnetization intensity mostly within ± 3 A/m was estimated. High magnetization intensities of up to 12 A/m, such as L1, L2, and L3, were observed around the Karoo volcanic basalt. The magnetization intensity within ± 5 A/m biased toward normal was observed in the north part of the offshore area, whereas a higher contrast (> 10 A/m) of magnetization intensity was observed in the south part of the offshore area. McKenzie and Sclater (1971) reported that the magnetization intensity of normal oceanic crust ranges from ± 5 to ± 10 A/m, and Vine and Matthews (1963) suggested ± 5 A/m for off-axis oceanic crust in the Indian Ocean. Therefore, I estimate that the borders of oceanic crust or other origins in the study area would have magnetizations of at least ± 5 A/m.

In the NNV, magnetization intensity is mostly within ± 5 A/m and biased toward normal magnetization, although there are highly magnetized areas (up to 12 A/m; the same as L1, L2, and L3) at P1 and V (Fig. 2-5b). Note that the reversed magnetization intensity in the NNV is almost more than −3 A/m. The location of the South Tugela Ridge (Goodlad et al., 1982), which is considered as a continental fragment, is surrounded by P1. In the N-SNV, the intensity of magnetization is mostly biased toward reversed magnetization and within ± 5 A/m, except around the AG, whereas in the S-SNV, magnetization intensity is generally more than ± 5 A/m and is concordant with that of normal oceanic crust. The magnetization intensity in the N-MOZR is mostly

within ± 5 A/m and is biased toward normal magnetization, as also observed in the NNV, although a highly magnetized area (up to 12 A/m) was observed at P2 (Fig. 2-5b). In contrast, a high magnetization intensity (more than + 5 A/m and less than −5 A/m) is mainly demonstrated in the S-MOZR.

2.3.4 Two-dimensional magnetic structure models

The model profile calculated using simple normal and reversed magnetized blocks does not fit the observed profile (Fig. 2-6a). Variable thicknesses and/or magnetization intensities are necessary to explain the observed geomagnetic anomaly profile in the NNV (Fig. 2-6b). Assuming a uniformly magnetized body with a magnetization intensity of 2.5 A/m and surrounding non-magnetized bodies, the calculated magnetic profile coincides well with the observed geomagnetic profile. The proportional length of non-magnetized bodies (117 km) along line 34 (363 km) is approximately 32%. The block with high-amplitude geomagnetic anomalies of 300–550 nT (NA and NB in Fig. 2-6b) has an estimated crustal thickness of 4–8 km. The large amplitude of the gravity anomaly is observed at NA and NB, indicating thicker or denser crust.

2.3.5 Crustal thickness

Crustal thickness is calculated using gravity data (Fig. 2-5c). Crustal thickness in the NNV is calculated as 11–14 km, which is more than 4 km thicker than that of normal oceanic crust (7.08 ± 0.78 km; White et al., 1992), and is almost equal to that of the Mozambique Coastal Plain (MOZCP) in this study located on the continental area of South Africa. This value is smaller than that of the previously reported crustal thickness of ~20–30 km obtained via seismic survey in the MOZCP (e.g., Domingues et al., 2016), which implies that my calculation assuming density of basaltic rock is underestimated. In contrast to the NNV, estimated crustal thickness in the S-SNV is approximately 8 ± 0.5 km, almost the same as the crustal thickness of the Mozambique Basin, which is regarded as normal oceanic crust. Between the NNV and SNV, the crustal thickness is 9–11 km, greater than that of normal oceanic crust. In the MOZR, estimated crustal thickness is mostly over 11 km, and thicker than that of normal oceanic crust, although it is slightly thinner (10–11 km) to the north of the 31°S MB boundary (Fig. 2-5c).

2.4 Discussion

Here, I divide the study area into five general regions, the NNV, N-SNV, S-SNV, N-MOZR, and S-MOZR (Fig. 2-7a), based on geomagnetic anomalies, boundary strikes, and gravity anomalies (Fig. 2-5d), to evaluate the nature of the crust. The NNV is bounded by the AG, and the SNV and MOZR are divided into two by the SB and MB, respectively.

2.4.1 Northern Natal Valley

The crust beneath the NNV is most likely stretched continental crust with basaltic intrusions. The observed geomagnetic anomaly profiles and magnetic boundary strikes are not explained by the E–W extinct ridge and seafloor spreading anomalies proposed by Tikku et al. (2002). The trend of the geomagnetic anomalies is NE–SW; however, the trends of the magnetic boundary strikes do not correspond with this direction. The magnetic boundary strikes proposed in my study show a lack of continuity (Fig. 2-7b). Moreover, the profile calculated from the two-dimensional magnetic structure model considering simple normal and reversed magnetized blocks does not fit the observed geomagnetic anomaly profile (Fig. 2-6a). Therefore, I infer that the observed geomagnetic anomaly profiles along the N–S observation lines do not show products of seafloor spreading. The ISDV peaks from geomagnetic data along the E–W observation lines are very low intensity, which indicates a topographic effect and/or low magnetization contrast (Fig. 2-2b). Thus, I conclude that the observed geomagnetic anomaly profiles in the NNV do not support a seafloor spreading origin.

I propose instead that the NNV was affected by basaltic intrusion. The observed geomagnetic anomalies in the NNV are explained well by the profile of the two-dimensional magnetic structure model using a combination of 2.5 A/m magnetized blocks with thicknesses of 1–8 km (Fig. 2-6b) and non-magnetized bodies. Highly magnetized areas correspond to strong gravity anomalies (NA and NB in Fig. 2-6c), indicating structural variation. Highly magnetized areas with magnetization intensity over ± 5 A/m are sparse, and poorly magnetized areas of less than ± 5 A/m dominate (Fig. 2-7b). The NE–SW and NW–SE trending magnetic boundary strikes correspond to structure boundaries shown by the magnetization data (Fig. 2-7d). Magnetization intensity of up to 12 A/m is observed in area V, which is enclosed by magnetic

boundary strikes. This intensity is similar to that observed in the area of the Karoo volcanic basalt in South Africa (for example; L1, L2, and L3 in Fig. 2-7b). I conclude that highly magnetized areas over ± 5 A/m represent basaltic intrusions, based on the magnetization distribution and magnetic boundary strikes. The presence of many areas of normal magnetization and a few areas of reversed magnetization likely indicate that the NNV was exposed to long-term volcanic activity, comprising both normal and reversed polarity periods.

I consider that the crust of the NNV is composed of a mixture of oceanic and continental crust. Relative to the interpretation of Tikku et al. (2002), Leinweber and Jokat (2011) suggested that the NNV is oceanic crust that formed during the Jurassic Quiet Zone (JQZ) because the observed profile showed very low geomagnetic anomaly amplitudes. The JQZ is characterized by high frequency of polarity changes (e.g., Sager et al., 1998; Tivey et al., 2006), which suggests small variations in the intensity of magnetization. Conversely, large variations of magnetization intensity in the NNV are required for the observed profile of the 2D magnetic structure model (Fig. 2-6b); therefore, the NNV cannot be oceanic crust formed during the JQZ. The other possible process for forming poorly magnetized thickened oceanic crust in the NNV (< ± 5 A/m) is hydrothermal alteration. However, high-temperature hydrothermal alteration should be local with a spatial scale of hundreds of meters; therefore, the widespread poorly magnetized area of the NNV likely was not formed by high-temperature hydrothermal alteration. However, the decrease in magnetization caused by the alteration of crustal magnetic minerals, likely due to reaction with seawater, is limited within the first 10–15 Ma (e.g., Dyment et al., 2015). It is difficult to conclude that the widespread magnetization decrease in the NNV is caused by the alteration of crustal magnetic minerals.

The other possibility for the origin of the poorly magnetized area is continental crust. The low intensity of magnetization in the NNV is comparable to that of continental crust in South Africa (< ± 5 A/m) with basaltic intrusions such as L1, L2, and L3, interpreted as Karoo volcanic basalt (Fig. 2-7b). Thus, I conclude that the area of low intensity of magnetization indicates continental crust. The presence of the continental crust mentioned above was affected by extensional stress, then basaltic magma, which carried strong magnetization after cooling and intruded along the extensional faults. The two-dimensional model calculation (Fig. 2-6b) is mostly consistent with the intensity of

magnetization derived from inversion analysis. A crustal thickness in the NNV of 11–15 km, estimated from gravity anomalies (Fig. 2-7c), is intermediate between that of normal oceanic crust (6–8 km) and typical continental crust (30–40 km), and I interpret it as representative of stretched continental crust. The stretching of continental crust occurred at the conjugate margins of the Falkland Plateau and Explora Escarpment during the initial break-up of Gondwana, likely after 183 Ma (e.g., Hinz and Krause, 1982; Jokat et al., 2004). I interpret that the continental crust beneath the NNV was stretched together with these conjugate areas. The NE–SW- and NW–SE-trending magnetic boundary strikes that dominate in the NNV are in accord with a fault direction resulting from N–S extension. Basaltic intrusion likely occurred at zones of weakness in the continental crust such as extensional faults, and strong magnetization contrasts formed between the basaltic and continental crust. Therefore, the magnetic boundary strike should be observed along extensional faults in this case. Orthogonally dominant trends of magnetic boundary strike in the NNV may indicate faults caused by N–S extensional stress between the continents of Africa, South America, and Antarctica after 183 Ma. The free-air gravity anomaly, which indicates topographic elevation, supports NE–SW- and NW–SE-trending structures (red lines in Figs. 2-5d and 2-7b). Additionally, previous seismic surveys by Raillard (1990) demonstrated the presence of faults across the NW–SE and NE–SW survey lines. Consequently, the magnetic boundary strikes in the NNV likely indicate extensional faults, and highly magnetized areas are likely the result of basaltic intrusion along these faults.

2.4.2 Southern Natal Valley

My estimates of crustal thickness and magnetization intensity indicate that the southern part of the SNV (S-SNV) is oceanic crust formed by seafloor spreading between Africa and South America. Therefore, magnetic boundary strikes with magnetization contrast in the SNV indicate magnetic polarity change. I interpreted M0–M10 isochrons on line 19 (Fig. 2-8); the observed geomagnetic anomaly profiles and magnetic boundary strikes on line 19 correlate with the M0–M10 isochrons of Goodlad et al. (1981) based on the synthetic model of Rabinowitz and LaBrecque (1979) (Fig. 2-8b). However, the magnetic boundary strikes indicate low ISDV peaks for M4 and M9 compared with M0, M2, and M10 (Fig. 2-8c). Seismic reflection data from Reznikov et al. (2005) indicate a sediment thickness around M4–M9 approximately

1 km thicker than that of the global sediment thickness model. The depth to the top of the magnetized layer depends on the thickness of the sediment. If the sediment thickens, the top depth of the magnetization layer deepens. If the top depth of the magnetization layer deepens, the peak value of the ISDV decreases (e.g., Fig. 2-3). Therefore, if the sediment thickens, the peak value of the ISDV decreases. I suggest that thick sediment likely influenced the peak values of ISDV for M4 and M9 on line 19.

On line 18, I identified M1–M10 isochrons based on magnetic boundary strikes; however, the M4 isochron was not observed (Fig. 2-8c). Reznikov et al. (2005) suggested that a fracture zone was distributed around the area where M4 was identified in my study; therefore, the geomagnetic anomaly profile and magnetic boundary strike here are probably disturbed. Geomagnetic anomaly profiles on lines 17 to 14 (Fig. 2-8a) are not continuous with the magnetic isochrons identified on lines 19 and 18, and both observation lines in previous work (Goodlad et al., 1982) and magnetic boundary strikes are irregular in direction. However, comparison with the magnetic isochrons on lines 19 and 18 and observation lines in previous work (Goodlad et al., 1982) suggests that the magnetic boundary strikes on lines 17 to 14 may conform to M1–M10 (Fig. 2-8a).

NW–SE-oriented magnetic boundary strikes are dominant in the S-SNV, and this finding may be indicative of geomagnetic anomaly lineations in the area, suggesting NE–SW-oriented seafloor spreading between Africa and South America. My results do not support the presence of a NNE–SSW-oriented extinct ridge in the S-SNV as suggested by Leinweber and Jokat (2011).

I identified three fracture zones in the S-SNV, F1, F2, and F3 (Fig. 2-7), which are offsets between geomagnetic anomaly profiles (m1, m2, and m3 shown in Fig. 2-1f) and magnetic boundary strikes (b1, b2, and b3 shown in Fig. 2-2c) of lines 19 and 18, 18 and 17, and 15 and 14, respectively (Fig. 2-8a). These NE–SW-oriented structural boundaries correspond to the position of offsets shown by the gravity anomalies (g1, g2, and g3 shown in Fig. 2-5d) and the distribution of magnetization (F1, F2, and F3 shown in Fig. 2-7b), and are perpendicular to the magnetic lineations in the S-SNV. Thus, I infer that these offsets are across NE–SW-trending fracture zones. The seafloor spreading rate (1.5 cm/year half rate) for M2–M0 in profile F of Goodlad et al. (1982) differs from that in their profiles A–E and my profile for line 19 (Figs. 2-8a and b). The M2–M0 isochrons in profile F were obtained near fracture zone F1 identified in this study, and were probably disturbed by the fracture zone.

2.4.3. Between the Northern Natal Valley and Southern Natal Valley (P1 and N-SNV)

I interpret that P1, which has an area of ~7,500 km^2 and is located to the west between the continental crust of the NNV and the oceanic crust of the SNV, was formed by intense volcanic activity along the continental rifted margin. The intensity of magnetization in P1 (Fig. 2-7b) is very high (up to 12 A/m), which suggests a large volcanic intrusion between the NNV and SNV. The estimated crustal thickness of P1 based on gravity anomalies is 10–12 km (Fig. 2-7c). This result agrees with the two-dimensional structure model, which requires a ± 2.5 A/m magnetized block with a thickness of 11–14 kilometers at P1. My interpretation supports Goodlad et al. (1982)'s suggestion that the area north of M10 consists of continental crust that underwent intense basaltic intrusion caused by volcanism. This volcanism likely preceded seafloor spreading in the S-SNV.

Conversely, I interpret the N-SNV, located to the east between the NNV and S-SNV, as stretched continental crust. Because of the absence of confirmed magnetic boundary strikes and the low amplitude of geomagnetic anomalies, magnetic lineations are not clearly recognized in the N-SNV (Fig. 2-5a). Although oceanic crust formed during the JQZ has low-amplitude geomagnetic anomalies, the 9–11-km-thick crust of the N-SNV (Fig. 2-7c) is thicker than that of normal oceanic crust, and is more likely to be stretched continental crust. Very low magnetization intensity is observed in the N-SNV (Fig. 2-7b), which indicates that it was not exposed to volcanic activity. Therefore, I conclude that the N-SNV is stretched continental crust without basaltic intrusion. Previous studies have also suggested that continental fragments are located to the south of the AG (e.g., Raillard, 1990). At around 146 Ma, the N-SNV was located at the edge of the spreading axis between Antarctica and South America during the initial break-up of Gondwana (e.g., König and Jokat, 2010). The spreading direction between Antarctica and South America is NW–SE, which implies that extension of the N-SNV is in the NW–SE direction, perpendicular to my observation lines. If the seafloor spreading direction is perpendicular to the observation lines, magnetic boundary strikes caused by the magnetic lineations are not detected. There is no evidence as to whether extension or seafloor spreading formed the N-SNV.

2.4.4. North part of the Mozambique Ridge

I interpret the N-MOZR as stretched continental crust with basaltic intrusion, as in the NNV. Its estimated crustal thickness of 11–13 km is similar to that of the NNV (Fig. 2-7c). The intensity of magnetization is low and biased toward positive (Fig. 2-7b), like that of the NNV. The distribution of magnetic boundary strikes and geomagnetic anomaly profiles in the N-MOZR is also similar to those of the NNV, which implies an origin other than by seafloor spreading. The results of the two-dimensional magnetic structure model of König and Jokat (2010) for the N-MOZR, in which poorly magnetized areas surrounding highly magnetized thick crust were observed, agree well with my two-dimensional magnetic structure model for the NNV. Thus, the N-MOZR was likely formed by the same process as that of the NNV. I conclude that there is mixture of continental and oceanic crust beneath the N-MOZR. The magnetic boundary strikes in the N-MOZR indicate the presence of extensional faults. Moreover, highly magnetized areas are likely the result of basaltic intrusion along these faults.

Magnetic boundary strikes on the south of the Galathea Plateau, located between 30.8ºS to 32ºS, are predominantly oriented E–W (Fig. 2-7b), whereas NE–SW- and NW–SE-oriented extensional faults would be formed by a N–S-oriented extensional stress field, as mentioned in Chapter 4.1. I suggest that the existence of the E–W-oriented magnetic boundary strikes is explained by the rotation of the south of the Galathea Plateau linked to stretching of the continental crust of the N-SNV, between the NNV and N-MOZR, as mentioned in Chapter 4.3 (Figs. 2-9). This deformation would drive the Galathea Plateau counterclockwise, resulting in a change in the direction of magnetic boundary strikes from NW–SE to E–W. In contrast, on the Dana and northern Galathea Plateaus, NW–SE- and NE–SW-oriented magnetic boundary strikes dominated. A few NNW–SSE-, NNE–SSW-, and E–W-oriented magnetic boundary strikes were also observed. I inferred that the Dana and northern Galathea Plateaus were also slightly rotated during the N–S extension, and various oriented faults were formed. The NE–SW- and NW–SE-oriented magnetic boundary strikes indicating extensional faults formed by the N–S extensional stress were preserved. Based on this concept, it is suggested that the AG, which is located between the NNV and N-SNV, was also formed by evolution of the N-SNV and rotation of the Dana and Galathea Plateaus (Figs. 2-9b and 2-9c). The eastern end of the AG reaches, but does not cross, the northern end of the Dana Plateau. This observation supports the idea that the Dana Plateau was also

affected by rotation linked to the N-SNV. I conclude that rotation of the Dana and Galathea Plateaus occurred because of the stretching linked to NW–SE rifting between South America and Antarctica after ~146 Ma (e.g., König and Jokat, 2010), and that the AG formed by evolution of the N-SNV and rotation of the Dana and Galathea Plateaus.

2.4.5. South part of the Mozambique Ridge

The S-MOZR is oceanic crust whose formation was accompanied by continuous intense volcanic activity. The crustal thickness of 11–13 km in the S-MOZR is the same as that of the N-MOZR, and more than 4 km thicker than that of normal oceanic crust (Fig. 2-7c). In contrast to the N-MOZR, normal and reversed magnetization intensity greater than ± 5 A/m is clearly observed in the S-MOZR (Fig. 2-7b), which implies that the S-MOZR formed during seafloor spreading. Therefore, I considered that magnetic boundary strikes with high magnetization contrast in the S-MOZR indicate a magnetic polarity change. The high magnetization contrasts of magnetic boundary strike in the S-MOZR predominantly trend NW–SE, similar to those in the S-SNV, which indicates that the NE–SW seafloor spreading occurred in the S-MOZR (Fig. 2-7b). Magnetic isochrons are not confirmed in this area, which I suggest is because of intense basaltic intrusion and extrusion that distorted the continuous magnetic lineations caused by seafloor formation. The thickened crust (11–13 km) supports this hypothesis (Fig. 2-7c). Generally, the thickness of normal oceanic crust is 7 ± 2 km because of the homogeneity of mantle temperature, temperature–pressure composition, and chemical composition under the mid-ocean ridge (McKenzie and Bickle, 1988). Seismic studies suggest that the lower crust of the S-MOZR was thickened by addition of large volumes of mantle-derived magma, likely associated with the Bouvet hotspot (Gohl et al., 2011). Consequently, my interpretation supports that of König and Jokat (2010), who suggested that the S-MOZR was formed by intense volcanic activity (likely associated with the Bouvet hotspot) during seafloor spreading.

2.4.6. Between the north and south part of Mozambique Ridge (P2)

P2, located in the northern part of the S-MOZR, was formed by intense basaltic intrusion into the rifted margin. The highly magnetized area (up to 12 A/m) is clearly surrounded by magnetic boundary strikes (Fig. 2-7b). The situation of P2 is similar to that of P1, indicating intense volcanic activity along the continental rifted margin. In the

south of P2, continental fragments such as the metamorphic rocks mentioned in Chapter 2.1.4 (Mougenot et al., 1991; Ben-Abraham et al., 1995) have been obtained via dredge sampling (DR1, DR3, and DBA in Fig. 2-1b). I propose that P2 was formed at a continental rifted margin with intense volcanic activity between the N-MOZR and S-MOZR. This process may lead to the preservation of remnant fragments of continental crust, such as Archean basement rock, and the metamorphic rock confirmed in DR1 and DBA in the S-MOZR. Further investigation, such as by seismic refraction or sub-seafloor drilling, is required to determine whether P2 volcanic rocks and inherent crust are oceanic or continental in origin.

2.4.7. Interpretation of the evolution of the study area

In this study, three specific crustal features of continental crust, oceanic crust, and basaltic intrusion were observed, and the COB was determined (Fig. 2-7d). In contrast to previous studies, in which the NNV, N-SNV, and N-MOZR were categorized as nearly all oceanic crust (e.g., Leinweber and Jokat, 2011), I infer that 32–49% of the area is occupied by stretched continental crust, based on the distribution of magnetization intensity and the two-dimensional magnetic structure model. To estimate the area of the original continental crust, I calculated the areas of the stretched continental crust between the Mateke-Sabi monocline and COB using a simple block model (Fig. 2-10). I assumed that this area was stretched with constant width in the E–W direction. Based on gravity anomalies and using a length of 780 km and an estimated crustal thickness of 9–14 km, the areas of stretched continental crust in the NNV, N-SNV, and N-MOZR was calculated as 2,870–4,395 km^2. Using a similar method and assuming that the whole MOZCP is stretched continental crust, I calculated an area of 7,540 km^2 in the MOZCP based on a length of 520 km and an estimated thickness of 14–15 km. Thus, I estimate the total area of stretched continental crust between the Mateke-Sabi monocline and the COB as 10,410–11,935 km^2. The thickness of the South African continental area estimated from gravity anomalies is approximately 22–28 km. Assuming an average thickness of 25 km for the original continental crust, I estimate an original length of 416–477 km. The location of the pre-stretching break-up boundary between Africa and Antarctica has been estimated using overlaps in recent reconstruction models (e.g., König and Jokat, 2010), which indicate that the length of the original continental crust between the Mateke-Sabi monocline and the boundary is

about 450 km, and agree well with my estimation of the length of the original continental crust. Thus, the overlap problem of the Antarctic continent onto the African continent (e.g., Cox, 1992; König and Jokat, 2010) is solved by my estimation of the pre-stretching COB.

I propose that the entirety of the conjugate margins, including the NNV, N-SNV, and N-MOZR, were affected by extensional stress during the initial break-up of Gondwana, about 183–130 Ma. Extensional tectonics with normal faulting occurred before the break-up of Gondwana at 183 Ma (Fig. 2-11a; Cox, 1970). After that, stretching of the continental crust occurred at conjugate margins such as the Falkland Plateau and the Explora Escarpment during the initial break-up of Gondwana at 183–130 Ma (e.g., Hinz and Krause, 1982; Jokat et al., 2004). These considerations support my findings (Fig. 2-11b). The main Karoo volcanic activity occurred at 183 Ma, and subsequent volcanism occurred during the initial break-up stage of Gondwana. The Lebombo and Mateke-Sabi monoclines were intruded by basaltic magma at 183–172 Ma (e.g., Jordan et al., 2008). I interpret that stretching and basaltic intrusion into the NNV, N-SNV, and N-MOZR represent the first stage of the break-up of Gondwana after 183 Ma (Fig. 2-11b). In addition, subsequent volcanism continued at the NNV and conjugate margins during seafloor spreading between the Mozambique Basin and the Riiser-Larsen Sea that began at about 163 Ma (Fig. 2-11c; e.g., König and Jokat, 2010).

In the second stage (Fig. 2-11d), the seafloor spreading between Antarctica and South America was begun about 146 Ma (e.g., König and Jokat, 2010). The N-SNV was stretched without basaltic intrusion, caused by NW–SE-oriented extension between Antarctica and South America. Rotation of the Dana and Galathea Plateaus occurred because of the stretching of the N-SNV. The AG was formed by extension of the N-SNV and rotation of the Dana and Galathea Plateaus (Fig. 2-9).

The third stage of the seafloor spreading between Africa and South America occurred at approximately M10 (Fig. 2-11e). The COB in the study area is thought to have formed at approximately M10. Goodlad et al. (1982) interpreted that the COB is located between M10 and M11 in the S-SNV, as it is approximately M10 in the conjugate Falkland Plateau. I follow their interpretation, and conclude that P1 and P2 (Fig. 2-7d) were exposed by intense basaltic intrusion that likely triggered subsequent seafloor spreading.

In the final stage, I propose that the S-MOZR and S-SNV were formed by seafloor

spreading between Africa and South America from M10 (Figs. 2-11e and f). The NW–SE magnetic boundary strikes that dominate in both the S-MOZR and S-SNV indicate that seafloor spreading of the S-MOZR and S-SNV occurred in the same period and in the same direction. The relationship between the S-MOZR and Bouvet hotspot that was implied by Leinweber and Jokat (2011) can be considered, although there is no clear evidence, such as rock samples of intense volcanism related to a hotspot or large igneous province (LIP) in the S-MOZR. Gohl et al. (2011) interpreted that the Agulhas Plateau, together with the Northeast Georgia Rise and Maud Rise, were formed when the region in the vicinity of the triple junction passed over the Bouvet hotspot. They also implied that the S-MOZR and Agulhas Plateau were formed in same magmatic regime. As demonstrated by the example of the Shatsky Rise (e.g., Sager, 2005), clear magnetic lineations were formed on the thickened oceanic crust through the ridge–hotspot interaction. NW–SE-dominated magnetic boundary strikes on the 11–13 km thick crust of the S-MOZR indicate the interaction between the seafloor-spreading ridge and the Bouvet hotspot. Thus, I conclude that the S-MOZR and the subsequent formation of the Agulhas Plateau–Maud Rise–North East Georgia Rise were formed by volcanic activity that occurred near the Bouvet triple junction and hotspot (Fig. 2-11f). In the S-SNV, the area with unclear magnetic isochrons (on line 17–14 in Fig. 2-8a) is next to the S-MOZR; therefore, this area was likely affected by S-MOZR volcanism.

In summary, the four stages of tectonic evolution are as follows:

1) 183–146 Ma, stretching of continental crust with basaltic intrusion caused by volcanism at the southeast area of the Lebombo and Mateke-Sabi monoclines;

2) 146–130 Ma, stretching and rotation related to seafloor spreading between Antarctica and South America, and formation of the AG; N–S-oriented stretching of continental crust with basaltic intrusion may have continued;

3) about 130 Ma, intense basaltic intrusion into the continental rift margin;

4) < 130 Ma, volcanism and seafloor spreading between Africa and South America.

One of the possible causes of the intense volcanism in the S-MOZR since 130 Ma and the subsequent volcanism of the Agulhas Plateau is the Bouvet hotspot near to the Bouvet triple junction. However, the location of the Bouvet hotspot track before the formation of Agulhas Plateau is still unclear (e.g., Hartnady and Le Roux, 1985; Duncan, 1984). Therefore, more detailed geophysical data and rock sampling are required to determine this relationship. Additionally, the formation and origin of the

N-SNV is still speculative; therefore, additional geophysical data, such as seismic refraction data, are necessary to understand the detailed formation processes of this area.

2.5. Summary of Chapter 2

I obtained sea-surface vector geomagnetic anomalies in the Natal Valley and Mozambique Ridge. The multiple analytical results of the dense vector geomagnetic anomaly and satellite gravity data lead to following conclusions:

1. I propose a new COB model for the Natal Valley and Mozambique Ridge. My COB model agrees with previous kinematic reconstruction models, and solves the overlap problem of the Antarctic continent onto the African continent, revealing the initial break-up process of Gondwana.
2. Faulting of the NNV and N-MOZR occurred because of extensional stress during the initial break-up after 183 Ma. Basaltic magma caused by Karoo volcanism was intruded along these faults. Thus, a mixture of stretched continental crust and basaltic crust formed beneath the NNV and N-MOZR.
3. The Galathea Plateau, which is a part of the N-MOZR, may have rotated because of rifting between Antarctica and South America after about 146 Ma. The N-SNV is stretched continental crust affected by the rifting between South America and Antarctica. The AG formed because of stretching of the N-SNV and rotation of the Galathea Plateau.
4. Intense basaltic magma intruded into the south edge of the NNV and N-MOZR, which indicates that this area was a continental rifted margin prior to seafloor spreading.
5. I identified magnetic isochrons M0–M10 in the S-SNV. The S-SNV formed as a result of seafloor spreading between Africa and South America from approximately M10. Several fracture zones in the S-SNV offset the magnetic isochrones.
6. The S-MOZR has been spreading, together with the S-SNV, since approximately M10. The crust beneath the S-MOZR became thickened because of intense volcanism, possibly associated with the presence of the Bouvet hotspot. A part of the S-SNV was also possibly formed by the hotspot interaction.

The cause of intense volcanism on the S-MOZR is still unclear, although volcanism related to the Bouvet hotspot is one possibility. The formation process of the N-SNV remains unknown, and additional geophysical and geological data are necessary to understand the detailed tectonic evolution of the study area.

Table 2-1

Location of the figure eight turns. *1: The distorted 'figure eight turn' was made without data for the roll on site 2; therefore, the data from this point were excluded from the calculation.

	Data	UTC	Latitude	Longitude
1	2009/4/15	08:49:15 – 10:30:05	–30.00028	36.22177
2[*1]	2009/4/22	13:53:17 – 14:45:11	–34.36578	33.4442
3	2009/5/7	12:17:48 – 13:03:38	–29.88457	31.54347
4	2009/5/22	01:52:42 – 02:49:17	–27.10802	33.74922
5	2009/5/27	19:21:26 – 20:08:55	–27.72087	34.3499
6	2009/5/28	12:06:31 – 12:53:18	–25.49985	34.15217
7	2009/5/31	04:58:07 – 05:52:30	–29.74617	32.02337

Table 2-2

Calculated matrix of $\tilde{B}$ and $\mathbf{H_{pb}}$. Sum of SD = 407.30

B(1,1)	B(1,2)	B(1,3)	H(1,1)	SD
1.06195	–0.07037	0.02388	–5602.4	139.4
B(2,1)	**B(2,2)**	**B(2,3)**	**H(2,1)**	**SD**
–0.0147	1.10979	–0.06223	–5801.3	145.1
B(3,1)	**B(3,2)**	**B(3,3)**	**H(3,1)**	**SD**
–0.11915	–0.10994	0.78634	–5379.5	122.8

Table 2-3

Classification of magnetized structure boundaries based on threshold levels of intensity of spatial differential vector (ISDV) peaks. Identified signatures for the MOZR, NNV, and SNV are sorted based on the simple two-dimensional magnetic structure models. The mean top depth of the magnetization layer is derived using topographic data from ETOPO1 (Amante and Eakins, 2009) and sediment thicknesses from the global sediment thickness model (Laske and Masters, 1997).

Region	High magnetization contrast boundary (type 1)	Low magnetization contrast boundary (type 2)	Topographic effect (Offset less than 0.5 km) (type 3)	Mean top depth of magnetization layer
MOZR	ISDV > 60 nT/km	60 nT/km > IDSV > 40 nT/km	ISDV < 40 nT/km	3.5 km
NNV	ISDV > 50 nT/km	50 nT/km > ISDV > 30 nT/km	ISDV < 30 nT/km	4 km
SNV	ISDV > 30 nT/km	30 nT/km > ISDV > 20 nT/km	ISDV < 20 nT/km	6 km

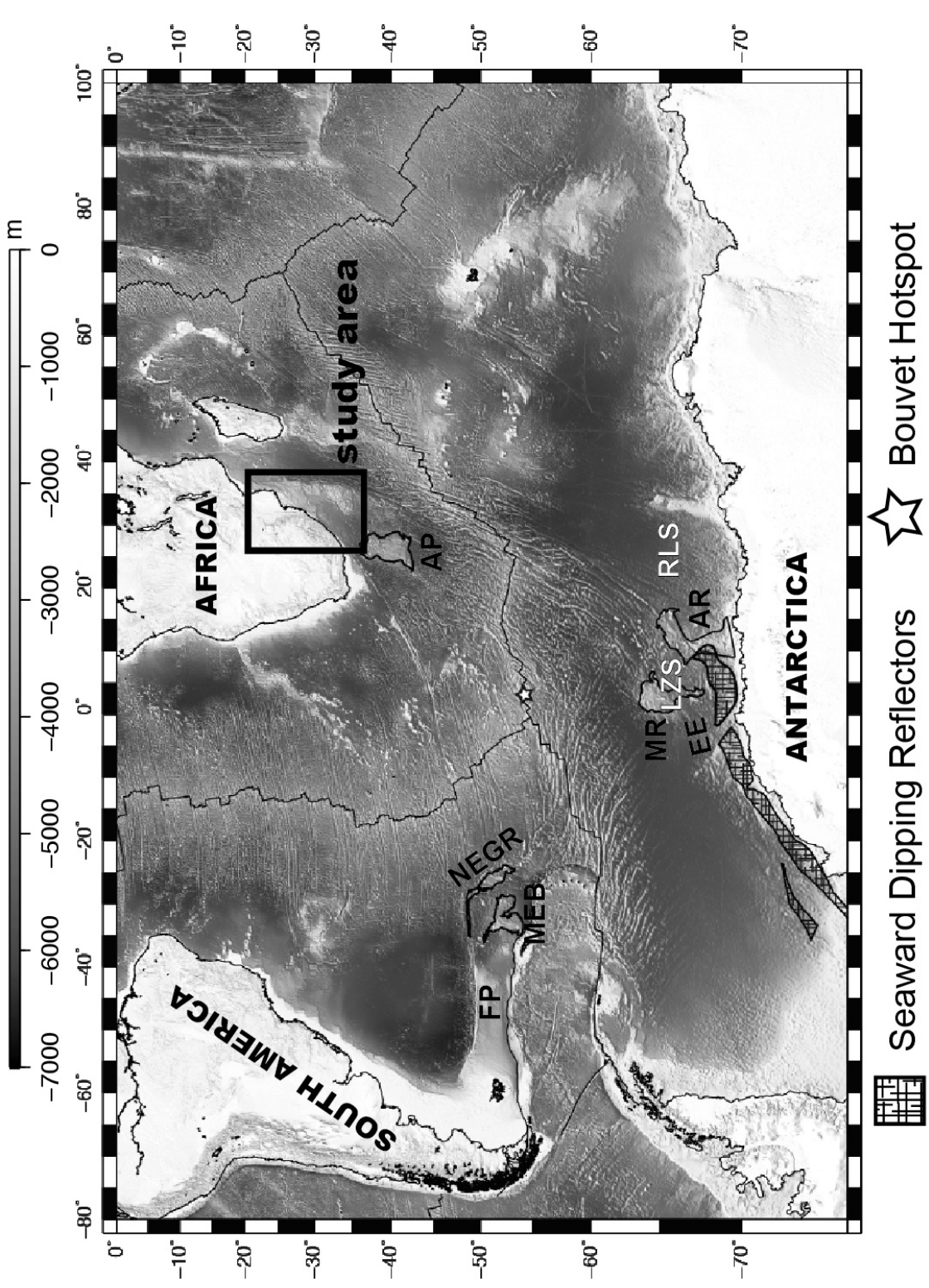
m
0
−1000
−2000
−3000
−4000
−5000
−6000
−7000
study area
AFRICA
SOUTH AMERICA
ANTARCTICA
AP
NEGR
MEB
FP
MR
LZS
EE
AR
RLS
Seaward Dipping Reflectors
Bouvet Hotspot

Fig. 2-1a

(continued)

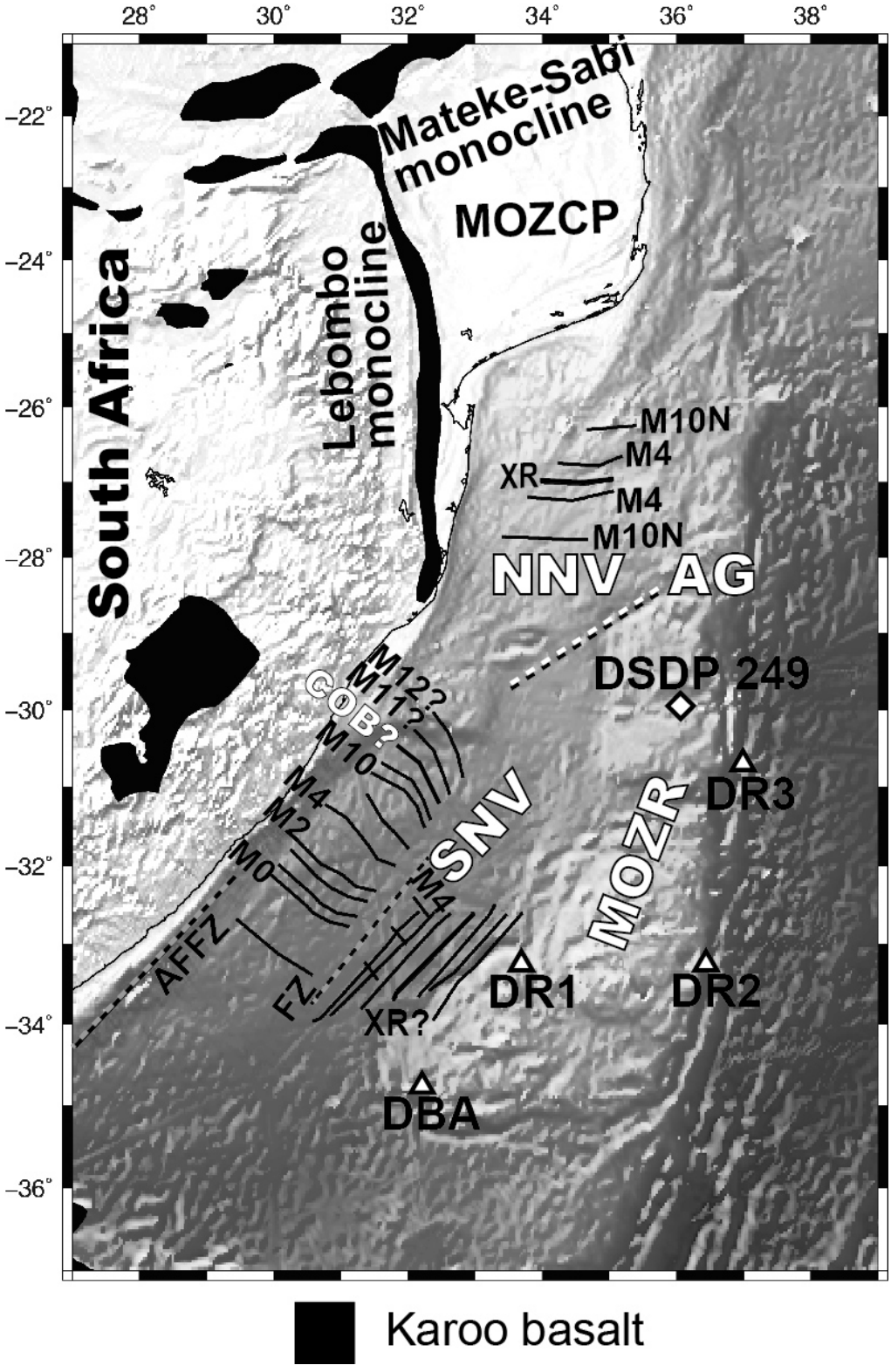

Fig. 2-1b

(continued)

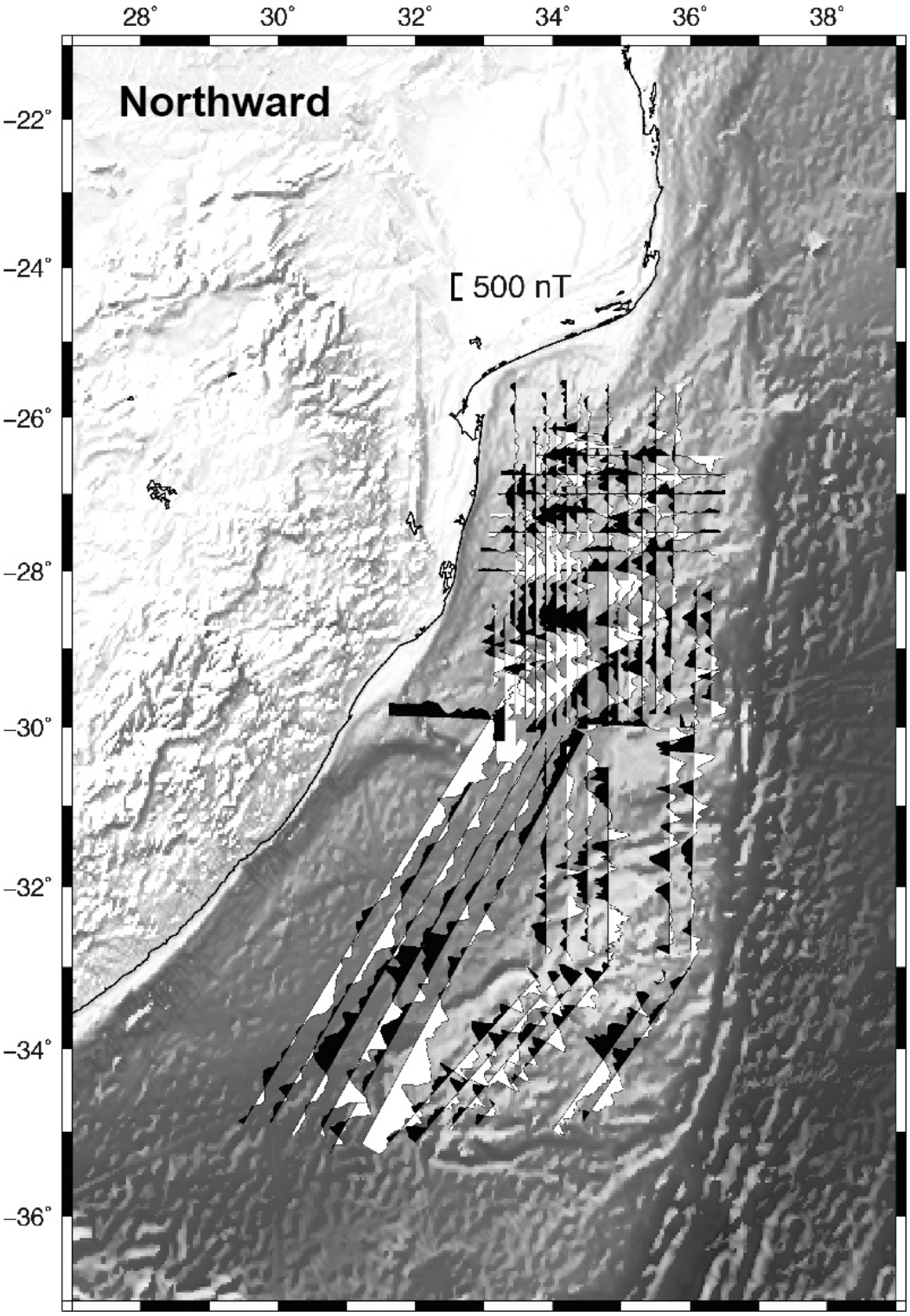

Fig. 2-1c

(continued)

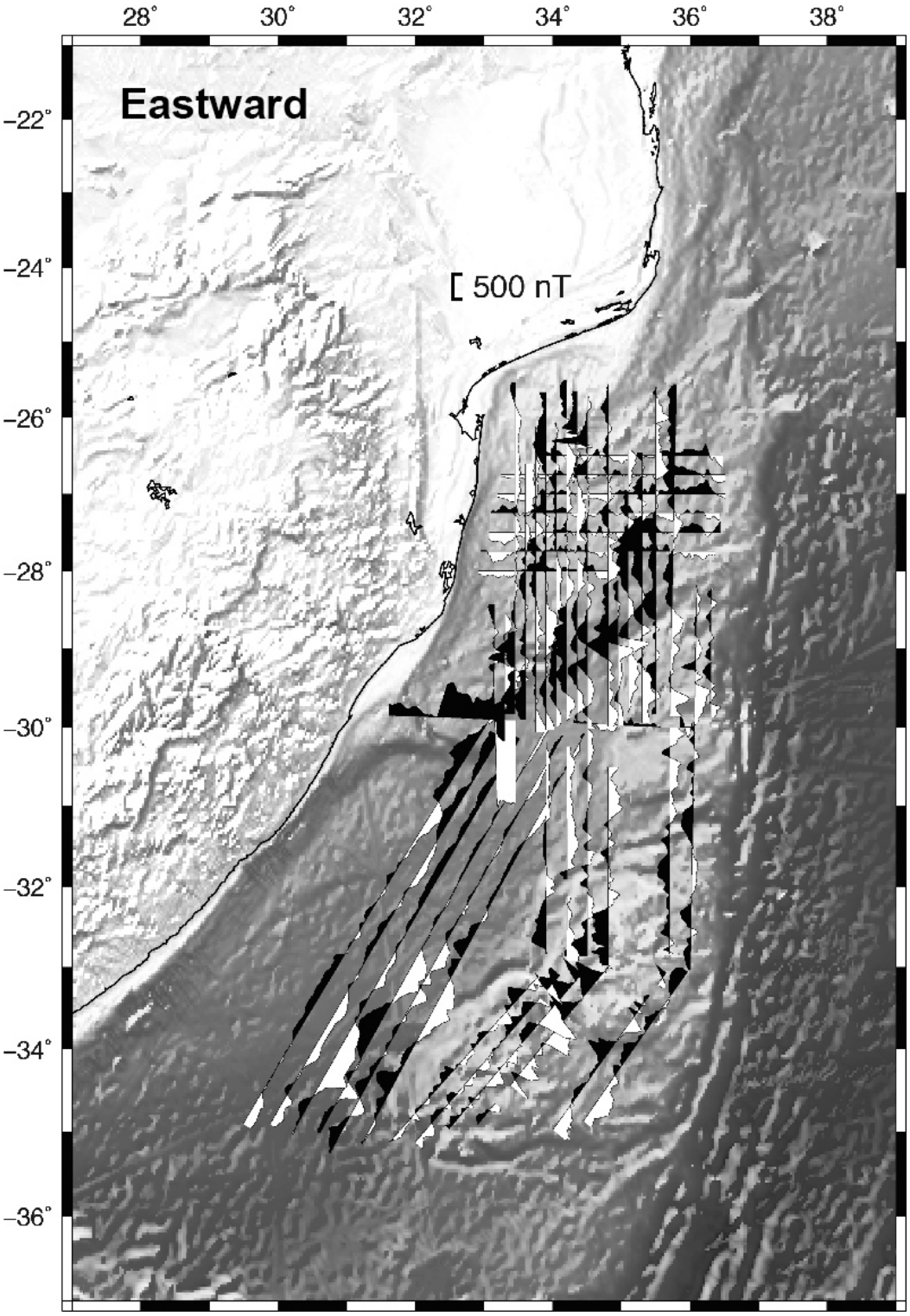

Fig. 2-1d

(continued)

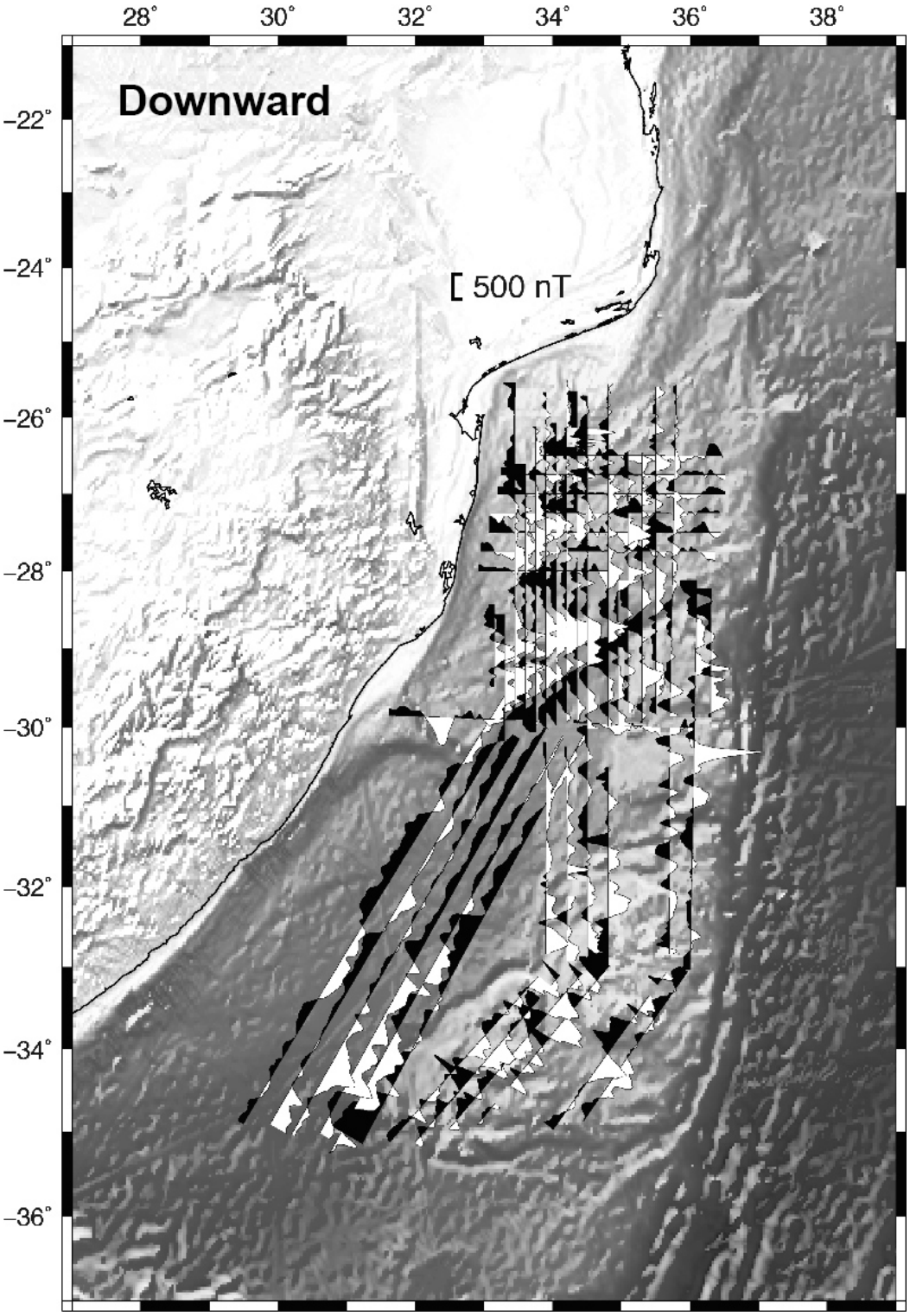

Fig. 2-1e

(continued)

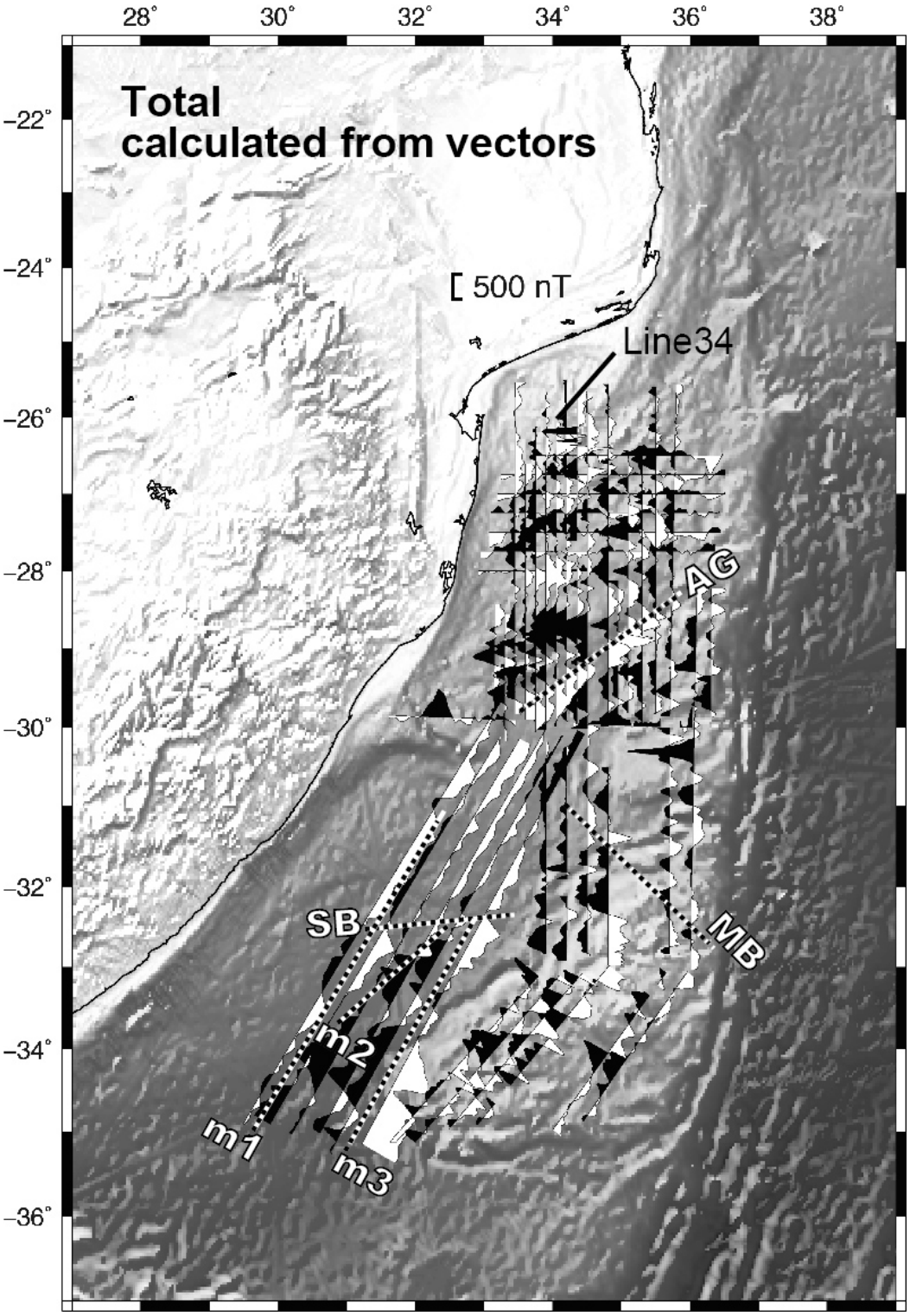

Fig. 2-1f

(continued)

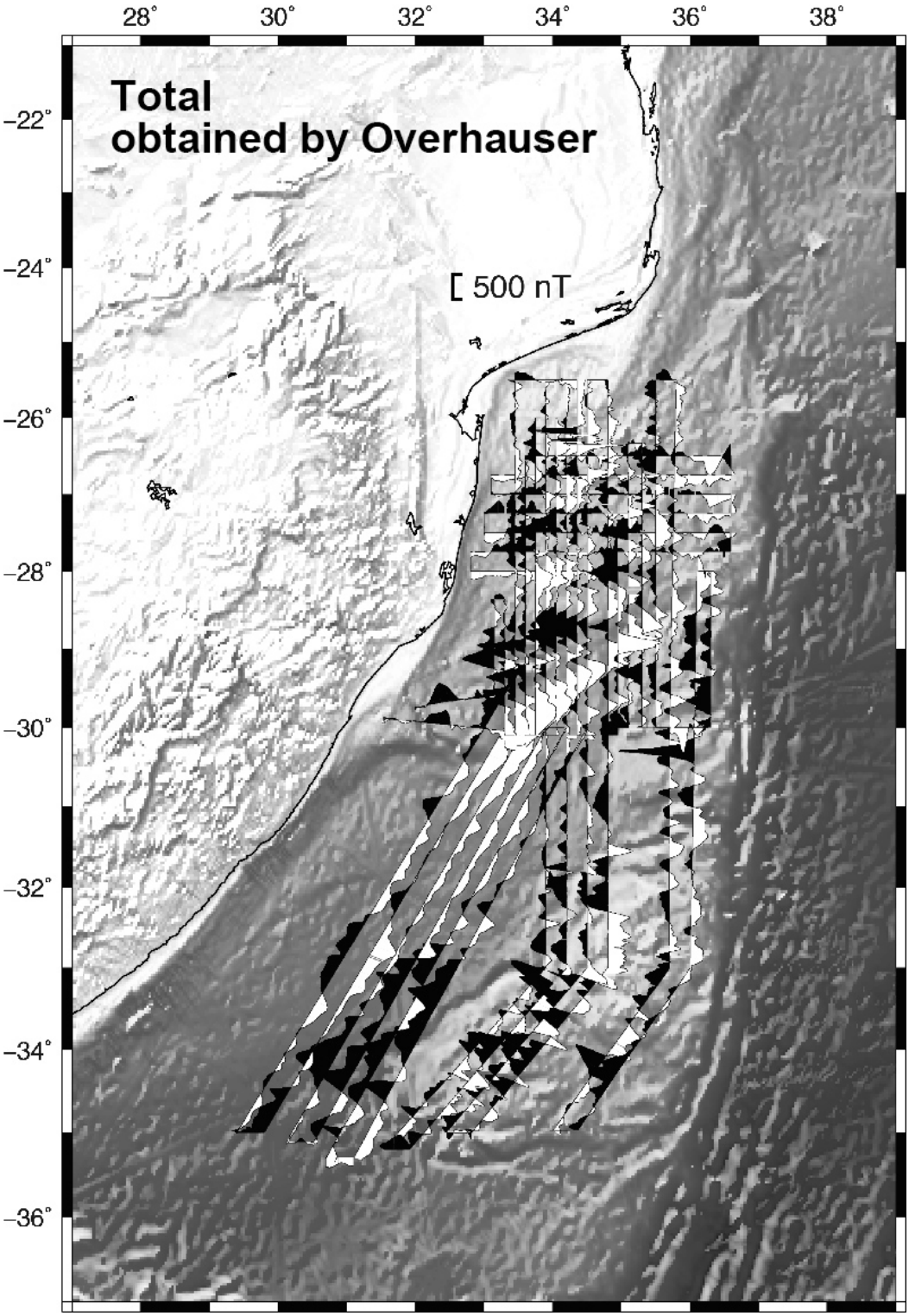

Fig. 2-1g

(continued)

Fig. 2-1

(a) Overview of the study area (Natal Valley and Mozambique Ridge) and conjugate areas superimposed on a topographic map (ETOPO1). Seaward-dipping reflectors of the Explora Escarpment (Hinz et al., 2004) are shown. Karoo: Karoo igneous province; FP, Falkland Plateau; MEB, Maurice Ewing Bank; NEGR, North East Georgia Rise; MR, Maud Rise; AR, Astrid Ridge; AP, Agulhas Plateau; EE, Explora Escarpment; LZS Lazarev Sea; RLS, Riiser-Larsen Sea. (b) Study area superimposed on topographic map (ETOPO1), showing the Karoo basalt area and the Ariel Graben (AG; dashed white line). The longer, NW–SE-oriented solid black lines with M12–M0 and the COB indicate magnetic spreading anomalies (magnetic isochrons) proposed by Goodlad et al. (1982). The shorter, NW–SE-oriented solid black lines with M4 indicate magnetic spreading anomalies proposed by Reznikov et al. (2005). E–W-oriented solid black lines with M10N, M4, and XR indicate magnetic spreading anomalies proposed by Tikku et al. (2002). The NNE–SSW-oriented extinct ridge (XR?) and geomagnetic anomaly sequences of Leinweber and Jokat (2011) are also shown by solid black lines. The dashed black line (FZ) indicates the fracture zone identified by Reznikov et al. (2005). Dredge sites are indicated by triangles (DR1, DR2, DR3, and DBA; Ben-Abraham et al., 1995; Mougenot et al., 1991). The diamond (DSDP249) represents Deep Sea Drilling Project site 249. NNV, Northern Natal Valley; SNV, Southern Natal Valley; MOZR, Mozambique Ridge; MOZCP, Mozambique Coastal Plains; AFFZ, Agulhas-Falkland fracture zone. (c) Geomagnetic anomaly profiles for the northward component (positive in black); (d) eastward component; and (e) downward component. (f) Total geomagnetic anomaly profiles calculated from vector magnetic anomalies; and (g) total geomagnetic anomalies obtained using a ship-towed Overhauser magnetometer (Leinweber and Jokat, 2011). SB, MB, m1, m2, and m3 are boundaries defined by geomagnetic anomaly pattern.

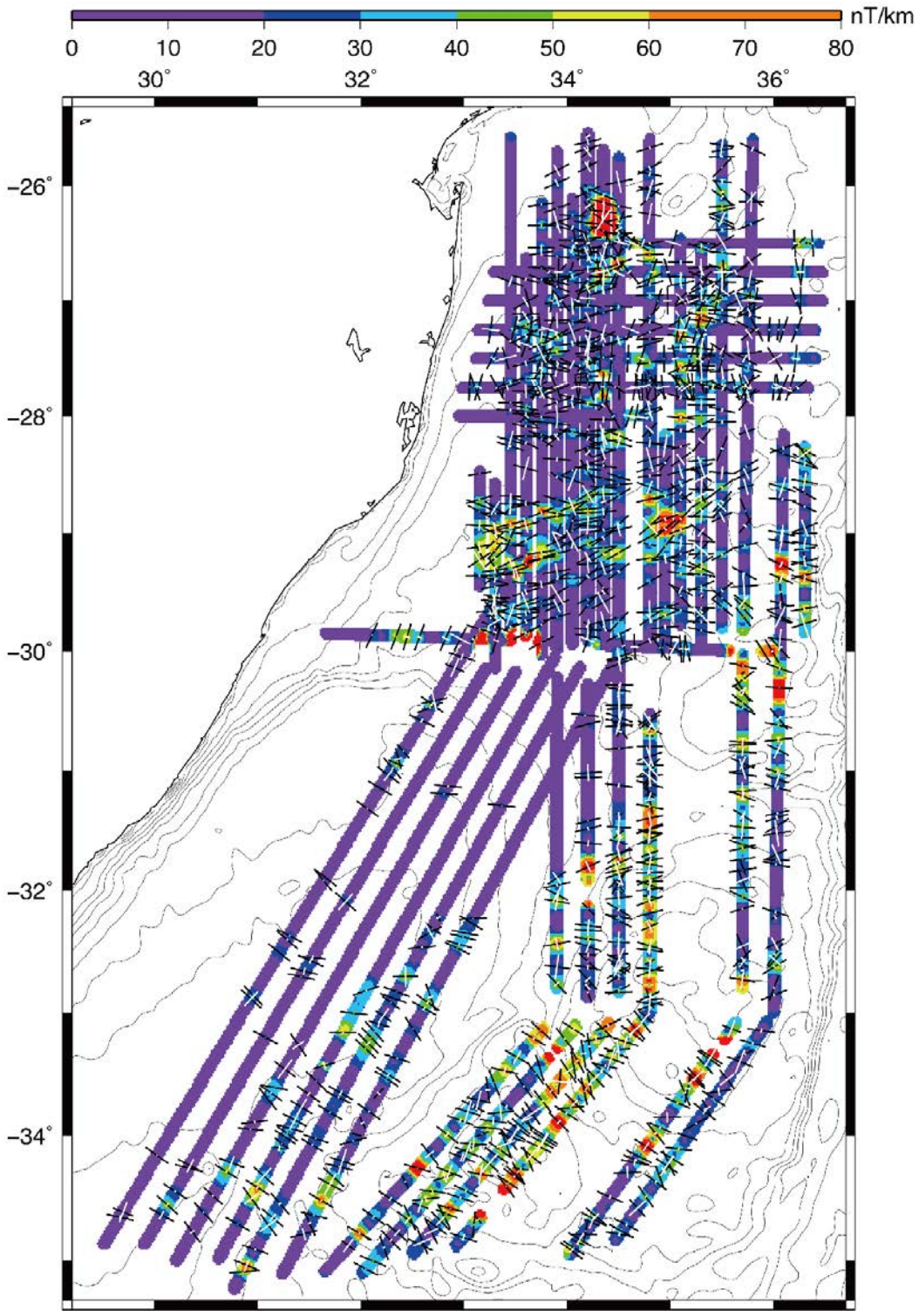

Fig. 2-2a

(continued)

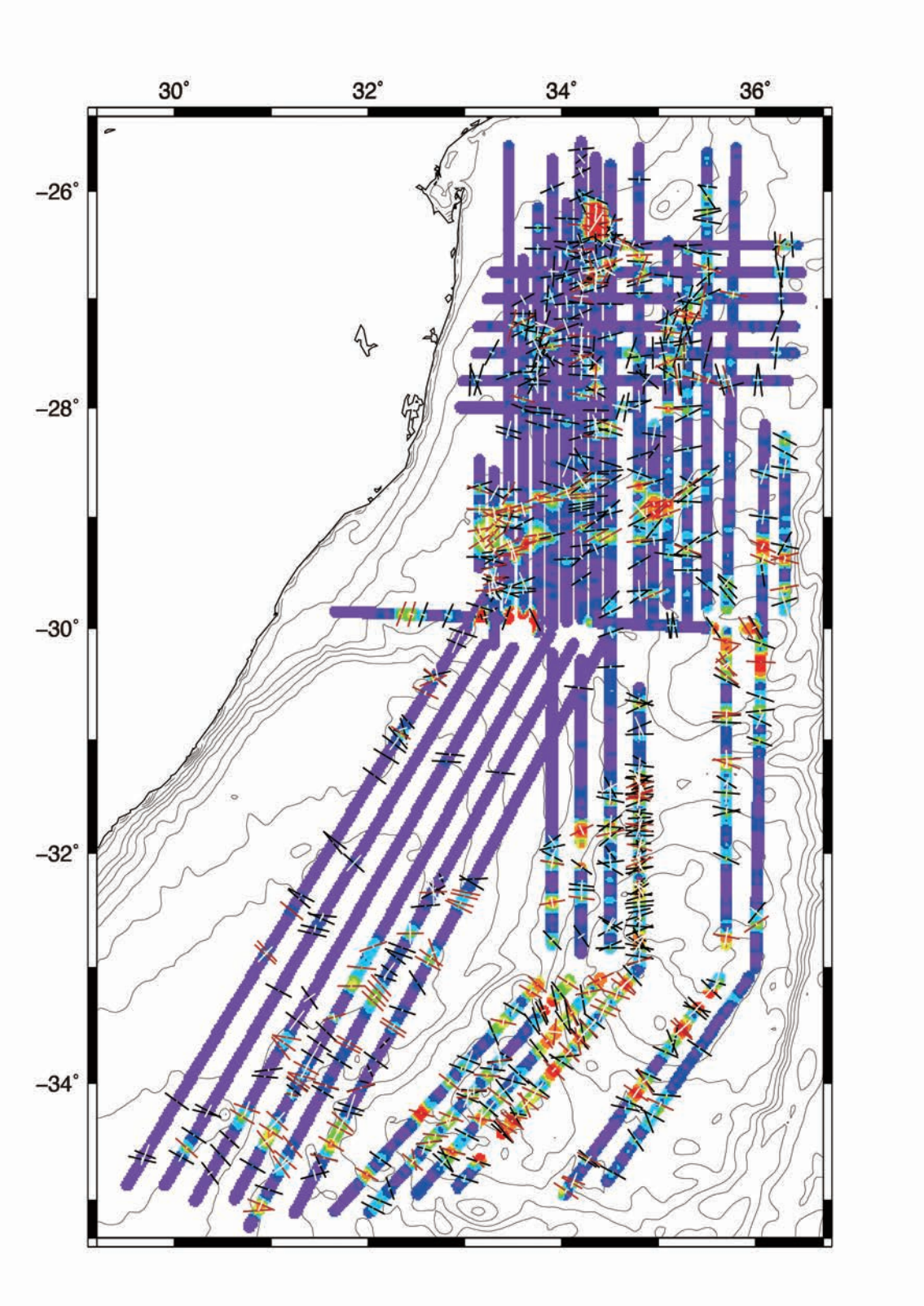

Fig. 2-2b

(continued)

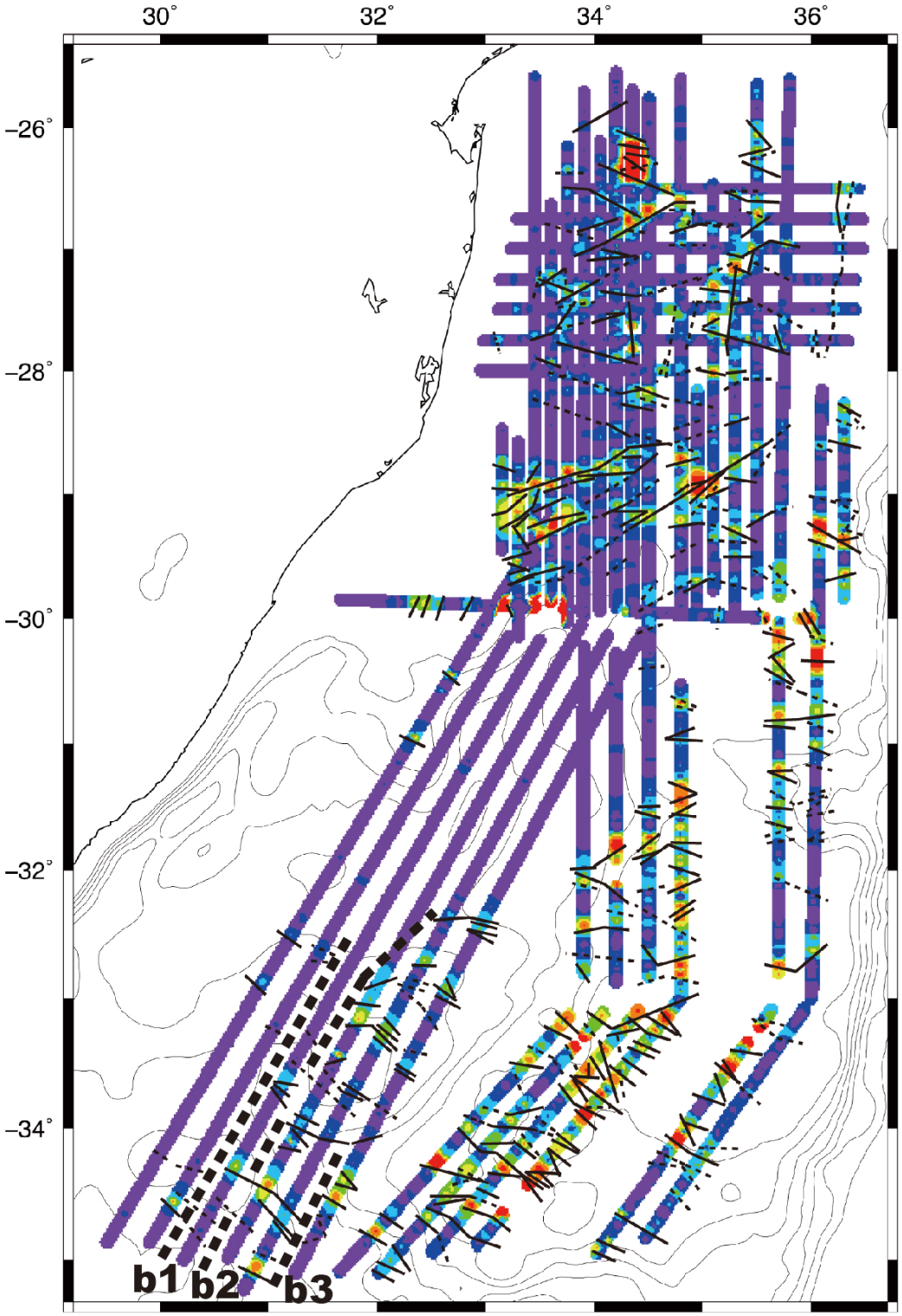

Fig. 2-2c

(continued)

Fig. 2-2

(a) The magnetic boundary strikes determined from vector geomagnetic anomalies superimposed on the calculated ISDV distribution and contours of the estimated top depth of the magnetization layer. Black bars indicate the magnetic boundary strikes. White bars indicate standard angular deviations. (b) Selected magnetic boundary strikes based on the threshold level of Table 2-3 in each region superimposed on the calculated ISDV distribution and contours of the estimated top depth of the magnetization layer. Red bars indicate the magnetic boundary strikes caused by the low magnetization contrast, and black bars indicate the magnetic boundary strikes caused by the high magnetization contrast. White bars indicate standard angular deviations. (c) The estimated magnetic boundary strikes interpreted as the result of high magnetization contrast boundaries (black solid line) and low magnetization contrast and/or topographic boundaries (black broken line) superimposed on the calculated ISDV distribution and crustal thickness contours. Solid dotted lines of b1, b2, and b3 are estimated boundaries between wiggles defined by the distribution of magnetic boundary strikes.

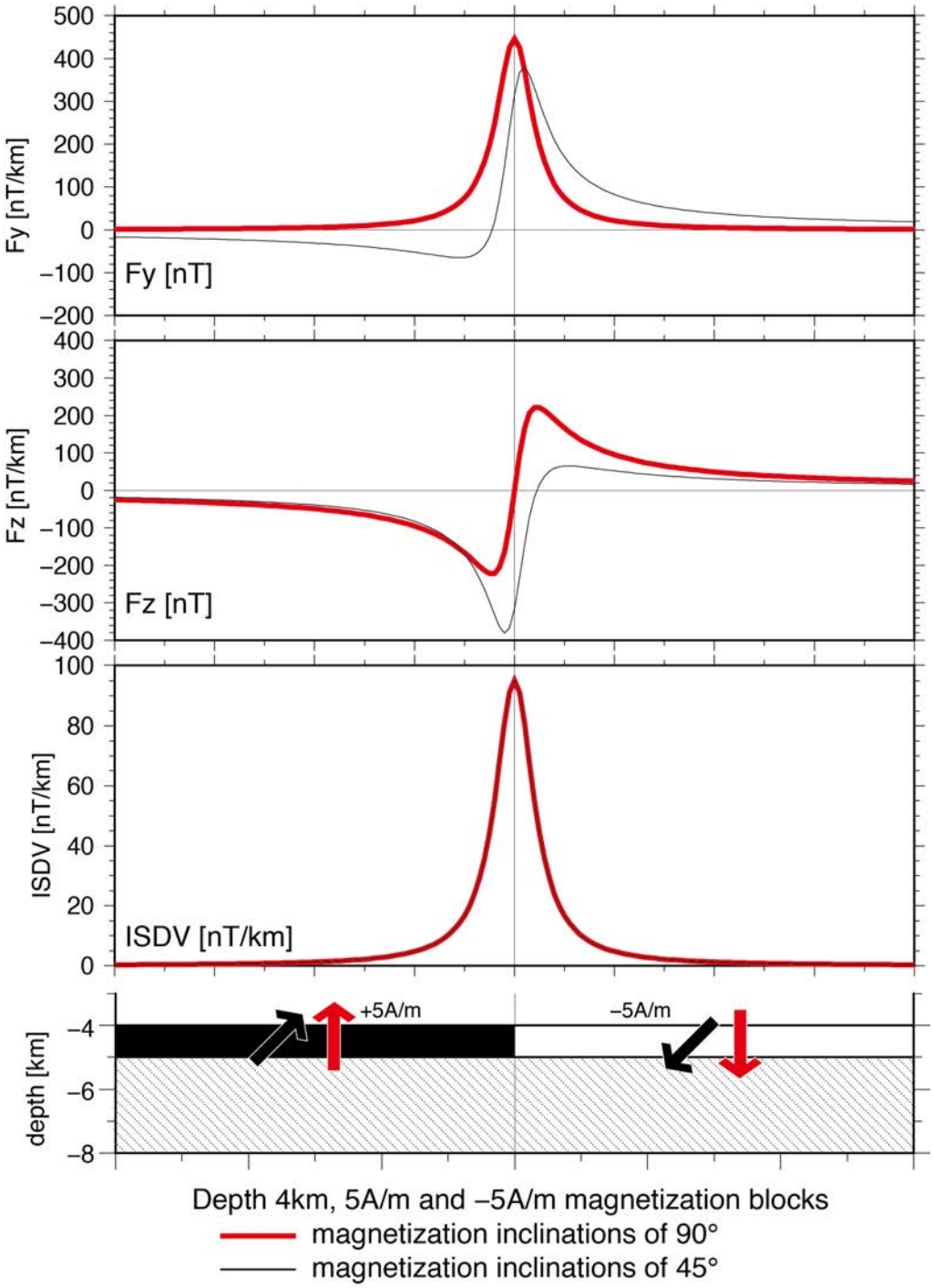
Fy [nT/km]
Fy [nT]
Fz [nT/km]
Fz [nT]
ISDV [nT/km]
ISDV [nT]
depth [km]
+5A/m
–5A/m
Depth 4km, 5A/m and –5A/m magnetization blocks
magnetization inclinations of 90°
magnetization inclinations of 45°

Fig. 2-3a

(continued)

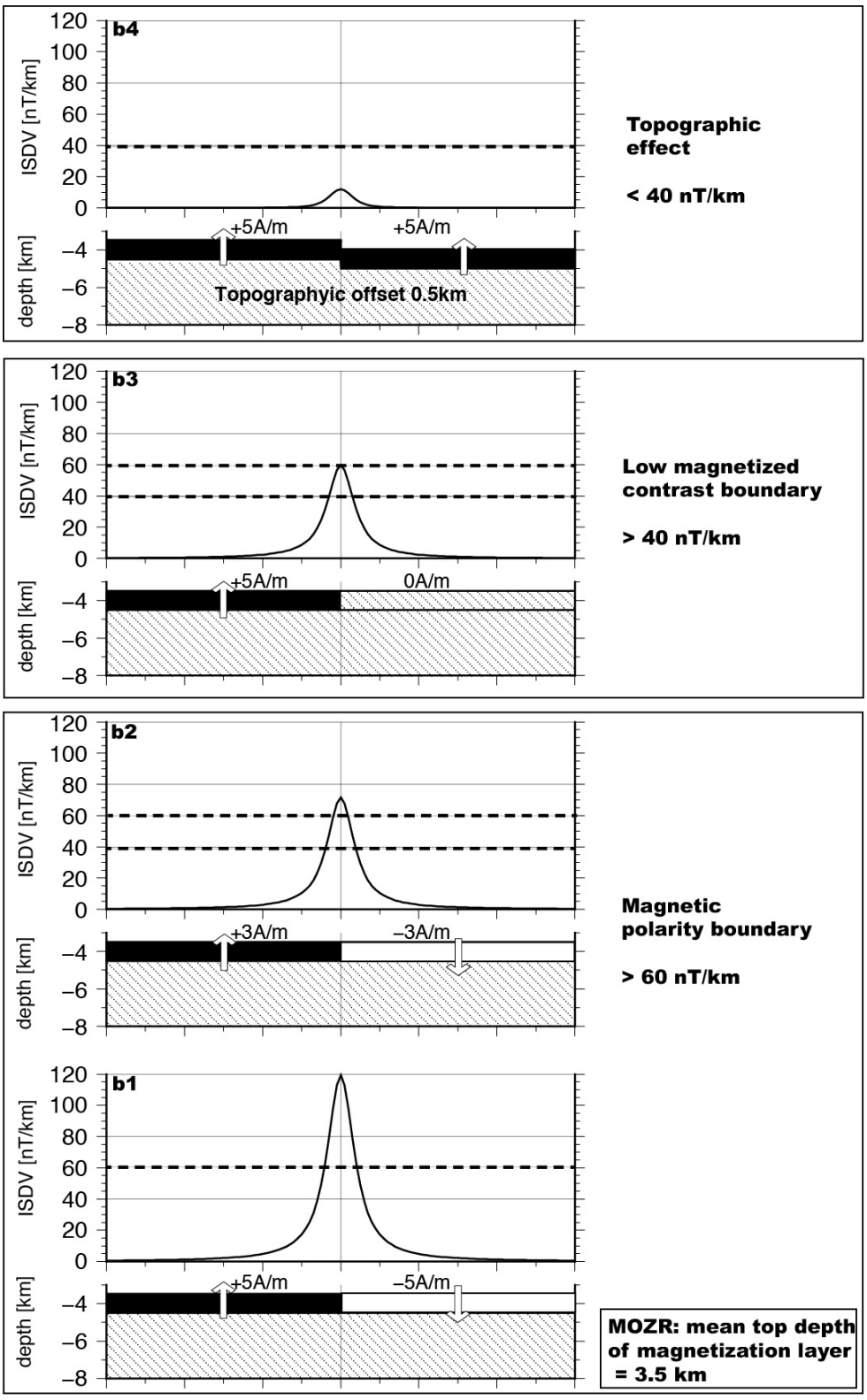

Fig. 2-3b

(continued)

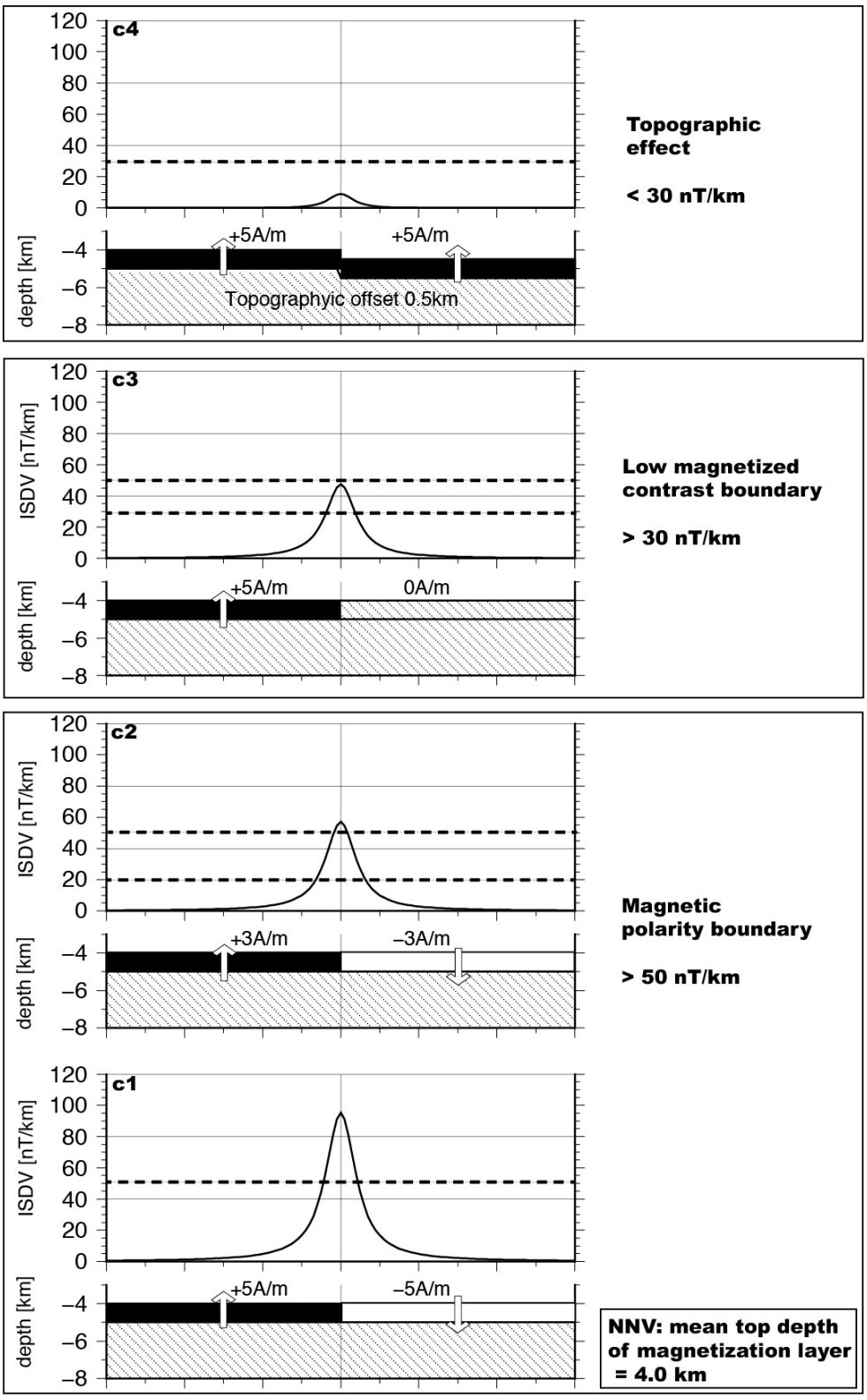

Fig. 2-3c

(continued)

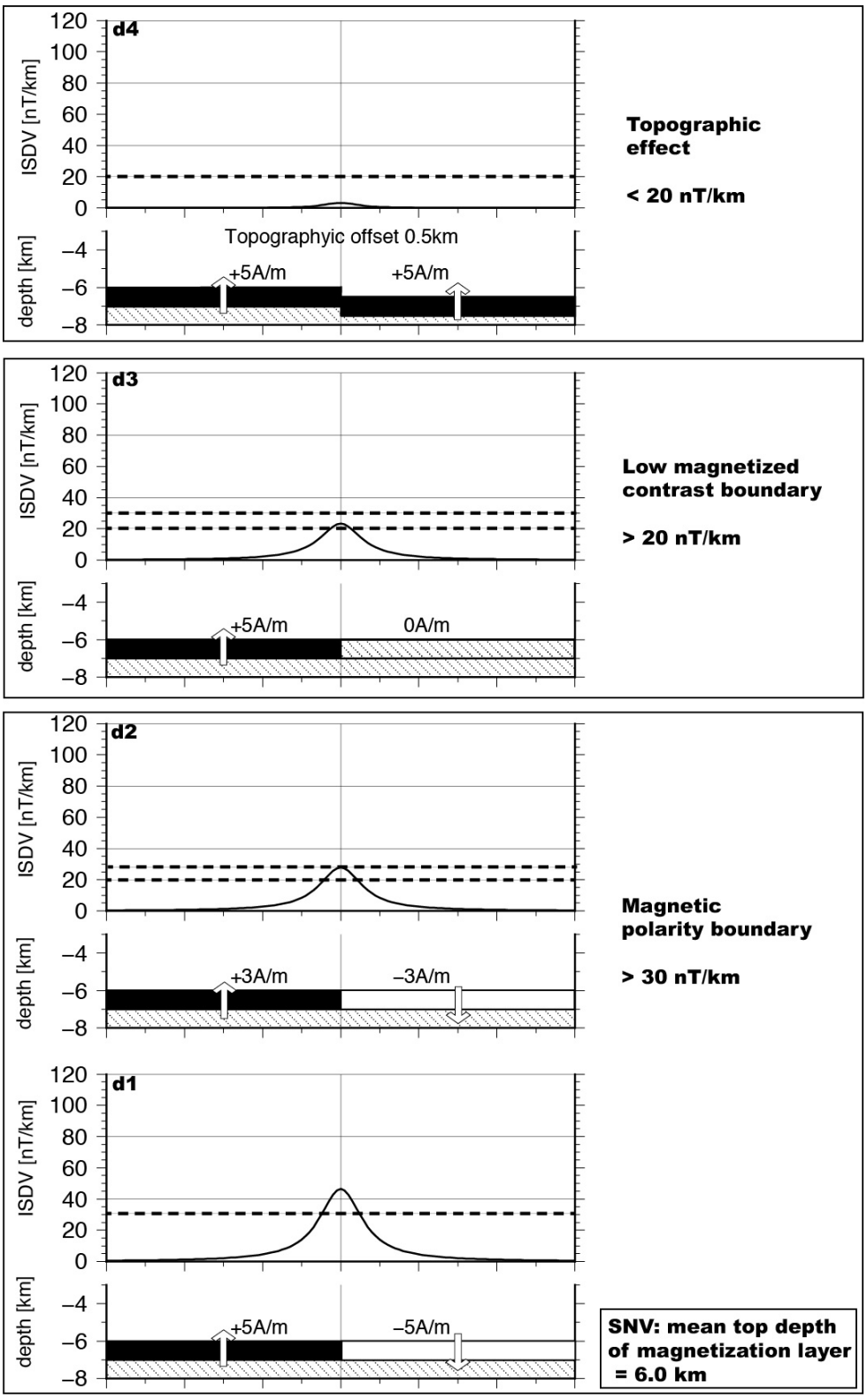

Fig. 2-3d

(continued)

Fig. 2-3

Synthetic examples for ISDV profiles calculated using simple two-dimensional magnetic structure models. The thickness of the magnetization layer is assumed as 1 km. (a) The effects of different inclinations. Surface depth of the magnetized layer is assumed as 4 km, and a +5 A/m, −5 A/m normal/reversed magnetized block model. Black and gray lines show source magnetization inclinations of 90° and 45°, respectively. (b)–(d) The effects of different surface depths of the magnetization layer and intensity of magnetization, where magnetization inclination is assumed constant at 90°. The surface depth of the magnetized layer in panels b–d is assumed as 3.5, 4, and 6 km respectively. (b1, c1, d1): +5 A/m and −5 A/m normal/reversed magnetized block model; (b2, c2, d2): +3 A/m and −3 A/m normal/reversed magnetized block model; (b3, c3, d3): +5 A/m magnetized block and non-magnetized block model; and (b4, c4, d4): +5 A/m magnetic structures with 0.5 km offset in the topography at the magnetic boundary. The thresholds in each situation are indicated by dotted lines.

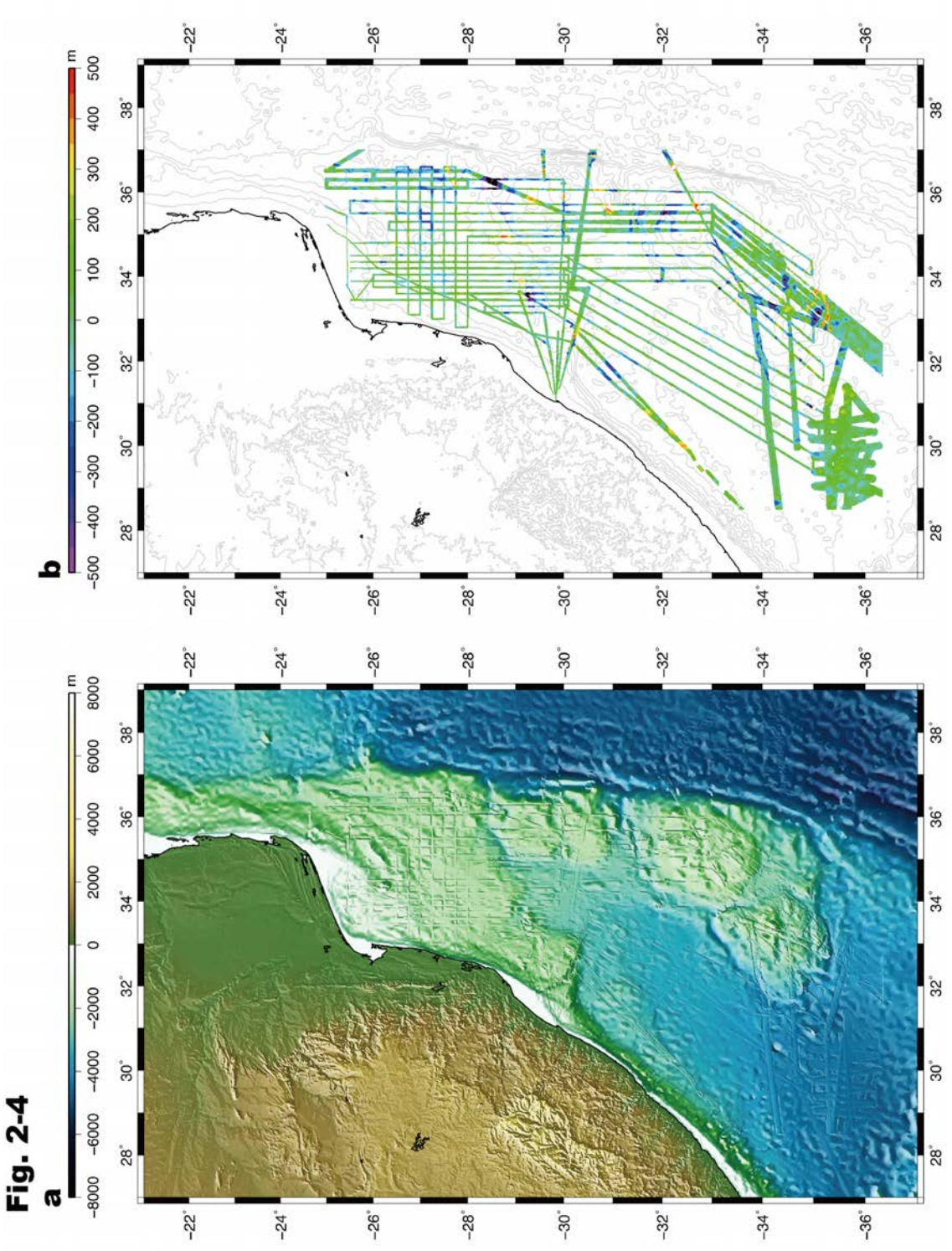
Fig. 2-4
a
b
m
8000
6000
4000
2000
0
−2000
−4000
−6000
−8000
500
400
300
200
100
0
−100
−200
−300
−400
−500
−22°
−24°
−26°
−28°
−30°
−32°
−34°
−36°
38°
36°
34°
32°
30°
28°

Fig. 2-4a and b

(continued)

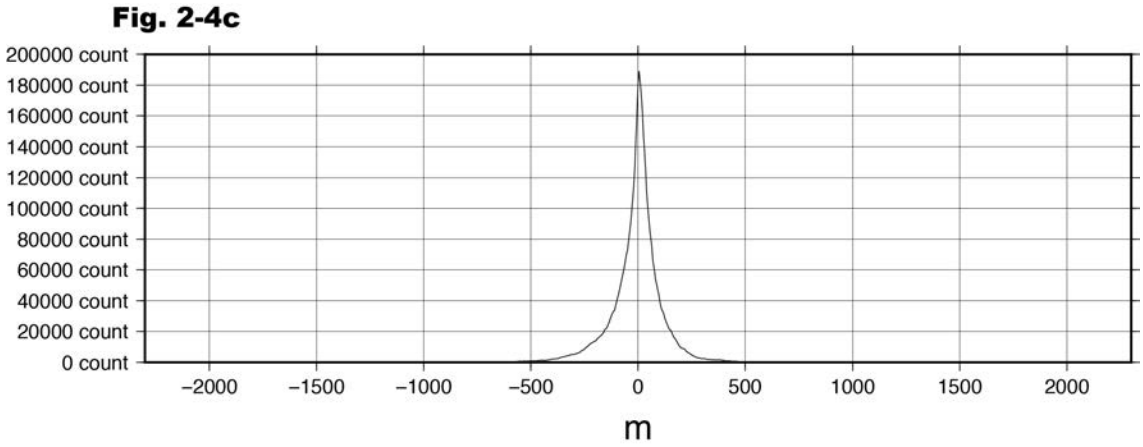

Fig. 2-4c

Fig. 2-4

(a) Multibeam sounding data superimposed on ETOPO1 bathymetric data. (b) The offset between ETOPO1 and multibeam sounding data. (c) Frequency distribution of offset between ETOPO1 and multibeam sounding data.

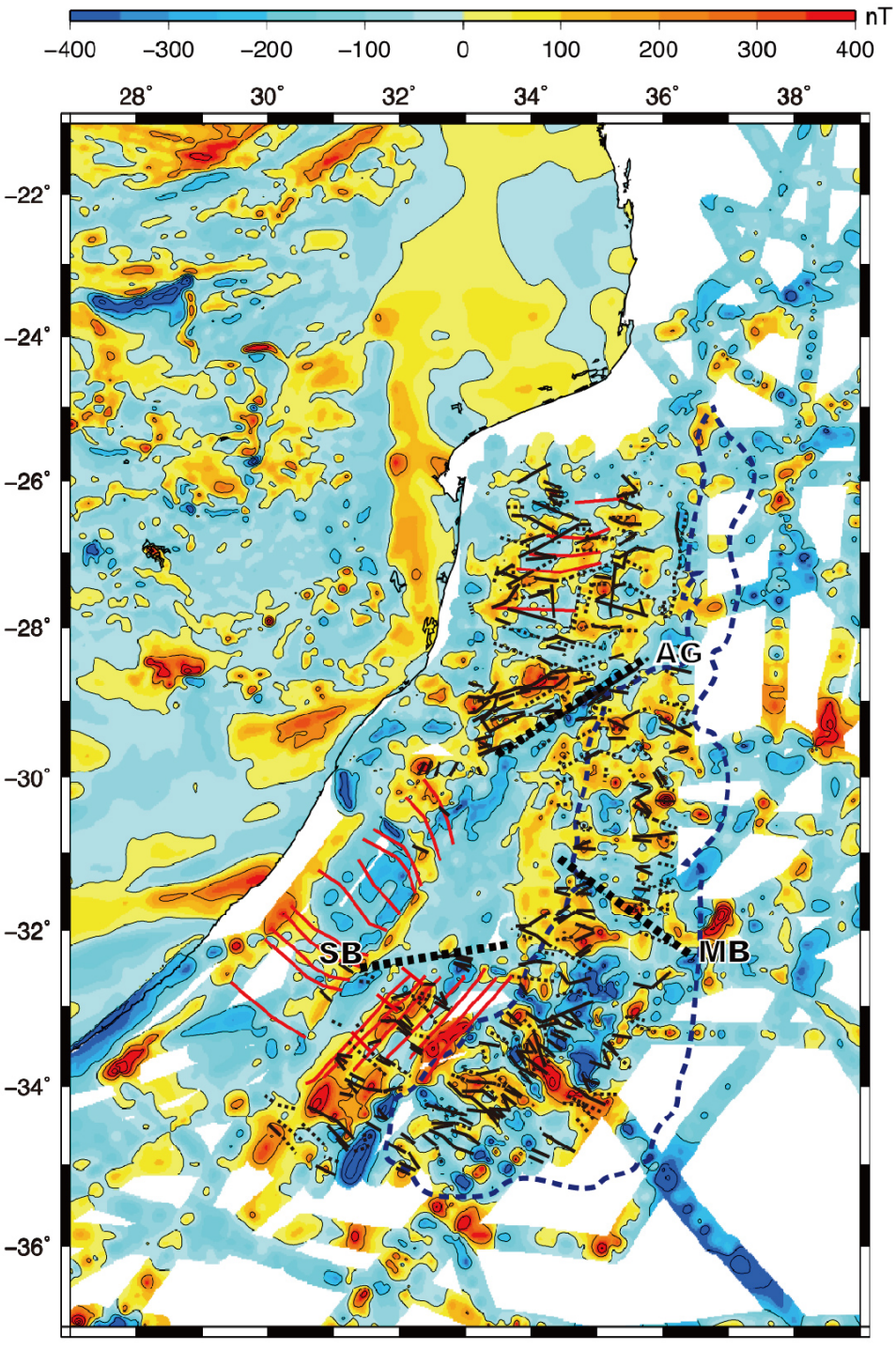
nT
−400
−300
−200
−100
0
100
200
300
400
28°
30°
32°
34°
36°
38°
−22°
−24°
−26°
−28°
−30°
−32°
−34°
−36°
AG
SB
MB

Fig. 2-5a

(continued)

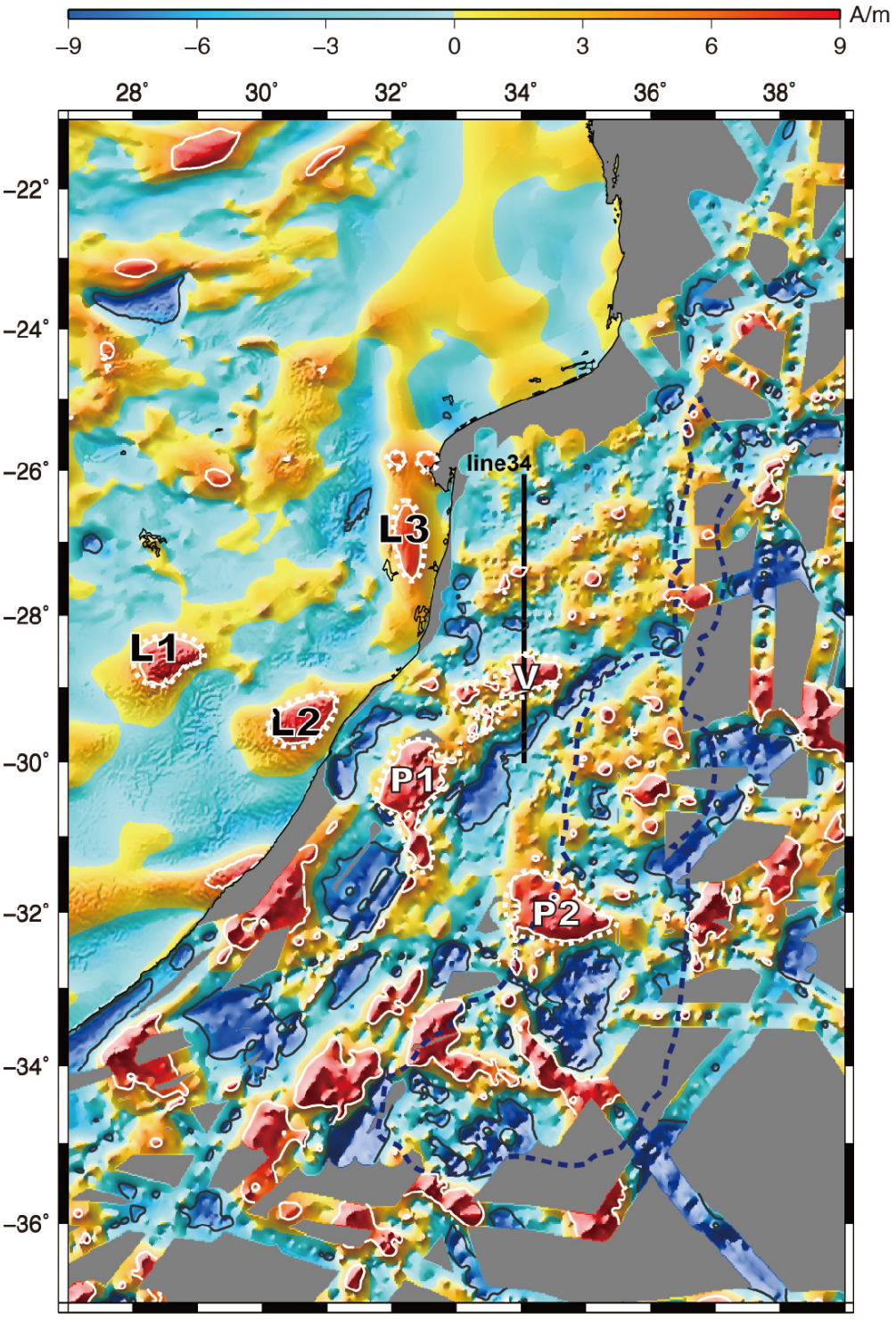

Fig. 2-5b

(continued)

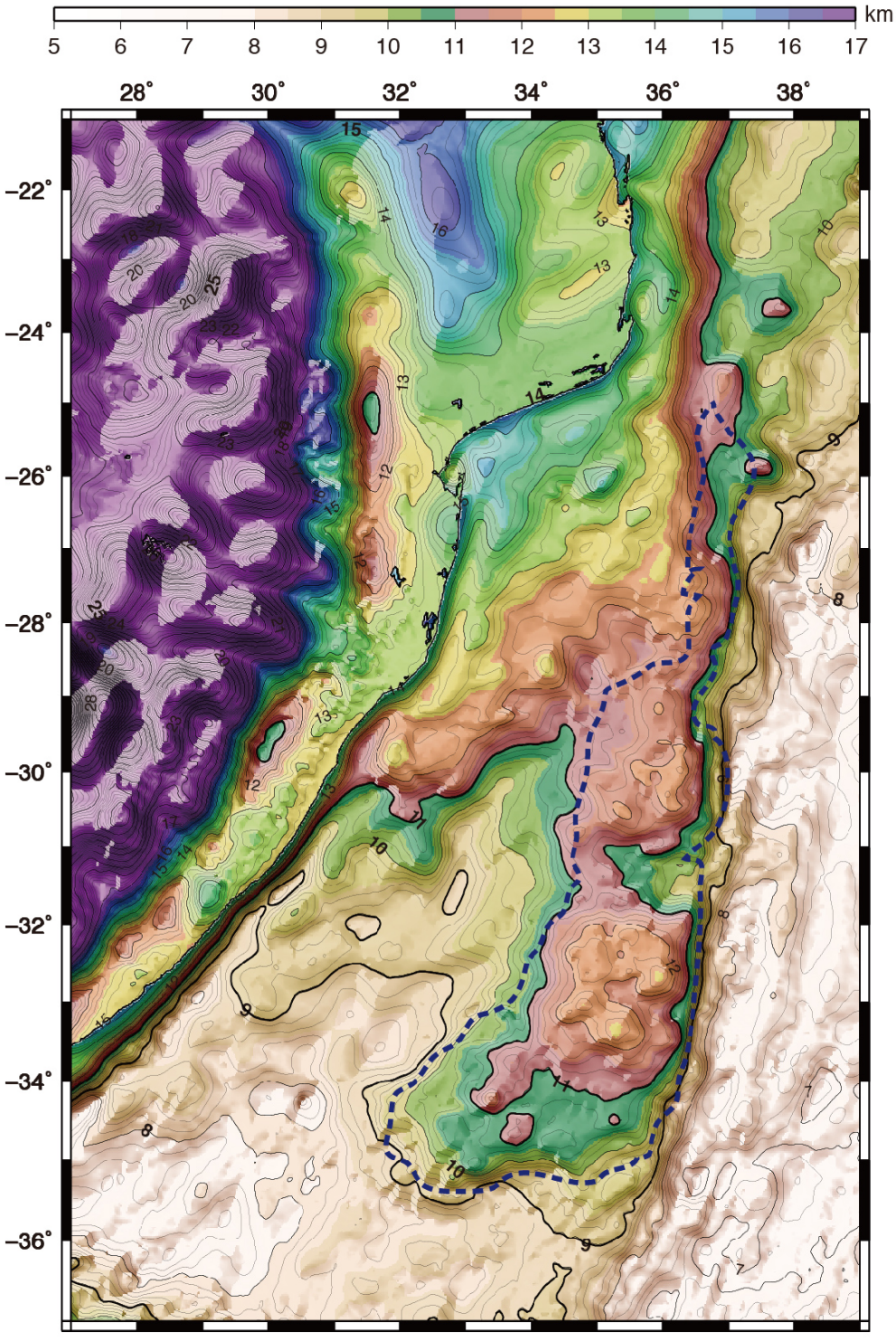

Fig. 2-5c

(continued)

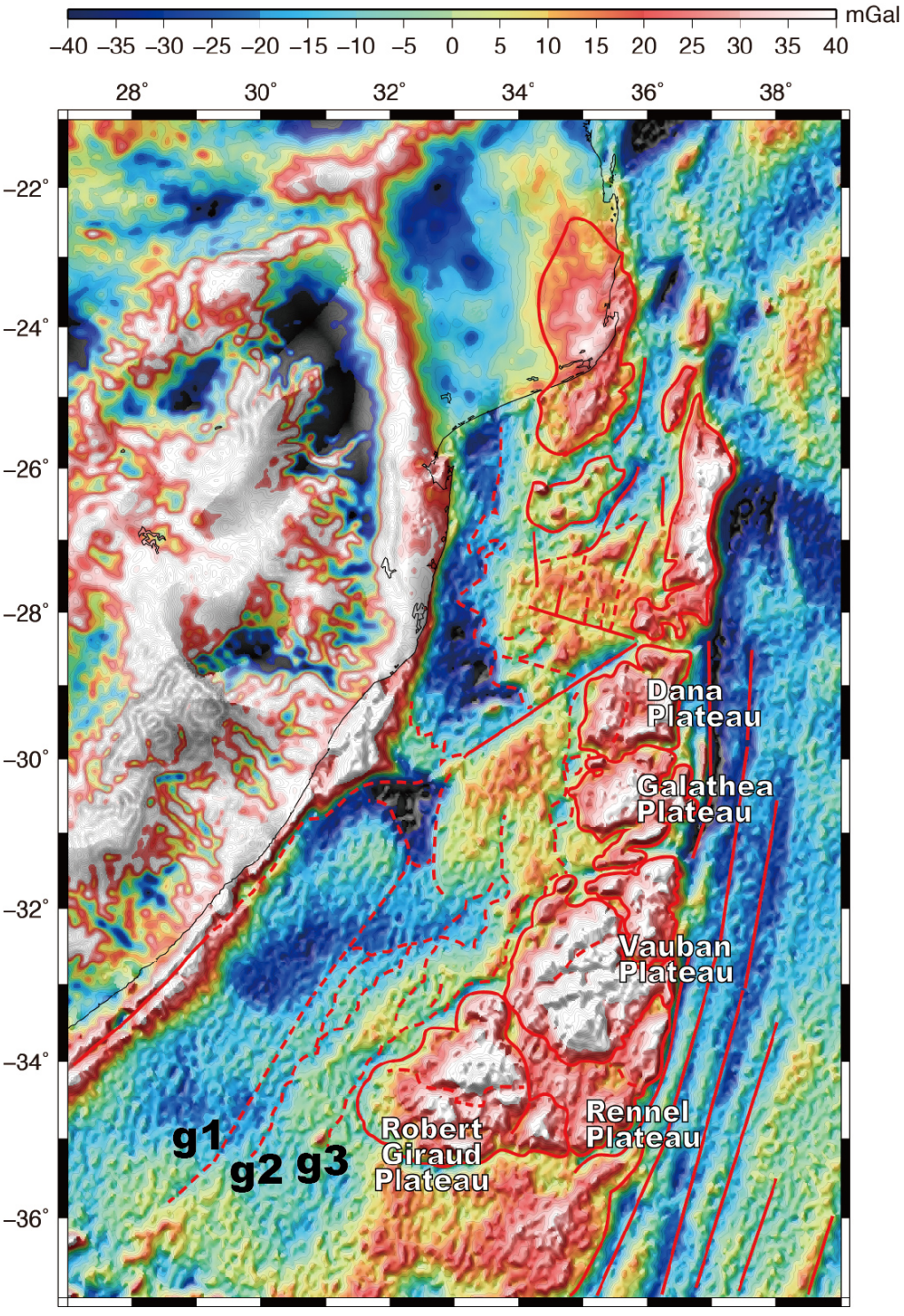

Fig. 2-5d

(continued)

Fig. 2-5

The blue dotted line indicates the plateau of the MOZR as deduced from free-air gravity and bathymetry data. (a) Total geomagnetic anomaly map and measured magnetic boundary strikes in the study area. Solid and dashed thin black lines indicate magnetic structure boundaries. Red lines indicate magnetic isochrons proposed in previous studies (Goodlad et al., 1982; Leinweber and Jokat, 2011; Tikku et al., 2001). The area of the MOZR is indicated by a dashed blue line. Abbreviations as in Fig. 2-1. (b) Intensity of magnetization distribution in the study area. White and gray lines mark areas with > +5 A/m and < −5 A/m magnetization intensity, respectively. L1, L2, and L3 indicate the areas associated with Karoo volcanism with > +5 A/m. P1, P2, and V indicate high magnetization areas of up to 12 A/m. (c) Estimated crustal thickness. Thick solid lines indicate 9-km and 11-km contours. (d) Satellite marine gravity map (Sandwell and Smith, 2008) for the offshore area and the Earth Gravitational Model (EGM2008; Pavlis et al., 2012) for the onshore area are shown. Structure boundaries estimated from offshore gravity anomalies are shown by solid and dashed red lines, including g1, g2, and g3.

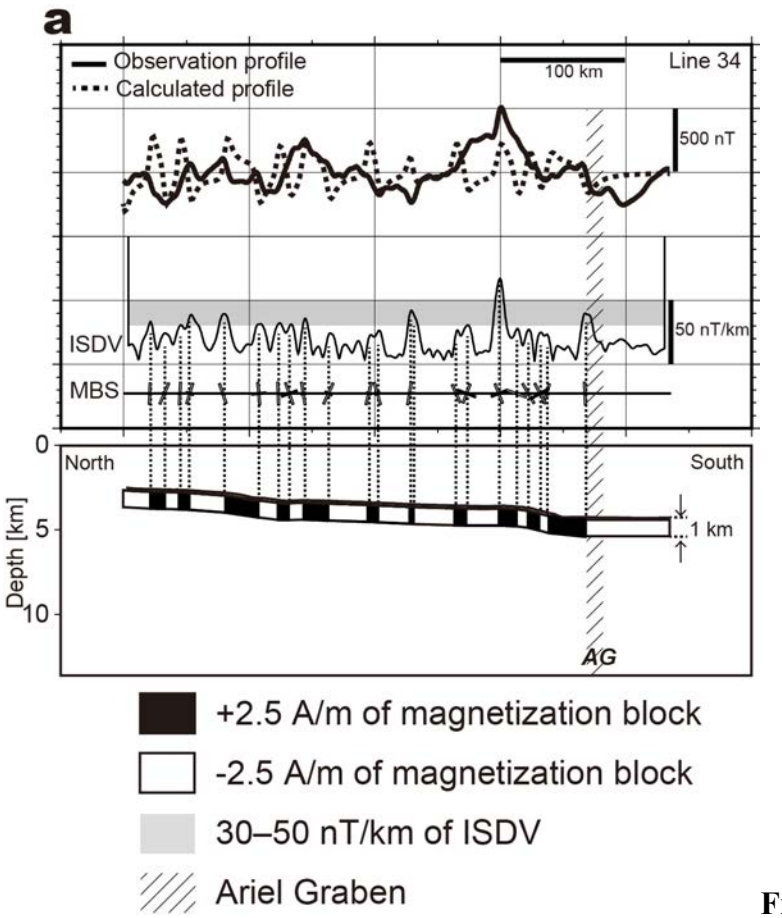
a
Observation profile
Calculated profile
100 km
Line 34
500 nT
ISDV
50 nT/km
MBS
0
North
South
Depth [km]
5
1 km
10
AG
+2.5 A/m of magnetization block
-2.5 A/m of magnetization block
30–50 nT/km of ISDV
Ariel Graben

Fig. 2-6a

(continued)

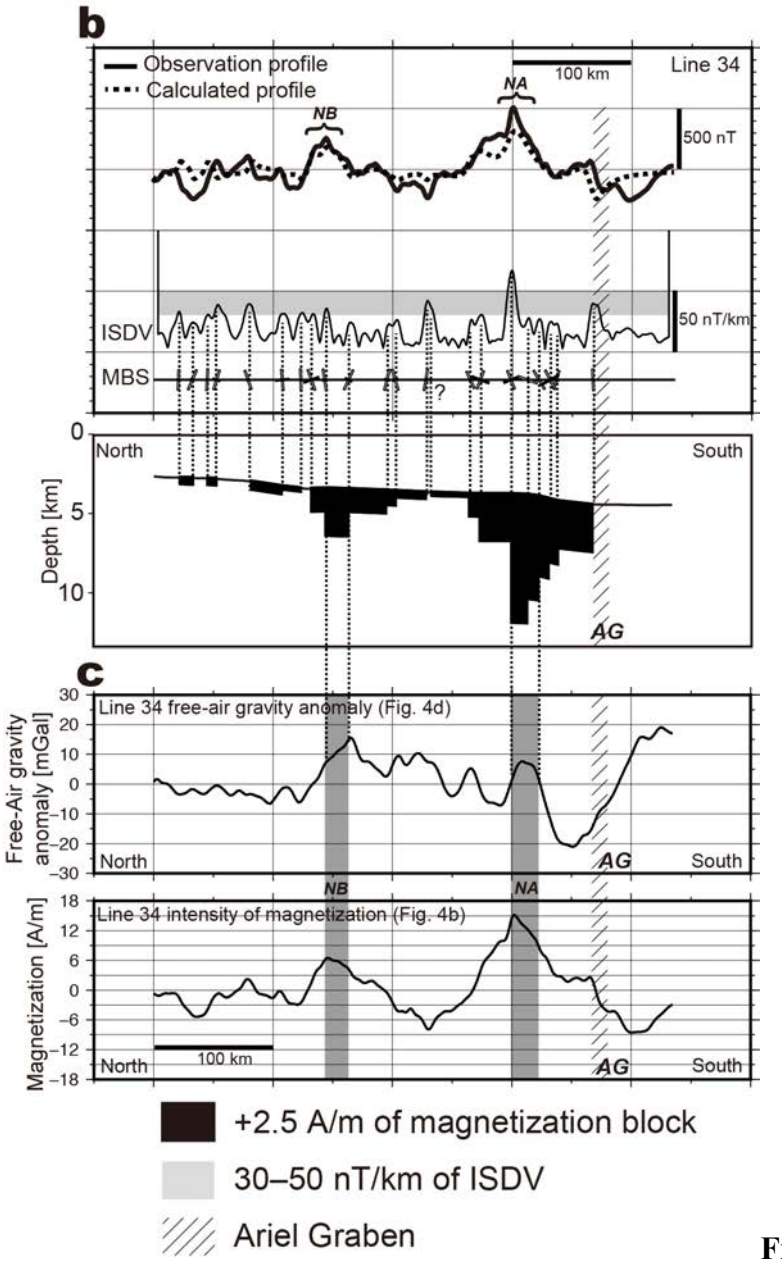

Fig. 2-6b

Fig. 2-6

Two-dimensional magnetized structure models. Boundaries of magnetized blocks are set to the measured magnetic boundary strikes: (a) simple normal–reversed pattern of fixed magnetization with constant thickness (1 km); (b) fixed magnetization with variable thickness blocks. MBS: magnetic boundary strikes; (c) Free-air gravity anomaly (Fig. 2-5d) and intensity of magnetization based on inversion analysis (Fig. 2-5b) along line 34. NA and NB: Large-amplitude geomagnetic anomalies of area with 300–550 nT. AG: Ariel Graben.

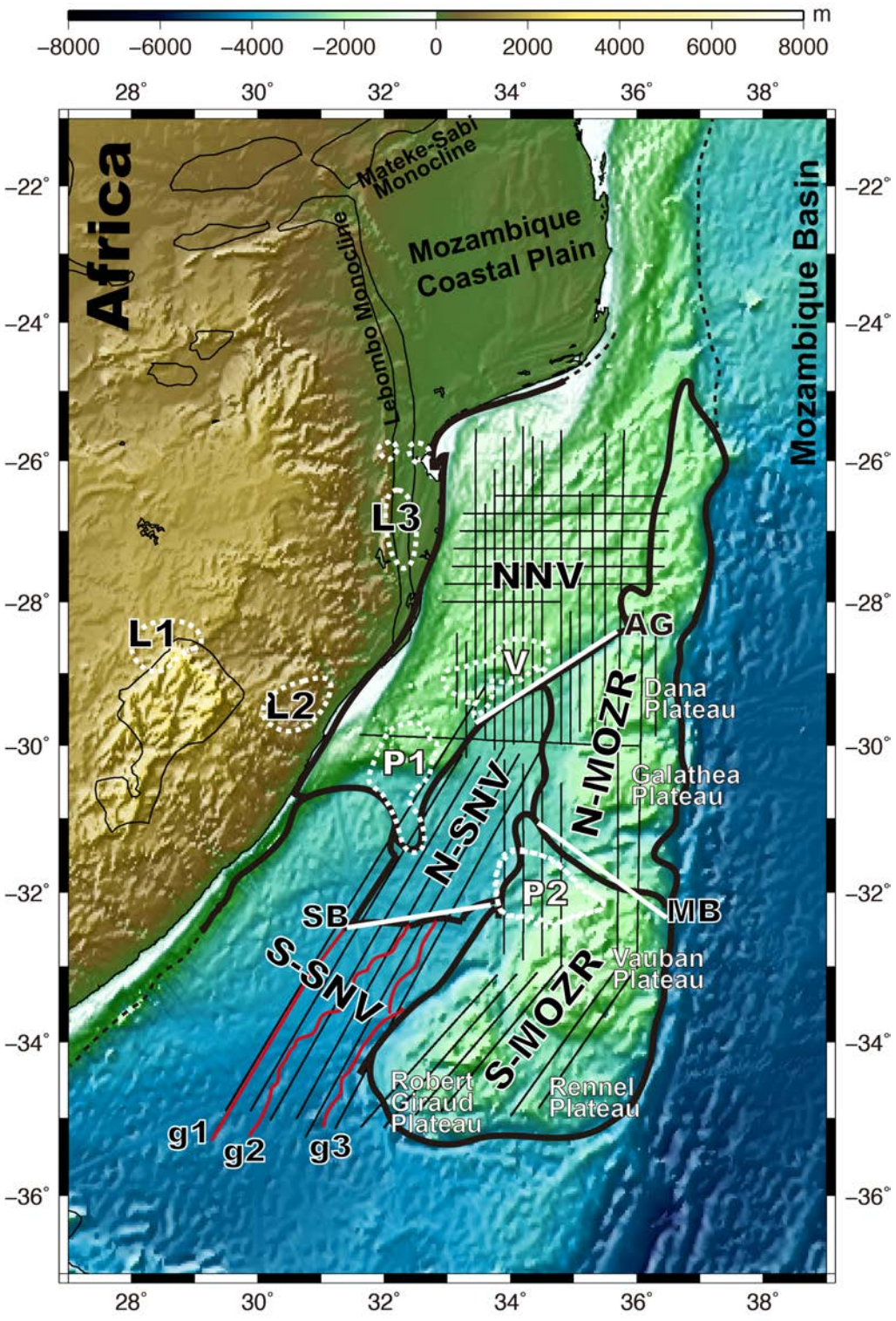
m
−8000
−6000
−4000
−2000
0
2000
4000
6000
8000
28°
30°
32°
34°
36°
38°
−22°
−24°
−26°
−28°
−30°
−32°
−34°
−36°
Africa
Mozambique Basin
Mateke-Sabi Monocline
Lebombo Monocline
Mozambique Coastal Plain
L1
L2
L3
P1
P2
V
NNV
AG
SB
MB
N-SNV
S-SNV
N-MOZR
S-MOZR
Dana Plateau
Galathea Plateau
Vauban Plateau
Robert Giraud Plateau
Rennel Plateau
g1
g2
g3

Fig. 2-7a

(continued)

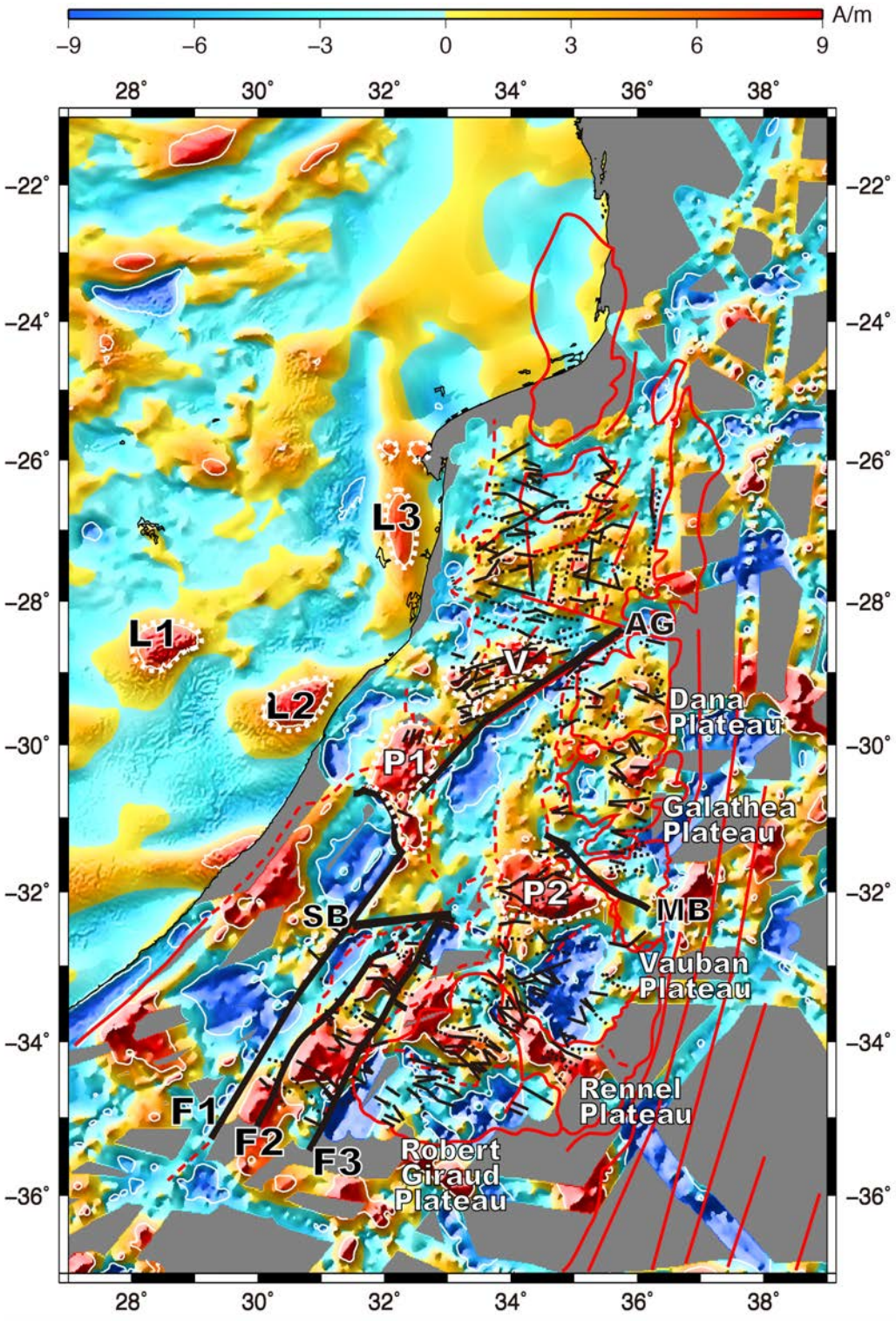

Fig. 2-7b

(continued)

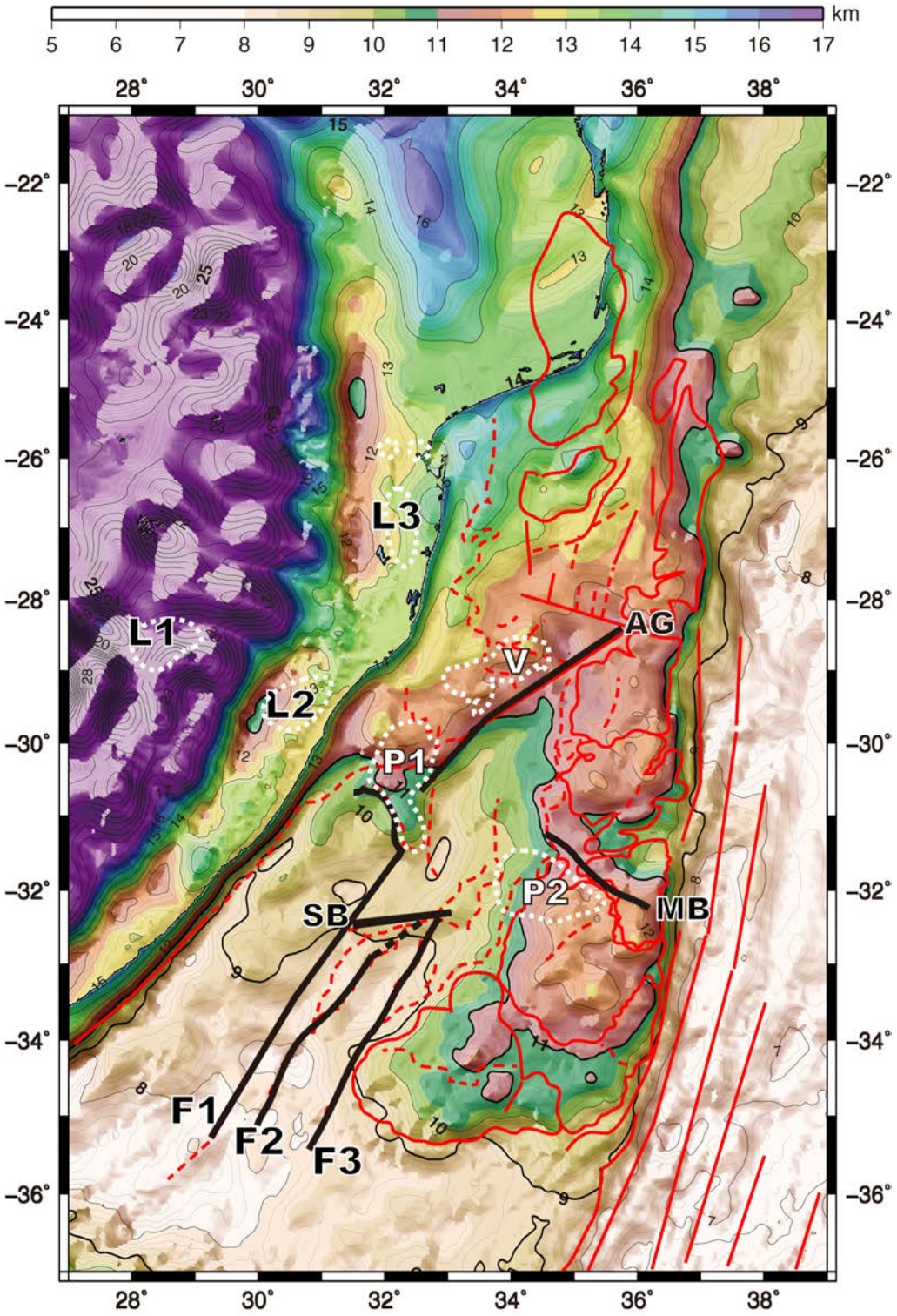

Fig. 2-7c

(continued)

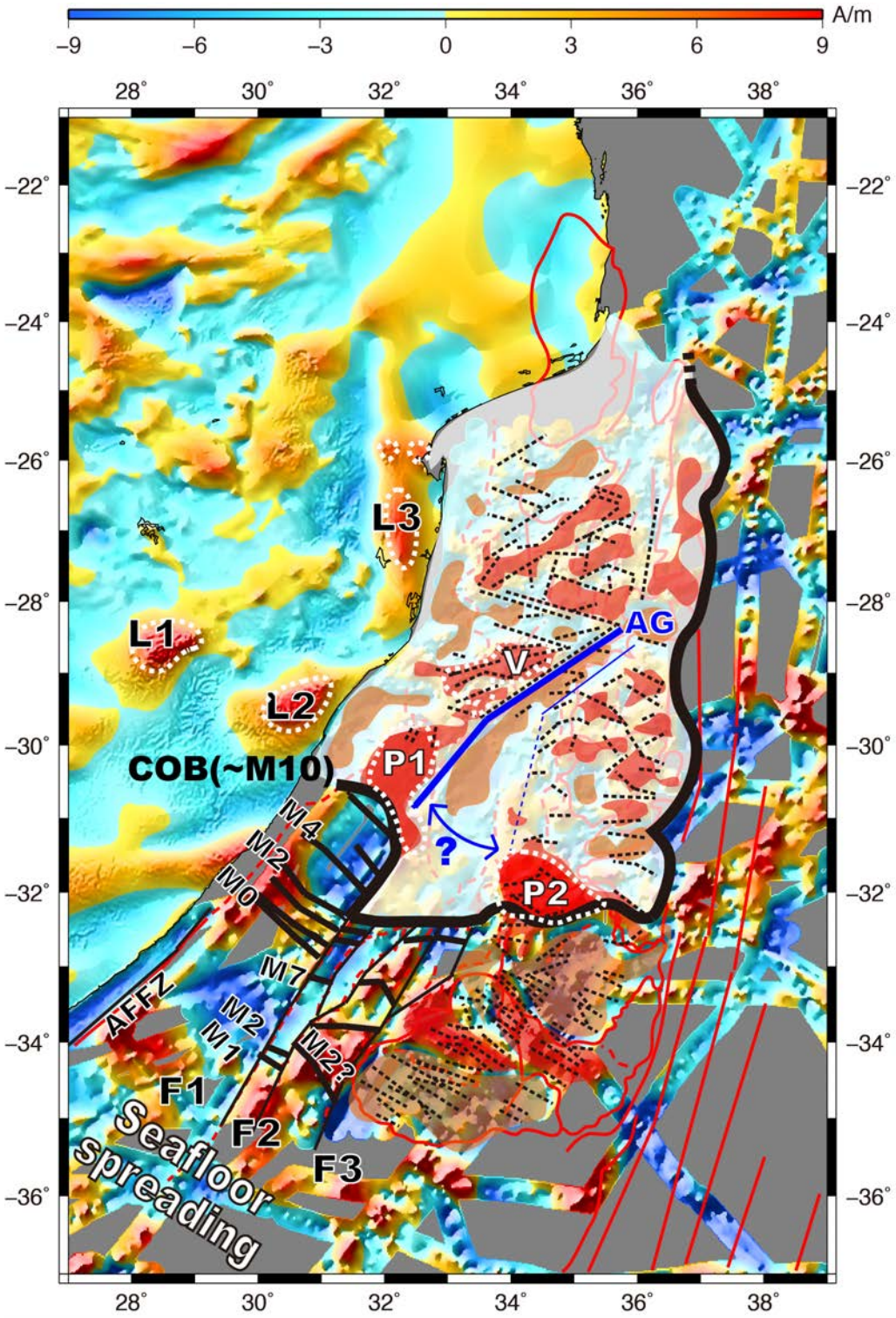

Fig. 2-7d

(continued)

Fig. 2-7

Geological interpretation of the study area superimposed on (a) the topographic map, (b) the intensity of magnetization map, and (c) the crustal thickness map. The distribution of newly identified fracture zones (F1, F2, and F3) is shown. White dotted lines indicate the boundaries of the AG, SB, and MB shown in Fig. 2-1f. Labels and lines are the same as in Figs. 2-1 and 2-5. (d) Interpreted geological features including the continent–ocean boundary (thick line), stretched continental crust (white area), basaltic intrusion with normal (red areas) and reversed (orange areas) magnetization, interpreted magnetization structure boundaries (thin broken lines), magnetic isochrons in the S-SNV (medium thickness lines), fracture zones (thin lines), and the AG (blue lines).

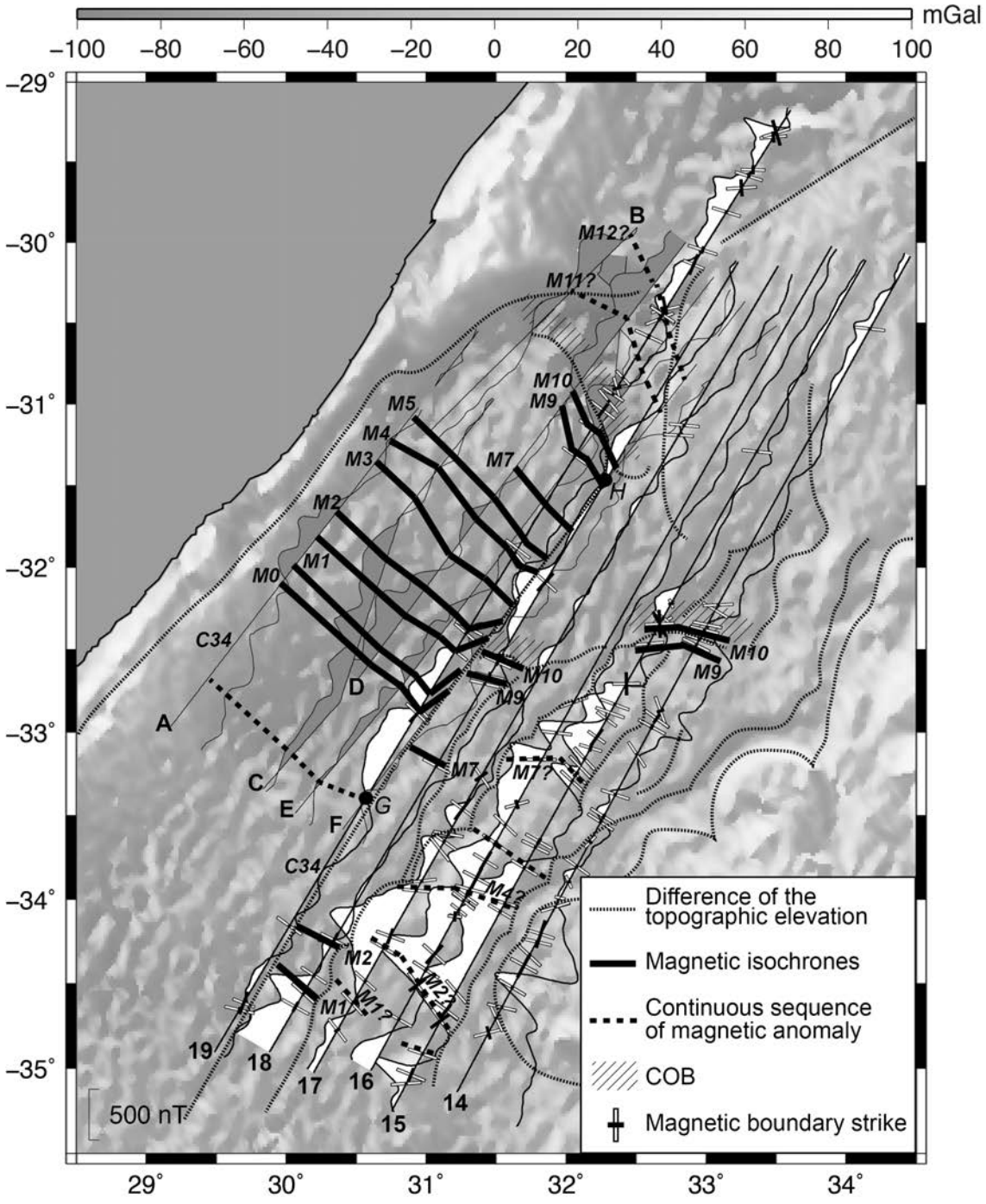
mGal
−100 −80 −60 −40 −20 0 20 40 60 80 100
−29°
−30°
−31°
−32°
−33°
−34°
−35°
29° 30° 31° 32° 33° 34°
B
M122
M11?
M10
M9
M5
M4
M3
M7
H
M2
M0
M1
C34
A
D
M10
M9
M10
M9
M7
M7?
C
E
F
G
C34
M2
M2
M1
M1?
19
18
17
16
15
14
500 nT
Difference of the topographic elevation
Magnetic isochrones
Continuous sequence of magnetic anomaly
COB
Magnetic boundary strike

Fig. 2-8a

(continued)

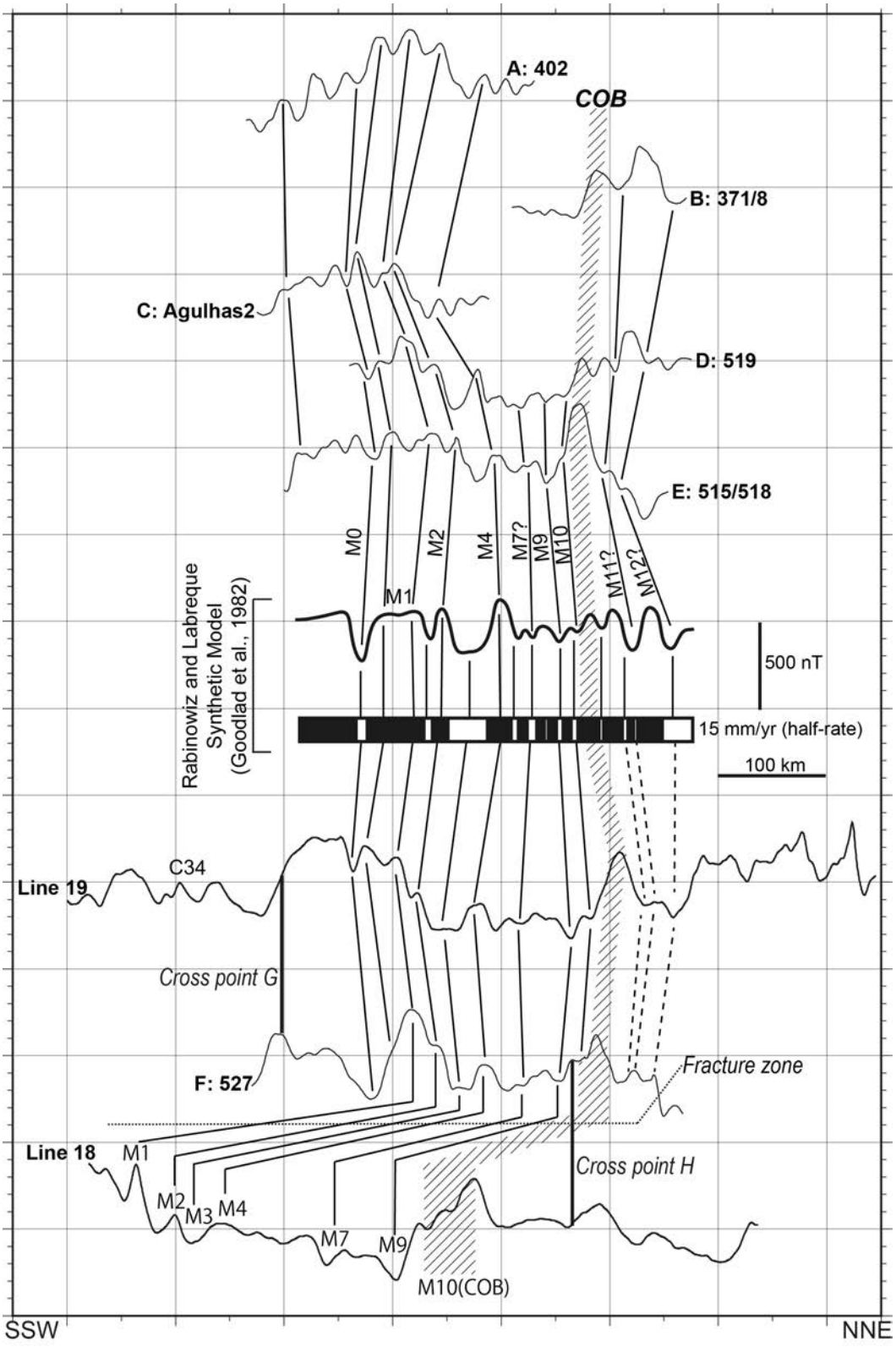

Fig. 2-8b

(continued)

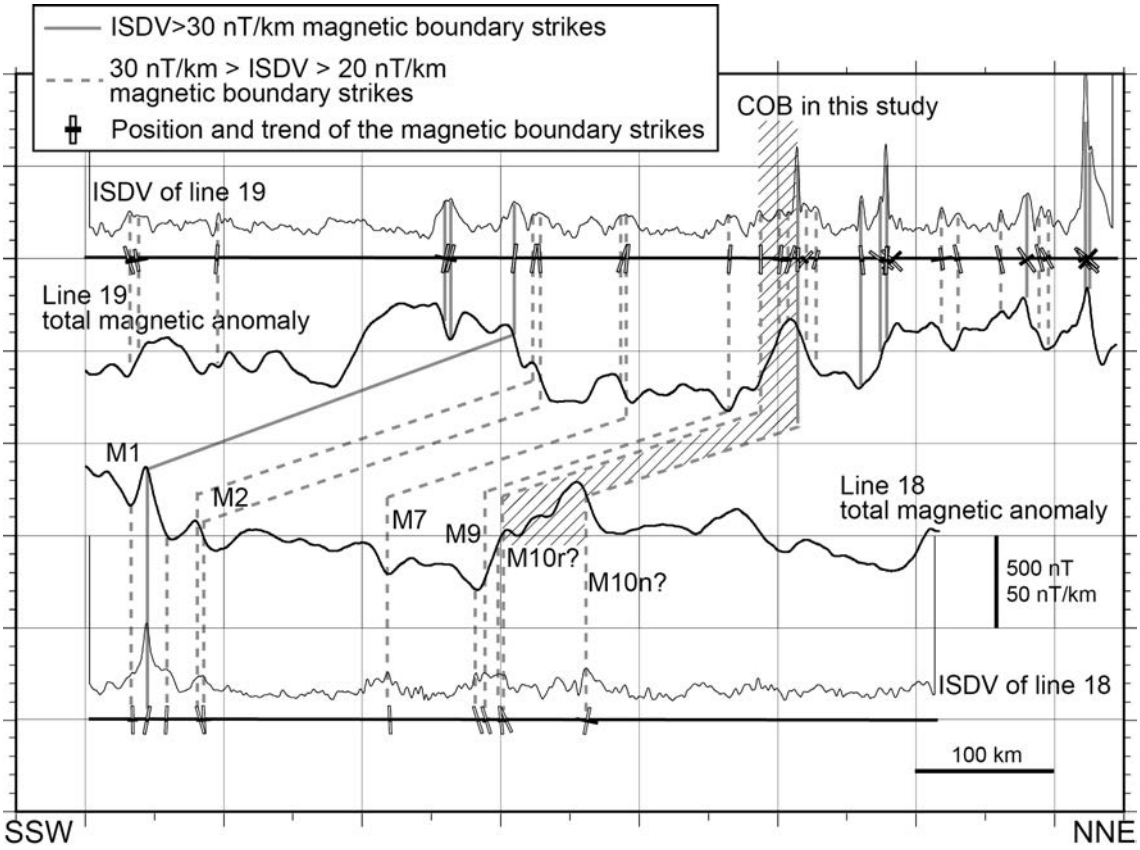

Fig. 2-8c

Fig. 2-8

(a) Detailed distribution of geomagnetic anomalies and magnetic boundary strikes for lines 14–19 (white wiggle) with geomagnetic anomalies from previous studies (gray wiggle; Goodlad et al., 1982) in the S-SNV. Magnetic isochrons (thick lines) and structure boundaries estimated from gravity anomalies (dashed gray lines) are shown. (b) Comparison of geomagnetic anomaly profiles derived from lines 18 and 19 (semi-thick lines) with those from previous studies (thin lines; Goodlad et al., 1982). Magnetic block model and profile (thick line; Rabinowiz and Labreaque, 1979) are also shown. The position of the COB is hatched (approximately M10). The fracture zone (thin broken line) is shown. (c) Comparison of magnetic boundary strikes on lines 18 and 19. ISDV profiles (gray lines) are also shown.

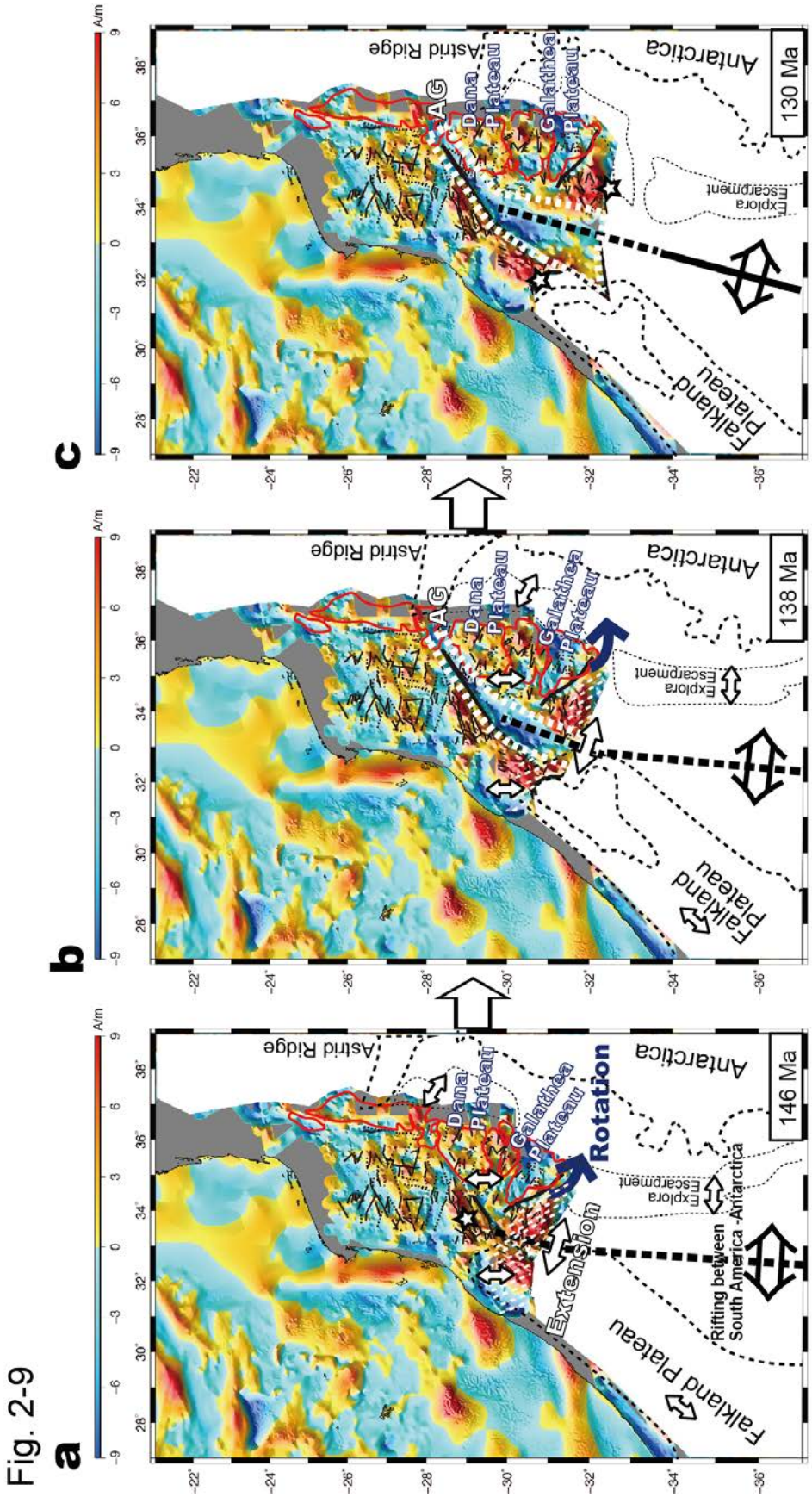
Fig. 2-9
a
b
c
A/m
9
6
3
0
-3
-6
-9
-22°
-24°
-26°
-28°
-30°
-32°
-34°
-36°
28°
30°
32°
34°
36°
38°
Antarctica
Astrid Ridge
AAG
Dana Plateau
Galathea Plateau
Explora Escarpment
Falkland Plateau
Rotation
Extension
Rifting between South America -Antarctica
146 Ma
138 Ma
130 Ma

Fig. 2-9

(continued)

Fig. 2-9

Proposed formation history of the N-SNV and AG. (a) First stage at about 146 Ma, showing a reconstructed highly magnetized body, possibly caused by intense basaltic intrusion (star) before extension. (b) Second stage at 138 Ma, during rotation of the Galathea Plateau, extension of the N-SNV, and formation of the AG caused by rifting between South America and Antarctica. (c) Third stage at about 130 Ma, when formation of the AG and N-SNV was complete. The Galathea Plateau is rotated counterclockwise, resulting in E–W magnetic boundary strikes.

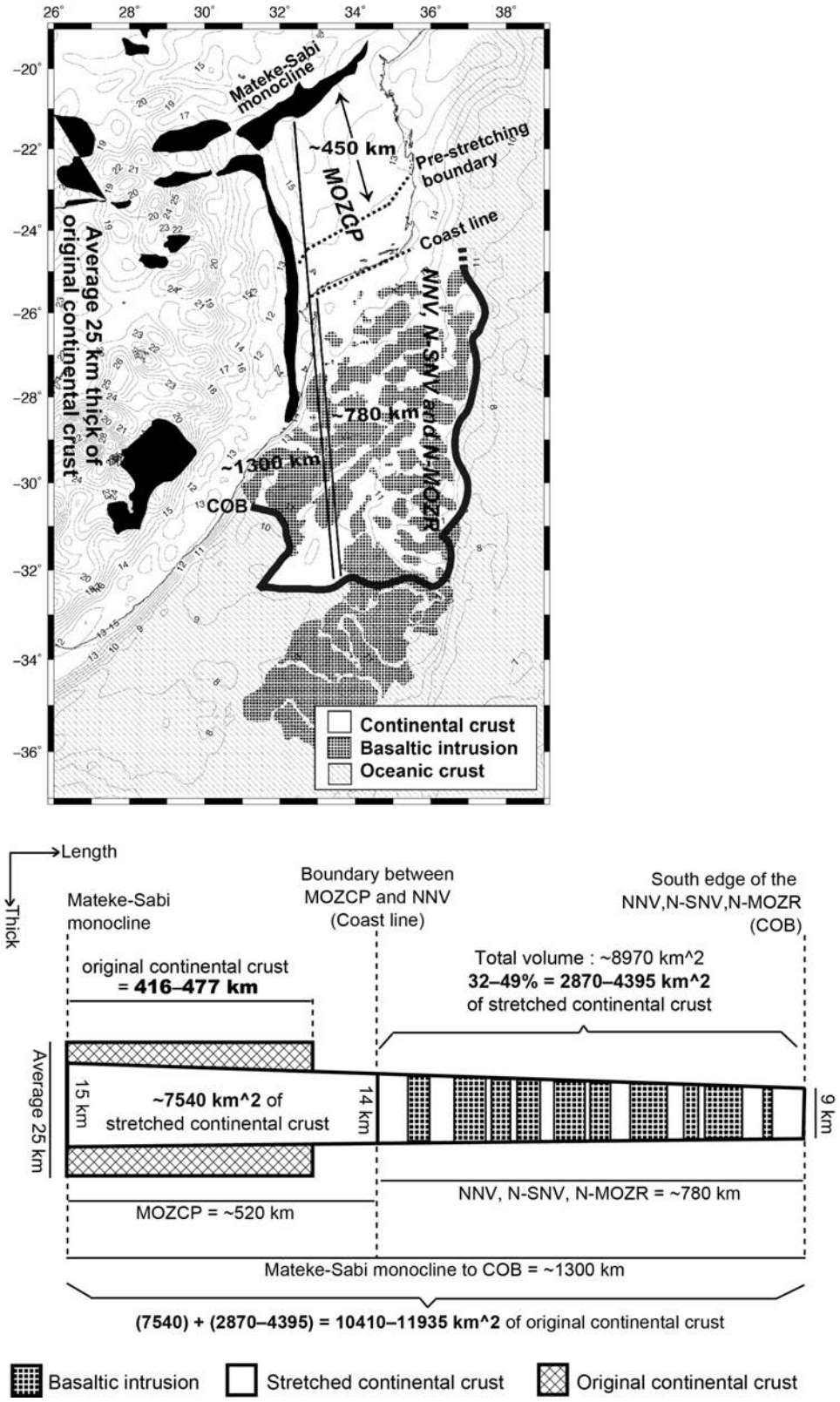

Fig. 2-10

Estimation of the areas of continental crust in the NNV, N-SNV, and N-MOZR. Abbreviations are the same as those used previously.

Fig. 2-11

a before 183 Ma

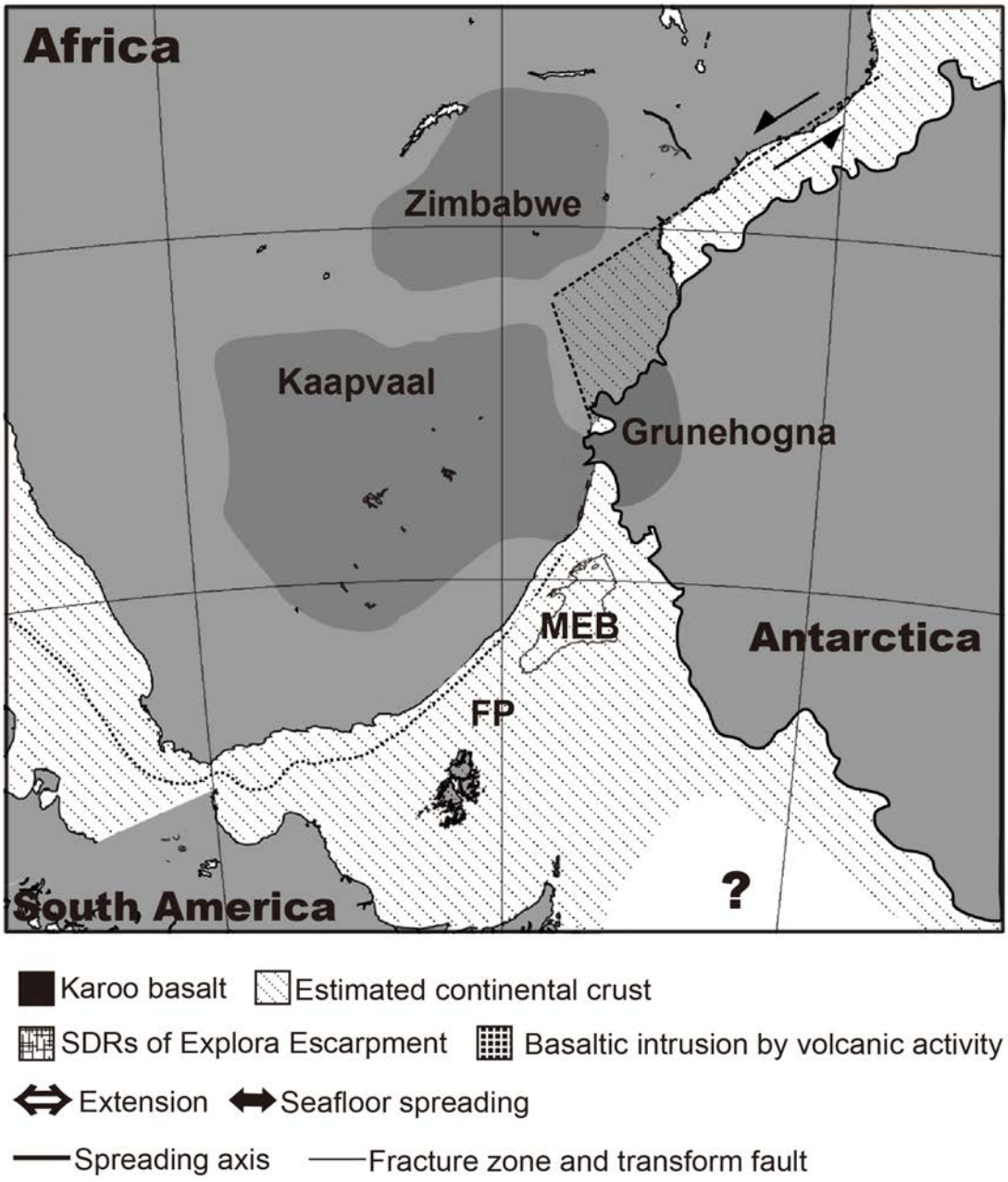

Fig. 2-11a

(continued)

Fig. 2-11

b 183 Ma

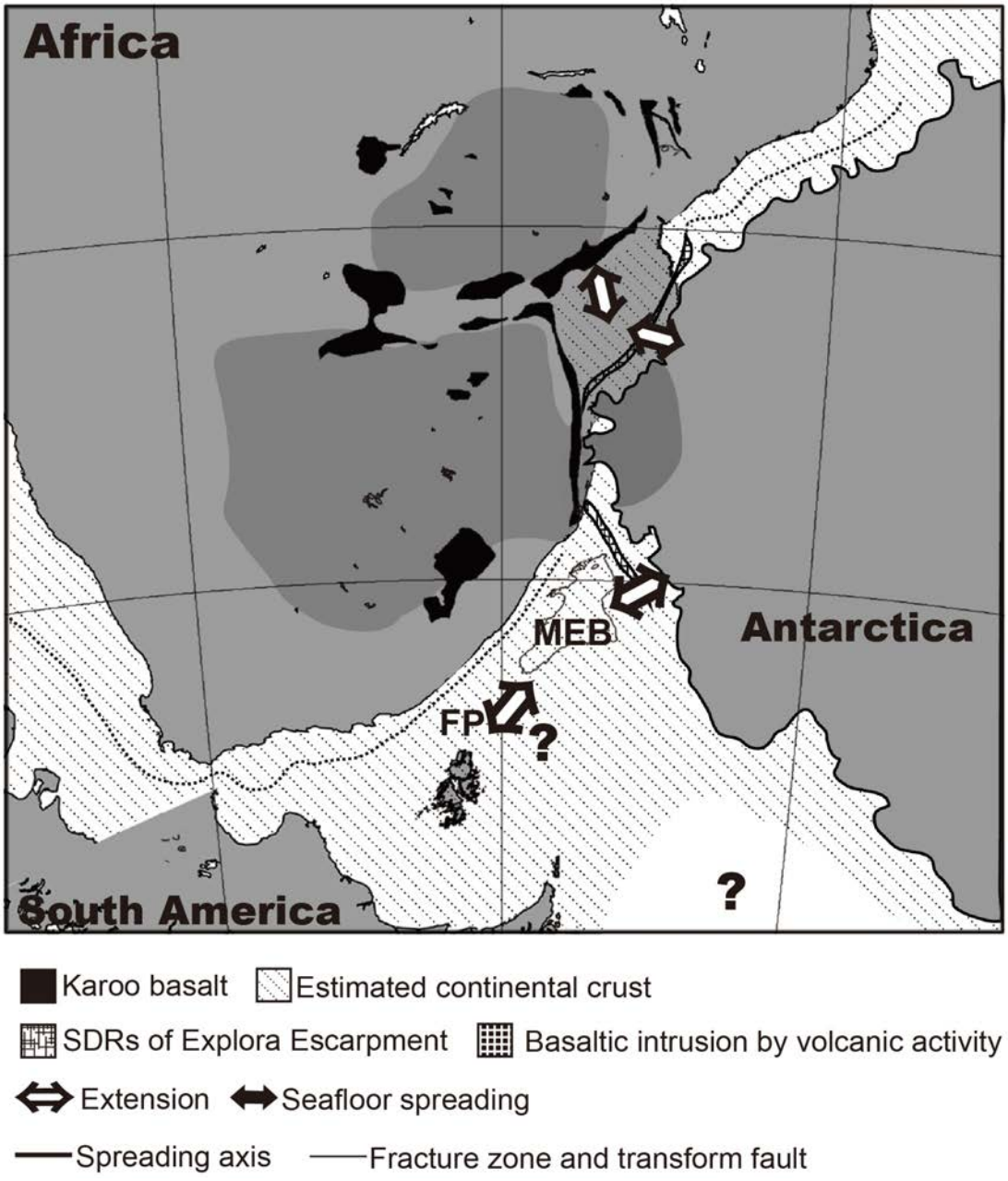

Fig. 2-11b

(continued)

Fig. 2-11

c 160 Ma

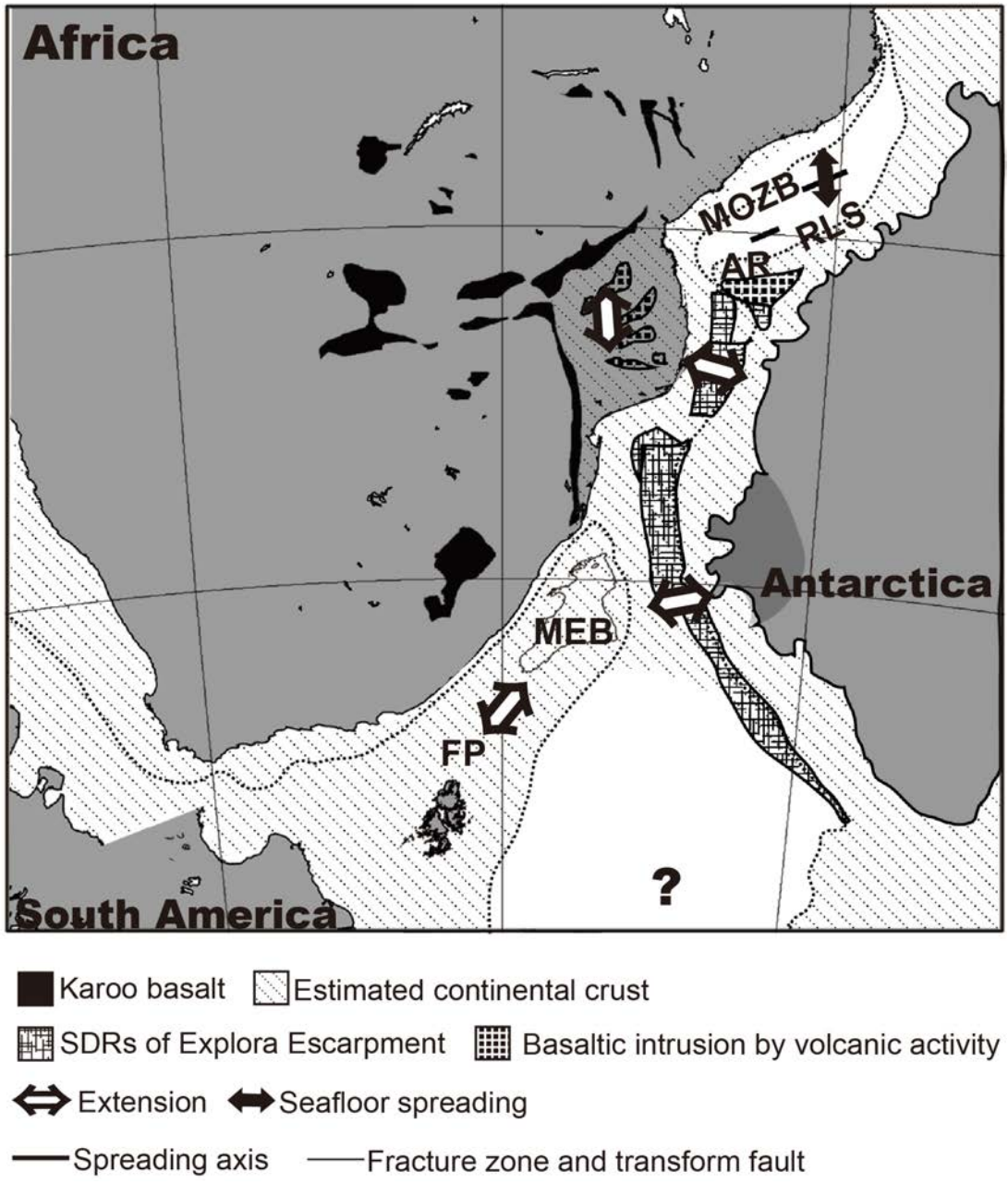

Fig. 2-11c

(continued)

Fig. 2-11

d 146 Ma

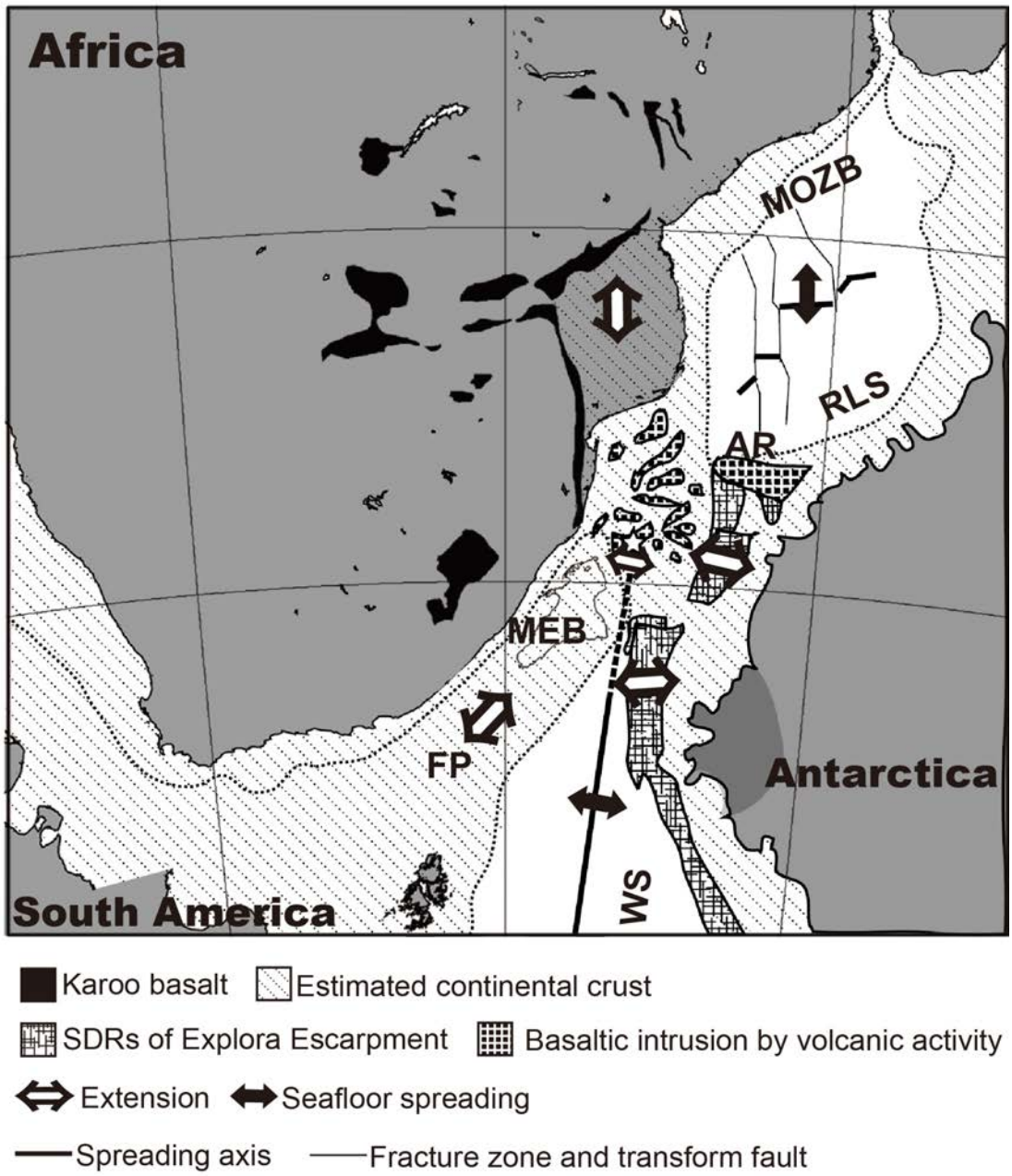

Fig. 2-11d

(continued)

Fig. 2-11

e 130 Ma

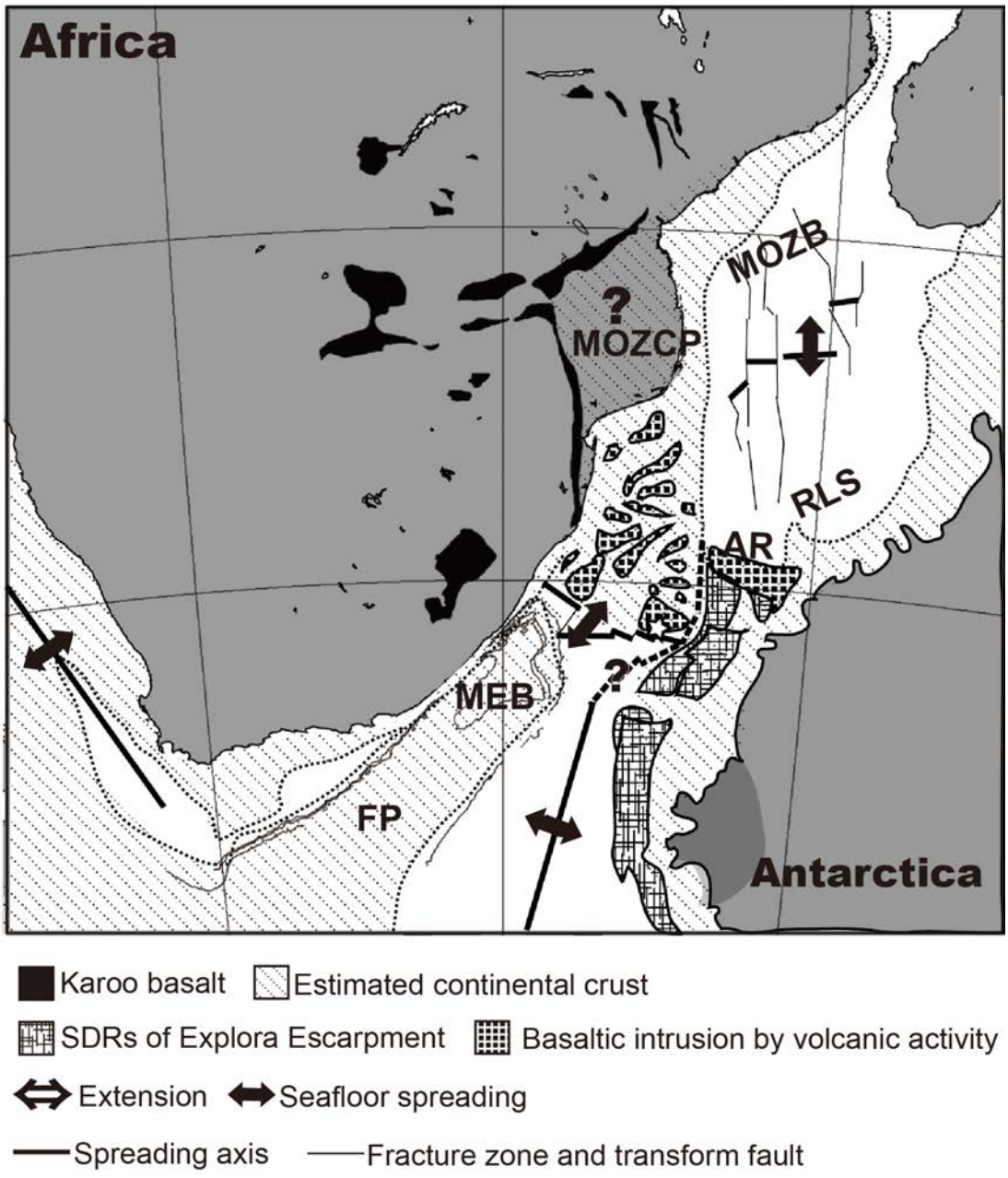

Fig. 2-11e

(continued)

Fig. 2-11

f 120 Ma

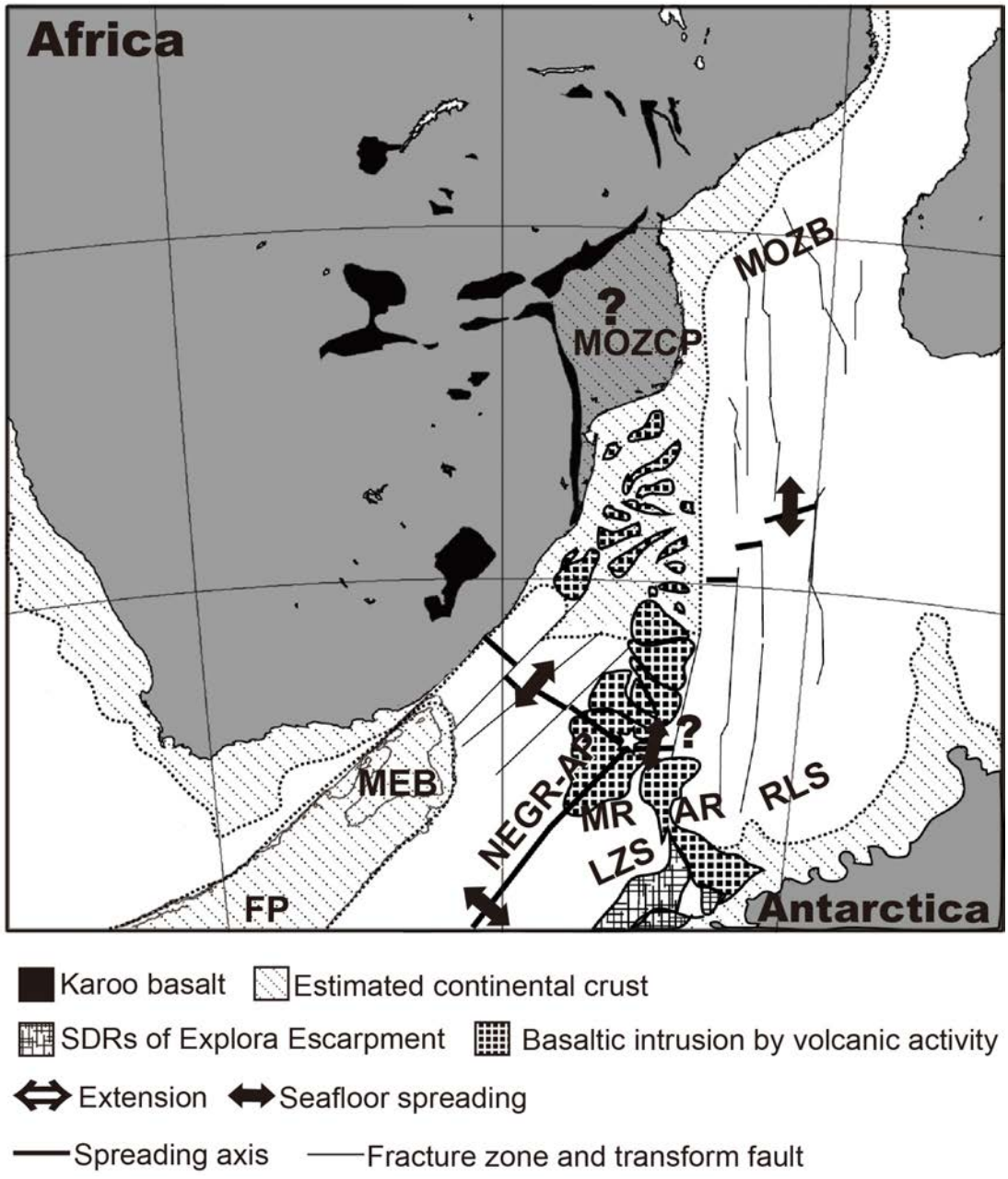

Fig. 2-11f

(**continued**)

Fig. 2-11

(a)–(f) Break-up and evolution processes around the Natal Valley and Mozambique Ridge. Positions of South America and Antarctica by each age are located based on the model of Leinweber and Jokat (2012). Precambrian cratons (dark gray areas), the COB (dashed line), and the hotspot (star) are shown. Seafloor-dipping reflectors of Explora Escarpment (Hinz et al, 2004) are also shown. SDRs; Seafloor-dipping reflectors, MEB, Maurice Ewing Bank; FP, Falkland Plateau; AR, Astrid Ridge; MOZB, Mozambique Basin; RLS, Riiser-Larsen Sea; MOZCP, Mozambique Coastal Plain; LZS, Lazarev Sea; NEGR-AP, North East Georgia Rise and Agulhas Plateau; MR, Maud Rise.

Chapter 3. Seafloor spreading history of the Cosmonauts Sea, off East Antarctica

3.1 Introduction

3.1.1 Geological setting

Gondwana break-up and reconstruction models have been created by some authors using geophysical data sets (e.g., Lawer et al., 1992; Royer and Coffin, 1992; Eagles and König, 2008; Seton et al., 2012). However, the early tectonic history of the Southern Indian Ocean remains unsolved, because of sparse marine geophysical data around Antarctica. The Cosmonauts Sea (Fig. 3-1a), located on the continental margin of East Antarctica, is a key area for investigating the initial break-up history of Gondwana between Antarctica and Sri Lanka/India (e.g., Talwani et al., 2016). There are three theories for the genesis of the Cosmonauts Sea: (1) seafloor spreading in the Mesozoic Era, with the oldest identified magnetic isochrons beginning at chron M11 (135.7 Ma) (Ramana et al., 2001; Desa et al., 2006) or M9 (132.8 Ma) (Gaina et al., 2007); (2) seafloor spreading during the Cretaceous Normal Superchron (CNS; 124.6–84 Ma) (e.g., Jokat et al., 2010); or (3) wide-spreading of the continent–ocean transition zone (COTZ) (e.g., Ritzwoller et al., 2001; Baranov and Morelli, 2013). As mentioned above, the seafloor spreading history of the Cosmonauts Sea has not yet been revealed because the magnetic isochrons proposed in previous studies were identified based only on a sparse marine geophysical data set. In this study, I reveal the formation process and seafloor spreading history of the Cosmonauts Sea using systematic vector geomagnetic data obtained during Japanese Antarctic Research Expedition (JARE) surveys.

3.1.2 Theories for the formation process of the Cosmonauts Sea

Before the 21st century, no magnetic isochrons had been identified in the Enderby Basin. The seafloor spreading direction in the Enderby Basin was only constrained by the SSE–NNW-oriented fracture zones observed in the gravity anomalies, and the timing of seafloor spreading between Antarctica and Sri Lanka/India was constrained by other means, such as the age determination of volcanic rocks obtained from onshore in Eastern India and from the southern Kerguelen Plateau (e.g., Lawer et al., 1992; Royer

and Coffin, 1992).

Subsequently, the initial break-up between India and Antarctica has been suggested to have occurred prior to M11, based on the identified magnetic isochrones M11–M0 (135.7 Ma–124.6 Ma) in the Bay of Bengal (half spreading rate of 34–36 mm/yr; Ramana et al., 1994) and the Cosmonauts Sea (Ramana et al., 2001). In addition, the magnetic isochrons M11–M0 (135.7–124.6 Ma), with several smaller segments and a half spreading rate of 15–55 mm/yr or 22–36 mm/yr, were identified in the south of Sri Lanka (Desa et al., 2006; Gaina et al., 2007). Those authors proposed that the seafloor spreading changed direction from NNW–SSE and NW–SE to N–S during M0–C34 (CNS; 84–124.6 Ma) based on the orientations of fracture zones. These identified magnetic isochrons served as new constraints for plate reconstruction models between Antarctica and Sri Lanka/India. However, the identification of the magnetic isochrons M11–M0 in the Cosmonauts Sea was based on only one observation line (Ramana et al., 2001). Gaina et al. (2007) identified the anomalies M9–M2 (132.8–127.6 Ma) caused by an extinct spreading ridge in the central Enderby Basin based on seismic and geomagnetic data. Chron M9 in the Cosmonauts Sea was identified based on only one observation line, which was also used in the identification by Ramana et al. (2001). They also suggested the presence of a wide-spreading COTZ in the south of chron M9. Consequently, different formation ages were proposed based on the same data set.

In contrast, Jokat et al. (2010) suggested that the formation of the Cosmonauts Sea may have occurred during the CNS (124.6–84 Ma), based on airborne geomagnetic anomalies, and the spreading direction was inferred as slightly oblique to the continental shelf, although they mentioned the results of Nogi et al. (1996) suggesting that the ESE–WNW or SE–NW magnetic boundary strikes may have been produced by seafloor spreading during the M-sequence based on vector geomagnetic data. They interpreted that the broad positive anomaly just north of a strong negative anomaly around 68°S/39°E–66°S/45°E was a part of the COTZ or represented chron M1n (125.0 Ma). They proposed that the break-up process between Antarctica and India started in the east and propagated towards the Gunnerus Ridge. However, the existing geophysical data set did not support their hypothesis (Ramana et al., 2001; Gaina et al., 2007), especially because no deep seismic data existed to constrain the onset of oceanic crust formation in the Cosmonauts Sea.

Meanwhile, wide spreading COTZ around the Enderby Land (Fig. 3-1a) was

proposed based on seismic studies. Based on the surface wave group and phase velocity measurement for a wide area (Ritzwoller et al., 2001), a 20–30-km thick crust, intermediate in thickness between that of typical oceanic crust (~6 km) and the crust of East Antarctica (30–50 km), was observed in the Cosmonauts Sea (Fig. 3-1b), which suggested that the crustal structure beneath the Cosmonauts Sea reflects continent–ocean transitional features. In addition, the Antarctic Moho model was constructed by merging information from all the seismic data and regional/global models (Baranov and Morelli, 2013), and a Moho depth of over 16 km was observed around 67–66°S in the Cosmonauts Sea. Potential field modeling was constructed using seismic refraction and reflection survey data from the Enderby Basin (Stagg et al., 2004), and implied that the continent–ocean boundary (COB) in the western Enderby Basin was located around 65°S.

An alternative kinematic reconstruction model between Antarctica and Sri Lanka/India was proposed by Eagles and König (2008). In their model, Sri Lanka was placed in the underlap east of Enderby Land with Elan Bank and part of the Kerguelen Plateau, although Sri Lanka is fixed in Lützow-Holm Bay in most of other models based on the geological studies. Because it is difficult to identify magnetic isochrons and fracture zones in the Bay of Bengal and Enderby Basin, India, Sri Lanka, and Madagascar's original position in Gondwana is not well constrained. Many recent reconstruction models have adopted the spreading theory of Ramana et al. (2001) or that of Gaina et al. (2007), which suggest that the almost N–S-oriented seafloor spreading in the Cosmonauts Sea occurred after M11 or M9 (e.g., Seton et al., 2012; Talwani et al., 2016). The direction and timing of the seafloor spreading in the Cosmonauts Sea remains a matter of speculation, because there is still a lack essential geomagnetic data.

3.2 Data and data processing

3.2.1 Geomagnetic survey

Systematic sea-surface vector geomagnetic data were acquired in the Cosmonauts Sea using a shipboard three-component magnetometer (STCM; Isezaki, 1986) aboard the Japanese icebreaker *Shirase* during the 54th JARE. Multibeam echo sounding data were also acquired. Four SE–NW survey lines were obtained. The total length of survey line was 1,096 km, with a line spacing of approximately 43 km. Sea-surface vector geomagnetic data sets were also acquired in the same region during other JARE expeditions, and were compiled for use in this study (Fig. 3-1b). Line numbers are allocated by each cruise number; for example, line 41L1.0001 was the first segment line of observation line 1 obtained in the JARE41 cruise. Diurnal variations of geomagnetic anomalies and the K-index were recorded at intervals of 1 second, using a fluxgate magnetometer at Syowa Station (Data Center for Aurora in NIPR: http://polaris.nipr.ac.jp/~aurora/). The 1-minute vector geomagnetic anomalies and K-index at Syowa Station were used to check for the occurrence of magnetic storms.

3.2.2 Analysis of vector geomagnetic anomalies

The vector geomagnetic field acquired during the 54th JARE was used to calculate vector geomagnetic anomalies by subtracting the 11th International Geomagnetic Reference Field (IGRF2010; International Associations of Geomagnetism and Aeronomy) using the same method described in Chapter 2.2.1 (Isezaki, 1986). The 'figure eight turn' was conducted seven times at different places during the 54th JARE (Table 3-1), and matrices related to the ship's permanent magnetic field ($\tilde{B}$) and the magnetic susceptibility of the ship (H_{pb}) were calculated using the least-squares method (Table 3-2). A large standard deviation was estimated. In fact, the calculated vector geomagnetic data of the entire JARE survey has a large trend, which depends on the *Shirase*'s heading direction (Fig. 3-2a). I assumed that the trend was linear, and subtracted this linear trend from the vector geomagnetic anomaly data of each line. After the correction, the total geomagnetic anomalies were calculated from the vector geomagnetic anomalies of each line.

I verified the influence of the ship's heading direction change on the observed magnetic fields. In general, the eastward component of a geomagnetic field is

geometrically related to its northward component. To minimize the influence of the ship's heading change, I selected observed data with a ship's heading change of less than three degrees (Fig. 3-2 b–e). I also regarded the data as influenced by magnetic storms when high K-index values were observed at Syowa Station (Fig. 3-2 b–e).

I corrected the total geomagnetic anomalies calculated from vector geomagnetic anomalies by subtracting the linear trend, which was deduced by comparing with total airborne geomagnetic anomalies (Fig. 3-2 b–e and Fig. 3-4 a–b).

3.2.3 Analysis of magnetic boundary strikes

The intensity of spatial differential vectors (ISDV) was calculated from the observed vector geomagnetic anomalies based on the same method described in Chapter 2.2.3 (Seama et al., 1993). The positions and directions of magnetic boundary strikes were estimated. In this study, ISDVs in the Cosmonauts Sea were classed into three types based on the results of simple two-dimensional magnetic structure models. Several models were applied to select the threshold levels of ISDV peaks. The thickness of the magnetization layer was assumed as 1 km, appropriate for oceanic crust. The mean top depth of the magnetization layer in the Cosmonauts Sea was estimated as 6 and 8 km, respectively, based on the ETOPO1 topographic data (Amante and Eakins, 2009), multibeam echo sounding data obtained by the JARE cruise, sediment thicknesses from the global sediment thickness model (Laske and Masters, 1997), and seismic reflection data (e.g., Stagg et al., 2004). In general, the magnetization intensity of oceanic crust is $> \pm 5$ A/m (e.g., McKenzie and Sclater, 1971); therefore, I assumed ± 5 A/m of magnetized bodies for the magnetic polarity boundary model (Fig. 3-3d). Taking into account some effects of decreased magnetization intensity in older crust (e.g., decreasing geomagnetic anomaly amplitude in the Cretaceous to Jurassic; Cande et al., 1978), intensity higher than ± 3 A/m for magnetized bodies was assumed for the magnetic polarity boundary model related to seafloor spreading in the study area (Fig. 3-3c). I assumed that lower magnetization was not indicative of seafloor spreading (Fig. 3-3b). The effect of basement topography with the same polarity of magnetized bodies was considered using the assumption of 0.5 km offset in the topography (Fig. 3-3a). Finally, magnetic signatures from the ISDV were categorized into three types (Fig. 3-3 and Table 3-3): 1) high-magnetization contrast boundary (e.g., magnetic polarity boundary); 2) low-magnetization contrast boundary; and 3) topographic effects

only (i.e., consideration for topographic gaps of the magnetized block assuming the same polarity and layer thickness.) Types 1 and 2 of magnetic boundary strikes were selected for further examination.

Data affected by the influence of the ship's heading change and the influence of magnetic storms were excluded from the estimation of magnetic boundary strikes for each line (Fig. 3-2).

3.2.4 Synthetic model

A two-dimensional magnetic structure model of the M-sequence was constructed based on the method described in Chapter. 2.2.3 (Talwani, 1964). The magnetic polarity time scale of Gradstein et al. (2008) was used to confirm the anomaly identification. The thickness of the magnetization layer was assumed as 0.5 km. The geomagnetic profile of observation line 0005 was considered as the key profile, because the surface geometry of the magnetization layer was assumed using multibeam echo sounding data, ETOPO1 topographic data, and sediment thicknesses from the global sediment thickness model on the observation line 0005. Magnetized body inclinations of the geocentric axial dipole were set to −77.45°.

3.3 Results

3.3.1 Geomagnetic anomalies

The calculated northward (x), eastward (y), and downward (z) components of geomagnetic anomalies and wiggles of the corrected total geomagnetic anomalies during the JARE54 cruise are shown in Figs. 3-2 and 3-4a, respectively. The influence of heading change of more than five degrees was observed, especially in the eastward component with short (15–60 min) intervals (Orange box; Fig. 3-2). The influence of a heading change of about three degrees was also observed in the east and north components with short (15–60 min) intervals (Orange dotted box; Fig. 3-2). The influence of magnetic storms on the data was also observed for each component of geomagnetic anomalies with long intervals (more than three hours) during times with high K-index values. Times with K-Index values > 5 were assumed as times when magnetic storms were occurring (Pink boxes; Fig. 3-2), and K-Index values of 3–4 were assumed to indicate geomagnetic disturbances (Pink dotted boxes; Fig. 3-2). During magnetic storms and geomagnetic disturbances, observed vector geomagnetic anomalies were disordered with short intervals (15–60 min). Thus, I have taken this concern into account in selecting data based on heading changes of 3 degrees and times of geomagnetic disturbance (Light blue boxes; Fig. 3-2).

Total corrected geomagnetic anomalies were obtained by subtracting the linear trend (Figs. 3-2 a–e). Crossover error correction was also performed by removing the linear trend for level adjustment, which was deduced by comparing with total airborne geomagnetic anomalies (Fig. 3-4a). The selected total geomagnetic anomalies (Fig. 3-4b) are concordant with total airborne geomagnetic anomalies, which have previously been collected in this study region. Short wavelengths of total geomagnetic anomalies were observed between observation lines of total airborne geomagnetic anomalies. Amplitudes of total geomagnetic anomalies in the Cosmonauts Sea were within ± 200 nT for the most part. The wavelength of the total geomagnetic anomaly profiles was almost within 50 km. The amplitude of a geomagnetic anomaly of approximately +300 nT was observed around 66°S/38.5°E on observation line 0003. Low-amplitude anomalies of about ± 120 nT were observed on the observation lines 0001, 32L5.003, 41L1.0064, 41L1.0074, 41L1.0073, 40L4.0021, 34L2.170, and 34L2.171, and southeast of 65.8°S/40.5°E on observation line 0007. The WSW–

ENE-trending pattern of geomagnetic anomalies was observed around the area of 66.4°S, 40.5°E–65.2S, 37°E (Fig. 3-4b).

3.3.2 Magnetic boundary strikes

Magnetic boundary strikes were calculated in the study area (Figs. 3-2 and 3-4c). They occur together with high magnetization contrasts (Type 1), low magnetization contrasts (Type 2), and topographic variation (Type 3) (e.g., Seama et al., 1993). The thresholds for the ISDV peaks were defined for each region (Fig. 3-4d) based on the mean surface depth of the magnetization layer estimated based on the ETOPO1 topographic data and the global sediment thickness model (Table 3-3 and Fig. 3-3). A value of 20 nT/km was assumed as the threshold for the boundary of magnetization contrast or topographic effects for 6 km depth of the magnetization layer, and 10 nT/km was assumed as the threshold for the boundary of magnetization contrast or topographic effects for 8 km depth of the magnetization layer. Based on the thresholds for the ISDV peak and the estimation of the influence of ship's heading change and of magnetic storms (Green boxes; Fig. 3-2), the magnetic boundary strikes indicating a 'high or low magnetization contrast' and 'topographic effect' were selected (Fig. 3-4d). Three-dimensional magnetic boundary strikes are excluded from identifying the magnetic isochrons.

The WSW–ENE-oriented magnetic boundary strikes of type 1 dominated in 66.4°S, 40.5°E–65.2°S, 37°E (area A, Fig. 3-4d) on lines 0001–0007. Magnetic boundary strikes in the south and east of area A did not show a dominant direction, including on line 0001. In addition, most of the magnetic boundary strikes in the south and east of area A showed topographic variation. The WSW–ENE-oriented magnetic boundary strikes of type 3 were observed in the northeast of area A, on lines 34L2.170 and 34L2.171, whereas in the northwest of 65.2°S, 39.5°E, the orientation of the magnetic boundary strikes changed from WSW–ENE to W–E or ESE–WNW. The dominant orientations of the magnetic boundary strikes in this study coincided well with those of obtained by Nogi et al. (1996) in each area.

3.3.3 Synthetic model

Synthetic magnetic anomalies were calculated along observation profiles based on a two-dimensional magnetic structure model in which the Mesozoic global geomagnetic

reversal timescale of Gradstein et al., (2008) was used (Fig. 3-5). The two stages of seafloor spreading during the M-sequence and the CNS were introduced in the central Enderby Basin, Bay of Bengal, and south of Sri Lanka between Antarctica and India/Sri Lanka (e.g., Ramana et al., 2001; Gaina et al., 2007); therefore, I have also taken into account seafloor spreading during the M-sequence in this region. The possibility of seafloor spreading during the CNS in this region was excluded because the magnetic boundary strikes indicated a high magnetization contrast along the observation lines 0003–0007. In addition, the possibility of an extinct spreading center in this region was excluded because the seafloor topography becomes gradually deeper farther from the continental shelf. I also estimate several models including the M-sequence with considering other possibilities. The model profile of the M-sequence was most concordant to the observation profile; therefore I adopt the M-sequence for model calculation.

I identified the magnetic isochrons M10N–M3n on the observation lines 0003–0007 based on the geomagnetic anomaly profiles and magnetic boundary strikes (Fig. 3-5a and 3-5b). The almost ESE–WNW-oriented spreading direction slightly oblique to the continental shelf was detected based on the magnetic boundary strikes. The half spreading rate along these lines was estimated as follows: line 0003, half spreading rate of 30.5 mm/yr with a ESE–WNW direction; line 0005, half spreading rate of 26.2 mm/yr with a NW–SE direction; and line 0007, half spreading rate of 26.4 mm/yr with a ESE–WNW direction (Fig. 3-5c).

3.4 Discussion

In this section, an evaluation of structure boundaries based on the free-air gravity anomalies and the vertical gravity gradient (VGG) of Sandwell et al. (2014) is provided. The VGG was calculated directly from the derivations of the vertical deflection grids. The geoid height is related to the gravitational potential:

$$N(\mathbf{x}) \cong \frac{1}{g_0} V(\mathbf{x}, 0)$$

where $\mathbf{x}(x, y)$ is the coordinates, g_0 is the average acceleration of gravity (9.81 m/s^2), $N(\mathbf{x})$ is the geoid height, and $V(\mathbf{x}, 0)$ is gravitational potential. The gravity anomaly is the vertical derivation of the potential; therefore, the gravity anomaly is described as:

$$\Delta g(\mathbf{x}) = -\frac{\partial V(\mathbf{x},0)}{\partial z}.$$

The east and north components of vertical deflection, defined by $\eta(\mathbf{x})$ and $\xi(\mathbf{x})$, are the slope of the geoid in the x and y directions, respectively:

$$\eta(\mathbf{x}) \equiv -\frac{\partial N}{\partial y} \cong -\frac{1}{g_0}\frac{\partial V}{\partial y}$$

$$\xi(\mathbf{x}) \equiv -\frac{\partial N}{\partial z} \cong -\frac{1}{g_0}\frac{\partial V}{\partial z}.$$

Laplace's equation can be arranged using these equations:

$$\frac{\partial^2 V}{\partial x^2} + \frac{\partial^2 V}{\partial y^2} + \frac{\partial^2 V}{\partial z^2} = 0$$

$$\frac{\partial^2 V}{\partial z^2} = -\left(\frac{\partial^2 V}{\partial x^2} + \frac{\partial^2 V}{\partial y^2}\right)$$

$$\frac{\partial \Delta g}{\partial z} = -g_0 \left(\frac{\partial \eta}{\partial x} + \frac{\partial \xi}{\partial y} \right). \qquad (13)$$

Equation (13) is used to calculate the vertical gravity gradient from the grids of the east and north vertical deflection. The vertical gravity gradient will be zero at the structure boundary, and makes it easier to detect structure boundaries such as the fracture zone than based on the free-air gravity anomalies alone.

3.4.1 Comparison with previous studies

I propose that the SE–NW-oriented seafloor spreading in the Cosmonauts Sea began at about chron M10N (134.3 Ma), based on the total geomagnetic anomaly profiles and magnetic boundary strikes (Fig. 3-5a and 3-5b). The magnetic isochrons of M10N–M3n in 66.4°S/40.5°E–65.2°S/37°E (area A) are newly identified.

The WSW–ENE-oriented magnetic boundary strikes did not support the spreading direction proposed by Ramana et al. (2001) and Gaina et al. (2007). The initiation process of the seafloor spreading in the Cosmonauts Sea proposed in the previous studies were constrained only by the SSW–NNE-oriented fracture zones. However, the signature of the SSW–NNE-oriented fracture zones was terminated at 65°S, and SE–NW-oriented structures appeared south of 65°S, based on the gravity anomalies and the VGG (Sandwell et al., 2014; Fig. 3-6). The ESE–WNW-oriented structures south of 65°S and the SSW–NNE-oriented fracture zones north of 65°S likely indicate a change in spreading direction at around 65°S.

Jokat et al. (2010) interpreted that the 67.7°S, 39°E–65.3°S, 45°E area within 200 nT of geomagnetic anomalies represented continent–ocean transition or chron M1n. They inferred that the northwest part of the 67.7°S, 39°E–65.3°S, 45°E (area B; Fig. 3-7) area either formed during the Cretaceous Normal Superchron, or perhaps was a continent–ocean transition zone. However, our results show a positive and negative geomagnetic anomaly pattern with up to 300 nT in area A, which is northwest of area B. In area A, bathymetric profiles gradually deepen from southeast to northwest, and there is no signature of intense volcanic activities based on the multibeam echo sounding data and gravity anomalies. Additionally, the WSW–ENE-oriented magnetic boundary strikes in area A, where the surface depth of the magnetization layer was about 7,000 m, indicate

the boundary between normal and reversed magnetized structures. Therefore, the observed geomagnetic anomalies and magnetic boundary strikes are not explained by magnetically quiet seafloor spreading during the Cretaceous Normal Superchron. M-sequence magnetic isochrons were proposed for the Bay of Bengal (e.g., Ramana et al., 1994), the central Enderby Basin (Gaina et al., 2003), and south of Sri Lanka (Desa et al., 2006). Thus, I suggest that the seafloor spreading of the Cosmonauts Sea also occurred during the M-sequence age.

The model profile of M10N-M3r, which was calculated using a two-dimensional magnetic structures model, was well concordant with observation profiles of line 0005. Magnetic isochrons M8–M3r were observed on line 0003, and magnetic isochrons M5r–M3n were observed on line 0007. I did not detect magnetic boundary strikes indicating a magnetic polarity change on line 0001 and line 34L2.171–172. The half spreading rate was estimated as about 27–31 mm/yr (Fig. 3-5c).

I estimated that there were several smaller segments in the Cosmonauts Sea. Offsets between each observation line likely show this segmentation (Fig. 3-5a). A few SE–NW magnetic boundary strikes likely indicate the segmentation boundaries (Fig. 3-5b), those were similar to the segmentation boundary appeared on present mid-ocean ridge. Several smaller segments were also observed at the conjugate margin, such as the Bay of Bengal and south of Sri Lanka (e.g., Desa et al., 2006). Our results are concordant with the segmentation at the conjugate margins. Additionally, the ESE–WNW structural trend was also observed in the gravity anomalies and the VGG (Fig. 3-6), and likely represents the smaller segmentation in the Cosmonauts Sea. The discontinuities of isochrons after M5n on line 0003 may have caused by the segmentation boundary near the observation line. I concluded that the ESE–WNW-oriented seafloor spreading with a half spreading rate of 27–31 mm/yr occurred with smaller segmentation in the 66.4°S, 40.5°E–65.2°S, 37°E area (area A; Fig. 3-7a) of the Cosmonauts Sea. In the northwest of observation lines 0001–0007, a V-shaped structure of positive geomagnetic anomalies of up to 200 nT (area C; Fig. 3-7b) and a small structure of negative geomagnetic anomalies of about 150 nT (area D; Fig. 3-7b) were observed in the total airborne geomagnetic anomalies. Based on my results, areas C and D may show M3n–M1n and M0r, and the distorted shape of M3n–M1n and M0r may represent the change in spreading direction during M3n–M0r.

I propose that there is wide spreading stretched continental crust beneath the

Cosmonauts Sea. I observed several magnetic boundary strikes indicating the boundary of high-contrast magnetization along the southern edge of areas B1 and B2 (Fig. 3-7b), which represent the continental shelf (Jokat et al., 2010). The initiation of seafloor spreading likely occurred at about chron M10N. Topographic or gravity signatures implying magmatic activity were not observed between the continental shelf and the location identified as chron M10N in area B2. The continent–ocean transition zone (COTZ) around area B2 was inferred in previous studies (e.g., Jokat et al., 2010; Gaina et al., 2007). Based on the gravity study, Kitada (2008) interpreted the wide COTZ south of around 67°S as the cause of steeply decreased crustal thickness from 30 km of the continental shelf to 8 km, around 67°S. In contrast, my results demonstrate that the COB is located at about 66°S. The relief of crustal thickness noted by Kitada (2008) is similar to the bathymetric relief. The global sediment thickness model (Laske and Masters, 1997) was applied in his estimation of the COTZ. Because the seismic data are poor in the Antarctic region, global sediment thickness model around Antarctica are estimated using gravity constraints. I considered that the effect of the sediment layer may remain in Kitada's estimation. The sediment thickness based on the recent seismic reflection data in this area was demonstrated to be more than 2 km thicker than that from the global sediment thickness model (Hochmuth et al., 2017). For the reasons mentioned above, the actual sediment thickness in the Cosmonauts Sea is still unclear. The magnetic boundary strikes, indicating only the topographic effect, are observed in areas B1 and B2. These magnetic boundary strikes represented that the B1 and B2 is not oceanic crust. Thus, I concluded the boundary between areas A and B indicates the COB based on the magnetic boundary strikes (Fig. 3-7b). The crustal thickness is likely decreased from the continental shelf seaward. In addition, 20-km-thick crust was observed southeast of the Cosmonauts Sea based on the seismic studies (e.g., Baranov and Morelli, 2013). The intermediate crustal thickness between continental and oceanic crust likely represents thinned continental crust in areas B1 and B2. The biased to normal geomagnetic anomalies of up to 200 nT in areas B1 and B2 likely represent the magnetization contrast of different types of crust, such as the edge effect (Fig. 3-7b). Thus, I suggest that there is thinned continental crust in areas B1 and B2, which likely stretched during the pre-spreading of the initial break-up. The VGG (Fig. 3–6) showed the ESE–WNW-oriented trend of the structure boundary around 66°S, 43°E–66.5°S, 36°E and the SSW–NNE trend of that south of 66.5°S. These trends likely

indicate the stretching direction.

3.4.2 Seafloor spreading history of the Cosmonauts Sea

I propose a four-stage model of the break-up process between Antarctica and Sri Lanka/India (Fig. 3-8) and the position of the COB in the Cosmonauts Sea, likely along area A (Fig. 7).

The first stage is the initiation of the break-up. I interpret that the initiation of seafloor spreading likely occurred as continental extension, because there was no signature of volcanism around chron M10N based on the magnetic boundary strikes. Gaina et al. (2007) also inferred that the break-up of central Gondwana was triggered by passive rifting driven by change in plate driving forces, not active rifting driven by mantle upwelling. The continental crust in areas B1 and B2 was stretched during this pre-seafloor spreading stage.

In the second stage, ESE–WNW-oriented seafloor spreading occurred during chron M10N–M3n. Smaller segments were likely formed because of the continental extension, and seafloor spreading occurred slightly obliquely to the continental shelf. South of Sri Lanka and the Bay of Bengal, NNW–SSE-oriented smaller segments were also observed (e.g., Ramana et al., 1994). The most recent reconstruction models proposed SSW–NNE-oriented seafloor spreading between the Cosmonauts Sea and south of Sri Lanka, although Eagles and König (2008) proposed a new fit position for Sri Lanka into the underlap east of the Enderby Land, because it is difficult to identify magnetic isochrons and fracture zones. Our results represent the ESE–WNW direction of seafloor spreading between the Cosmonauts Sea and south of Sri Lanka. Re-examining the magnetic isochrons and fracture zones south of Sri Lanka and the Bay of Bengal is necessary to understand the detailed seafloor spreading history between Antarctica and Sri Lanka/India.

In the third stage, the direction of seafloor spreading in the Cosmonauts Sea changed from ESE–WNW to SSW–NNE during chrons M3n–M0r. This change also occurred south of Sri Lanka, in the Bay of Bengal, and at the western margin of Australia at around M0 (e.g., Gibbons et al., 2012; Desa and Ramana, 2016).

In the final stage, SSW–NNE-oriented seafloor spreading began at about 120 Ma (chron M0). There is no clear pattern of the positive and negative geomagnetic anomalies in the north of 65°S because the seafloor likely formed during the CNS

period. The SSW–NNE-oriented fracture zones are only constrained for the direction of seafloor spreading during the CNS.

Based on this model, I propose reinterpretation of the Kainan-Maru Seamount (G1; Fig. 3-8), which was considered part of the Gunnerus Ridge, as continental crust. The Kainan-Maru Seamount was divided from the main part of the Gunnerus Ridge. I suggest that the SE–NW-directed continental extension and seafloor spreading moved the Kainan-Maru Seamount from the continental shelf to its present position. The change in spreading direction during M3n–M0r produced the tilt of the Kainan-Maru Seamount. Because of this deformation, the Kainan-Maru Seamount became part of Gunnerus Ridge in appearance. This replacement and deformation process of Kainan-Maru Seamount is only speculation; additional observation, such as rock sampling, will be necessary to understand the origin and formation process of the Gunnerus Ridge.

The previous Gondwana reconstruction models (e.g., Seton et al., 2012) assumed N–S seafloor spreading for the Cosmonauts Sea. However, my results indicating ESE–WNW-oriented seafloor spreading in the Cosmonauts Sea newly constrain the Gondwana reconstruction model, as well as the formation processes of conjugate areas such as south of Sri Lanka and the Bay of Bengal. The re-examination of the magnetic isochrons and fracture zones south of Sri Lanka and in the Bay of Bengal is necessary to investigate the break-up process of Gondwana in detail.

3.5 Summary of Chapter 3

I present new sea-surface vector geomagnetic anomalies in the Cosmonauts Sea. Multiple analytical results of systematic vector geomagnetic anomalies and satellite gravity data led to the following conclusions:

1. I newly propose that ESE–WNW-oriented seafloor spreading with several smaller segments occurred in the Cosmonauts Sea during M10N–M3n.
2. Thinned continental crust in the south and east of M10N–M3n was inferred based on magnetic boundary strikes. The large geomagnetic anomaly amplitude of about 200 nT in this region represents the edge effect between the continental and oceanic crust. The area of thinned continental crust differs from the previous interpretations of Gaina et al. (2007), Kitada (2008), and Jokat et al. (2010) based on gravity, seismic, and geomagnetic studies. The thick sedimentation may be the cause of this difference. I propose a new position for the continent–ocean boundary in the Cosmonauts Sea.
3. The spreading direction changed from ESE–WNW to SSW–NNE during M3n–M0r. Modern seafloor recording this spreading direction change is located around 65°S.
4. One possible explanation for the origin of the Kainan-Maru Seamount is proposed based on my results. The Kainan-Maru Seamount is where part of the Gunnerus Ridge may have been replaced from the continental shelf, based on the ESE–WNW-directed continental extension and seafloor spreading.

The newly proposed model described above is key for revealing the initial break-up of Gondwana. For further investigation, re-examination of the magnetic isochrons and fracture zones south of Sri Lanka and in the Bay of Bengal is necessary to understand the detailed seafloor spreading history between Antarctica and Sri Lanka/India.

Table 3-1

Location of the figure eight turns during the 54th JARE. *1: This distorted 'figure eight turn' was made without roll data from site 1; therefore, this data point was excluded from the calculation.

	Date	UTC	Latitude	Longitude
1[*1]	2012/12/1	10:17–10:37	37-38S	111-35E
2	2012/12/4	03:19–03:43	50-36S	110-04E
3	2013/2/22	04:34–04:52	66-02S	45-00E
4	2013/3/4	01:18–01:37	62-00S	90-01E
5	2013/3/7	14:10–14:31	62-21S	130-01E
6	2013/3/9	23:20–23:39	63-12S	149-15E
7	2013/3/12	06:06–06:24	55-57S	150-03E
8	2013/3/14	16:46–17:07	46-01S	152-00E

Table 3-2

Calculated matrix of $\tilde{B}$ and $\mathbf{H_{pb}}$ during the 54th JARE. Sum of SD = 12333.2

B (1,1)	**B (1,2)**	**B (1,3)**	**H (1,1)**	**SD**
0.749818	0.045451	0.081288	–6109	4485
B (2,1)	**B (2,2)**	**B (2,3)**	**H (2,1)**	**SD**
–0.000264	0.58318	–0.032464	5251	6620.5
B (3,1)	**B (3,2)**	**B (3,3)**	**H (3,1)**	**SD**
0.177022	0.003055	1.016641	3062	1227.7

Table 3-3

Classification of magnetic boundary strikes based on the threshold levels of intensity of spatial differential vectors (ISDV) peaks. Identified signatures for the Cosmonauts Sea were sorted based on simple two-dimensional magnetic structure models. The mean surface depth of magnetization layer was estimated using ETOPO1 topographic data (Amante and Eakins, 2009) and the global sedimentation thickness model (Laske and Masters, 1997).

Mean surface depth of magnetization layer	High magnetization contrast boundary (type 1)	Low magnetization contrast boundary (type 2)	Topographic effect (offset less than 0.5 km) (type 3)
6 km	ISDV > 30 nT/km	20 nT/km < ISDV < 30 nT/km	ISDV < 20 nT/km
8 km	ISDV > 30 nT/km	10 nT/km < ISDV < 20 nT/km	ISDV < 10 nT/km

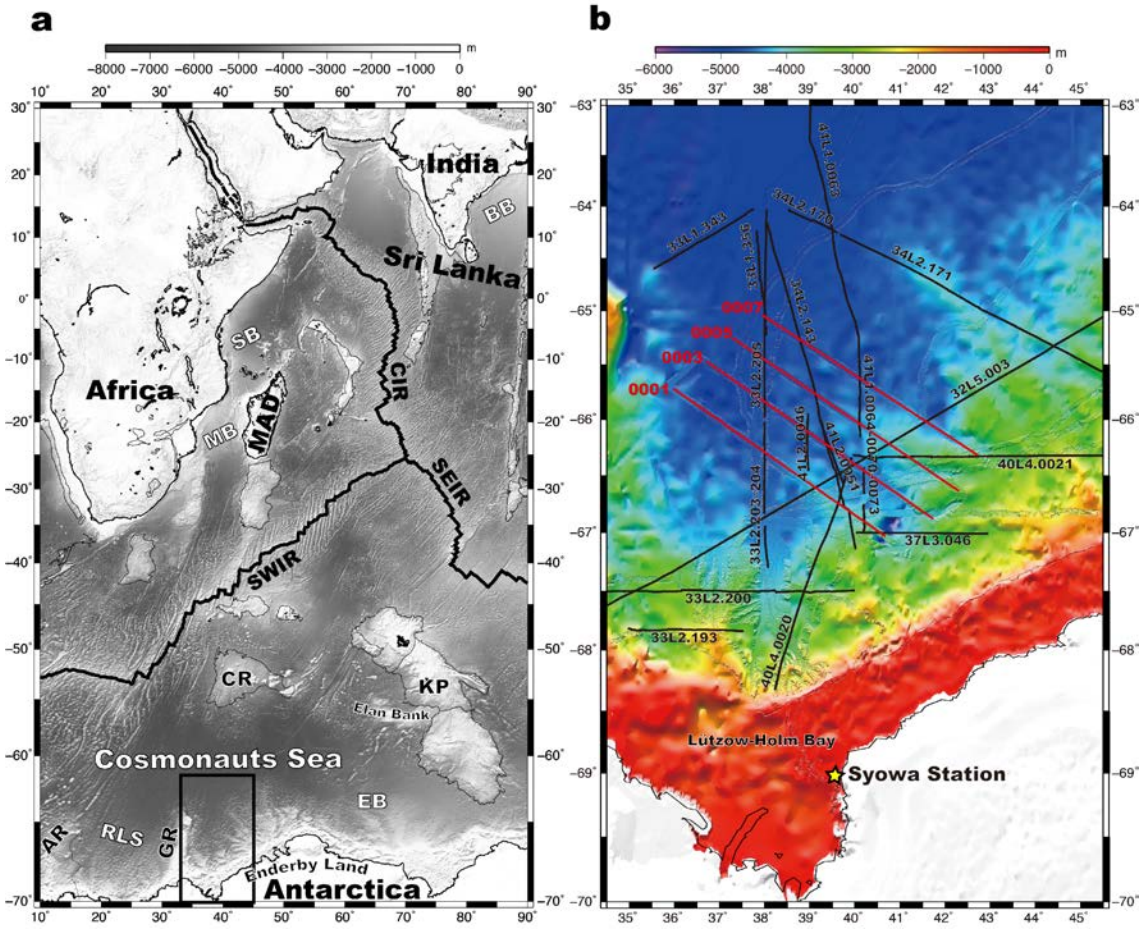

Fig. 3-1

(a) Overview of the study area (Cosmonauts Sea) and conjugate areas superimposed on a topographic map (ETOPO1). MAD, Madagascar; CIR, Central Indian Ridge; SWIR, Southwest Indian Ridge; SEIR, Southeast Indian Ridge; RLS, Riiser-Larsen Sea; EB, Enderby Basin; MB, Mozambique Basin; SB, Somali Basin; BB, Bay of Bengal; CR, Conrad Rise; KP, Kerguelen Plateau; AR, Astrid Ridge; GR, Gunnerus Ridge. (b) Observation lines superimposed on the topographic data. Red lines show the observation lines obtained on the JARE 54 cruise. Black lines show the observation lines obtained on other JARE cruises. The location of Syowa Station is shown as a star.

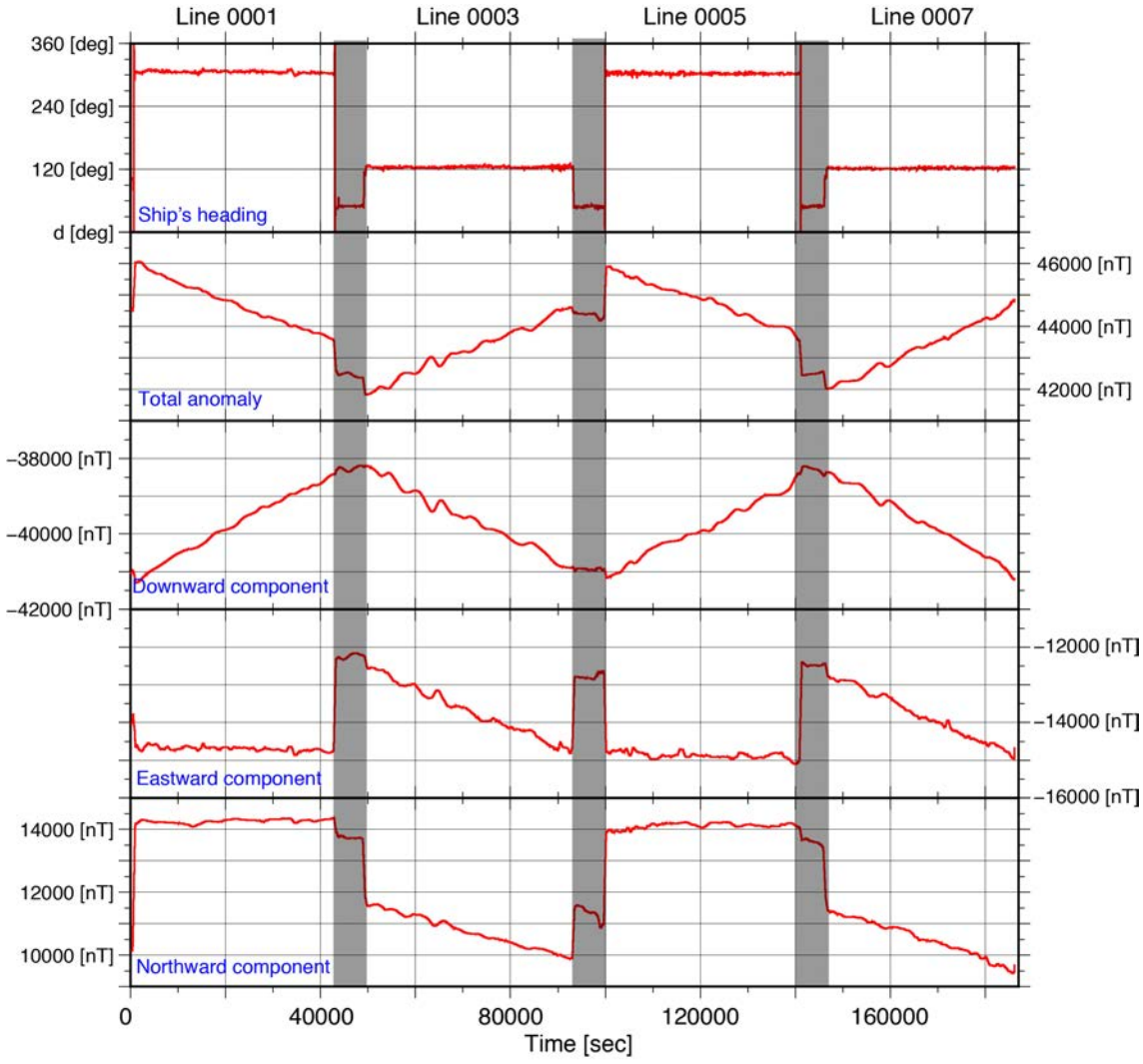
Line 0001
Line 0003
Line 0005
Line 0007
360 [deg]
240 [deg]
120 [deg]
d [deg]
Ship's heading
46000 [nT]
44000 [nT]
42000 [nT]
Total anomaly
−38000 [nT]
−40000 [nT]
−42000 [nT]
Downward component
−12000 [nT]
−14000 [nT]
−16000 [nT]
Eastward component
14000 [nT]
12000 [nT]
10000 [nT]
Northward component
0
40000
80000
120000
160000
Time [sec]

Fig. 3-2a

(continued)

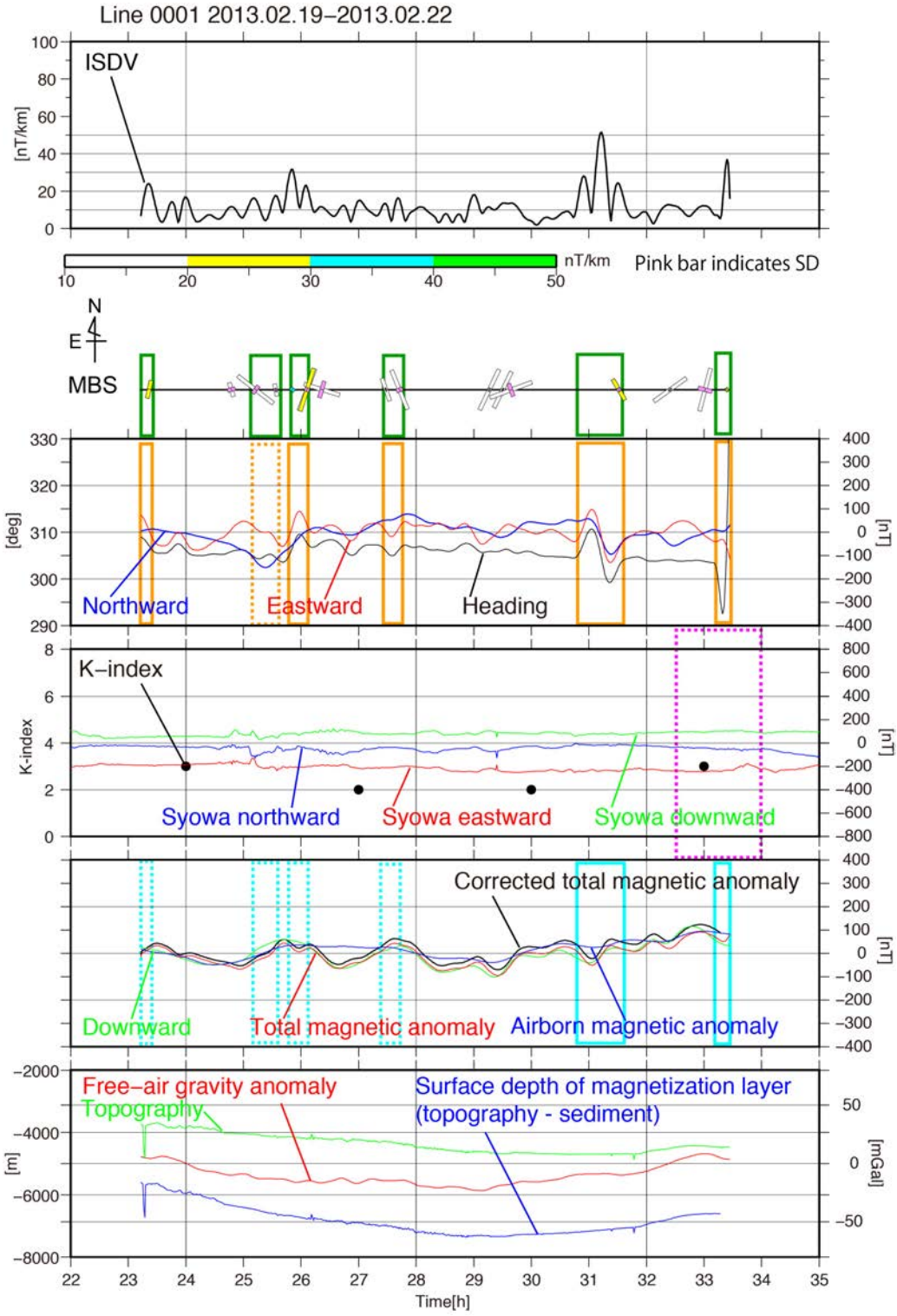

Fig. 3-2b

(continued)

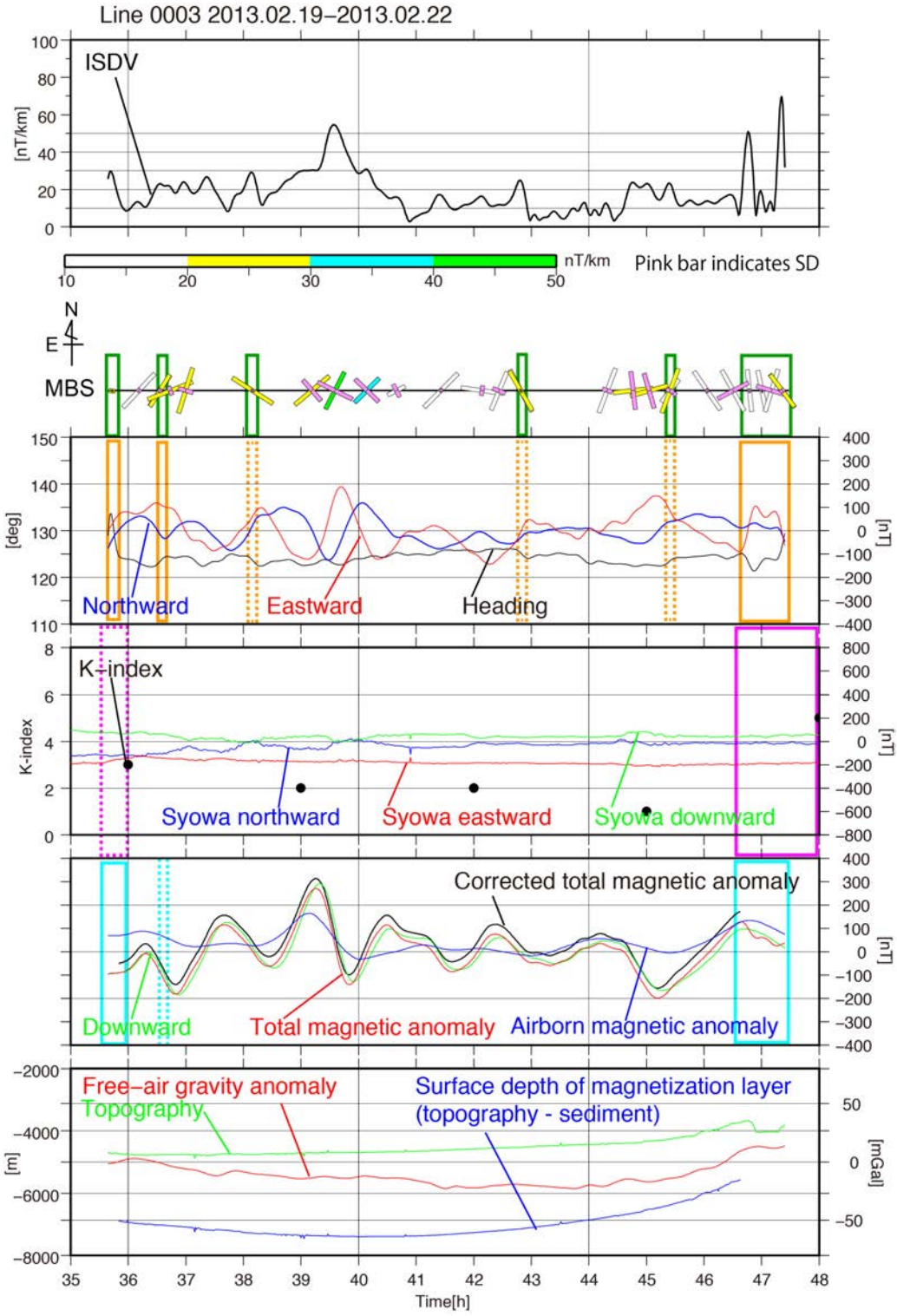

Fig. 3-2c

(continued)

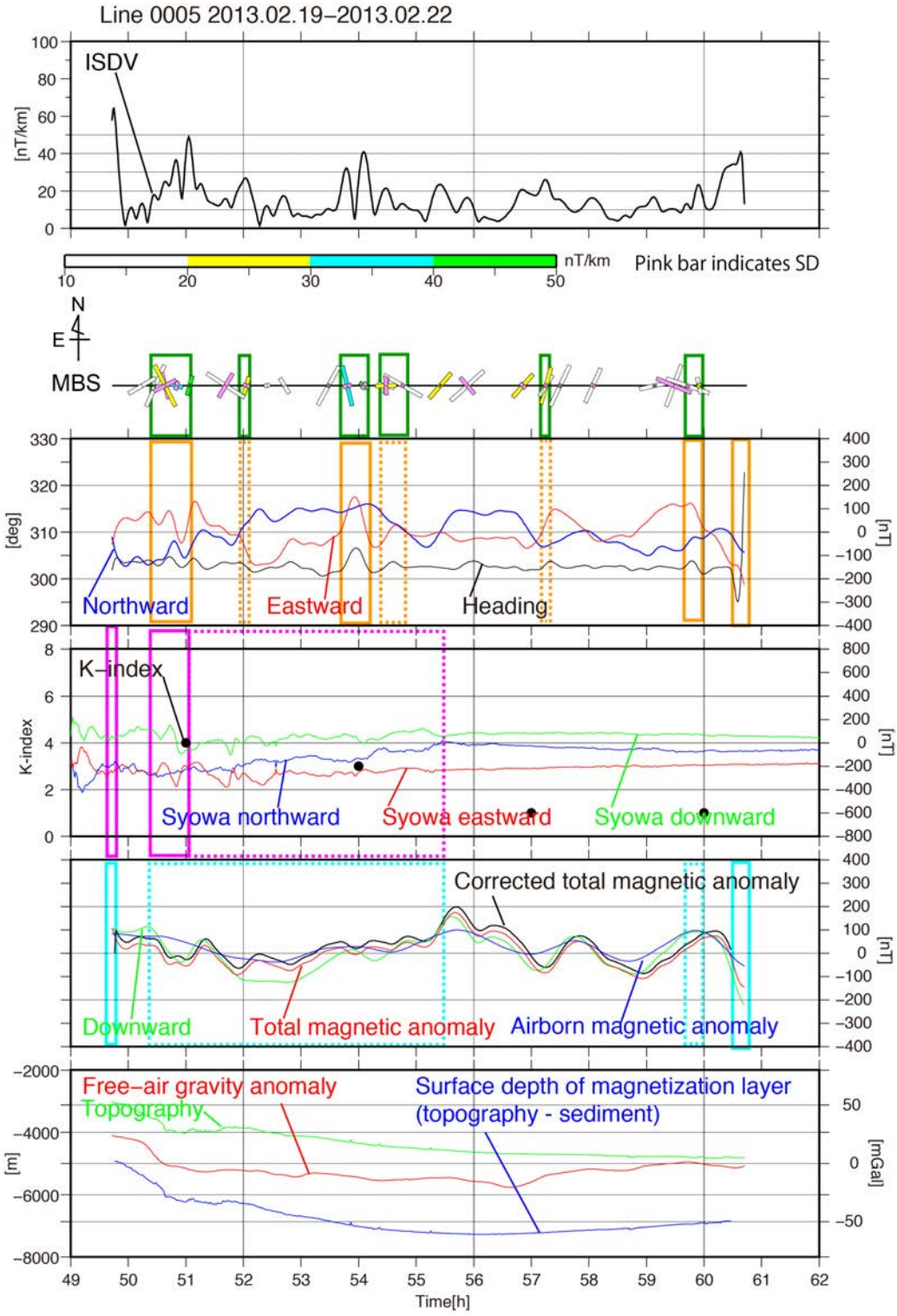

Fig. 3-2d

(continued)

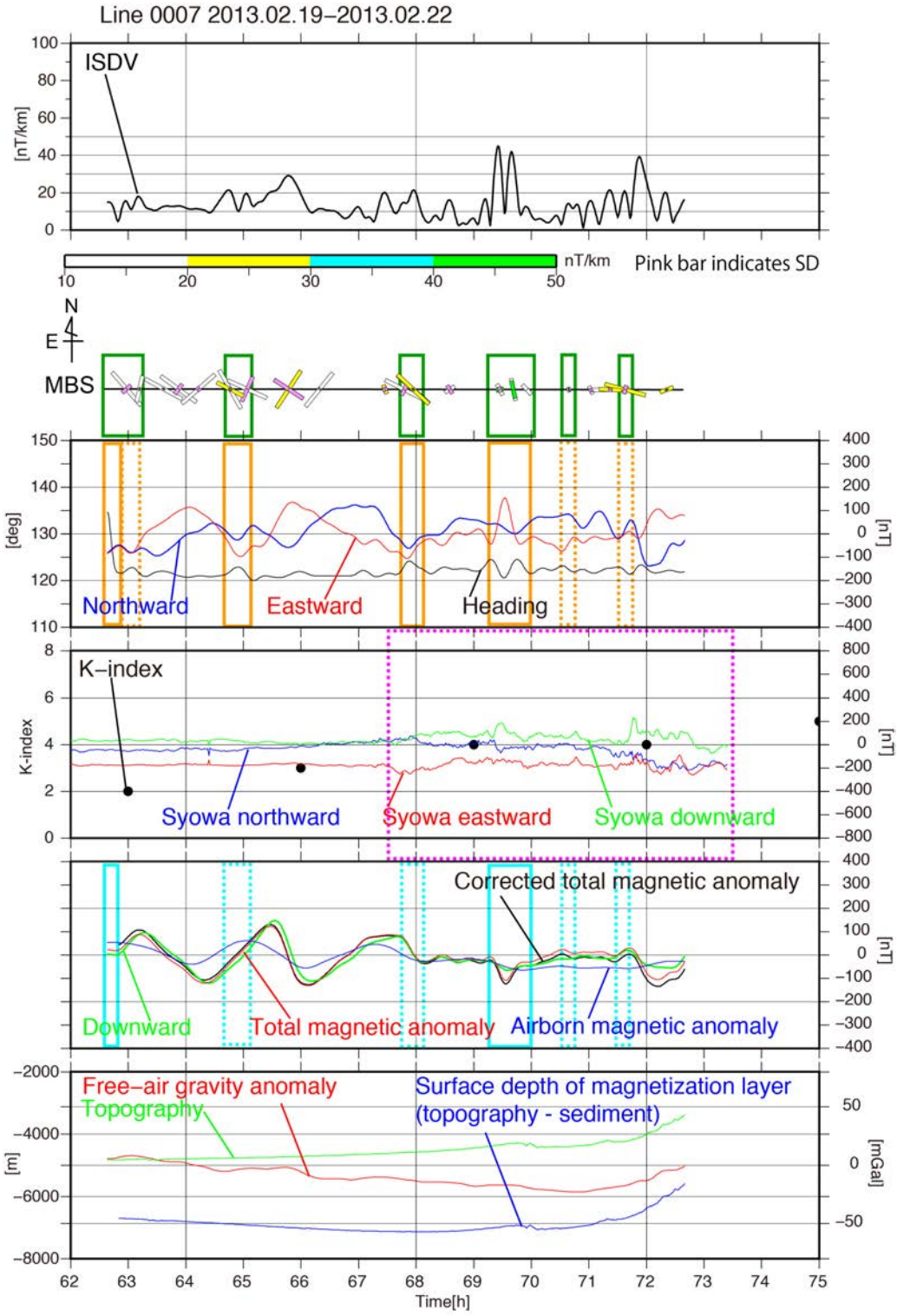

Fig. 3-2e

(continued)

Fig. 3-2

The observed profiles and ship heading data of the 54th JARE geomagnetic survey are shown in (a). The profile after subtracting linear trends along (b) line 0001, (c) line 0003, (d) line 0005, and (e) line 0007. The intensity of the spatial differential vectors is shown as the blue line in the first graph (black line). Calculated magnetic boundary strikes (MBS) are shown in the second graph. The white, yellow, blue, and green bars indicate position and direction of the MBS. This classification by color is based on the intensity of ISDV. Pink bars indicate the standard angular deviation of the MBS. Green boxes show the excluded data. The northward component and eastward component of the vector geomagnetic anomalies are shown as blue and red lines respectively in the third graph. The heading of the ship is also shown as a black line in the third column. Orange boxes show the ship's heading change of more than five degrees. Orange boxes show the ship's heading change of about three degrees. In the fourth graph, vector geomagnetic anomalies and the K-Index are shown as blue (northward), red (eastward), and light green (downward) lines, and black circles respectively. Times with K-Index values > 5 were shown in pink boxes, and K-Index values of 3–4 were shown in pink dotted boxes. The downward component of shipboard vector geomagnetic anomalies, calculated total geomagnetic anomalies, and corrected total geomagnetic anomalies in this study are shown as light green, red, and black lines respectively in the fifth graph. Airborne total geomagnetic anomalies of Jokat et al. (2010) are also shown as the blue line in the fifth graph. The excluded data was shown by light blue boxes. Total magnetic anomalies data shown by light blue boxes were not excluded. In the sixth graph, the satellite-derived free-air gravity anomalies (Sandwell, 2014), the ETOPO1 topographic data, and the surface depth of the magnetization layer estimated based on the ETIOI1 topographic data and the global sediment thickness model are shown in red, green, and blue lines respectively.

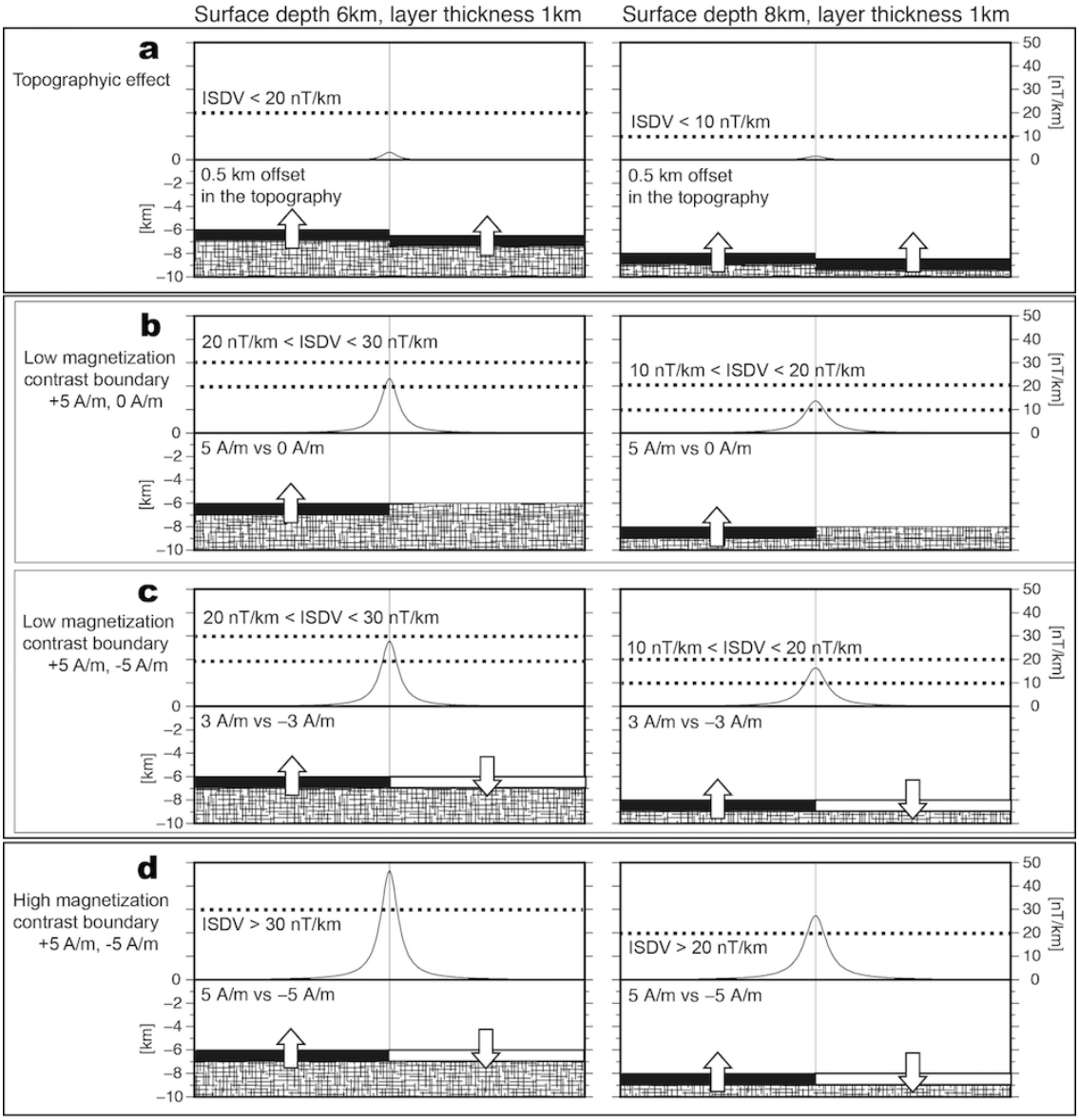

Fig. 3-3

Synthetic example of ISDV profiles calculated using a simple two-dimensional magnetic structure model. The thickness of the magnetization layer is assumed as 1 km. The left column shows the models for 6 km surface depth of the magnetization layer. The right column shows the models for 8 km surface depth of the magnetization layer. (a) +5 A/m magnetic structures with 0.5 km offset in the topography in the magnetic boundary model. (b) +5 A/m magnetized block and non-magnetized block model. (c) +3 A/m and −3 A/m of normal/reversed magnetized block model. (d) +5 A/m and −5 A/m of normal/reversed magnetized block model.

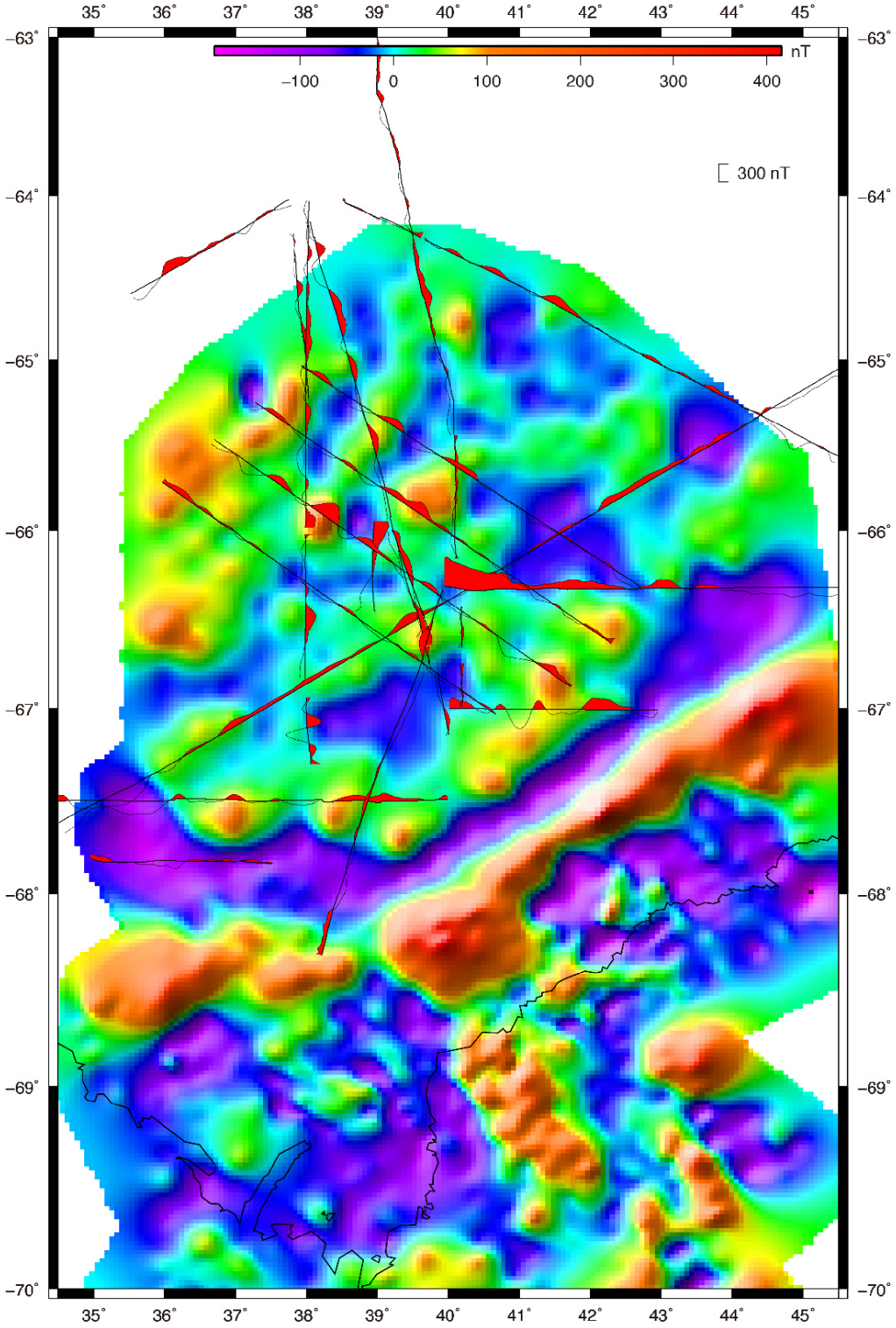
35°
36°
37°
38°
39°
40°
41°
42°
43°
44°
45°
−63°
−64°
−65°
−66°
−67°
−68°
−69°
−70°
nT
−100
0
100
200
300
400
300 nT

Fig. 3-4a

(continued)

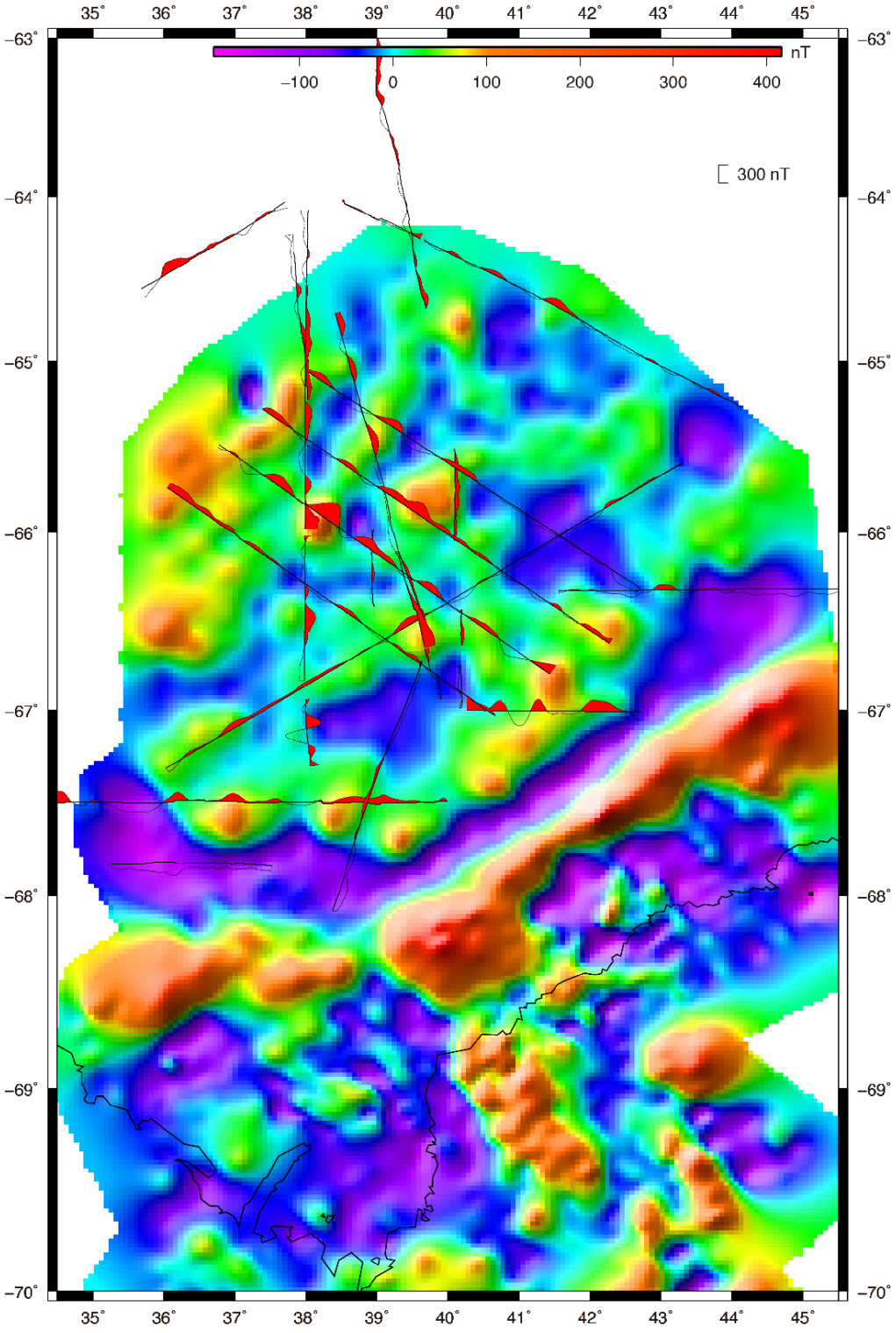

Fig. 3-4b

(continued)

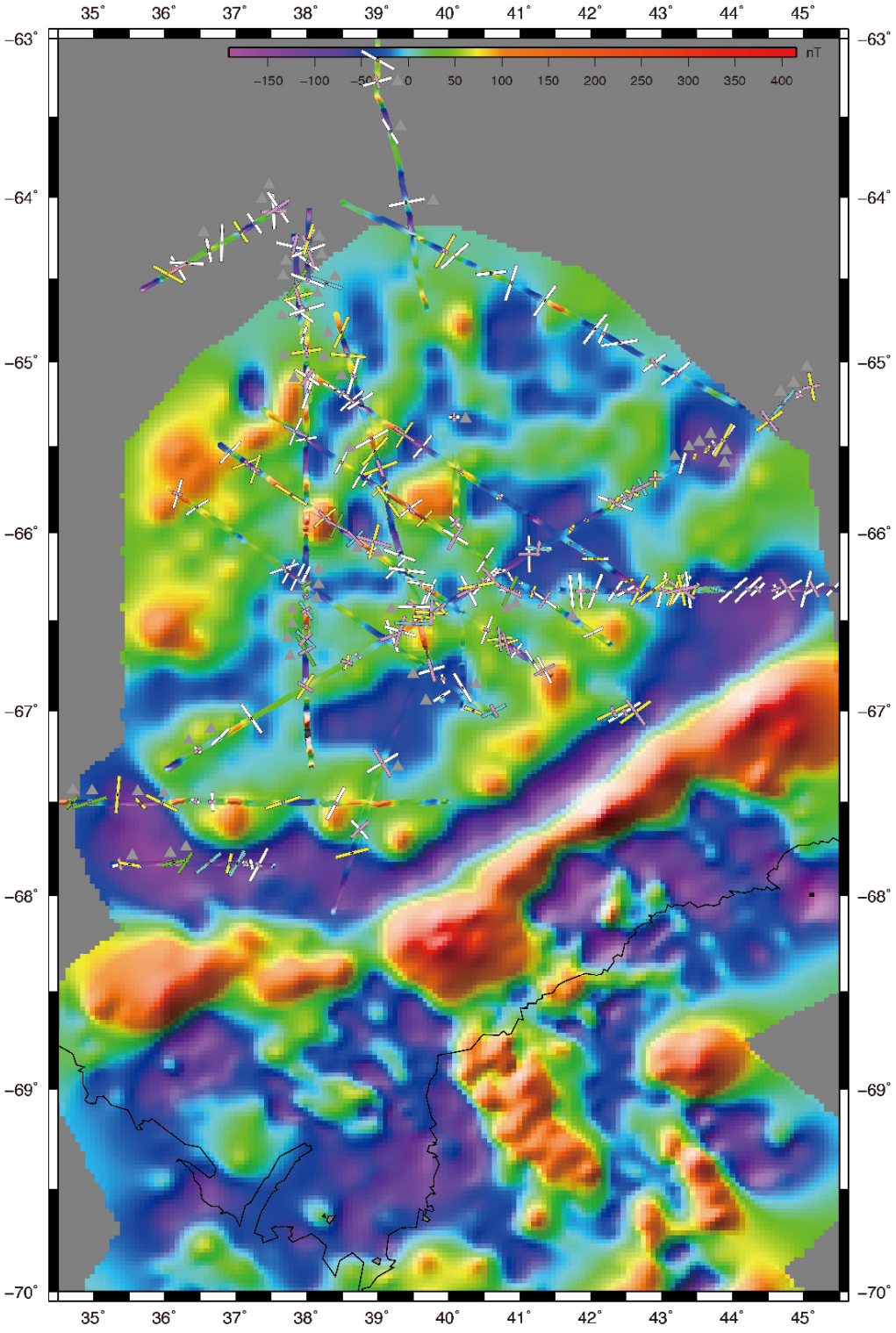

Fig. 3-4c

(continued)

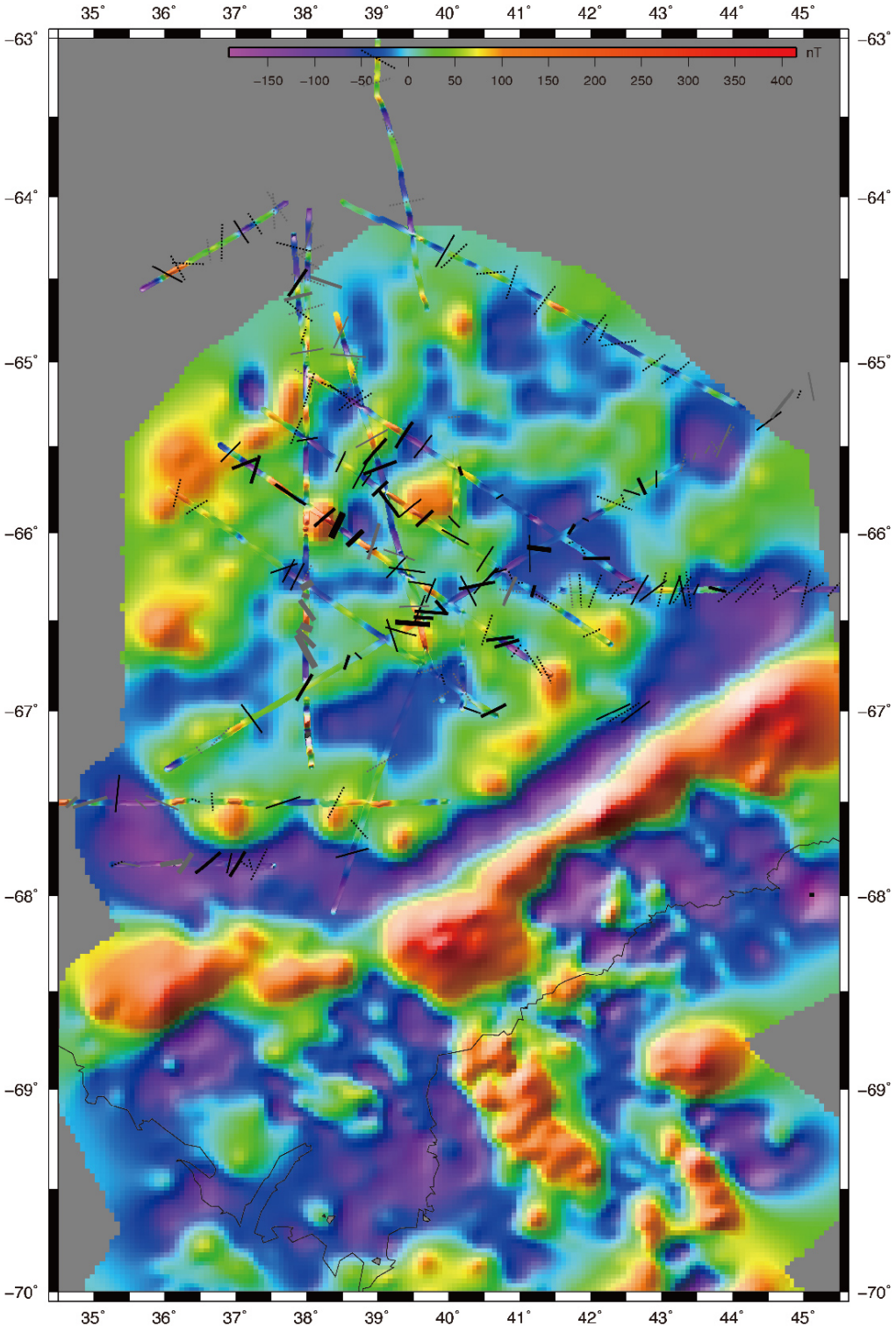

Fig. 3-4d

(continued)

Fig. 3-4

(a) Total geomagnetic anomaly wiggles in this study superimposed on the total airborne geomagnetic anomaly map (Jokat et al., 2010). (b) Corrected total geomagnetic anomaly wiggles in this study superimposed on the total airborne geomagnetic anomaly map. (c) Distribution of magnetic boundary strikes on the magnetic anomaly grid, with compilation of the corrected total geomagnetic anomalies in this study and the total airborne geomagnetic anomaly grid. White, yellow, blue, and green bars indicate the position and direction of the magnetic boundary strikes (intensities of ISDV are same as in Fig. 2 b–e). Pink bars indicate standard angular deviation of the magnetic boundary strikes. (d) Corrected magnetic boundary strikes on the magnetic anomaly grid.

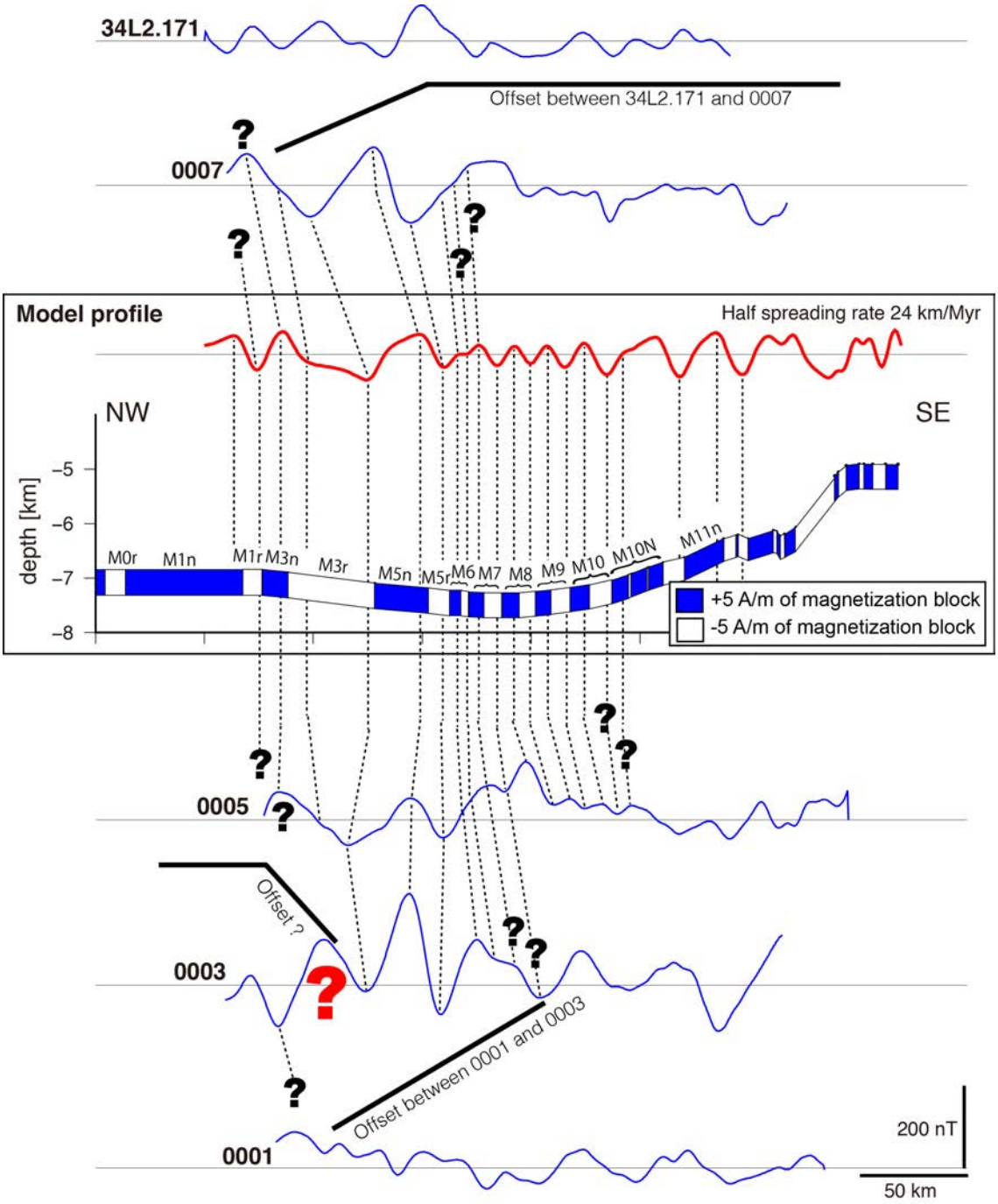
34L2.171
Offset between 34L2.171 and 0007
0007
Model profile
Half spreading rate 24 km/Myr
NW
SE
depth [km]
−5
−6
−7
−8
M0r
M1n
M1r
M3n
M3r
M5n
M5r
M6
M7
M8
M9
M10
M10N
M11n
+5 A/m of magnetization block
-5 A/m of magnetization block
0005
Offset ?
0003
Offset between 0001 and 0003
0001
200 nT
50 km

Fig. 3-5a

(continued)

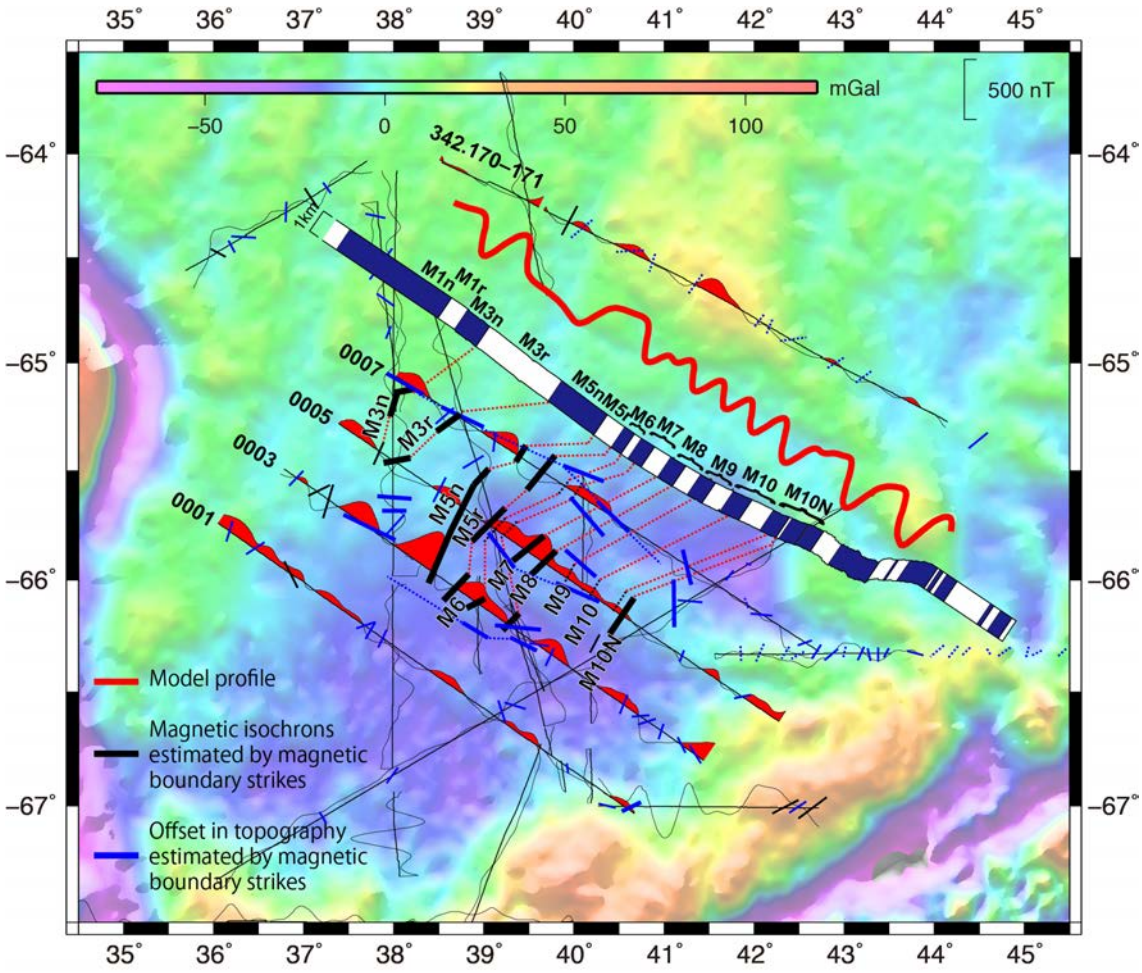

Fig. 3-5b

(continued)

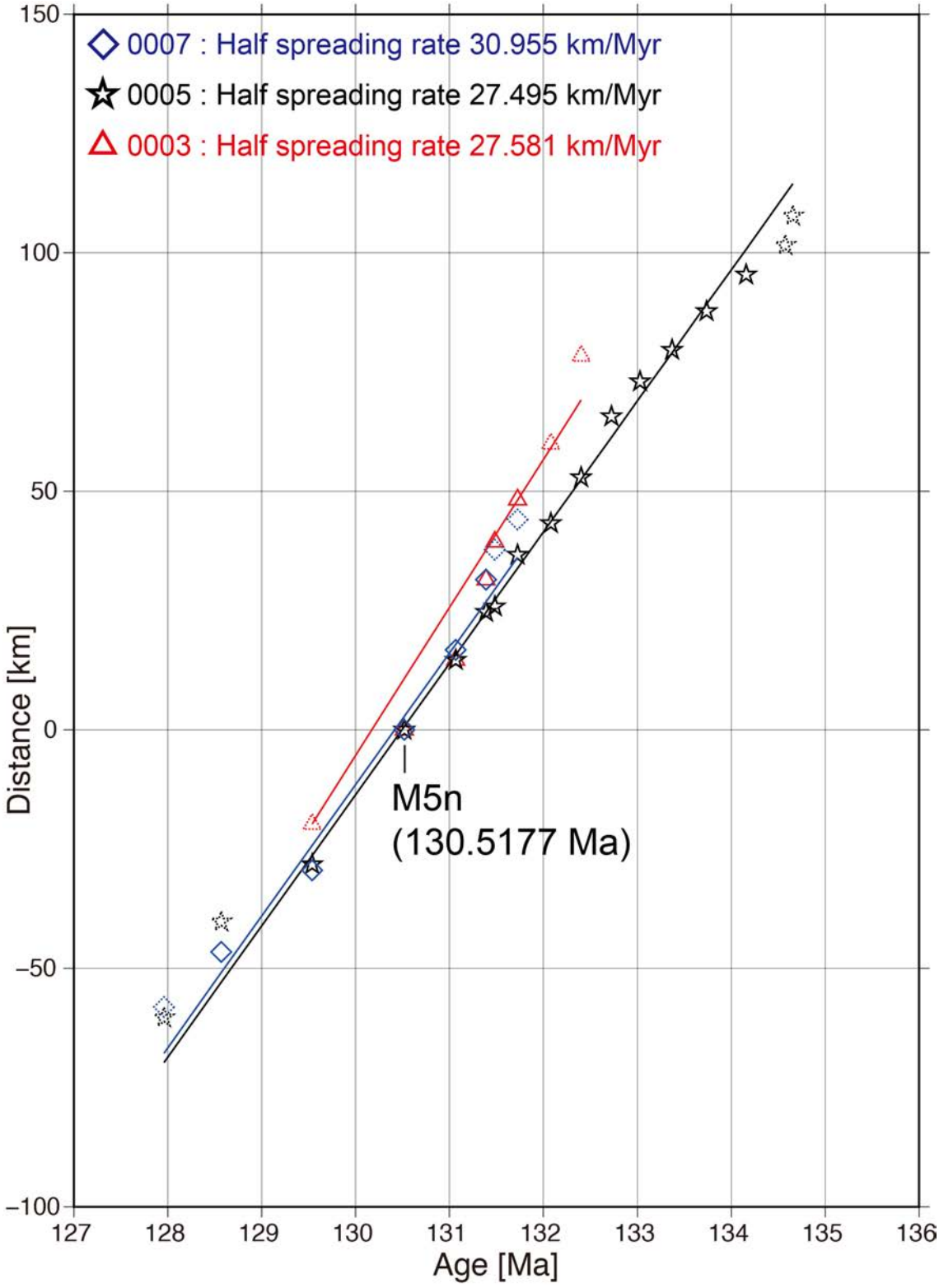

Fig. 3-5c

(continued)

Fig. 3-5

(a) Synthetic model profile calculated using the two-dimensional magnetic structure model of the M-sequence based on the geological polarity timescale of Gradstein (2008) and geomagnetic anomaly profiles on observation lines 0001–0007 and 34L2.170–171. To construct the block model, the thickness of the magnetization layer was assumed as 0.5 km, and its surface geometry was assumed using multibeam sounding data, ETOPO1 topographic data (Amante and Eakins, 2009), and sediment thicknesses from the global sediment thickness model (Laske and Masters, 1997) on line 0005. Magnetized body inclinations of the geocentric axial dipole are set to −77.45°. (b) The total geomagnetic anomaly wiggles and identified magnetic isochrons superimposed on the satellite-derived free-air gravity anomalies of Sandwell (2014). Magnetic boundary strikes indicating the magnetic isochrons, such as the high contrast magnetization boundary, are shown in solid black lines. Black dotted lines indicate the magnetic boundary strikes, showing the low contrast. Magnetic boundary strikes indicating the offset in topography are shown in blue lines. Synthetic model profile (red line) and model blocks are also shown. (c) Spreading rates of each magnetic isochron are calculated based on the geomagnetic anomaly profiles and magnetic boundary strikes.

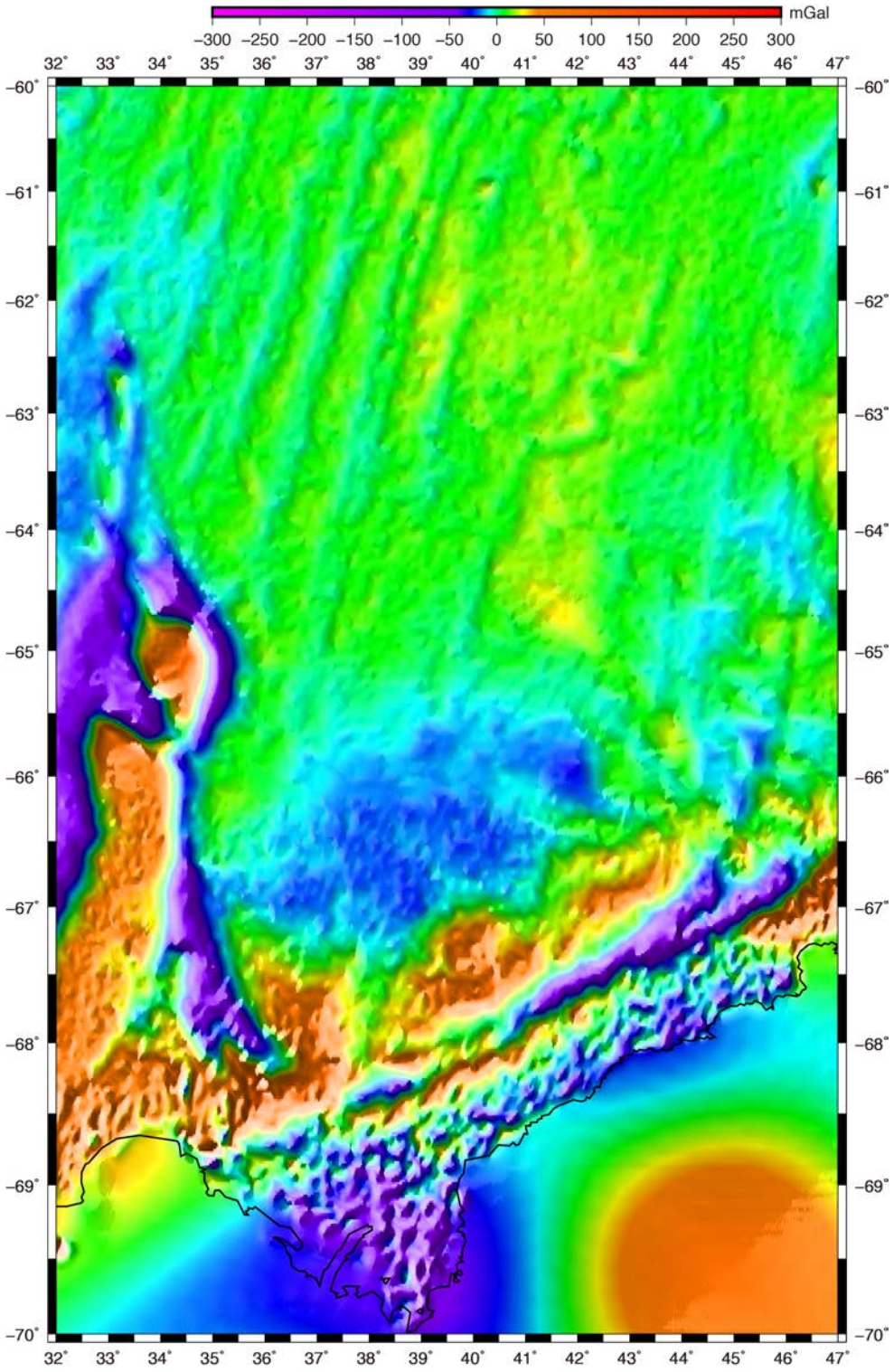
mGal
−300 −250 −200 −150 −100 −50 0 50 100 150 200 250 300
32° 33° 34° 35° 36° 37° 38° 39° 40° 41° 42° 43° 44° 45° 46° 47°
−60° −61° −62° −63° −64° −65° −66° −67° −68° −69° −70°

Fig. 3-6a

(continued)

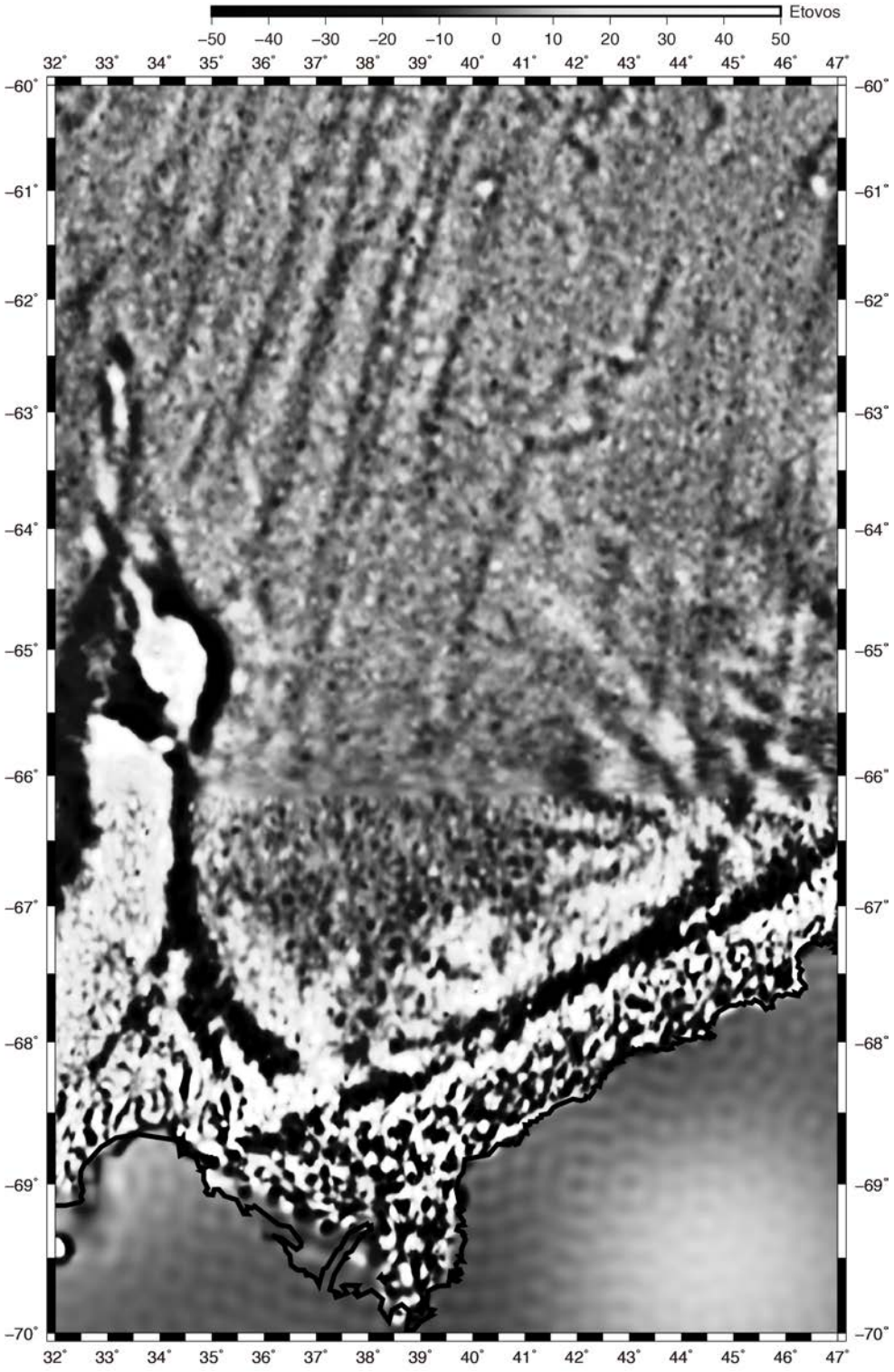

Fig. 3-6b

(continued)

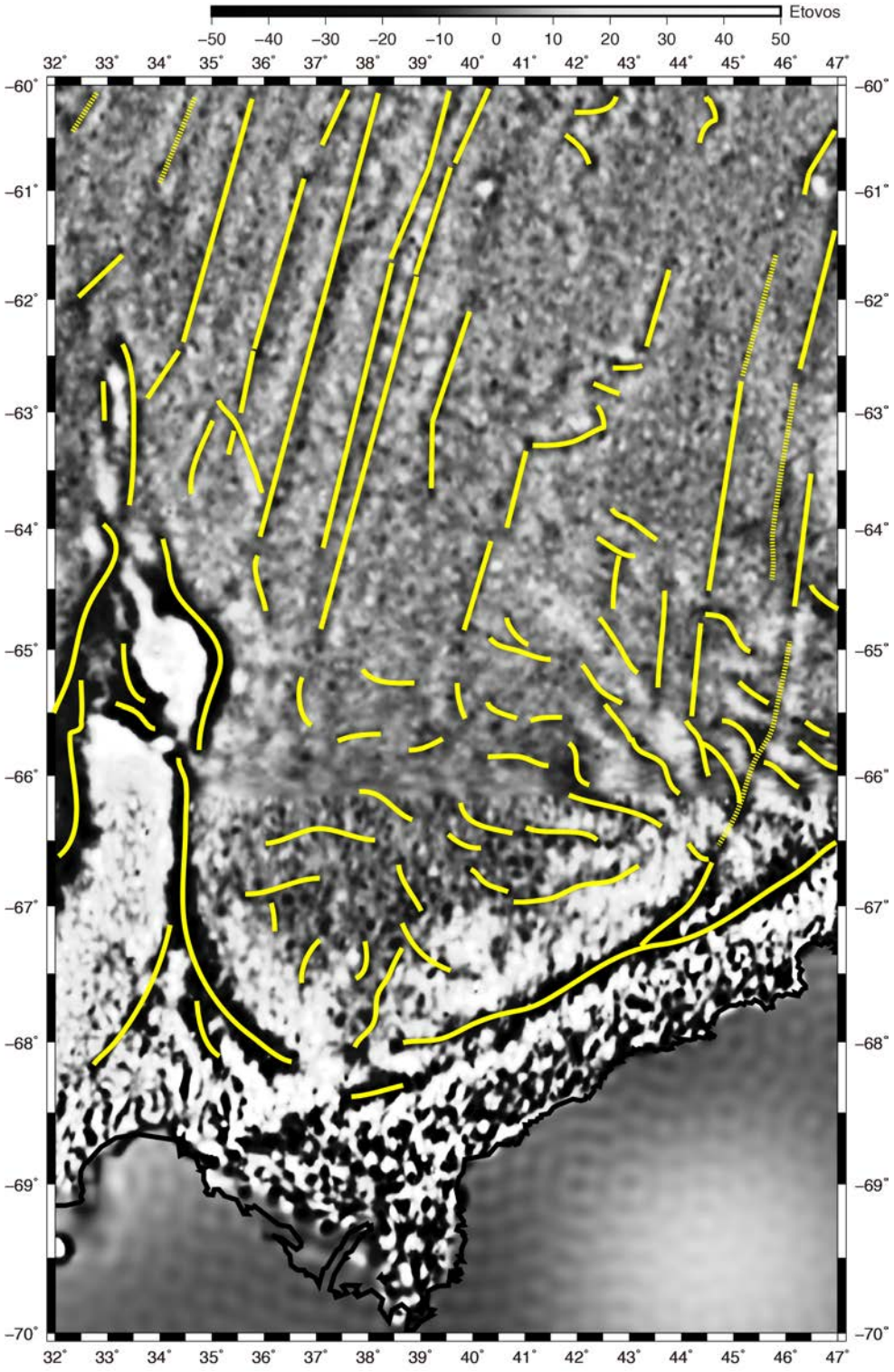

Fig. 3-6c

(continued)

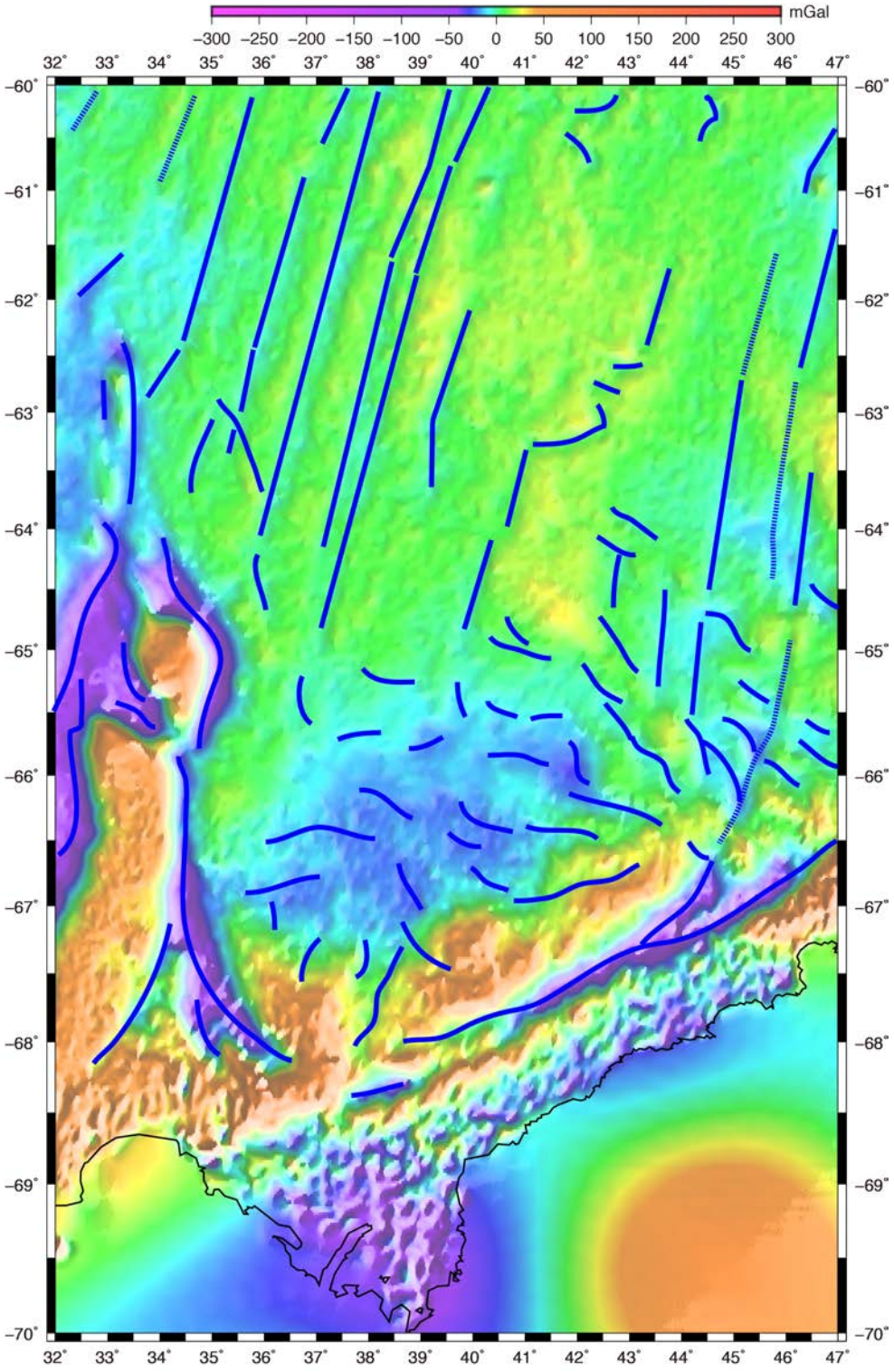

Fig. 3-6d

(continued)

Fig. 3-6

(a) Satellite-derived free air gravity anomaly map, and (b) Vertical gravity gradient (VGG) map of Sandwell (2014). (c) Structure boundaries estimated using the VGG are shown in yellow lines, superimposed on the VGG map. (d) Structure boundaries shown in blue lines superimposed on the satellite-derived free air gravity anomaly map.

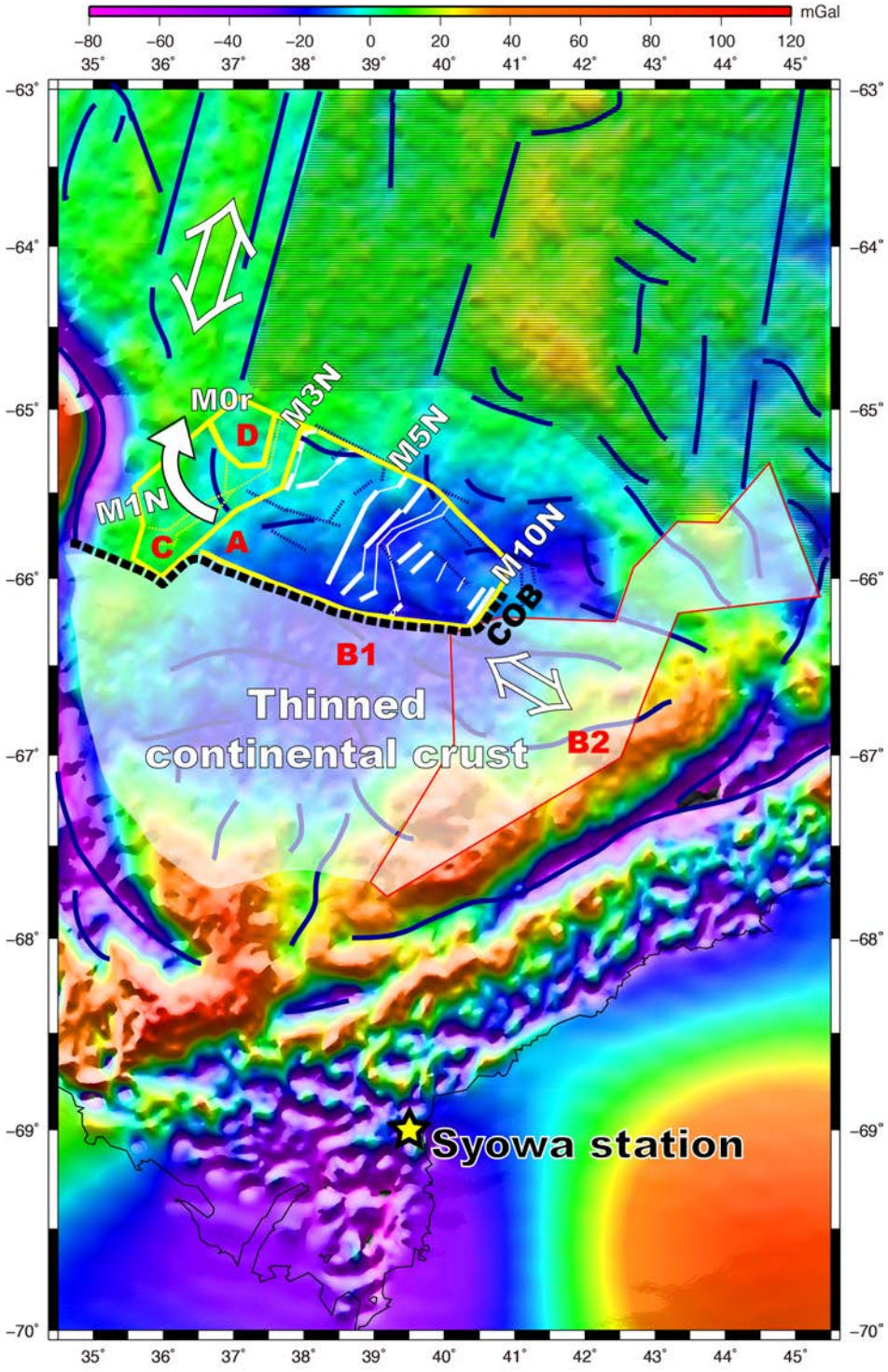
mGal
−80 −60 −40 −20 0 20 40 60 80 100 120
35° 36° 37° 38° 39° 40° 41° 42° 43° 44° 45°
−63°
−64°
−65°
−66°
−67°
−68°
−69°
−70°
M0r
M3N
M5N
M10N
M1N
D
C
A
COB
B1
B2
Thinned
continental crust
Syowa station

Fig. 3-7a

(continued)

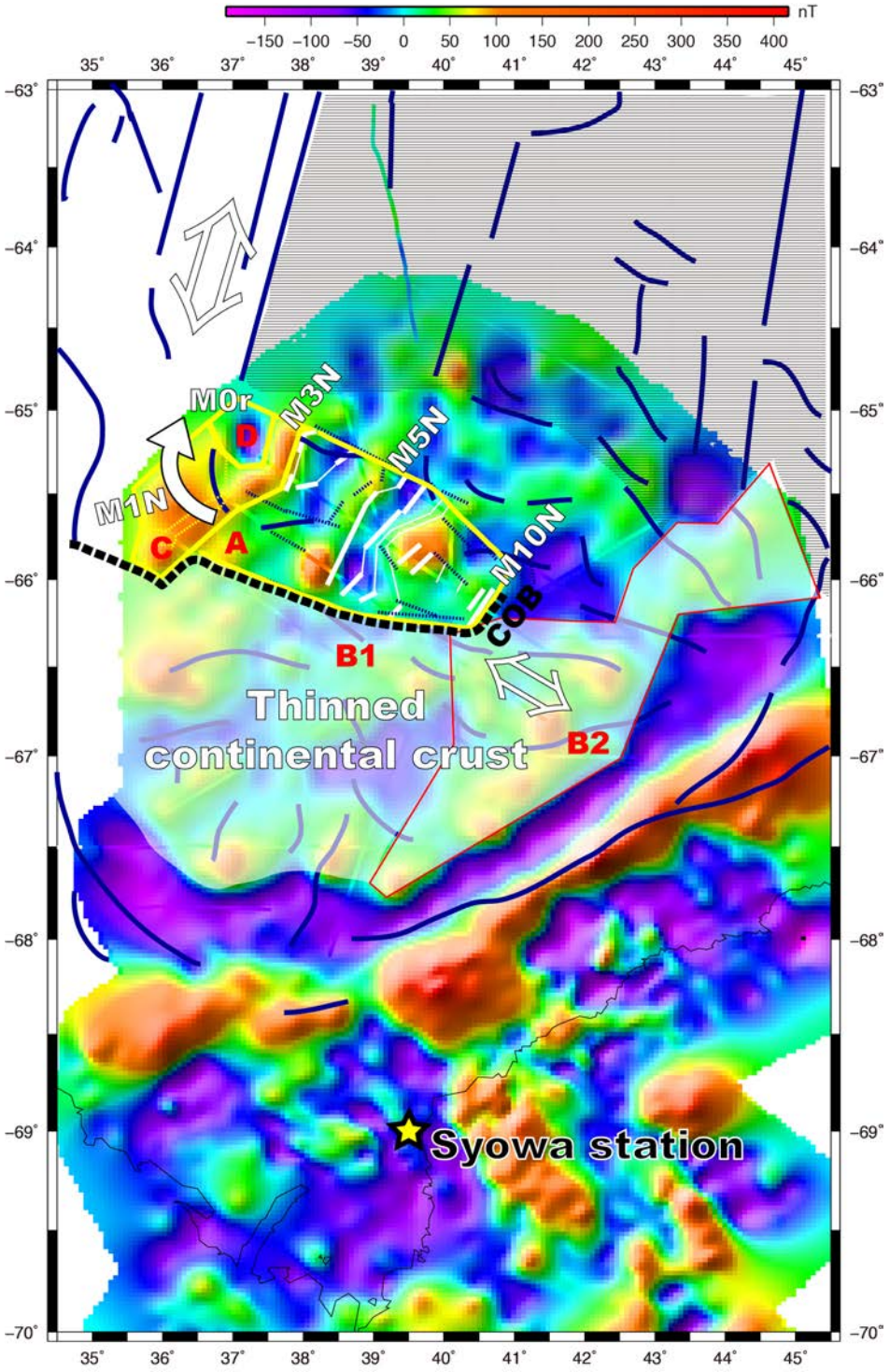

Fig. 3-7b

(continued)

Fig. 3-7

Interpretation of the formation process of the Cosmonauts Sea superimposed on the (a) satellite-derived gravity anomaly map, and (b) magnetic anomaly grid. Black lines show the structure boundaries estimated based on the VGG. B2 is the COTZ proposed in previous study (Jokat et al., 2010). Thick white lines show the magnetic isochrons estimated based on the magnetic boundary strikes. Thin white lines are the estimated magnetic isochrons that could not be detected from the magnetic boundary strikes. Black dotted lines show the segment boundaries estimated based on the magnetic boundary strikes. The white shaded area indicates the thinned continental crust. COB indicate continent–ocean boundary in this study.

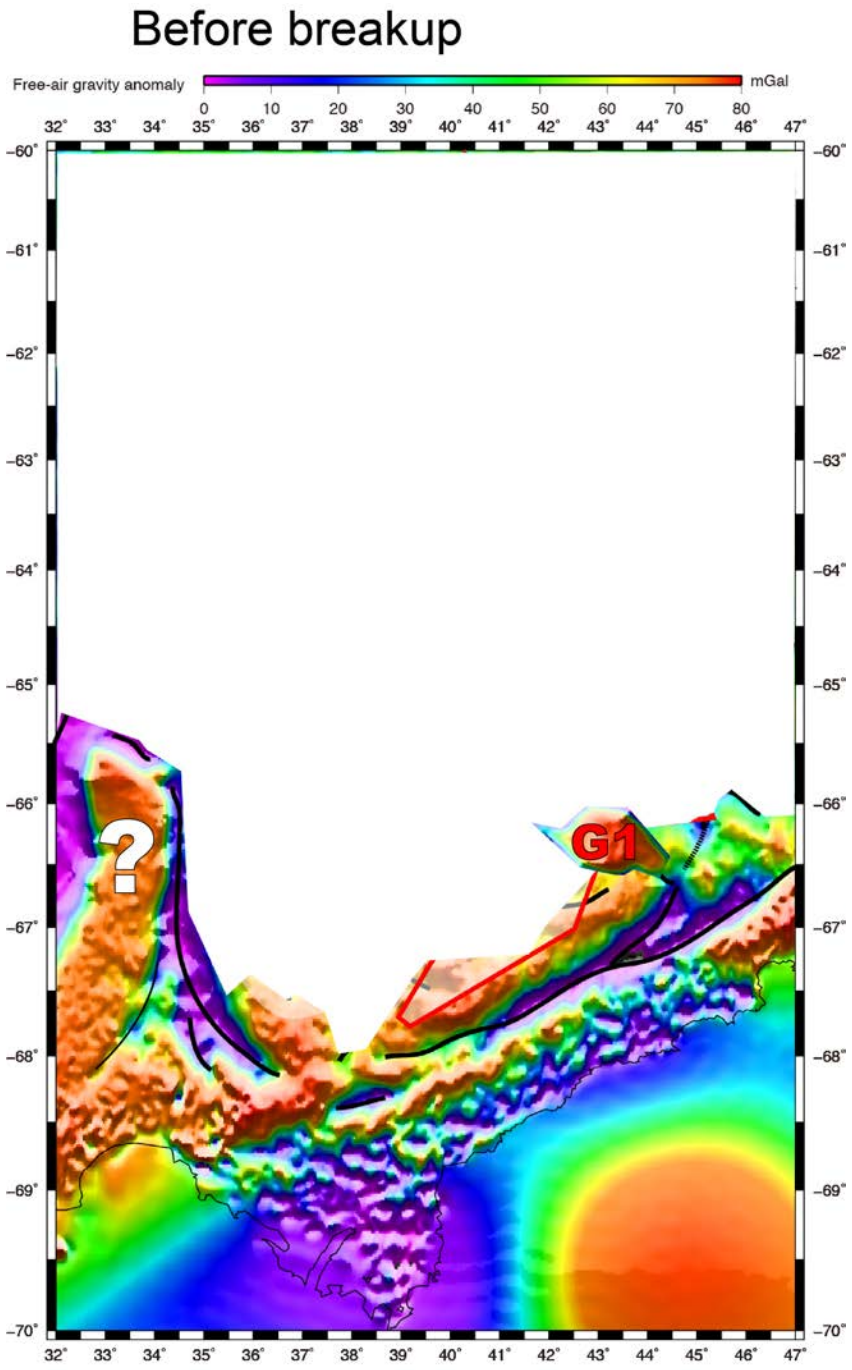
Before breakup
Free-air gravity anomaly
mGal
0 10 20 30 40 50 60 70 80
32° 33° 34° 35° 36° 37° 38° 39° 40° 41° 42° 43° 44° 45° 46° 47°
-60° -61° -62° -63° -64° -65° -66° -67° -68° -69° -70°
?
G1

Fig.3-8a

(continued)

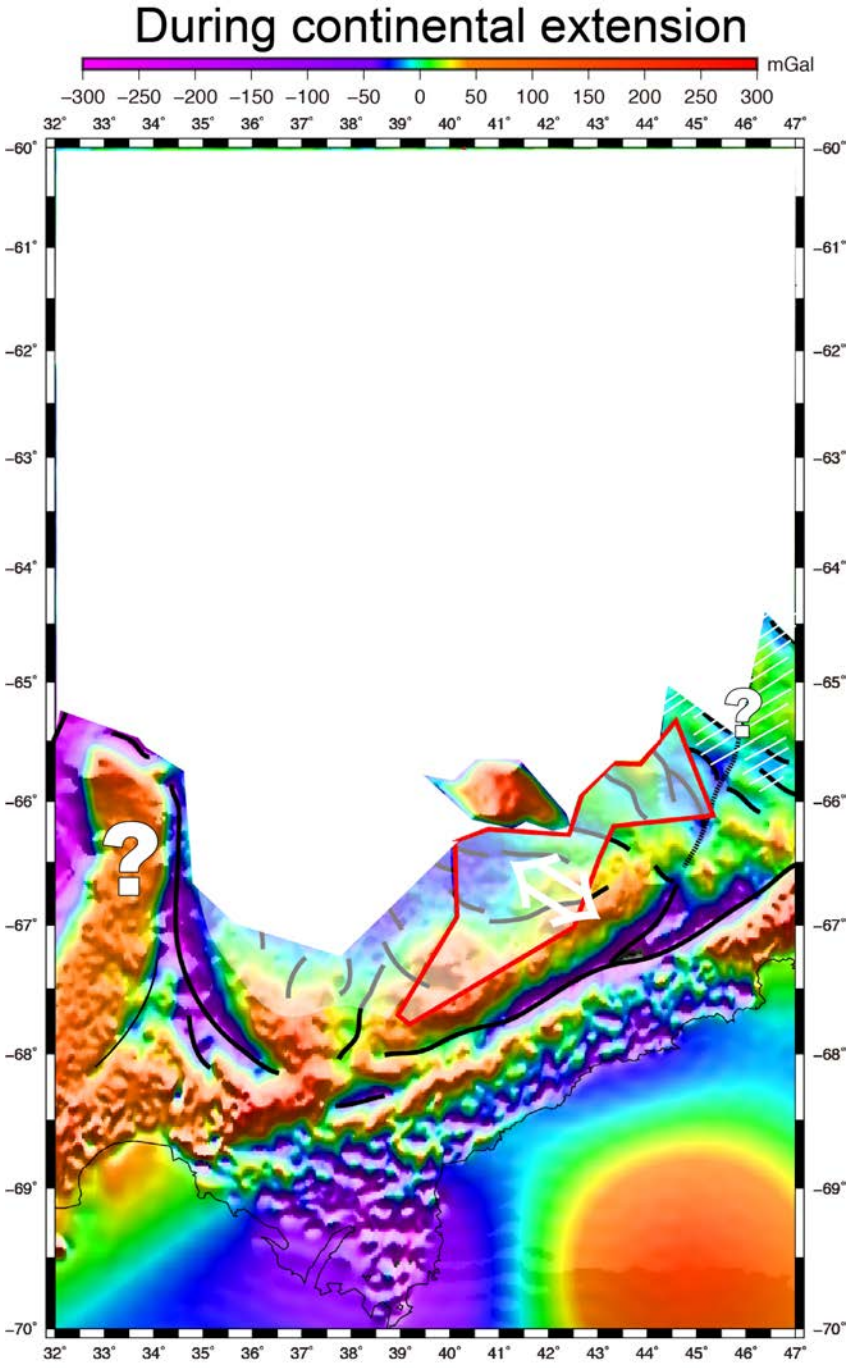

Fig.3-8b

(continued)

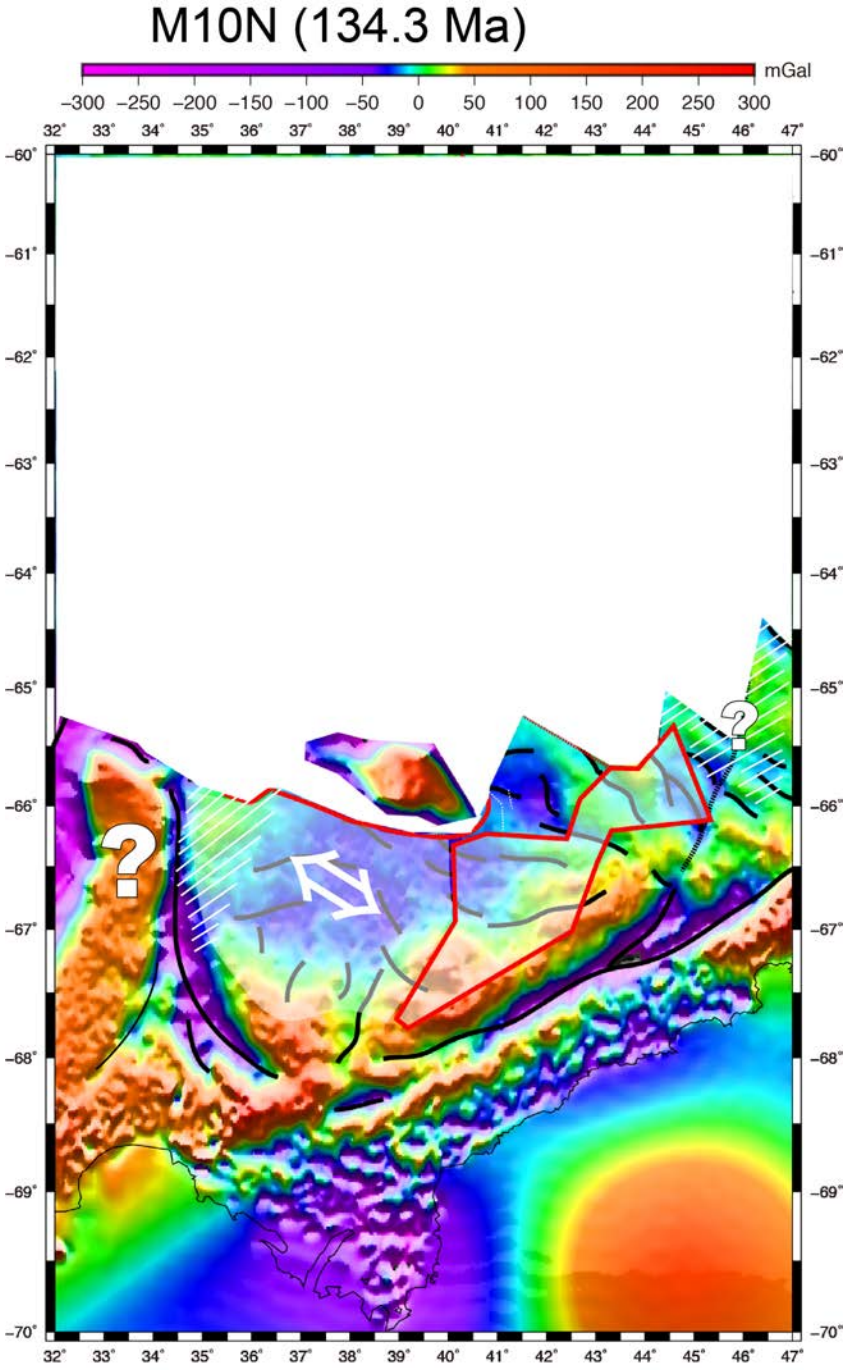

Fig.3-8c

(continued)

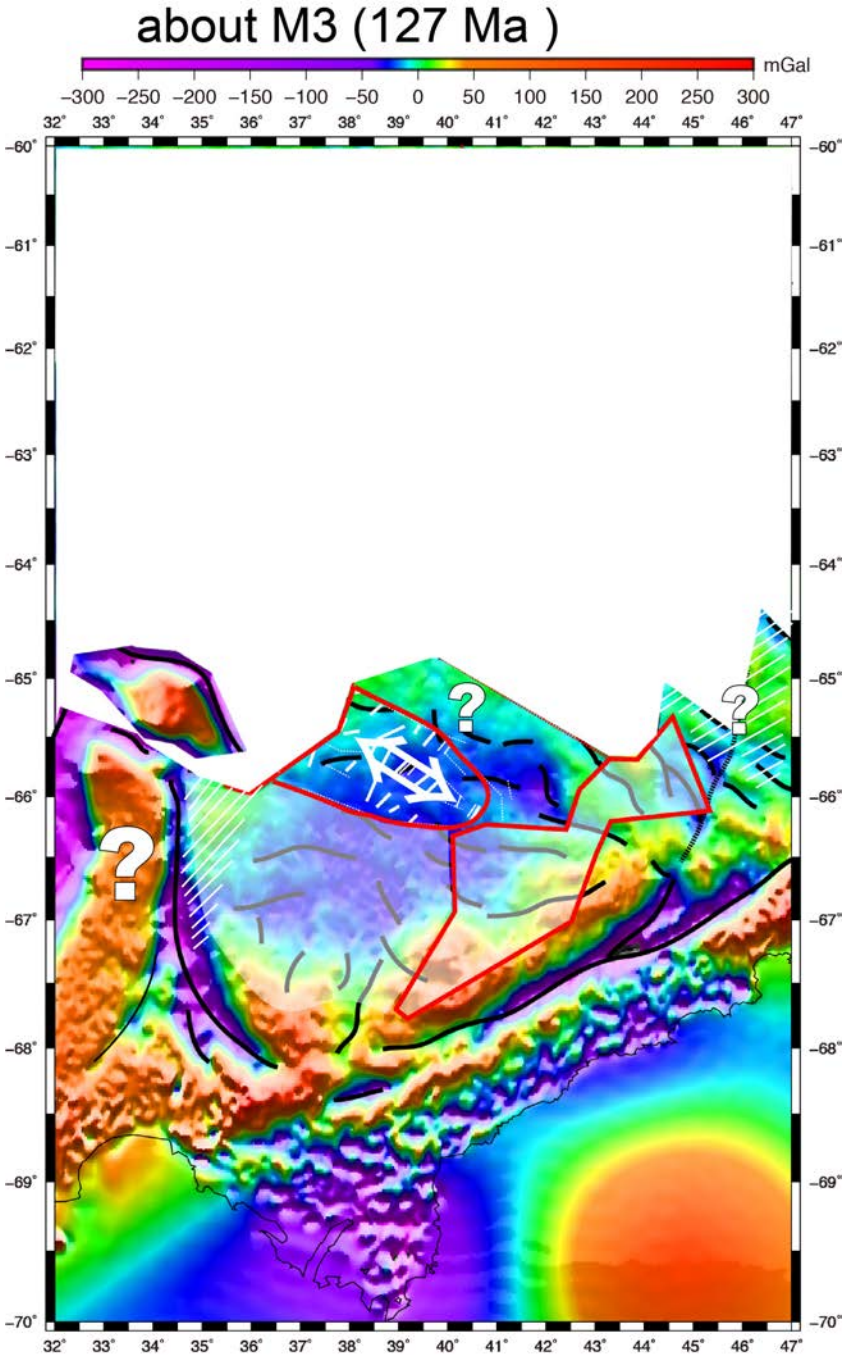

Fig.3-8d

(continued)

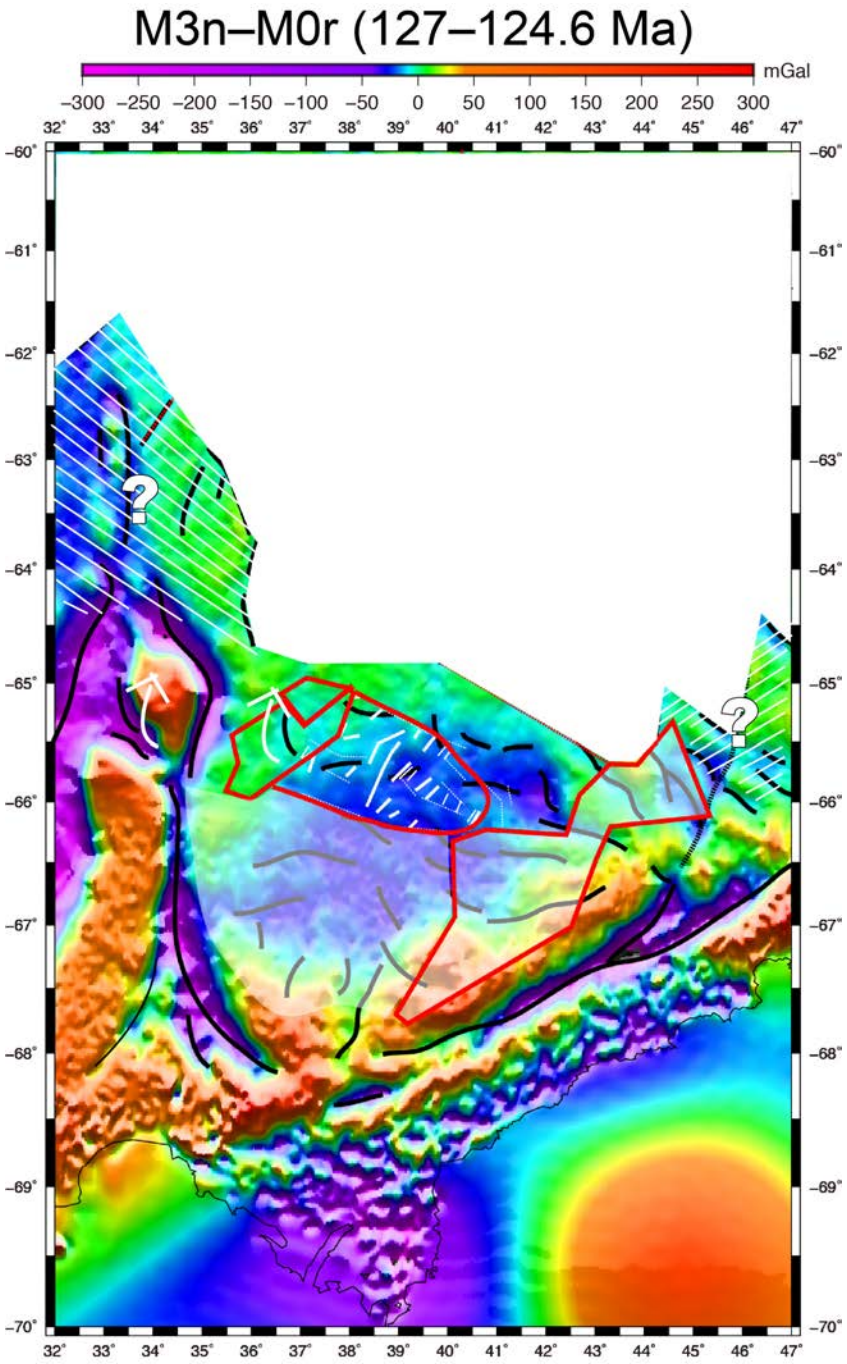

Fig.3-8e

(continued)

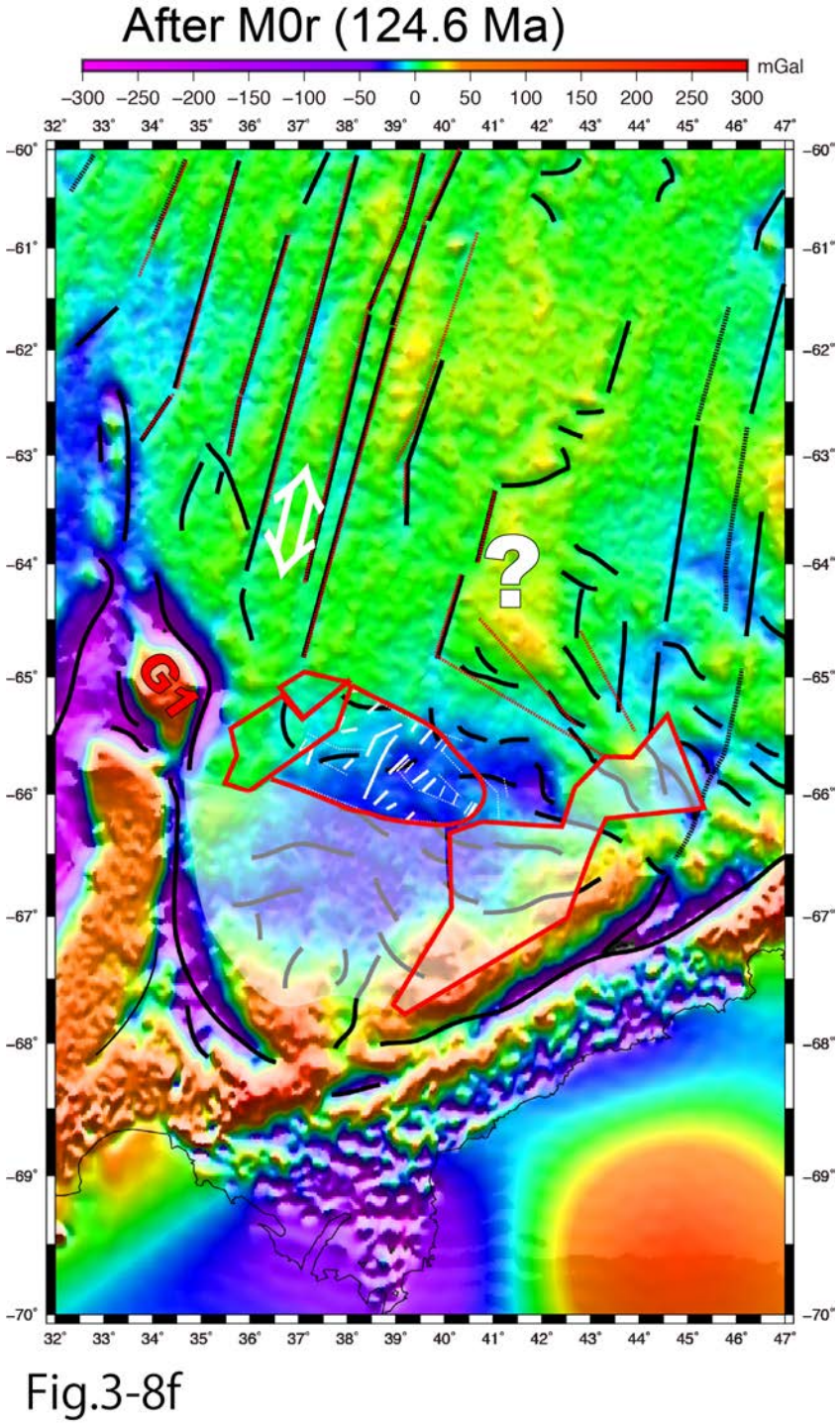

Fig.3-8f

Fig. 3-8

(a)–(f) Break-up model in the Cosmonauts Sea since break-up to the CNS. G1, Kainan-Maru Seamount. Black lines show the structure boundaries estimated based on the VGG. Thick white lines show the magnetic isochrons estimated based on the magnetic boundary strikes.

Chapter 4. General Discussion: Interpretation of the initial break-up process of Gondwana in the Indian Ocean

In this thesis, I have presented the initial break-up process of Gondwana in regions both off Africa and off Antarctica using vector geomagnetic anomalies, as well as satellite gravity data. In this chapter, magnetic isochron ages are unified using the geological time scale of Gradstein (2008).

In Chapter 2, the formation and evolution processes in the Natal Valley and Mozambique Ridge were revealed. The mixture of continental and basaltic (oceanic) crust under the northern part of this region was represented by multiple analytical results of dense vector geomagnetic anomalies, as well as satellite gravity data. Magnetic isochrons M10–M0 (about 133.5–124.6 Ma) with a NE–SW spreading direction were identified in the southern Natal Valley, and were well correlated with the isochrons in the west of this area proposed by previous studies. In the southern Mozambique Ridge, seafloor spreading likely began at the same time as in the southern Natal Valley. Magnetic isochrons in the southern Mozambique Ridge and part of the southern Natal Valley were disturbed because of the interaction of intense volcanic activity, which may have been related to the Bouvet hotspot. The NE–SW spreading direction indicates that the seafloor spreading occurred between South America and South Africa. The location of the continent–ocean boundary (COB) is around M10, at 30ºS–32ºS. Continental extension and basaltic intrusion likely occurred until the initiation of seafloor spreading at about M10 (133.5 Ma).

In Chapter 3, the process of continental extension to seafloor spreading in the Cosmonauts Sea was revealed using multiple analytical results of the systematic vector geomagnetic anomalies obtained by the icebreaker *Shirase*, as well as satellite gravity data. Wide-spreading thinned continental crust south of around 66ºS was inferred. The isochrons M10N–M3n (about 134.3–127.6 Ma) with an almost ESE–WNW spreading direction around 66ºS–65ºS were newly identified with several smaller segments. SSW–NNE-oriented fracture zones appeared north of around 65ºS, indicating the change in direction of seafloor spreading from SE–NW to SSW–NNE around 65ºS. In terms of timing, the change in spreading direction likely occurred during chron M3n–M0r (about

127.6–124.6 Ma), based on the pattern of the total airborne geomagnetic anomalies. The north portion of the Gunnerus Ridge, named the Kainan-Maru seamount, which was interpreted to be continental crust, may have been displaced from the pre-stretching boundary along Antarctica to its present position accompanied by the ESE–WNW-oriented continental extension and seafloor spreading during pre-stretching to chron M0r. After 124.6 Ma, the direction of the seafloor spreading was only constrained by the SSW–NNE-oriented fracture zones, because no magnetic reversal was observed during the Cretaceous Normal Superchron. However, the structure direction estimated from the vertical gravity gradient shows an ambiguous spreading direction between the fracture zones of around 37ºE, 65ºS–44ºE, 65.5ºS.

The Natal Valley and Mozambique Ridge off South Africa (AFR) are a conjugate pair with the Falkland Plateau off South America (SA) and the Lazarev Sea off Antarctica (ANT). These regions formed as a result of West Gondwana fragmentation, between AFR–SA–ANT. However, the Cosmonauts Sea in the west Enderby Basin off ANT is a conjugate pair with the south of Sri Lanka (SL) and the Bay of Bengal off India (IND). The Gunnerus Ridge is considered to be a conjugate pair with Madagascar (MAD) and/or SL. These regions formed as a result of East Gondwana fragmentation, between ANT–MAD/SL/IND–Australia (AUS).

In West Gondwana, seafloor spreading between SA–AFR occurred at chron M12–M10. The half-spreading rate between SA and AFR during chron M12–M0 was estimated as 10–17 mm/yr, indicating a slow spreading ridge (Rabinowitz and Rabrecque, 1979; Martin et al., 1982; Goodlad et al., 1982; this study). After chron M0, the spreading rate between SA, AFR, and ANT increased up to about 40–55 mm/yr (Rabinowitz and Rabrecque, 1979; Martin et al., 1982). Stretched continental crust, considered one of the largest COTZs with a width of more than 200 km, like the northern part of the Natal Valley and Mozambique Ridge, was also proposed to exist beneath the Santos Basin off SA (e.g., Davison, 1997) and the Lazarev Sea off ANT (Explora Escarpment; Hinz et al., 2004). In addition, the formation of the largest COTZ was likely caused by the large igneous province of Paranà–Etendeka (about 137–127 Ma) of the SA–AFR (e.g., Hawkesworth et al., 2000), which occurred at the initiation of the seafloor spreading. This situation is similar to that of the Natal Valley and Mozambique Ridge, which was probably associated with the Karoo volcanism. In addition, there is a great deal of hotspot activity, such as that of the St. Helena (after

106 Ma: e.g., Coulon et al., 1996) and Tristan-Gough (after 130 Ma: e.g., O'Connor and Duncan, 1990) hotspots along the MAR, and ridge-hotspot interaction around the MAR was inferred based on petrological studies. My results implied that the Mozambique Ridge was formed by the ridge–hotspot interaction around the Bouvet hotspot. The Agulhas Plateau off South Africa, the North East Georgia Rise off South America, and the Maud Rise off Antarctica were also likely formed by ridge–hotspot interactions on the Bouvet triple junction (around 120 Ma; e.g., Gohl et al., 2011). Basically, the largest stretched continental crust and regional intense basaltic intrusion caused by volcanic activity characterized the break-up and evolution process of the West Gondwana margins.

In East Gondwana, magnetic isochrons of M10–M0r with NW–SE and/or WNW–ESE-oriented seafloor spreading were observed south of SL (Desa et al., 2006; Gaina et al., 2007), in the Bay of Bengal (Ramana et al., 1994), and at the western margin of AUS (Gibbons et al., 2012). The spreading direction and rate, with an average of about 35 mm/yr in these regions, coincide well with those of the Cosmonauts Sea based on my results. After chron M0, the spreading rate between SA, AFR, and ANT sped up to about 22–40 mm/yr in the central Enderby Basin and the western margins of AUS, and to 40–42 mm/yr in the Bay of Bengal (Desa and Ramana, 2016). The spreading rate in the north of the Cosmonauts Sea was estimated as about 40 mm/yr, although there is no reliable geomagnetic data indicating magnetic lineation, likely because of the CNS. My interpretation requires re-examination of the geomagnetic and seafloor structure properties in the south of SL, where the ultraslow spreading rate of 6 mm/yr during the CNS period was estimated (Desa et al., 2006). The continental extension between IND and AUS was suggested to have initiated as early as 160 Ma (Gibbons et al., 2013). Continental extension during East Gondwana fragmentation was likely less than that of West Gondwana fragmentation. COTZs with widths of a few hundreds of kilometers were observed around the West Gondwana margins (e.g., Brune et al., 2014; Gibbons et al., 2013; this study), and the continental blocks that contain the non-volcanic basement were observed around the western margin of AUS (Symonds et al., 1998). Our results for the Cosmonauts Sea also show that there was no intense volcanic activity between ANT–IND/SL, at least before 120 Ma. In other words, there was no volcanic interaction for the initial evolution of the East Gondwana margins.

Based on my results and previous studies as mentioned above, I compiled the

following stages of Gondwana break-up: (1) seafloor spreading started about M12–M10 in Gondwana; (2) seafloor spreading continued during the CNS period in Gondwana; and (3) intense volcanism occurred before about 124.6 Ma in Gondwana (Table 4 and Fig. 4-1). The remarkable point is that the most of the seafloor spreading started around chron M12–M10 in both East and West Gondwana. Moreover, the spreading rate and/or spreading direction changed at about M0 in both East and West Gondwana. I considered that a possible change in pulling force originated from the subduction zones that surrounded Gondwana and caused these seafloor-spreading events. First, before 140 Ma, it is suggested that there was a subduction zone along the south of the Eurasian continent (e.g., Metcalfe, 2011; Van der Voo, 1999). The Meso-Tethys Sea was located between the Lhasa block and Eurasia around present central Tibet to Kazakhstan (Van der Voo, 1999). During 140–130 Ma, the Meso-Tethys was closed because of the subduction zone at the southern edge of Eurasia. Then, the Lhasa–Eurasia collision occurred around 130 Ma. Because of this collision, the subduction of the Neo-Tethys, which was south of the Lhasa block, was initiated. Subduction of the Neo-Tethys likely forced the change in spreading regime in Gondwana, such as the formation of a triple junction at the north of IND caused by the initiation of seafloor spreading between IND and AUS. Next, during 130–120 Ma, a part of the subduction zone between the Phoenix Plate and SA/ANT/AUS in the Pacific side was extinct (e.g., Storey, 1995; Müller et al., 2016), based on the onshore paleo-geomagnetic data, marine geomagnetic anomalies, crustal thickness, fracture zones, and hotspot tracks, mainly around the Pacific Ocean. The extinction of the subduction zone at the east of AUS likely coincided with a distinct change in the absolute velocity of AUS (Matthews et al., 2010). Then, the seafloor spreading direction was changed by the transition in velocity that may have reflected the change in pulling force caused by subduction around Gondwana. Based on this concept, I constructed a new model for the initial break-up process of Gondwana focused during 137–124.6 Ma (Fig. 4-2), as follows:

(1) First stage: before 137 Ma (Fig. 4-2a)

After the initiation of the break-up of Gondwana at about 183 Ma, continental extension occurred around each continental margin, caused by the pulling force of several subduction zones surrounding Gondwana. Mantle plume upwelling and eruption, such as the Karoo volcanism, also started, and likely set up the large continental–ocean

transition zone around the SA–AFR margins. Small intrusions into the stretched continental crust occurred in some parts of the continental margins because of these volcanisms. Seafloor spreading started in the central and eastern parts of the continental margins of Gondwana after 153 Ma (e.g., Eagles and König, 2008; Gibbons et al., 2012).

(2) Second stage: 137–133 Ma (M12–M10) (Fig. 4-2a to Fig. 4-2b)

The Lhasa–Eurasia collision in present Tibet to Kazakhstan caused: 1) the extinction of the subduction of the Meso-Tethys; and 2) the beginning of the subduction of the Neo-Tethys. These configuration change of the subduction zones forced a change in the break-up regime of Gondwana. The seafloor spreading at SA–AFR, ANT–IND/SL, and IND-AUS began. Seafloor spreading between ANT–IND/SL/MAD and IND–AUS started with a 22–35 mm/yr average half spreading rate, indicating normal seafloor spreading. In contrast, SA–AFR was far from the east of EUR; therefore, seafloor spreading with a slow average rate of 15 mm/yr was produced between SA and AFR in this period.

(3) Third stage: about 124.6 Ma (M0) (Fig. 4-2b to Fig. 4-2c)

Part of the subduction zone between the Phoenix Plate and SA/ANT/AUS, located south of ANT/AUS, became extinct. A change in the driving force caused changes in the spreading regime, such as the direction and/or spreading rate, around the continental margins. The seafloor spreading of the mid-ocean ridge located at the north of IND was extinct, and the seafloor spreading between AFR–MAD was also extinct. Seafloor spreading between AFR and ANT likely started in this period.

(4) Final stage: < 124.6 Ma (Fig. 4-2c)

Spreading at AFR–ANT, ANT–IND/SL/MAD, and IND–AUS was oriented in the same direction. The half spreading rate of each margin was almost the same, with values of up to 40–55 mm/yr, like normal seafloor spreading.

I suggest that the upwelling of the large mantle plume was not indispensable for the initial fragmentation of the supercontinent Gondwana, and that intense volcanic activities, such as LIPs and hotspots, were therefore limited to local effects during the initial break-up of Gondwana.

An ultraslow spreading rate of 6 mm/yr was estimated based on the distance and age between 124.6–84 Ma as M0 and C34 (CNS) for the observed magnetic isochrons south of SL. In contrast, a normal spreading rate of up to 55 mm/yr was observed around conjugate areas such as the Bay of Bengal, the western margin of AUS, and the central Enderby Basin during the CNS. Compression of the seafloor was suggested between south of SL to the 85°E ridge (Ramana et al., 1997). The deformation of the seafloor between M0–C34 caused by the compression stress is one possible explanation for the differentiation in estimated spreading rates south of SL during the CNS. High-resolution geomagnetic data are necessary to reveal the formation and evolution processes for south of SL. New constraints will be obtained by vector geomagnetic surveying conducted south of SL.

The central Enderby Basin (CEB) is located between the Cosmonauts Sea to the west and the western margin of AUS to the east. The seafloor spreading before M0 was in the SE–NW direction in the Cosmonauts Sea and the western margin of AUS, whereas a N–S-oriented extinct ridge formed during M9–M0 was observed in the CEB in previous studies. There is an inconsistency in spreading direction and spreading scheme between the Cosmonauts Sea, the western margin of AUS, and the CEB. Thick sediment around the ANT margin produces ambiguous magnetic signals. Additionally, the volcanism of the Kerguelen Plateau at about 118 Ma (e.g., Frey et al., 2000) likely disturbed the continuous magnetic lineation. Moreover, the location of the continent–ocean boundary and continent–ocean transition zone in the CEB was only constrained by gravity anomalies, sparse seismic data, and sparse geomagnetic data. Therefore, vector geomagnetic observations that reveal the magnetic lineations and structure boundaries in the CEB are necessary for understanding the seafloor spreading history of the CEB.

In summary, my new findings constrain the initial break-up process of Gondwana in the Indian Ocean, especially around chrons M10 (133.5 Ma) and M0 (124.6 Ma). A relationship between the initial break-up process of Gondwana and the configuration of the subduction zones around Gondwana is proposed. The large extended continental crust with basaltic intrusion between the AFR, SA, and ANT was produced during the long period of the break-up process of West and East Gondwana. The timing of the spreading between AFR and ANT in my interpretation provides new constraints on Gondwana reconstruction models. Fragmentation of East Gondwana, such as the

present position and motion of the SL/IND/MAD, should be discussed based on my results from the Cosmonauts Sea. Further investigation, especially in the CEB and south of SL, may potentially lead to more detail on the initial break-up process of Gondwana. In the CEB, most geomagnetic observation lines that have been conducted were in the N–S or W–E directions. Between ANT–SL and IND, seismic surveys and drilling in the Cosmonauts Sea, including the Kainan-Maru Seamount, and south of SL will be needed to understand the fragmentation process of these continental blocks. Moreover, based on this study, SE–NW vector geomagnetic observation lines in the CEB will be required for my future work. Between the AFR and ANT, seafloor was formed during the CNS. Because revealing the seafloor spreading history during the CNS is a task that is global in scale, additional near-surface geomagnetic, seismic, and rock sampling surveys around the continental margins are necessary.

Table 4-1

Stages in Gondwana based on this study and previous studies. (a) Seafloor spreading started at about M12–M10. (b) Seafloor spreading after M0. (c) Intense volcanism before M0. Works in the gray-shaded cells are contradicted by the results of this study.

Table 4-1 (a)

Location	Half spreading rate	Spreading direction	Reference
Northern Natal Valley	*** <Extension>**	***N-S**	**This study**
	Extinct ridge with M4–M10: 13 mm/yr	N-S	Tikku et al. (2002)
Southern Natal Valley	**M10–N0: 13–16 mm/yr**	**NE-SW**	Martin et al. (1982)
			Goodlad et al. (1982)
			This study
	M4–M0: *no identification of rate*	NE-SW	Reznikov et al. (2005)
	No identification	NW-SE	Leinwever and Jokat (2011)
Falkland Plateau	M10–M0: 15–17 mm/yr	W-E	Martin et al. (1982)
South Atlantic	M12–M0: 10–15 mm/yr	W-E	Rabinowitz & RaBrecque (1979)
Central Enderby Basin	Extinct ridge with M0-M4: 30.5 mm/yr	N-S	Gibbons et al. (2013)
	M9–M4: 40 mm/yr, M4-M0: 16 mm/yr	N-S &WNW-ESE	Gaina et al. (2003)
Cosmonauts Sea	**M10N–M1n: 27–31 mm/yr**	**WNW-ESE in south**	**This study**
	M2–M4: 22 mm/yr, M4–M9: 39 mm/yr	NNE-SSW	Gaina et al. (2007)
	M11–M0: 28–65 mm/yr variable	N-S	Ramana et al. (2001)
	No identification *(M-series was inffered)*	WNW-ESE & NW-SE in south	Nogi et al. (1996)
South of Sri Lanka	M11–M10: 55 mm/yr, M10–M4: 52 mm/yr, M4–M0: decrease to 15 mm/yr	NNW-SSE & NW-SE	Desa et al. (2006)
	22–36 mm/yr	NNW-SSE & NW-SE	Gaina et al. (2007)
Bay of Bengal	M11–M9: 36 mm/yr, M4–M0: 34 mm/yr	NW-SE	Ramana et al. (1994)

(continued)

Table 4-1 (b)			
Location	Half spreading rate	Spreading direction	Reference
Southern Natal Valley	42–55 mm/yr average	NE-SW to ENE-WSW	Martin et al. (1982)
Falkland Plateau	42–55 mm/yr average	NE-SW to ENE-WSW	Martin et al. (1982)
South Atlantic	40–50 mm/yr	W-E	Rabinowitz and RaBrecque (1979)
Central Enderby Basin	22–40 mm/yr	S-N to SSW-NNE	Desa and Ramana (2016)
Cosmonauts Sea	*No identification*	**SE-NW to SSW-NNE**	**This study**
South of Sri Lanka	6 mm/yr	NNW-SSE & NW-SE to almost N-S	Desa et al. (2006)
South of Sri Lanka	*No identification*	NNW-SSE & NW-SE to almost N-S	Gaina et al. (2007)
Bay of Bengal	40–42 mm/yr	NNW-SSE & NW-SE to almost N-S	Desa and Ramana (2016)
Western of Australia	22–40 mm/yr	SE-NW to S-N	Desa and Ramana (2016)

(continued)

Table 4-1 (c)				
Location	Intense Volcanism	Name	Age	Reference
Antarctica	Observed	Explora Escarpment	183 Ma	Hinz et al. (2004)
Lazarev Sea	Observed	Astrid Ridge	183–120 Ma	e.g., eagles & König (2008)
	Observed	Maud Rise	120 Ma	e.g., Gohl et al. (2011)
Africa	Observed	Karoo	183–176 Ma	Jordan et al. (2008)
Northern Natal Valley	**Estimated**	**Related to Karoo?**	**183–130 Ma**	**This study**
North of Mozambique Ridge	**Estimated**	**Related to Karoo?**	**183–130 Ma**	**This study**
South of Mozambique Ridge	**Estimated**	**Interaction with Bouvet hotspot?**	**130–120 Ma**	**This study** e.g., König and Jokat (2010)
Off south Africa	Observed	Agulhas Plateau (Bouvet?)	After 120 Ma	e.g., Gohl et al. (2011)
South America–Africa	Observed	Paranà-Etendeca	133 Ma	e.g., Hawkesworth et al. (2000)
South Atlantic	Observed	St Helena	106 Ma	e.g., Coulon et al. (1996)
	Estimated	Tristan-Gough	After 130 Ma	eg., O'Connor and Duncan (1990)
Falkland Plateau	Observed	Northeast Georgia Rise	After 120 Ma	e.g., Gohl et al. (2011)
Central Enderby Basin	Observed	Kerguelen	After 118 Ma	e.g., Duncan (2002)
India	Observed	Rajmahal Traps	After 118 Ma	e.g., Baksi et al. (1987)
Cosmonauts Sea	*Not observed*			e.g., **This study**
south of Sri Lanka	*Not observed*			e.g., Desa et al. (2006)
Bay of Bengal	*Not observed*			e.g., Ramana et al. (1994)
Western margin of Australia	*Not observed*			e.g., Gibbons et al. (2012)

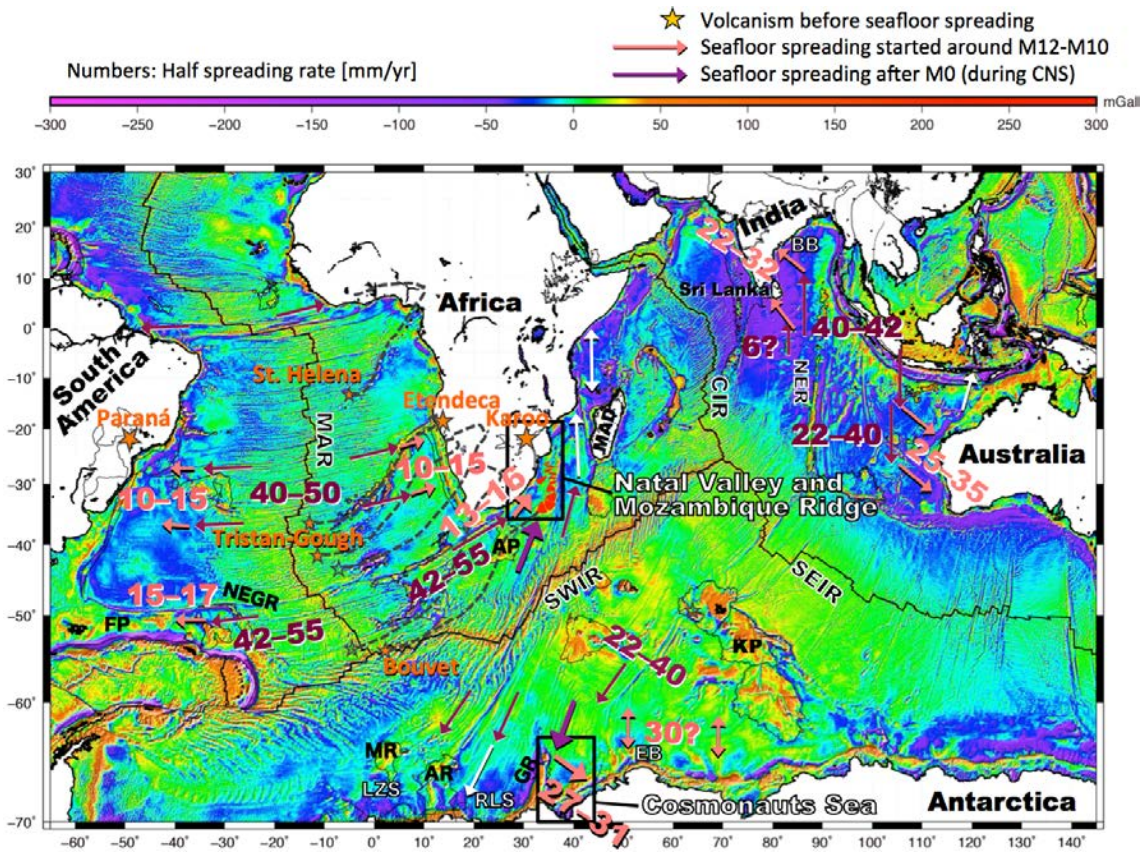

Fig. 4-1

Stages in Gondwana based on this study and previous studies superimposed on the free-air gravity anomaly map (Sandwell, 2014). Orange stars indicate volcanism, such as Large Igneous Provinces, before the occurrence of seafloor spreading. Pink arrows indicate seafloor spreading during M12–M0. Purple arrows indicate seafloor spreading after M0. The corresponding half spreading rates are also shown in the same colors as the arrows. MAD, Madagascar; MAR, Mid-Atlantic Ridge; SWIR, Southwest Indian Ridge; SEIR, Southeast Indian Ridge; CIR, Central Indian Ridge; NER, Ninety East Ridge; FP, Falkland Plateau; NEGR, North East Georgia Rise; AP, Agulhas Plateau; MR, Maud Rise; AR, Astrid Ridge; GR, Gunnerus Ridge; KP, Kerguelen Plateau; LZS, Lazarev Sea; RLS, Riiser-Larsen Sea; EB, Enderby Basin; BB, Bay of Bengal.

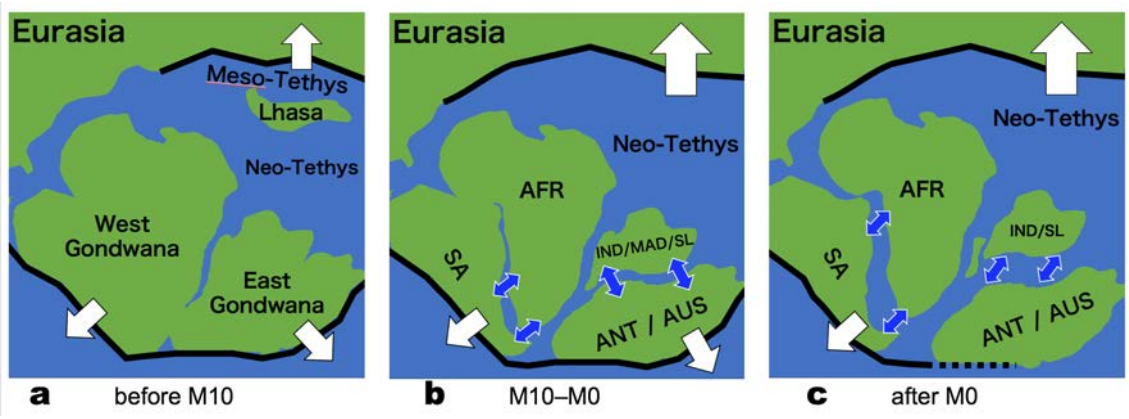

Fig. 4-2

Schematics of the Gondwana break-up (a) before M10, (b) at about M10–M0, and (c) after M0. Black lines show the subduction zones. Blue arrows indicate the seafloor spreading direction. White arrows indicate the direction of plate motion.

Chapter 5. Conclusion

To understand the initial break-up process of Gondwana, I investigated the Natal Valley and Mozambique Ridge, off South Africa, and the Cosmonauts Sea, off Antarctica, using vector geomagnetic field data. The multiple analytical results of vector geomagnetic anomalies and satellite-derived free-air gravity anomalies revealed the continental extension and seafloor spreading processes in both regions.

The nature of the Natal Valley and Mozambique Ridge was classified into four categories: (1) mixture of the stretched continental and oceanic crust; (2) stretched continental crust; (3) normal oceanic crust; and (4) oceanic crust interacted with volcanism. Magnetic isochrons of M10–M0 with NW–SE spreading direction were identified. I concluded that the seafloor spreading between South America and Africa in this region started at M10. The seafloor spreading between Antarctica and Africa likely started after M0, south of this region. I presented the first detailed formation and evolution model of the Natal Valley and Mozambique Ridge.

The crust of the Cosmonauts Sea was classified into two categories: (1) thinned continental crust, and (2) oceanic crust. The magnetic isochrons M10N–M3n with a WSW–ENE spreading direction were newly identified. Change in the spreading direction during M3n–M0r was inferred, and the SSW–NNE-oriented seafloor spreading during the Cretaceous Normal Superchron was implied. I presented the processes of continental extension and seafloor spreading in the Cosmonauts Sea.

Vector geomagnetic anomalies with a few systematic observation lines make it possible to detect the distinct direction of the seafloor spreading and the position of the polarity change. Vector geomagnetic anomalies are an efficient tool for understanding the structural boundaries that are buried by thick sediment and disturbed by volcanic intrusion, and formed during the Cretaceous Normal Superchron.

I compiled the initial break-up processes of Gondwana, focused on around M10–M0. Configuration of the subduction zones surrounding likely forced the seafloor spreading during the periods of M12–M10 and M0. Intense volcanic activities, such as LIPs and hotspots, were not indispensable for the initial fragmentation of Gondwana. My new findings concerning the initial break-up process of Gondwana contribute greatly to the understanding of solid earth dynamics, such as the relationship with mantle convection.

The Gondwana reconstruction model should be constrained based on my results, especially in terms of (1) the timing of the seafloor spreading between Africa and Antarctica, and (2) the present positions and motion of Sri Lanka, India, and Madagascar.

Further investigation of tectonic history, especially in the south of Sri Lanka and the central Enderby Basin, may provide more detail on the initial break-up process of Gondwana. Moreover, revealing the seafloor spreading history during the Cretaceous Normal Superchron is a task of global scale. Additional near-surface geomagnetic, seismic, and rock sampling surveys around the continental margins will provide stable constraints for the detailed initial break-up process of Gondwana.

Acknowledgments

I first would like to express my sincere gratitude to my supervisor Yoshifumi Nogi for providing me with this precious study opportunity and continuous support of my PhD studies, and for his patience, motivation, and immense knowledge. He has also provided me with many opportunities to meet a number of domestic and foreign researchers, which helped to widen the scope of my research.

I am also deeply grateful to my advisor Masakazu Fujii for invaluable discussion, comments, and suggestions on my research. He encouraged and helped my work from the processing of data to the publication of articles. The various discussions we had regarding magnetic anomalies were essential for this work, and will be the basis of my future studies.

I am very grateful to my advisors Kyoko Okino at the Atmosphere & Ocean Research Institute, University of Tokyo (AORI), Toshiya Fujiwara at the Japan Agency for Marine-Earth Science and Technology (JAMSTEC), and Hiroshi Sato at the School of Business Administration, Senshu University, for their elaborate guidance, considerable encouragement, and discussions that enabled the great achievement of my research and made my research experience unforgettable.

In addition, I would like to extend my gratitude to Kazuo Shibuya, Hiroshi Funaki, Kouichrou Doi, Tomokazu Hokada, Yuichi Aoyama, Jyunichi Okuno, Yusuke Suganuma, and Tomoe Andou for their motivation, enthusiasm and kind words of encouragement.

Fieldwork was supported by a number of people. I especially thank Wilfried Jokat at the Alfred Wegener Institute for Polar and Marine Research (AWI) and Volker Thor Leinweber for their support and discussions on various aspects of this research during the AISTEK-III cruise.

I am grateful to many researchers for offering sound advice in the meetings, workshops, and research cruises, including Makoto Yamano at the Earthquake Research Institute, The University of Tokyo (ERI), Tadanori Goto at Kyoto University, Nobukazu Seama at Kobe University, Minoru Ikehara at the Center for Advanced Marine Core Research, Kochi University, Kentaro Nakamura at JAMSTEC, Kiyoshi Baba at ERI, Hideki Hamamoto at the Center for Environmental Science in Saitama, Nobutatsu Mochizuki at Kumamoto University, Tetsuo Matsuno in Kobe University,

Kazuya Kitada at JAMSTEC, Ryoko Senda at Kyushu University, Taichi Sato at the National Institute of Advanced Industrial Science and Technology (AIST), Miho Asada at JAMSTEC, Ayanori Misawa at AIST, Yuka Masaki at JAMSTEC, Daisuke Sasano at the Meteorological Research Institute, Kiichirou Kawamura at Fukada Geological Institute, Tomomi Minamizawa at Nippon Marine Enterprises Ltd., Chiori Tamura at AORI, and Shinichirou Yokogawa at Marine Works Japan Ltd.

For providing great support on board ship and during field observations during the 53th Japanese Antarctica Research Expedition (JARE53), I thank expedition leader Hisao Yamagishi, deputy leader Kenji Ishizawa, and the Geophysics team: Toshihiro Higashi at TerraGrav LLC, Takahito Kazama at Kyoto University, Shingo Ohsono at GNSS Technologies Inc., Hideaki Hayakawa at NIPR, Harumi Ohta at Global Ocean Development Inc., and Noriaki Izumi at Japan Coast Guard.

I also thank the crew of R/Vs *Pelagia*, *Kairei*, *Tansei-Maru*, and *Hakuho-Maru*, and the icebreaker *Shirase* for their kind help during the AISTEK-III, KR08-10, KT-08-25, KH-09-5 leg.3–leg.4, KH-10-6, KH-10-7, and JARE53 cruises.

I am very grateful to Graeme Eagles at AWI for supplying total magnetic anomaly data and multibeam sounding data from AISTEK II and AISTEK III, and for his helpful comments on my study. I would like to thank Jerome Dyment at the Institute de Physique du Globe Paris for his advices and discussion. I have been financially supported by the National Institute of Polar Research through Project Research KP-7 and KP-306.

I am grateful to my academic seniors and colleagues in the Graduate University for Advanced Studies [SOKENDAI]: Yukiko Tanabe, Takeshi Inoue, Yuuta Tanoue, Kaoru Shiramizu, and Masahiro Yasutake, for their encouragement and helpful advice for my study.

My heartfelt appreciation goes to members of my previous workplace, including Naoya Wada, Yoshinari Awaji, and Hideo Furukawa at the Photonic Network System Laboratory, National Institute of Information and Communications Technology, for providing me fresh opportunity and encouragement.

Finally, I would like to express my indebtedness to my family, and friends since my undergraduate years at Tokyo Metropolitan University: Yoshinobu Takahashi, Motoki Shinoda, Ryuji Fujiwara, and Kazuyuki Fuchigami, for their support, understanding, and warm encouragement throughout my studies.

References

Amante, C., & Eakins, B. W. (2009). *ETOPO1 1 arc-minute global relief model: procedures, data sources and analysis*. US Department of Commerce, National Oceanic and Atmospheric Administration, National Environmental Satellite, Data, and Information Service, National Geophysical Data Center, Marine Geology and Geophysics Division Colorado.

Baranov, A., & Morelli, A. (2013). The Moho depth map of the Antarctica region. *Tectonophysics*, *609*, 299–313.

Ben-Avraham, Z., Hartnady, C. J. H., & Leroex, A. P. (1995). Neotectonic Activity on Continental Fragments in the Southwest Indian Ocean: Agulhas Plateau and Mozambique Ridge. *Journal of Geophysical Research: Solid Earth*, *100*(B4), 6199–6211. doi.org/10.1029/94jb02881

Brune, S., Heine, C., Pérez-Gussinyé, M., & Sobolev, S. V. (2014). Rift migration explains continental margin asymmetry and crustal hyper-extension. *Nature Communications*, *5*.

Cande, S. C., Larson, R. L., & LaBrecque, J. L. (1978). Magnetic lineations in the Pacific Jurassic quiet zone. *Earth and Planetary Science Letters*, *41*(4), 434–440.

Coulon, C., Vidal, P., Dupuy, C., Baudin, P., Popoff, M., Maluski, H., & Hermitte, D. (1996). The Mesozoic to early Cenozoic magmatism of the Benue Trough (Nigeria); Geochemical evidence for the involvement of the St Helena plume. *Journal of Petrology*, *37*(6), 1341–1358.

Cox, K. G. (1970). Tectonics and vulcanism of the Karroo period and their bearing on the postulated fragmentation of Gondwanaland. In *African magmatism and tectonics* (pp. 211–235). Oliver and Boyd Edinburgh.

Cox, K. G. (1992). Karoo igneous activity, and the early stages of the break-up of Gondwanaland. *Geological Society, London, Special Publications*, *68*(1), 137–148. doi.org/10.1144/GSL.SP.1992.068.01.09

Darracott, B. W. (1974). On the crustal structure and evolution of southeastern Africa and the adjacent Indian Ocean. *Earth and Planetary Science Letters*, *24*(2), 282–290. doi.org/10.1016/0012-821X(74)90106-X

Davison, I. A. N. (1997). Wide and narrow margins of the Brazilian South Atlantic. *Journal of the Geological Society*, *154*(3), 471–476.

Desa, M. A., & Ramana, M. V. (2016). Middle Cretaceous geomagnetic field anomalies in the Eastern Indian Ocean and their implication to the tectonic evolution of the Bay of Bengal. *Marine Geology*, *382*, 111–121.

Desa, M., Ramana, M. V, & Ramprasad, T. (2006). Seafloor spreading magnetic anomalies south off Sri Lanka. *Marine Geology*, *229*(3), 227–240.

Dietz, R. S. (1961). Continent and ocean basin evolution by spreading of the sea floor. *Nature*, *190*(4779), 854–857.

Dietz, R. S., & Holden, J. C. (1970). Reconstruction of Pangea: Breakup and dispersion of continents, Permian to Present. *Journal of Geophysical Research*, *75*(26), 4939–4956.

Domingues, A., Silveira, G., Ferreira, A. M. G., Chang, S.-J., Custódio, S., & Fonseca, J. F. B. D. (2016). Ambient noise tomography of the East African Rift in Mozambique. *Geophysical Journal International*, *204*(3), 1565–1578.

Duncan, R. A. (1984). Age progressive volcanism in the New England Seamounts and the opening of the central Atlantic Ocean. *Journal of Geophysical Research: Solid Earth*, *89*(B12), 9980–9990. doi.org/10.1029/JB089iB12p09980

Dyment, J., Choi, Y., Hamoudi, M., Lesur, V., & Thebault, E. (2015). Global equivalent magnetization of the oceanic lithosphere. *Earth and Planetary Science Letters*, *430*, 54–65. doi.org/10.1016/j.epsl.2015.08.002

Eagles, G. (2007). New angles on South Atlantic opening. *Geophysical Journal International*, *168*(1), 353–361.

Eagles, G., & König, M. (2008). A model of plate kinematics in Gondwana breakup. *Geophysical Journal International*, *173*(2), 703–717.

Eagles, G., Pérez-Díaz, L., & Scarselli, N. (2015). Getting over continent ocean boundaries. *Earth-Science Reviews*. doi.org/10.1016/j.earscirev.2015.10.009

Erlank, A. J., & Reid, D. L. (1974). Geochemistry, mineralogy, and petrology of basalts, LEG 25, Deep Sea Drilling Project. *Initial Reports of the Deep Sea Drilling Project*, *25*, 543–551.

Frey, F. A., Coffin, M. F., Wallace, P. J., Weis, D., Zhao, X., Wise, S. W., et al. (2000). Origin and evolution of a submarine large igneous province: the Kerguelen Plateau and Broken Ridge, southern Indian Ocean. *Earth and Planetary Science Letters*, *176*(1), 73–89.

Gaina, C., Müller, R. D., Brown, B., Ishihara, T., & Ivanov, S. (2007). Breakup and early seafloor spreading between India and Antarctica. *Geophysical Journal International*, *170*(1), 151–169. doi.org/10.1111/j.1365-246X.2007.03450.x

Gibbons, A. D., Barckhausen, U., den Bogaard, P., Hoernle, K., Werner, R., Whittaker, J. M., & Müller, R. D. (2012). Constraining the Jurassic extent of Greater India: Tectonic evolution of the West Australian margin. *Geochemistry, Geophysics, Geosystems*, *13*(5).

Gibbons, A. D., Whittaker, J. M., & Müller, R. D. (2013). The breakup of East Gondwana: Assimilating constraints from Cretaceous ocean basins around India into a best-fit tectonic model. *Journal of Geophysical Research: Solid Earth*, *118*(3), 808–822.

Gohl, K., Uenzelmann-Neben, G., & Grobys, N. (2011). Growth and dispersal of a Southeast African large igneous province. *South African Journal of Geology*, *114*(3–4), 379–386. doi.org/10.2113/gssajg.114.3-4.379

Goodlad, S. W., Martin, A. K., & Hartnady, C. J. H. (1982). Mesozoic magnetic anomalies in the southern Natal Valley. *Nature, 295(5851), 686-688*. doi.org/10.1038/295686a0

Gradstein, F. M., Ogg, J. G., & van Kranendonk, M. (2008). On the Geologic Time Scale 2008. *Newsletters on Stratigraphy*, *43*(1), 5–13. doi.org/10.1127/0078-0421/2008/0043-0005

Hartnady, C. J. H., & Le Roex, A. P. (1985). Southern Ocean hotspot tracks and the Cenozoic absolute motion of the African, Antarctic, and South American plates. *Earth and Planetary Science Letters*, *75*(2–3), 245–257.

Hawkesworth, C. J., Gallagher, K., Kirstein, L., Mantovani, M. S. M., Peate, D. W., & Turner, S. P. (2000). Tectonic controls on magmatism associated with continental break-up: an example from the Paraná–Etendeka Province. *Earth and Planetary Science Letters*, *179*(2), 335–349.

Hinz, K., & Krause, W. (1982). The continental margin of Queen Maud Land, Antarctica: Seismic sequences, structural elements and geological development. *Geologisches Jahrbuch, E23,* 17–41.

Hinz, K., Neben, S., Gouseva, Y. B., & Kudryavtsev, G. A. (2004). A compilation of geophysical data from the Lazarev Sea and the Riiser-Larsen Sea, Antarctica. *Marine Geophysical Researches*, *25*(3–4), 233–245. doi.org/10.1007/s11001-005-1319-y

Hochmuth, K., Gohl, K., Leitchenkov, G., Whittaker, J., De Santis, L., Olivo, E. (2017). Paleobathymetric grids of the Cenozoic Southern Oceanan update on a community based project, *Abstract of Past Antarctic Ice Sheet Dynamics (PAIS) Conference 2017, Italy*.

Holmes, A. (1931). XVIII. Radioactivity and Earth Movements. *Transactions of the Geological Society of Glasgow*, *18*(3), 559–606.

Isezaki, N. (1986). A new shipboard three-component magnetometer. *Geophysics*, *51*(10), 1992–1998. https://doi.org/10.1190/1.1442054

Jokat, W., Nogi, Y., & Leinweber, V. (2010). New aeromagnetic data from the western Enderby Basin and consequences for Antarctic-India break-up. *Geophysical Research Letters*, *37*(21), doi.org/10.1029/2010GL045117

Jokat, W., Ritzmann, O., Reichert, C., & Hinz, K. (2004). Deep crustal structure of the continental margin off the Explora Escarpment and in the Lazarev Sea, East Antarctica. *Marine Geophysical Researches*, *25*(3–4), 283–304. doi.org/10.1007/s11001-005-1337-9

Jourdan, F., Féraud, G., Bertrand, H., Watkeys, M. K., & Renne, P. R. (2008). The 40Ar/39Ar ages of the sill complex of the Karoo large igneous province: Implications for the Pliensbachian-Toarcian climate change. *Geochemistry, Geophysics, Geosystems*, *9*(6). doi.org/10.1029/2008GC001994

Kitada, K. (2008). ポテンシャル場を用いた大陸分裂と海洋底拡大の研究, *Doctoral Thesis. Kobe University.*

König, M., & Jokat, W. (2010). Advanced insights into magmatism and volcanism of the Mozambique Ridge and Mozambique Basin in the view of new potential field data. *Geophysical Journal International*, *180*(1), 158–180. doi.org/10.1111/j.1365-246X.2009.04433.x

Kuo, B. Y., & Forsyth, D. W. (1988). Gravity anomalies of the ridge transform system in the South Atlantic between 31 and 34.5°S: Upwelling centres and variations in crustal thickness. *Marine Geophysical Researches*, *10*, 205–232.

Laske, G., & Masters, G. (1997). A global digital map of sediment thickness. *Eos, Transactions American Geophysical Union*, *78*(78), F483.

Lawver, L. A., Gahagan, L. M., & Coffin, M. F. (1992). The development of paleoseaways around Antarctica. *The Antarctic Paleoenvironment: A Perspective on Global Change: Part One*, 7–30.

Lawver, L. A., Gahagan, L. M., & Dalziel, I. W. D. (1998). A Tight fit-Early Mesozoic Gondwana, a Plate Reconstruction Perspective. *Memoirs of National Institute of Polar Research. Special Issue*, *53*, 214–229. Retrieved from http://ci.nii.ac.jp/naid/110000010427/

Leinweber, V. T., & Jokat, W. (2011). Is there continental crust underneath the northern Natal Valley and the Mozambique Coastal Plains? *Geophysical Research Letters*, *38*(14), 1–7. doi.org/10.1029/2011GL047659

Leinweber, V. T., & Jokat, W. (2012). The Jurassic history of the Africa-Antarctica corridor: New constraints from magnetic data on the conjugate continental margins. *Tectonophysics*, *530–531*, 87–101. doi.org/10.1016/j.tecto.2011.11.008

Ludwig, W. J., Nafe, J. E., Simpson, E. S. W., & Sacks, S. (1968). Seismic-refraction measurements on the Southeast African Continental Margin. *Journal of Geophysical Research*, *73*(12), 3707. doi.org/10.1029/JB073i012p03707

Martin, A. K., Goodlad, S. W., Hartnady, C. J. H., & du Plessis, A. (1982). Cretaceous palaeopositions of the Falkland Plateau relative to southern Africa using Mesozoic seafloor spreading anomalies. *Geophysical Journal of the Royal Astronomical Society*, *71*(3), 567–579. doi.org/10.1111/j.1365-246X.1982.tb02784.x

Matthews, K. J., Hale, A. J., Gurnis, M., Müller, R. D., & DiCaprio, L. (2011). Dynamic subsidence of Eastern Australia during the Cretaceous. *Gondwana Research*, *19*(2), 372–383.

Maus, S., Barckhausen, U., Berkenbosch, H., Bournas, N., Brozena, J., Childers, V., Von Frese, R. R. B., et al. (2009). EMAG2: A 2–arc min resolution Earth Magnetic Anomaly Grid compiled from satellite, airborne, and marine magnetic measurements. *Geochemistry, Geophysics, Geosystems*, *10*(8).

McKenzie, D. P., & Sclater, J. G. (1971). The Evolution of the Indian Ocean since the Late Cretaceous. *Geophysical Journal of the Royal Astronomical Society*, *25*, 437–528. doi.org/10.1038/scientificamerican0573-62

McKenzie, D., & Bickle, M. J. (1988). The volume and composition of melt generated by extension of the lithosphere. *Journal of Petrology*, *29*(3), 625–679.

Metcalfe, I. (2011). Palaeozoic–Mesozoic history of SE Asia. *Geological Society, London, Special Publications*, *355*(1), 7–35.

Morley, L. W., & Larochelle, A. (1964). Paleomagnetism as a means of dating geological events. *Geochronology in Canada*, (8), 39.

Mougenot, D., Gennesseaux, M., Hernandez, J., Lepvrier, C., Malod, J. A., Raillard, S., et al., (1991). La ride du Mozambique (Océan Indien): Un fragment continental individualisé lors du coulissement de l'Amérique et de l'Antarctique le long de l'Afrique de l'Est? *Comptes rendus de l'Académie des sciences. Série 2, Mécanique, Physique, Chimie, Sciences de l'univers, Sciences de la Terre*, *312*(6), 655–662. Retrieved from http://cat.inist.fr/?aModele=afficheN&cpsidt=19815705

Müller, R. D., Seton, M., Zahirovic, S., Williams, S. E., Matthews, K. J., Wright, N. M., et al., (2016). Ocean basin evolution and global-scale plate reorganization events since Pangea breakup. *Annual Review of Earth and Planetary Sciences*, *44*, 107–138.

Nogi, Y., Seama, N., Isezaki, N., & Fukuda, Y. (1996). Magnetic anomaly lineations and fracture zones deduced from vector magnetic anomalies in the West Enderby Basin. *Geological Society, London, Special Publications*, *108*(1), 265–273.

Parker, R. L. (1972). The rapid calculation of potential anomalies. *Geophysical Journal of the Royal Astronomical Society*, *31*(4), 447–455.

Parker, R. L., & Huestis, S. P. (1974). The inversion of magnetic anomalies in the presence of topography. *Journal of Geophysical Research*, *79*(11), 1587–1593. doi.org/10.1029/JB079i011p01587

Pavlis, N. K., Holmes, S. A., Kenyon, S. C., & Factor, J. K. (2012). The development and evaluation of the Earth Gravitational Model 2008 (EGM2008). *Journal of Geophysical Research: Solid Earth*, *117*(B4). doi.org/10.1029/2011JB008916

Rabinowitz, P. D., & LaBrecque, J. (1979). The Mesozoic South Atlantic Ocean and Evolution of Its Continental Margins. *Journal of Geophysical Research*, *84*(B11), 5973–6002. doi.org/10.1029/JB084iB11p05973

Raillard, S. (1990). *Les marges de l'Afrique de l'Est et les zones de fracture associées: Chaine Davie et Ride du Mozambique*.

Ramana, M. V, Nair, R. R., Sarma, K., Ramprasad, T., Krishna, K. S., Subrahmanyam, V., … Subrahmanyam, A. S. (1994). Mesozoic anomalies in the Bay of Bengal. *Earth and Planetary Science Letters*, *121*(3–4), 469–475.

Ramana, M. V, Ramprasad, T., & Desa, M. (2001). Seafloor spreading magnetic anomalies in the Enderby Basin, East Antarctica. *Earth and Planetary Science Letters*, *191*(3), 241–255.

Ramana, M. V, Subrahmanyam, V., Chaubey, A. K., Ramprasad, T., Sarma, K., Krishna, K. S., Subrahmanyam, C., et al. (1997). Structure and origin of the 85 E Ridge. *Journal of Geophysical Research: Solid Earth*, *102*(B8), 17995–18012.

Reeves, C., & de Wit, M. (2000). Making ends meet in Gondwana: Retracing the transforms of the Indian Ocean and reconnecting continental shear zones. *Terra Nova*, *12*(6), 272–280. doi.org/10.1046/j.1365-3121.2000.00309.x

Reznikov, M., Ben-Avraham, Z., Hartnady, C., & Niemi, T. M. (2005). Structure of the Transkei Basin and Natal Valley, Southwest Indian Ocean, from seismic reflection and potential field data. *Tectonophysics*, *397*(1–2 SPEC. ISS.), 127–141. doi.org/10.1016/j.tecto.2004.11.002

Ritzwoller, M. H., Shapiro, N. M., Levshin, A. L., & Leahy, G. M. (2001). Crustal and upper mantle structure beneath Antarctica and surrounding oceans. *Journal of Geophysical Research: Solid Earth*, *106*(B12), 30645–30670.

Royer, J.-Y., & Coffin, M. F. (1992). 50. Jurassic to Eocene plate tectonic reconstructions in the Kerguelen Plateau Region1. In *Proceedings of the Ocean Drilling Program: Scientific results* (p. 917).

Sager, W. W. (2005). What built Shatsky Rise, a mantle plume or ridge tectonics? *Geological Society of America Special Papers*, *388*(0), 721–733. doi.org/10.1130/0-8137-2388-4.721

Sager, W. W., Weiss, C. J., Tivey, M. A., & Johnson, H. P. (1998). Geomagnetic polarity reversal model of deep-tow profiles from the Pacific Jurassic Quiet Zone. *Journal of Geophysical Research: Solid Earth*, *103*(B3), 5269–5286.

Sandwell, D. T., Müller, R. D., Smith, W. H. F., Garcia, E., & Francis, R. (2014). New global marine gravity model from CryoSat-2 and Jason-1 reveals buried tectonic structure. *Science*, *346*(6205), 65–67.

Sandwell, D. T., & Smith, W. H. F. (2009). Global marine gravity from retracked Geosat and ERS-1 altimetry: Ridge segmentation versus spreading rate. *Journal of Geophysical Research: Solid Earth*, *114*(1), 1–18. doi.org/10.1029/2008JB006008

Schettino, A., & Scotese, C. R. (2005). Apparent polar wander paths for the major continents (200 Ma to the present day): A palaeomagnetic reference frame for global plate tectonic reconstructions. *Geophysical Journal International*, *163*(2), 727–759. doi.org/10.1111/j.1365-246X.2005.02638.x

Scrutton, R. A. (1976). Continental breakup and deep crustal structure at the margins of southern Africa. *Anais Da Academia Brasileira De Ciencias*, *48*, 275–286.

Scrutton, R. A. (1973). Structure and evolution of the sea floor south of South Africa. *Earth and Planetary Science Letters*, *19*(2), 250–256. doi.org/10.1016/0012-821X(73)90125-8

Seama, N., Nogi, Y., & Isezaki, N. (1993). A new method for precise determination of the position and strike of magnetic boundaries using vector data of the

geomagnetic anomaly field. *Geophysical Journal International*, *113*(1), 155–164. doi.org/10.1111/j.1365-246X.1993.tb02536.x

Seton, M., Müller, R. D., Zahirovic, S., Gaina, C., Torsvik, T., Shephard, G., Maus, S., et al. (2012). Global continental and ocean basin reconstructions since 200 Ma. *Earth-Science Reviews*, *113*(3), 212–270.

Seton, M., Whittaker, J. M., Wessel, P., Müller, R. D., DeMets, C., Merkouriev, S., et al. (2014). Community infrastructure and repository for marine magnetic identifications. *Geochemistry, Geophysics, Geosystems*, *15*(4), 1629–1641.

Shephard, G. E., Müller, R. D., & Seton, M. (2013). The tectonic evolution of the Arctic since Pangea breakup: Integrating constraints from surface geology and geophysics with mantle structure. *Earth-Science Reviews*, *124*, 148–183.

Stagg, H. M. J., Colwel, J. B., Direen, N. G., O'Brien, P. E., Bernardel, G., Borissova, I., et al. (2004). Geology of the continental margin of Enderby and Mac. Robertson Lands, East Antarctica: Insights from a regional data set. *Marine Geophysical Researches*, *25*(3–4), 183–219.

Storey, B. C. (1995). The role of mantle plumes in continental breakup: Case histories from Gondwanaland. *Nature*, *377*(6547), 301.

Symonds, P. A., Planke, S., Frey, O., & Skogseid, J. (1998). Volcanic evolution of the Western Australian continental margin and its implications for basin development. *The Sedimentary Basins of Western Australia*, *2*, 33–54.

Talwani, M. (1964). Computation of magnetic anomalies caused by two dimensional structures of arbitrary shape. *Computers in the Mineral Industries*, *1*, 464–480.

Talwani, M., Desa, M. A., Ismaiel, M., & Sree Krishna, K. (2016). The Tectonic origin of the Bay of Bengal and Bangladesh. *Journal of Geophysical Research: Solid Earth*, *121*(7), 4836–4851. doi.org/10.1002/2015JB012734

Tikku, A. A., Marks, K. M., & Kovacs, L. C. (2002). An Early Cretaceous extinct spreading center in the northern Natal valley. *Tectonophysics*, *347*(1–3), 87–108. doi.org/10.1016/S0040-1951(01)00239-6

Tivey, M. A., Sager, W. W., Lee, S. M., & Tominaga, M. (2006). Origin of the Pacific Jurassic quiet zone. *Geology*, *34*(9), 789–792. doi.org/10.1130/G22894.1

Torsvik, T. H., & Voo, R. Van der. (2002). Refining Gondwana and Pangea Palaeogeography: Estimates of Phanerozoic non-dipole (octupole) fields. *Geophysical Journal International*, *151*(3), 771–794.

Van der Voo, R., Mauk, F. J., & French, R. B. (1976). Permian-Triassic continental configurations and the origin of the Gulf of Mexico. *Geology*, *4*(3), 177–180.

Van der Voo, R., Spakman, W., & Bijwaard, H. (1999). Tethyan subducted slabs under India. *Earth and Planetary Science Letters*, 171(1), 7–20.

Vine, F. J., & Matthews, D. H. (1963). Magnetic anomalies over oceanic ridges. *Nature*, *199*(4897), 947–949.

Wegener Alfred, L. (1912). *The Origin of Continents and Oceans.* Methuen, London.

Wessel, P., & Smith, W. H. F. (1998). New, improved version of Generic Mapping Tools released. *Eos, Transactions American Geophysical Union*, *79*(47), 579.

White, R. S., McKenzie, D., & O'Nions, R. K. (1992). Oceanic crustal thickness from seismic measurements and rare earth element inversions. *Journal of Geophysical Research: Solid Earth*, *97*(B13), 19,683-19,715.

Wilson, J. T. (1968). A revolution in earth science. *Canadian Mining and Metallurgical Bulletin*, *61*, 185.

Wilson, J. T. (1968). Static or mobile earth: The current scientific revolution. *Proceedings of the American Philosophical Society*, *112*(5), 309–320.